

Doctoral thesis

Doctoral theses at NTNU, 2023:144

Erick Fernando Alves

# Optimization of Energy Storage for Frequency Control in Autonomous AC Power Systems

Frameworks for Planning and Operation

**NTNU**  
Norwegian University of Science and Technology  
Thesis for the Degree of  
Philosophiae Doctor  
Faculty of Information Technology and Electrical  
Engineering  
Department of Electric Energy



Norwegian University of  
Science and Technology



Erick Fernando Alves

# **Optimization of Energy Storage for Frequency Control in Autonomous AC Power Systems**

Frameworks for Planning and Operation

Thesis for the Degree of Philosophiae Doctor

Trondheim, May 2023

Norwegian University of Science and Technology  
Faculty of Information Technology and Electrical Engineering  
Department of Electric Energy



Norwegian University of  
Science and Technology

**NTNU**

Norwegian University of Science and Technology

Thesis for the Degree of Philosophiae Doctor

Faculty of Information Technology and Electrical Engineering  
Department of Electric Energy

© Erick Fernando Alves

ISBN 978-82-326-5254-9 (printed ver.)

ISBN 978-82-326-5867-1 (electronic ver.)

ISSN 1503-8181 (printed ver.)

ISSN 2703-8084 (online ver.)

IMT-report 2023:144

Doctoral theses at NTNU, 2023:144

Printed by NTNU Grafisk senter



**NTNU**

*Norges teknisk-naturvitenskapelige universitet*

Norwegian University of Science and Technology

Thesis for the Degree of Philosophiae Doctor  
Faculty of Information Technology and Electrical Engineering  
Department of Electric Energy

Submitted 14/11/2022;

Approved 11/04/2023;

Date of defense 15/05/2023; Rådssrommet G144 | (13:15)

Supervisors

Prof. Elisabetta Tedeschi & Prof. Magnus Korpås

Assessment Committee

- ▶ 1st opponent  
Prof. Dr. Igor Kuzle,  
University of Zagreb  
Zagreb, Croatia
- ▶ 2nd opponent  
Dr. Fei Teng,  
Imperial College London  
London, United Kingdom
- ▶ Additional members of the committee and administrator  
Prof. Karen Byskov Lindberg

---

**OPTIMIZATION OF ENERGY STORAGE FOR FREQUENCY CONTROL IN AUTONOMOUS AC  
POWER SYSTEMS: FRAMEWORKS FOR PLANNING AND OPERATION**

Chapters 1-2,9-11 © 2022 Author (unless otherwise stated)

Chapters 3-4 © 2019 Author (unless otherwise stated)

Chapter 5 © 2020 Elsevier

Chapters 6-7 © 2020 Author (unless otherwise stated)

Chapters 8 © 2021 Author (unless otherwise stated)

ISBN 978-82-326-5254-9 (printed ver.)

ISBN 978-82-326-5867-1 (electronic ver.)

ISSN 1503-8181 (printed ver.)

ISSN 2703-8084 (online ver.)

Doctoral theses at NTNU, 2023:144

Printed by NTNU Grafisk senter



*Dedicated to my dearest  
Penélope*

*And to all  
patient teachers I had in my life.*



There are many hypotheses in science which are wrong. That's perfectly all right: it's the aperture to finding out what's right. Science is a self-correcting process. To be accepted, new ideas must survive the most rigorous standards of evidence and scrutiny.

- Carl SAGAN, Cosmos



Try and leave this world a little better than you found it, and when your turn comes to die you can die happy in feeling that at any rate you have not wasted your time but have done your best.

- Robert Stephenson BADEN-POWELL, B-P's Last Will



## *Abstract*

---

AC power systems have been designed to balance active power from the generation side, adopting technologies that offer three important properties: dispatch capability, ability to participate in frequency control, and large energy storage capacity. Such technologies have been displaced by variable renewable energy sources, such as wind and solar power, interfaced to the system via power electronic converters, which do not offer concurrently the three key properties of established equipment, thus introducing new dilemmas for planning and operation of power systems.

Alternative schemes are being deployed to increase control of power flows and optimize energy storage capacity. Flexible loads and distributed energy storage devices, for instance, can be coordinated by energy management systems to provide power balancing mechanisms. Such advances, on the one hand, allow adequate power dispatch, balancing reserves, and storage capacity to be reached. On the other hand, they have major technical and economic impacts, affecting capital and operational expenditures, security of supply, and power system stability. Therefore, it is necessary to review and improve the tools and methods employed for planning and operation of power systems to accommodate these changes. This issue becomes more critical in autonomous grids, where a limited number of generators and storage devices are regularly available.

This thesis is a collection of eight publications addressing this challenge. Together, they: 1) review the active power balance problem and the principles of frequency control and stability in ac power systems, 2) identify gaps in current modeling practices that can affect planning and operation of autonomous systems where high penetration of variable renewable energy sources exists, and 3) explore how frequency control and stability constraints can be integrated into different power system optimization models. The main result is a set of frameworks that can be applied to optimization problems typically employed in planning and operation of autonomous systems. They are used for optimal sizing or scheduling of equipment and for ensuring stable and secure operation under dynamic uncertainty in different case studies of industrial oil and gas installations. Despite the focus in oil and gas applications, the main ideas and propositions can be generalized and applied to other autonomous systems, such as microgrids in islanded mode.





## Preface

---

This thesis is submitted as partial fulfillment of the requirements for the Philosophiæ Doctor degree at the Norwegian University of Science and Technology. This doctoral work has been carried out in the Department of Electric Energy, Faculty of Information Technology and Electrical Engineering. Professors Elisabetta Tedeschi and Magnus Korpås were the main supervisor and co-supervisor, respectively.

Over four years, the researcher:

- executed the research work described in this thesis (from September 2018 to October 2022).
- performed research duties at the Department of Electric Energy in the European Union’s Horizon 2020 project IMAGINE: Innovative Method for Affordable Generation IN ocean Energy under grant agreement No. 764066 (from October 2018 to September 2020).
- collaborated with Total Energies and the research group of Professor Gilles Guerassimoff at the Centre for Applied Mathematics, MINES ParisTech PSL (from August 2021 to March 2022).

This doctoral work was funded by the Research Council of Norway through the program PETROMAKS2, grant number 281986, project “[Innovative Hybrid Energy System for Stable Power and Heat Supply in Offshore Oil & Gas Installation \(HES-OFF\)](#)”.

### SCOPE AND OBJECTIVES

One of the key challenges in the real-time operation of electric ac power systems<sup>1</sup> is to balance active power demand and production at every instant. This balance is typically observed in the electrical frequency: if the latter rises above its rated value, there is power surplus in the system; if it lowers, there is power deficit. Power systems are considered frequency stable if their control systems are capable of riding through power imbalances and curbing frequency deviations to predefined limits. Electrical frequency stability is therefore a necessary

---

<sup>1</sup>Denoted “power systems” in the rest of the document. The applications and challenges of electric dc power systems are not discussed in this thesis.

condition for the safe and reliable operation of power systems, which shall be prepared to withstand events that affect the active power balance and restore it in the shortest possible interval and at the minimum incurred cost. Examples of such events include loss of generation, short-circuits in transmission lines, and sudden load variations, among others. Restoring active power balance is possible if and only if the system has enough energy reserves and controlled active sources or drains that quickly regulate the active power flow based on the deviation of the electrical frequency from its rated value, meaning it is possible to tackle this problem from the load or the generation side.

Power systems have historically been designed to balance active power from the generation side, adopting technologies that simultaneously offer three important properties: broad power dispatch capability, ability to participate in frequency control, and large **energy storage (ES)** capacity. Thermal power plants based, for instance, on fossil fuels rely on turbines as controlled power sources and have embedded storage capabilities in the energy carrier. Turbine governors can, through the controlled release of substantial amounts of energy stored in natural gas or coal, regulate the active power flow in a flexible manner and reestablish power balance whenever necessary. The same analogy can be expanded to hydro plants. Moreover, turbines and synchronous machines provide another useful form of **ES**: heavy rotating masses storing a considerable amount of kinetic energy, also referred to as “inertia”.<sup>2</sup>

This status quo of electric power systems has nonetheless been questioned in recent decades and the climate crisis has been pushing the sector hard to find alternatives to fossil fuels. Increased investments in renewable energy sources led to a dramatic reduction of their **levelized cost of energy (LCOE)** in the last two decades driven by technology advances in materials science and engineering, power electronics systems and components, information and communication technology, and manufacturing techniques, among others. Traditional concepts for electric power generation are therefore being gradually displaced by **variable renewable energy sources (VRESs)**, such as wind power and solar **photovoltaic (PV)**, interfaced to power systems through **power electronic converters (PECs)**, which by themselves cannot store energy and offer a sufficient range of dispatch and frequency control mechanisms.

Alternative concepts and technologies have, however, been under deployment on the load side, aiming to increase control of power flows and optimize **ES** capacity and operation. Hydrogen has, for instance, been proposed as a carbon-free energy carrier and long-term storage alternative to fossil fuels. Electrolyzers can produce it using the power from **VRESs** or nuclear plants and, at the same time, serve as flexible loads providing frequency control. Hydrogen

---

<sup>2</sup>Note that kinetic energy and inertia are related but distinguishable physical concepts and quantities. These two terms are nonetheless used indistinctly many times in the electric power community.

can then be transported using existing natural gas infrastructure and used by fuel cells, gas turbines, heaters, compressors, pumps, or industrial processes. Kinetic energy stored in rotating machines can also be converted to bursts of electric power by **PECs** when small speed deviations are allowed in mechanical systems and assist in short-term power balancing problems. The load of electric heaters and heat pumps may likewise be temporarily increased or reduced according to allowed temperature variations; the same principle is applicable to compressors and pumps according to allowed pressure variations. Electrochemical batteries have reached levels of cost, power, energy capacity, and efficiency that allow them to be used in bulk power systems for short-term energy storage and frequency control. All these flexible loads and distributed **energy storage devices (ESDs)** can nowadays be coordinated by advanced **energy management systems (EMSs)** and integrated into the dispatch centers of system operators. In summary, many recent advances allow more flexibility on the load side of power systems and operation of distributed storage as loads or generators.

When all these trends compound, new challenges for the planning and operation of power systems are introduced. It is technically feasible, on the one hand, to reach adequate levels of power dispatch, frequency control, and **ES** capacity when flexible loads, distributed forms of **ES**, and **VRESs** are interfaced to fully-controlled **PECs**. Such choices may, on the other hand, have major technical and economic impacts, as they affect capital and operational expenditures, security of supply, and power system stability. Examples include decisions about allocation of reserves for frequency control, the charge or discharge of **ES** devices, and curtailment of loads and **VRESs**. It is, therefore, increasingly important to integrate proper stability and security constraints directly into the optimization tools and algorithms used for planning and operation of power systems. Such constraints may allow power systems to run at minimum cost and maximize the return on investment of its compounds while avoiding taking decisions that hinder security and stability. This problem in general becomes more complex in isolated grids, where typically a limited number of generators and **ES** devices is available, with islands, ships, remote communities, industrial or military installations being notable examples. A reduced amount of kinetic energy storage (or inertia) in these autonomous power systems can turn large active power disturbances into considerable frequency deviations and jeopardize frequency stability. It is, therefore, critical to properly size **VRES** sources, **ES** capacity, and specify desired properties of **PECs** in optimization algorithms for planning and operation.

Given this context, the main objectives of this doctoral work are the following:

- O1.** Review the active power balance problem and the principles of frequency

control and stability in ac power systems based on first principles.

02. Identify gaps in current modeling practices that can affect planning and operation of low-inertia, autonomous power systems where high penetration of VRESs exists.
03. Explore how frequency control and stability constraints can be integrated into different power system optimization models.

Most of the results and findings of this thesis are presented in the context of the HES-OFF project using the case study of an offshore oil and gas (O&G) platform in the North Sea that shall be interconnected to an offshore wind farm. A secondary but important objective of this doctoral work is to apply a framing that is as general as possible despite the narrow application of HES-OFF. This is to be achieved by deriving main ideas and propositions based on general principles that can be expanded and applied to other types of autonomous power systems and microgrids in islanded mode.

## RESEARCH CONTRIBUTIONS

The key ideas and arguments from this doctoral work are:

- Some established models and assumptions used for active power balance and frequency control in traditional power systems may not produce the expected results where high penetration of VRESs in autonomous, low-inertia power systems exist due to the nonlinear effects that are present when large frequency deviations occur.
- The techno-economical problem involved in planning and operation of power systems requires a granularity in the decision making from five minutes and up to one hour to make the optimization problem tractable from a computational and operational perspective when long time horizons (days, weeks, months, years) are considered.
- The active power balance and frequency control problems involve optimization of power flows and use of ES in several time scales. A finer granularity (lower than one second) may be required when there is coupling between the dynamics in the faster time scales.
- The results from different case studies suggest that overestimation of the economic and environmental benefits from VRESs and oversizing of ES may occur where constraints from faster time scales (below five minutes) are ignored.

- Coupling effects in the faster time scales can be partially integrated into optimization algorithms when applying proper assumptions, model reduction techniques, and methods from disciplines such as mathematical optimization, data science, and nonlinear control theory.

This thesis presents, to this end, the following scientific contributions:

- SC1.** An investigation into *power quality and stability issues* in autonomous offshore platforms fed by gas turbines but where high penetration of wind power is possible. This analysis evaluates the effect of wind power variations on gas turbine operation, frequency, and voltage dynamics in a time scale of seconds. It demonstrates also *how energy storage can improve power quality* and discusses *factors that affect storage sizing*.
- SC2.** An *algebraic equation* that provides sufficient conditions for *frequency stability* where power systems are subject to *nonlinear effects and large frequency variations*. This equation is based on four parameters that are typically defined on security assessments, grid codes, or industry standards requirements, and allows frequency stability constraints to be included in optimization algorithms without resorting to time-domain simulations or unnecessary linearization of the power balance equations.
- SC3.** A framework to *size hybrid energy storage systems (ESSs)* for the *faster time scales* in frequency control, namely inertial and primary control, where *algebraic equations* are used to define requirements for **ES** rated energy and power capacity, and a *systematic procedure* is presented to specify the main components of **PECs**. The use of algebraic equations, therefore, allows calculations to be included in *power system optimization models*. To obtain a certain *frequency control performance*, the proposed procedure was applied in a case study of the **HES-OFF** project, indicating that the system designer can take advantage of **ES** technologies having distinct characteristics.
- SC4.** A framework to include *frequency stability constraints* in the *nonlinear optimization problem* of a multi-domain energy system based on time-domain simulations of a surrogate model of the ac power system. This technique was applied in a planning problem, namely the case study of the **HES-OFF** project, where results suggest that  $CO_2$  savings might be overestimated and **ES** capacity oversized where frequency stability constraints are neglected.
- SC5.** A framework to include *frequency stability constraints* in *power system optimization models*, which are solved by **mixed integer linear programming**

(MILP). The method was first applied on a planning problem in the case study of an industrial plant, where solar PV and battery ESS are sized to reduce the LCOE of the system. Analyses of the results corroborated the initial findings from the HES-OFF study case showing that, where frequency stability constraints are neglected, CO<sub>2</sub> savings and LCOE reductions might be overestimated and ES capacity oversized. The same method was then extended and applied in an operational problem, where the algorithm for the EMS of a generalized autonomous power system allocates time-varying optimal frequency control reserves to achieve optimal scheduling and to secure a frequency stable operation under dynamic uncertainty.

Those resulted in the scientific publications below, listed in the order they are presented in this document:

- P1.** **Erick Alves**, Santiago Sanchez, and Elisabetta Tedeschi. [Power quality in wind-powered oil and gas platforms](#). Conference poster presentation at EERA Deep Wind'19 - 16th Deep Sea Offshore Wind R&D conference (January 2019).<sup>3</sup>
- J1.** **Erick Alves**, Santiago Sanchez, Danilo Brandao, and Elisabetta Tedeschi. [Smart Load Management with Energy Storage for Power Quality Enhancement in Wind-Powered Oil and Gas Applications](#). *Energies* 12 (15), 2985 (August 2019). ISSN 1996-1073.
- C1.** Luca Riboldi, **Erick F Alves**, Marcin Pilarczyk, Elisabetta Tedeschi, and Lars O. Nord. [Innovative Hybrid Energy System for Stable Power and Heat Supply in Offshore Oil & Gas Installation \(HES-OFF\): System Design and Grid Stability](#). In *Proceedings of the 30 European Symposium on Computer Aided Process Engineering (ESCAPE30)*, volume A, pages 211–216 Milano, Italy (May 2020). Elsevier.
- J2.** Luca Riboldi, **Erick F. Alves**, Marcin Pilarczyk, Elisabetta Tedeschi, and Lars O. Nord. [Optimal Design of a Hybrid Energy System for the Supply of Clean and Stable Energy to Offshore Installations](#). *Frontiers in Energy Research*, 8:326, December 2020. ISSN 2296-598X.
- J3.** **Erick Alves**, Gilbert Bergna-Diaz, Danilo Brandao, and Elisabetta Tedeschi. [Sufficient Conditions for Robust Frequency Stability of AC Power Systems](#). *IEEE Transactions on Power Systems*, 36 (3), 2684–2692, May 2021. ISSN 0885-8950, 1558-0679.

---

<sup>3</sup>Recipient of the Best Poster Award.

- J4. Erick Fernando Alves**, Daniel dos Santos Mota, and Elisabetta Tedeschi. *Sizing of Hybrid Energy Storage Systems for Inertial and Primary Frequency Control*. *Frontiers in Energy Research*, 9:649200, May 2021. ISSN 2296-598X.
- J5. Erick Fernando Alves**, Louis Polleux, Gilles Guerassimoff, Magnus Korpås, and Elisabetta Tedeschi. *Allocation of spinning reserves for autonomous grids subject to frequency stability constraints and short-term solar power variations*. *Re-submitted to Applied Energy*, September 2022.
- J6.** Spyridon Chapaloglou, **Erick Alves**, Vincenzo Trovato, and Elisabetta Tedeschi. *Optimal Energy Management in Autonomous Power Systems with Probabilistic Security Constraints and Adaptive Frequency Control*. *Submitted to IEEE Transactions on Power Systems*, August 2022.

## OUTLINE

Part I of this thesis is composed of two chapters and provides some of the required background and foundations used in the contributions listed above. [Ch. 1](#) presents a technical perspective of the power balance problem and uses first principles to establish the relationship between active power unbalance and frequency deviation from its rated value. It then describes the available frequency control mechanisms in power systems and discusses how the introduction of [PECs](#) and the reduction of inertia may affect frequency dynamics and system stability. [Ch. 2](#) provides an economic perspective and reviews the challenge of optimizing the size of equipment, power production, frequency reserves, and [ES](#) to match energy demand at a minimum cost under uncertain scenarios. This family of mathematical optimization problems is known as security-constrained unit commitment.

Several frameworks integrating these two perspectives are the main results of this thesis, which are described in Part II and presented as a collection of one conference poster presentation, one published conference article, four published journal papers, and two manuscripts under review, systematically organized in [Chs. 3 to 10](#). The published materials are presented in their accepted, pre-print versions, with copyright information and author contributions given in the first page of each chapter. All materials have been re-typeset from their original sources for integration into this thesis. The manuscripts under review might undergo further modifications and the accepted versions could, therefore, differ from those presented here.

Finally, Part III is the epilogue of this thesis, composed of [Ch. 11](#) that presents the closing remarks of this research work and an outlook for further research.

**RELATED WORK**

The following publications, models, software, and data repositories derived from the doctoral research but are not discussed in this thesis:

- R1. Erick F. Alves.** [Efantnu/ips-freq-stability: Models and data repository from “Sufficient Conditions for Robust Frequency Stability of AC Power Systems”](#). Zenodo (November 2020).
- R2. Erick F. Alves** and Daniel Dos Santos Mota. [Efantnu/hybrid-ess-design: Models and data repository from “Sizing of Hybrid Energy Storage Systems for Inertial and Primary Frequency Control”](#). Zenodo (March 2021).
- S1.** Roberto Agromayor, Luca Riboldi, and **Erick F. Alves.** [RoberAgro/HES-OFF: A research-based prototype tool in Python](#). GitHub (November 2021).
- S2. Erick F. Alves** and Daniel Dos Santos Mota. [Efantnu/pwrsys-matlab: NTNU Power Systems Library for Matlab/Simulink](#). Zenodo (December 2021).
- R3. Erick F. Alves** and Louis Polleux. [efantnu/drep-2021-collab-MINESParisTech-NTNU: Data repository of the paper “Allocation of spinning reserves for autonomous grids subject to frequency stability constraints and short-term solar power variations”](#). Zenodo (March 2021).
- C2.** Daniel dos Santos Mota, **Erick Fernando Alves**, Santiago Acevedo-Sanchez, Harald G. Svendsen, and Elisabetta Tedeschi. Offshore Wind Farms and Isolated Oil and Gas Platforms: Perspectives and Possibilities. *In Proceedings of the ASME 2022 41st International Conference on Ocean, Offshore & Arctic Engineering OMAE 2022*, Hamburg, Germany (June 2022). ASME. (*In Press*)
- J7.** Daniel dos Santos Mota, **Erick Fernando Alves**, Santiago Sanchez-Acevedo, and Elisabetta Tedeschi. Coordination of Frequency Reserves in an Isolated Industrial Grid Equipped with Energy Storage and Dominated by Constant Power Loads. *Submitted to IEEE Transactions on Power Systems*, October 2022.

**UNRELATED WORK**



The following scientific articles were published during the period of the doctoral work but are not related to this thesis:

- C3.** J. K. Nøland, M. Gisét, and **E. F. Alves**. [Continuous Evolution and Modern Approaches of Excitation Systems for Synchronous Machines](#). In *2018 XIII International Conference on Electrical Machines (ICEM)* pages 104–110 Alexandroupoli, Greece (September 2018). IEEE. ISBN 978-1-5386-2477-7.<sup>4</sup>
- J8.** Jonas Kristiansen Nøland, Stefano Nuzzo, Alberto Tassarolo, and **Erick Fernando Alves**. [Excitation System Technologies for Wound-Field Synchronous Machines: Survey of Solutions and Evolving Trends](#). *IEEE Access* 7, 109699–109718 (2019). ISSN 2169-3536.<sup>5</sup>
- C4.** **Erick F Alves**, Jonas K Nøland, Giancarlo Marafioti, and Geir Mathisen. [Online parameter identification of synchronous machines using Kalman filter and recursive least squares](#). In *IECON 2019 - 45th Annual Conference of the IEEE Industrial Electronics Society* volume 1 page 7 Lisbon, Portugal (October 2019). IEEE. ISBN 978-1-72814-879-3.<sup>6</sup>
- J9.** Jonas Kristiansen Nøland, **Erick Fernando Alves**, Atila Pardini, and Urban Lundin. [Unified Reduced Model for a Dual-Control Scheme of the High-Speed Response Brushless Excitation System of Synchronous Generators](#). *IEEE Transactions on Industrial Electronics* 67 (6), 4474–4484 (June 2020). ISSN 0278-0046, 1557-9948.<sup>7</sup>
- C5.** Ersi Ago, Harold Chamorro, **Erick F. Alves**, Francisco Gonzalez-Longatt, Wilfredo C. Flores, Vijay K. Sood, and Wilmar Martinez. [Non-Synchronous Generation Impact on Frequency Response - A Case from Albania](#). In *2020 IEEE Electric Power and Energy Conference (EPEC)* page 7 Edmonton, Alberta, Canada (2020). IEEE. ISBN 978-1-72816-489-2.
- C6.** Luca Castellini, Federico Gallorini, Giacomo Alessandri, **Erick Alves**, Dan Montoya, and Elisabetta Tedeschi. [Performance Comparison of Offline and Real-Time Models of a Power Take-Off for Qualification Activities of Wave Energy Converters](#). In *2021 Sixteenth International Conference on Ecological Vehicles and Renewable Energies (EVER)* pages 1–8 Monte-Carlo, Monaco (May 2021). IEEE. ISBN 978-1-66544-902-1.<sup>8</sup>

<sup>4</sup>Result of a collaboration with Prof. Jonas Nøland from the Norwegian University of Science and Technology before this doctorate work started.

<sup>5</sup>See footnote 4

<sup>6</sup>Work derived from the [master thesis](#) of the Ph.D. candidate.

<sup>7</sup>See footnote 4

<sup>8</sup>Result of the research duties at the IMAGINE project.

- C7. Giacomo Alessandri, Federico Gallorini, Luca Castellini, Dan El Montoya, **Erick Fernando Alves**, and Elisabetta Tedeschi. [An Innovative Hardware-In-the-Loop Rig For Linear Power-Take-Off Testing](#). In *2021 European Wave and Tidal Energy Conference (EWTEC)* pages 1–10 Plymouth, UK (Sep 2021). EWTEC.<sup>9</sup>
- J10. Luca Castellini, Federico Gallorini, Giacomo Alessandri, **Erick Fernando Alves**, Dan Montoya, Bhavana Mudigonda, and Elisabetta Tedeschi. [Comparison of Offline, Real-Time Models and Hardware-In-the-Loop Test Results of a Power Take-Off for Wave Energy Applications](#). *Journal of Marine Science and Engineering* 10(11), 1744 (2022). ISSN 0278-0046, 1557-9948.<sup>10</sup>

### NAVIGATING THIS PH.D. THESIS

Some effort was spent to aid the reader in browsing the content of this thesis, with the main navigation features being listed below:

1. The reference section is given at the end of each chapter on purpose, as this simplifies the work of those reading the physical copy of this document. Readers might find, therefore, duplicated references in other chapters.
2. The page of each citation is listed at the end of each reference, so readers of the digital copy of this document do not have to remember the page where they were before clicking on a specific reference.
3. There is a two-way link between any item displayed in the table of content and any chapter/section/subsection, allowing quick back and forth navigation from the table of contents.

The reader shall refer to the [colophon](#) at the very end of this document for further detail.

---

<sup>9</sup>See footnote 8

<sup>10</sup>See footnote 8

## Acknowledgements

---

It is obvious that any acknowledgment attempt will always be incomplete in such endeavor as a doctoral work. There are over one hundred individuals that directly or indirectly helped me during my [Ph.D.](#) fellowship at [NTNU](#) and to whom I am eternally in debt. In this case, however, “I’d rather attempt to do something great and fail than to attempt to do nothing and succeed” to use the words of Rev. Robert H. Schuller.

First, I thank my dearest wife Penélope Psillakis for her unconditional support and pampering throughout this period, even when she was struggling herself. Popy, I do not have words to express my gratitude.

A big thanks also goes to my supervisor Prof. Elisabetta Tedeschi, not only for giving me the opportunity to pursue an academic career after so many years in industry and mentoring me throughout my doctoral work, but also for becoming a friend. I also extend my gratitude to Prof. Magnus Korpås for his co-supervision and valuable input, which made this thesis much better.

I really appreciated the opportunity to work with Prof. Danilo Brandão, Prof. Gilbert Bergna-Diaz, Prof. Lars O. Nord, Dr. Luca Riboldi, Dr. Santiago Sanchez, Prof. Vincenzo Trovato, which were outstanding in their support and became unofficial supervisors of parts of this thesis. I am extremely grateful as well for all other distinguished collaborators in this thesis, namely Daniel Mota, Prof. Gilles Guerassimof, Dr. Louis Polleux, Dr. Marcin Pylarczik, and Spiros Chapaloglou.

Many names are not printed in the publications included in this thesis but were indispensable sources of inspiration, knowledge and support. Those include Prof. Augusto Alonso, Babek Abdolmaleki, Prof. Fernando Marafão, Prof. Florian Dörfler, Prof. Francisco Gonzalez-Longatt, Prof. Hana Gustafsson, Prof. Kristin Y. Pettersen, Kjell Ljøkelsøy, Prof. Jan Tommy Gravdahl, Dr. Jon Are Suul, Dr. Harald G. Svendsen, Ola Furuhaug, Dr. Salvatore D’Arco, Prof. Saverio Bolognani, Steffen Vogel, and Thomas S. Haugan.

This work would not be possible without the financial support of the Research Council of Norway, Prototech (now Clara Ventures), and Lundin Energy (now Aker BP). Special thanks to all involved in the [HES-OFF](#) project, in particular Dr. Dmitry Bokach, Dr. Sonia Faaland, Arild Vik, Dr. Arnljot Skogvang, and Anne Årrestad.

There is an extensive list of people working in the background to make

the “magic happen” in the Department of Electric Energy and the Faculty of Information Technology and Electrical Engineering. I am glad to have had their support during my period at the Norwegian University of Science and Technology, chiefly Anders Gytri, Anne Danielsen, Dr. Anyuan Chen, Aksel Hanssen, Dr. Basanta Pokhrel, Bodil Wold, Halsten Aastebøl, Harald Lenschow, John Arild Wiggen, Koharu Høydalsvik, Kurt Salmi, Marta Braconi, Silje Berg, Svein Norum, Thomas Haugnæss, and Åshild Meistad.

Last, I learned enjoying being the dumbest person in the room during my time at the Norwegian University of Science and Technology. In this sense, I was lucky to have worked with so many bright colleagues and great human beings, that gave me the pleasure of several fruitful discussions and an open and receptive environment. Thanks to Dr. Abel Taffese, Alessandra Follo, Dr. Andreas Giannakis, Dr. Andrzej Holdyk, Amar Abideen, Dr. Anirudh Acharya, Dr. Angjerd Pleyrn, Aravinda Pereira, Prof. Arne Nysveen, Arkaitz Rabanal, Atousa Elahidoost, Aurora Flataker, Ayotunde Adeyemo, Bhavana Mudigonda, Dr. Chendan Li, Dr. Dan El Montoya, Dr. Danielle Ferreira, Daniel Baltensperger, Daniel Phillips, Prof. Damiano Varagnolo, Prof. Dimosthenis Peftitsis, Prof. Eilif Hansen, Prof. Erling Ildstad, Erik Bjørnerem, Fanny Skirberk, Prof. Frank Mauseth, Dr. Fredrik Göthner, Gard Rødal, Prof. Geir Mathisen, Dr. Gerd Kjøle, Dr. Giancarlo Marafioti, Dr. Hallvar Haugdal, Dr. Hossein Ehya, Prof. Hossein Farahmand, Ida Fuchs, Prof. Irina Oleinikova, Hugo de Brito, Prof. Kaveh Niayesh, Krister Haugen, Linn Emelie Schaffer, Dr. Jon Olav Tande, Prof. Jonas Nøland, Jordon Grant, Joseph Banda, Dr. Kasper Thorvaldsen, Kaushik Kumar, Prof. Kaveh Niayesh, Prof. Kjell Sand, Prof. Kjetil Uhlen, Prof. Lars Norum, Lorrana Rocha, Prof. Marta Molinas, Matteo Leandro, Prof. Mohammad Amin, Mohammad Kataoulai, Prof. Olav Fosso, Dr. Ole Christian Sprø, Prof. Ole-Morten Midtgård, Dr. Olve Mo, Prabhat Bana, Pål Glimen, Prof. Pål Keim Olsen, Philippe de Rua, Dr. Raymundo Torres-Olguín, Razieh Fard, Prof. Robert Nilssen, Prof. Roy Nilsen, Dr. Salman Zaferanlouei, Dr. Sigurd Bjarghov, Dr. Sigurd Jakobsen, Sjur Føyen, Prof. Steve Völler, Timm Baumann, Tobias Ubostad, Dr. Tor Inge Reigstad, Prof. Tore Undeland, Prof. Trond Toftevåg, Valéria de Souza, Dr. Venkat Lakshmanan, Prof. Vijay Vadlamudi, Yannick Karakezi, Yoga Vivekanandham, and Dr. Yusuf Gupta.

# Contents

---

ABSTRACT **VII**

PREFACE **IX**

ACKNOWLEDGEMENT **XIX**

LIST OF FIGURES **XXVII**

LIST OF TABLES **XXXIII**

ABBREVIATIONS **XXXV**

SYMBOLS **XXXIX**

---

## **PART I BACKGROUND 1**

CHAPTER 1 THE ACTIVE POWER BALANCE PROBLEM FROM A TECHNICAL PERSPECTIVE **3**

- 1.1 The correlation between active power disturbances and frequency deviations in power systems **3**
- 1.2 Frequency control and power reserves in power systems **5**
- 1.3 The equivalence between power electronic converters and synchronous machines for frequency control **8**
- 1.4 References **11**

CHAPTER 2 THE ACTIVE POWER BALANCE PROBLEM FROM AN ECONOMIC PERSPECTIVE **15**

- 2.1 Challenges in the optimal planning and operation of power systems **15**

|     |   |    |
|-----|---|----|
| 2.2 | Security-constrained active power flow problems | 18 |
| 2.3 | References                                      | 24 |

---

## **PART II RESULTS 29**

|           |  |    |
|-----------|--|----|
| CHAPTER 3 | CONFERENCE POSTER 1: POWER QUALITY IN WIND-POWERED OIL AND GAS PLATFORMS | 31 |
|-----------|--|----|

|           |   |    |
|-----------|---|----|
| CHAPTER 4 | JOURNAL PAPER 1: SMART LOAD MANAGEMENT WITH ENERGY STORAGE FOR POWER QUALITY ENHANCEMENT IN WIND-POWERED OIL AND GAS APPLICATIONS | 35 |
|-----------|---|----|

Abstract 36

|       |                             |    |
|-------|-----------------------------|----|
| 4.1   | Introduction                | 36 |
| 4.2   | The Case Study              | 38 |
| 4.2.1 | Energy Storage System       | 40 |
| 4.3   | Simulation Results          | 42 |
| 4.4   | Simplified Model            | 45 |
| 4.4.1 | Model Validation            | 47 |
| 4.5   | Discussion and Further Work | 49 |
| 4.6   | References                  | 51 |

|           |   |    |
|-----------|---|----|
| CHAPTER 5 | CONFERENCE PAPER 1: INNOVATIVE HYBRID ENERGY SYSTEM FOR STABLE POWER AND HEAT SUPPLY IN OFFSHORE OIL & GAS INSTALLATION (HES-OFF): SYSTEM DESIGN AND GRID STABILITY | 57 |
|-----------|---|----|

Abstract 58

|       |                            |    |
|-------|----------------------------|----|
| 5.1   | Introduction               | 58 |
| 5.2   | The HES-OFF hybrid concept | 59 |
| 5.3   | Modeling framework         | 59 |
| 5.3.1 | Process components         | 60 |
| 5.3.2 | Offshore grid              | 60 |

|           |   |     |
|-----------|---|-----|
| 5.4       | Results   | 61  |
| 5.4.1     | Long-term system design   | 61  |
| 5.4.2     | Short-term grid stability analysis  | 62  |
| 5.5       | Conclusions   | 64  |
| 5.6       | References  | 65  |
|           |   |     |
| CHAPTER 6 | JOURNAL PAPER 2: OPTIMAL DESIGN OF A HYBRID ENERGY SYSTEM FOR THE SUPPLY OF CLEAN AND STABLE ENERGY TO OFFSHORE INSTALLATIONS | 67  |
|           | Abstract  | 68  |
| 6.1       | Introduction  | 68  |
| 6.2       | Materials and Methods   | 71  |
| 6.2.1     | Principles of the proposed concept  | 71  |
| 6.2.2     | Integrated model  | 72  |
| 6.2.3     | Process models  | 72  |
| 6.2.4     | Electric grid model   | 76  |
| 6.2.5     | Long-term analysis  | 78  |
| 6.2.6     | Short-term analysis   | 79  |
| 6.2.7     | Optimization framework  | 80  |
| 6.3       | Results   | 81  |
| 6.3.1     | Case study  | 81  |
| 6.3.2     | Parametric analysis   | 82  |
| 6.3.3     | Integrated results using the optimization framework   | 84  |
| 6.4       | Conclusions   | 90  |
| 6.5       | References  | 93  |
|           |   |     |
| CHAPTER 7 | JOURNAL PAPER 3: SUFFICIENT CONDITIONS FOR ROBUST FREQUENCY STABILITY OF ISOLATED AC POWER SYSTEMS                            | 99  |
|           | Abstract  | 100 |
| 7.1       | Introduction  | 100 |
| 7.2       | Nonlinear average model of an ac power system   | 102 |

- 7.3 Sufficient conditions for robust frequency stability 103
- 7.4 Validation using the IEEE 39-bus test system 107
  - 7.4.1 Load Damping 110
  - 7.4.2 Generator 10 outage 110
  - 7.4.3 Islanding 112
- 7.5 Discussion 113
- 7.6 Conclusion 115
- 7.7 Appendix A: Equilibrium analysis 116
- 7.8 Appendix B: The effects of time delays 116
- 7.9 Appendix C: Input-to-State Stability Theorem 118
- 7.10 References 118

CHAPTER 8 JOURNAL PAPER 4: SIZING OF HYBRID ENERGY STORAGE SYSTEMS FOR INERTIAL AND PRIMARY FREQUENCY CONTROL 123

- Abstract 124
- 8.1 Introduction 124
- 8.2 Materials and Methods 127
  - 8.2.1 Frequency Control in AC Power Systems 127
  - 8.2.2 Sizing of the Converter-Interfaced ESS Elements 133
- 8.3 Results 141
  - 8.3.1 Case study: a wind-powered offshore platform in the North Sea 141
  - 8.3.2 Sizing of the Energy Storage System 143
  - 8.3.3 Sizing validation 145
- 8.4 Conclusions 150
- 8.5 References 152



|            |  |            |
|------------|--|------------|
| CHAPTER 9  | JOURNAL PAPER 5: ALLOCATION OF SPINNING RESERVES FOR AUTONOMOUS GRIDS SUBJECT TO FREQUENCY STABILITY CONSTRAINTS AND SHORT-TERM SOLAR POWER VARIATIONS | <b>159</b> |
|            | Abstract   | 160        |
| 9.1        | Introduction   | 160        |
| 9.1.1      | Literature review  | 161        |
| 9.1.2      | Paper contributions  | 162        |
| 9.2        | Addressing frequency stability with linear constraints   | 163        |
| 9.2.1      | Frequency stability and spinning reserves  | 163        |
| 9.2.2      | Formulation 1: constraints for sudden load or generation loss  | 165        |
| 9.2.3      | Formulation 2: constraints for short-term power variations   | 166        |
| 9.3        | Case study of an industrial installation   | 168        |
| 9.3.1      | MILP algorithm formulation   | 169        |
| 9.3.2      | Optimal sizing with static and dynamic frequency constraints   | 172        |
| 9.3.3      | Validation with time-domain simulations  | 175        |
| 9.4        | Discussion   | 176        |
| 9.5        | Conclusion   | 179        |
| 9.6        | Appendix A: Generation of solar PV power drop scenarios  | 180        |
| 9.7        | Appendix B: Power system model used for validation   | 181        |
| 9.8        | References   | 181        |
| CHAPTER 10 | JOURNAL PAPER 6: OPTIMAL ENERGY MANAGEMENT IN AUTONOMOUS POWER SYSTEMS WITH PROBABILISTIC SECURITY CONSTRAINTS AND ADAPTIVE FREQUENCY CONTROL          | <b>187</b> |
|            | Abstract   | 188        |
| 10.1       | Introduction   | 188        |
| 10.1.1     | Literature review  | 189        |

- 10.1.2 Paper contributions 190
- 10.2 Method 191
  - 10.2.1 Frequency Control and Reserves Allocation 192
  - 10.2.2 Optimal and Bounded Energy Management under Uncertainty 194
  - 10.2.3 Probabilistically Constrained EMS 197
  - 10.2.4 Proposed Convex Reformulation 199
- 10.3 Simulations 200
  - 10.3.1 Capabilities of adaptive uncertainty quantification 201
  - 10.3.2 Effect of optimal and bounded frequency support from ESS 202
  - 10.3.3 Comparative analysis and effect of bounds 203
- 10.4 Conclusions 205
- 10.5 References 206

---

## **PART III EPILOGUE 215**

- CHAPTER 11 CLOSING REMARKS 217
  - 11.1 Objective 1: Review the active power balance problem and the principles of frequency control and stability in ac power systems based on first principles 218
  - 11.2 Objective 2: Identify gaps in current modeling practices that can affect planning and operation low-inertia, autonomous power systems where high penetration of VRESs exists 219
  - 11.3 Objective 3: Explore how frequency control and stability constraints can be integrated into different power system optimization models 220
  - 11.4 Recommendations for future research 221

- COPYRIGHT PERMISSIONS 225

## List of Figures

---

### CHAPTER 1

- 1.1 Idealized representation of a **synchronous machine** as a fly-wheel with inertia and damping. 4
- 1.2 The typical periods of frequency variation (arrest, rebound, and recovery) and control actions (inertial, primary, and secondary) following a perturbation caused by lack of generation. 7
- 1.3 Idealized representation of a **voltage source converter** with a capacitor  $C_{dc}$  in its dc link and a LCL filter on the ac side. 9

### CHAPTER 2

- 2.1 Typical costs to be minimized in power systems. 16
- 2.2 Overview of the traditional frequency control architecture in power systems. 18

### CHAPTER 3

- 3.1 Conference poster presented at the EERA Deep Wind'19 32
- 3.2 Recognition from the Poster Award Committee at the EERA Deep Wind'19 33

### CHAPTER 4

- 4.1 Main elements of the electric power system for a wind-powered OOGPs 39
- 4.2 Frequency response of the low-pass filter combined with the wash-out filter. This combination is equivalent to a band-pass filter 41
- 4.3 Block diagram of the proposed controller considering non-linear effects 42

- 4.4 Active power, ESS active (p) versus apparent (s) power, PCC frequency and voltage for  $10 < t < 76$  s. 44
- 4.5 Detail of the period where a 10 MW load is switched on. 45
- 4.6 Detail of the period where a 10 MW load is switched off. 46
- 4.7 Simplified model of the hybrid energy system as a synchronous generator 47
- 4.8 Detailed versus simplified model without energy storage system 48
- 4.9 Detailed versus simplified model with energy storage system 49

CHAPTER 5

- 5.1 Schematic of the Innovative Hybrid Energy System for Stable Power and Heat Supply in Offshore Oil & Gas Installation system proposed. 59

CHAPTER 6

- 6.1 Schematic representation of the proposed Innovative Hybrid Energy System for Stable Power and Heat Supply in Offshore Oil & Gas Installation (HES-OFF). 72
- 6.2 Flowchart of the proposed design methodology combining models of the process and electric domains. 73
- 6.3 Ideal representation of the electric grid as a rotating mass with inertia and damping. 77
- 6.4 Pareto front 1 - the reference case, (A) shows a limited reduction of  $CO_2$  emissions, (B) highlights the different fuel cell stack size ranges, and (C) the different electrolyser stack size ranges. 87
- 6.5 Pareto front 1B - constant performance of fuel cell and electrolyser stacks, (A) shows a larger reduction of  $CO_2$  emissions when compared to Pareto 1, (B) highlights the different fuel cell stack size ranges, and (C) the different electrolyser stack size ranges. 89
- 6.6 (A) Pareto front 2 shows a larger reduction of  $CO_2$  emissions when compared to Pareto 1, while (B) Pareto front 1C has fewer feasible solutions when compared to Pareto 1. 90

## CHAPTER 7

- 7.1 Single-line diagram of the IEEE 39-bus test system. 108
- 7.2 Center of inertia (COI) frequency after increasing bus 4 load by 100 MW. 111
- 7.3 Center of inertia (COI) frequency after the outage of generator 10. 112
- 7.4 Center of inertia (COI) frequency after the system is islanded. 113

## CHAPTER 8

- 8.1 Frequency-droop, the main mechanism for primary frequency control. 129
- 8.2 The three periods of frequency variation (arrest, rebound and recovery) and the control actions (inertial, primary and secondary) following a perturbation caused by lack of generation. 132
- 8.3 Elements of a converter-interfaced energy-storage system. 134
- 8.4 Schematic representation of the dc link, the grid converter and its LC filter. 139
- 8.5 Histogram of the platform active power demand showing an average load of 0.6377 pu and maximum variation of 0.0428 pu with 99.9% of probability when outliers below 0.6 pu are ignored. 143
- 8.6 Schematic representation of the case study ac power systems. 145
- 8.7 Overview of the MATLAB Simulink model used to validate the proposed sizing of the energy storage device responsible for primary control in the case study. 146
- 8.8 Generalized nonlinear droop controller with deadband, permanent droop (proportional gain), transient droop (derivative gain), output compensation, setpoint and output limitation. 146

- 8.9 Case-study behavior during a load increase of 3 MW with and without the proposed ESS: Normalized angular speed **(A)** during the whole transient and **(B)** detail of the first minute; Turbo-generator and wind-farm active power in pu **(C)** during the whole transient and **(D)** detail of the first minute; Active power of the ES devices responsible for primary control (ES1) and secondary control (ES2) **(E)** during the whole transient and **(F)** detail of the first minute. 148
- 8.10 Case-study behavior during the wind farm disconnection under full production (12 MW) with and without the proposed ESS: Normalized angular speed **(A)** during the whole transient and **(B)** detail of the first minute; Turbo-generator and wind-farm active power in pu **(C)** during the whole transient and **(D)** detail of the first minute; Active power of the ES devices responsible for primary control (ES1) and secondary control (ES2) **(E)** during the whole transient and **(F)** detail of the first minute. 149

## CHAPTER 9

- 9.1 Idealized response of an autonomous power system to a cloud-passage event. 168
- 9.2 Overview of the case study installation. 168
- 9.3 Hourly available and injected PV profile and battery requirements on Jan 1st. 175
- 9.4 Grid simulation of PV ramp  $r_2$  and one GT loss at  $t = 10$  s. 177
- 9.5 Process of worst-case ramp identification from high-resolution timeseries to convex hulls  $\mathcal{H}_h^{max}$  in the lower-right figure. 180
- 9.6 Power system model implemented in Matlab/Simulink. 181

## CHAPTER 10

- 10.1 Hierarchical control system schematic where the upper layer optimal discrete time control is integrated with the lower time scale continuous adaptive primary frequency control. 191

- 10.2 Visualization of the proposed adaptive and probabilistic step-like net **active power disturbance** quantification at a time instant in the continuous range between the discrete points in time where decisions are taken. 193
- 10.3 Demonstration of adaptive uncertainty quantification by using auto-regressive probabilistic forecasting for the load time-series. 210
- 10.4 Effect of the optimally calculated participation of the **ESS** in providing frequency support for a step load change when only 1 **GT** is on. 211
- 10.5 Trajectories of the optimally designed system inertia (top) and damping (bottom) and optimal split between primary control provision by the **GTs** and the **ESS** for different bounds considerations. 212
- 10.6 State of charge trajectories from the optimal scheduling and primary control design of the **ESS**, during the simulation period, for the cases of not including bounds on the resulting energy deviation from the participation in primary frequency control (top) and the one when including the bounds (bottom). 213





## List of Tables

---

|     |   |     |
|-----|---|-----|
| 4.1 | Summary of the model parameters for the case study.   | 55  |
| 4.2 | Metrics obtained from the detailed model simulation results.  | 56  |
| 4.3 | Metrics comparing the detailed and simplified models.   | 56  |
| 5.1 | Input parameters for the long-term system design.   | 62  |
| 5.2 | Output results of the HES-OFF concept based on the LM2500 GT  | 63  |
| 5.3 | Output results of the HES-OFF concept based on the LM6000 GT  | 63  |
| 5.4 | Input parameters for the short-term grid stability analysis.  | 64  |
| 6.1 | Input parameters for the optimization problem   | 80  |
| 6.2 | Designs based on the LM2500 GT - Comparative analysis between a standard concept on GTs only (GTs), a concept involving GTs and wind turbines (GTs+wind turbines), and the proposed concept (HES-OFF) | 85  |
| 6.3 | Designs based on the LM6000 GT - Comparative analysis between a standard concept on GTs only (GTs), a concept involving GTs and wind turbines (GTs+wind turbines), and the proposed concept (HES-OFF) | 85  |
| 6.4 | Optimal designs of the reference case - Pareto 1  | 87  |
| 6.5 | Optimal designs of the constant fuel cell and electrolyser performance case - Pareto 1B   | 88  |
| 6.6 | Optimal designs of the alternative wind data case - Pareto 2  | 89  |
| 6.7 | Optimal designs accounting for grid dynamics - Pareto 1C  | 91  |
| 7.1 | Initial conditions of the study-case.   | 109 |

- 7.2 Relevant data of each generator and its primary frequency controller when  $S_b = 100$  MW. 109
- 8.1 Parameters of the ac power systems of an offshore oil and gas platform in the Norwegian Continental Shelf and the requirements for its converter-interfaced ESS. 144
- 8.2 Parameters of the primary controllers used during the validation. 147
- 8.3 Summary of the ESS parameters obtained using the proposed procedure. 151
- 9.1 Case study parameters 169
- 9.2 The first 4 elements of the convex hull  $\mathcal{H}_{11}^{max}$  171
- 9.3 Techno-economic input parameters 172
- 9.4 Techno-economic optimization results for each scenario 173
- 9.5 Required battery ESS capacity for the first 4 elements of the convex hull  $\mathcal{H}_{11}^{max}$  174
- 10.1 Performance comparison for the whole simulation period. 204

## Abbreviations

---

| <b>Notation</b> | <b>Description</b>  |
|-----------------|---|
| ACPS            | ac power systems  |
| AGC             | automatic generation control  |
| APD             | active power disturbance  |
| APS             | autonomous power system   |
| BPS             | bulk power system   |
| CAPEX           | capital expenditure   |
| CDF             | cumulative distribution function  |
| CIG             | converter-interfaced generator  |
| COI             | center of inertia   |
| DSO             | distribution system operator  |
| ECTS            | European Credit Transfer System   |
| ED              | economic dispatch   |
| EL              | electrolyser  |
| EMS             | energy management system  |
| ES              | energy storage  |
| ESD             | energy storage device   |
| ESS             | energy storage system   |
| FC              | fuel cell   |
| FCR             | frequency containment reserve   |
| FFR             | fast frequency reserve  |
| FLL             | frequency-locked loop   |
| FRR             | frequency restoration reserve   |
| FSM             | frequency sensitivity mode  |
| GDP             | gross domestic product  |
| GEP             | generation expansion planning   |
| GHG             | greenhouse gases  |
| GT              | gas turbine   |
| HES             | hybrid energy system  |
| HES-OFF         | Innovative Hybrid Energy System for Stable Power and Heat Supply in Offshore Oil & Gas Installation |
| IPS             | isolated power system   |
| LCOE            | levelized cost of energy  |

| <b>Notation</b> | <b>Description</b>                             |
|-----------------|--|
| MET Norway      | The Norwegian Meteorological Institute         |
| MG              | microgrid                                      |
| MILP            | mixed integer linear programming               |
| MIMO            | multiple-input, multiple-output                |
| MPC             | model predictive control                       |
| NMSE            | normalized mean square error                   |
| NPV             | net present value                              |
| NTNU            | Norwegian University of Science and Technology |
| O&G             | oil and gas                                    |
| OOGP            | offshore oil and gas platform                  |
| OPEX            | operational expenditures                       |
| OPF             | optimal power flow                             |
| PCC             | point of common coupling                       |
| PEC             | power electronic converter                     |
| PEM             | proton exchange membrane                       |
| Ph.D.           | Philosophiæ Doctor                             |
| PID             | proportional-integral-derivative               |
| PLL             | phase-locked loop                              |
| pu              | per unit                                       |
| PV              | photovoltaic                                   |
| RES             | renewable energy source                        |
| RF              | random forest                                  |
| RMSE            | root mean square error                         |
| RoCoF           | rate of change of frequency                    |
| RR              | replacement reserve                            |
| SCADA           | supervisory control and data acquisition       |
| SCUC            | security constrained unit commitment           |
| SG              | synchronous generator                          |
| SISO            | single-input, single-output                    |
| SM              | synchronous machine                            |
| SOC             | state of charge                                |
| SoE             | state of energy                                |
| TDS             | time-domain simulation                         |
| TG              | turbogenerator                                 |
| TSO             | transmission system operator                   |
| UC              | unit commitment                                |
| VRES            | variable renewable energy source               |
| VSC             | voltage source converter                       |
| VSM             | virtual synchronous machine                    |

---

| <b>Notation</b> | <b>Description</b>       |
|-----------------|--------------------------|
| WHRU            | waste heat recovery unit |
| WT              | wind turbine             |

---



## Symbols

---

| <b>Notation</b> | <b>Description</b>   |
|-----------------|--|
| $\tilde{f}$     | frequency deviation from its rated value                                   |
| $\omega$        | equivalent (center of inertia) angular speed                               |
| $\omega_s$      | synchronous or rated angular speed   |
| $p_G$           | total power generation in pu   |
| $P_G$           | total active power generation in Watts                                     |
| $p_L$           | total power consumption in pu  |
| $P_L$           | total active power consumption in Watts                                    |
| $u_{dc}$        | dc link voltage of a voltage source converter in pu                        |
| $U_{dc}$        | dc link voltage of a voltage source converter in V                         |
| $\dot{u}_{dc}$  | time derivative of the dc link voltage of a voltage source converter in pu |
| $\dot{U}_{dc}$  | time derivative of the dc link voltage of a voltage source converter in V  |
| $u_{gca}$       | ac voltage of a voltage source converter in pu                             |
| $U_{gca}$       | ac voltage of a voltage source converter in V                              |





Part I

# BACKGROUND



# CHAPTER 1

## *The Active Power Balance Problem from a Technical Perspective*

---

This chapter describes the active power balance problem from a technical perspective. Its main goal is to introduce relevant definitions and the dynamic models used in the problem evaluation. [Sec. 1.1](#) derives the equivalent electromechanical model of a synchronous machine that correlates active power disturbances with frequency deviations in power systems using first principles from Physics. This nonlinear model, also known as the Swing Equation model, presents the main system parameters and variables influencing the frequency dynamics. [Sec. 1.2](#) introduces the three main power balance mechanisms in power systems (inertial, primary, and secondary frequency control) and their associated power reserves (FFR, FCR, and FRR). It also describes the three periods of frequency control (arrest, rebound, and recovery) after a sudden active power disturbance. [Sec. 1.3](#) provides proof of the equivalence between synchronous machines and PECs where the latter are combined with ESDs and respect certain conditions. This last section also highlights and discusses the main assumptions to establish this equivalence, specifying topics that are included and excluded from the scope of this thesis.

### **1.1 THE CORRELATION BETWEEN ACTIVE POWER DISTURBANCES AND FREQUENCY DEVIATIONS IN POWER SYSTEMS**

The first concepts for bulk electric ac power generation were devised in the second half of the nineteenth century. These designs were dominated by the so-called [synchronous machine](#), an electromechanical equipment that converts rotational kinetic energy into electric energy and rotates in sync with the frequency of the supply current. The reason for this dominance involves several technical and economical advantages of electric three-phase power systems and synchronous machines that are well documented in the literature, such as in [1]. This type of power conversion equipment has been commonly represented, since those early days [2–4], by using the physical model of a flywheel spinning at a rated angular speed  $\omega_s$  in  $[\text{rad s}^{-1}]$ , as seen in [Fig. 1.1](#).

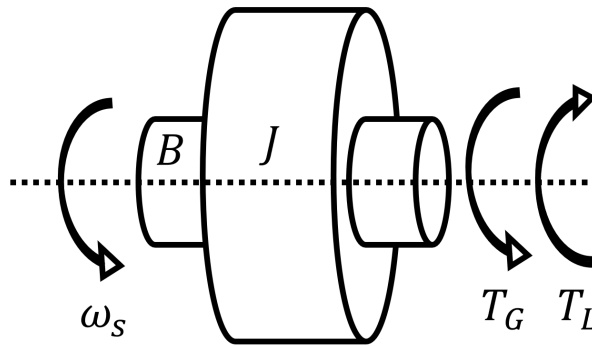


**FIGURE 1.1.** Idealized representation of a [synchronous machine](#) as a flywheel with inertia and damping. © Erick F. Alves, 2022.

The rotating mass of the flywheel is portrayed by an equivalent moment of inertia  $J$ , whereas positive work is done by a turbine through the torque  $T_G$  on one end of the shaft, while negative work is done by electric loads and losses through the torque  $T_L$  on the other end. The turbine is typically driven by a fluid (air, vapor, and water), the flow of which is controlled by a governor, being a single coefficient  $B$  used to represent the natural and controlled damping of this electromechanical system composed by the turbine, synchronous machine, and governor.

$$\frac{1}{2}J(t)\omega^2 = W_G(t, \omega) - W_L(t, \omega) - \int B(t)(\omega - \omega_s)dt \quad (1.1)$$

$$J(t)\omega\dot{\omega} = P_G(t, \omega) - P_L(t, \omega) - B(t)(\omega - \omega_s) \quad (1.2)$$

The work-energy theorem can be applied to this flywheel when assuming this is a closed, conservative system, resulting in Eq. (1.1). This equation expresses the kinetic energy change of the flywheel by the net work done on the body by  $T_G$  and  $T_L$ , where  $J(t)$  is the moment of inertia in  $[\text{kg m}^2]$  and  $B(t)$  is the damping coefficient in  $[\text{N m s rad}^{-1}]$ , both terms being function of the time  $t$ . The angular speed  $\omega$  is in  $[\text{rad s}^{-1}]$ , and the work done by the turbine  $W_G(t, \omega)$  and loads  $W_L(t, \omega)$  are in  $[\text{J}]$ .

Eq. (1.2) presents the time derivative of Eq. (1.1) when  $\dot{J}(t) \approx 0$ , where  $P_G(t, \omega)$  and  $P_L(t, \omega)$  are in  $[\text{W}]$ , those depicting respectively the active power delivered by the turbine and the active power consumed by loads and losses. This equation can be normalized using the base apparent power  $S_b$   $[\text{VA}]$  of the power system as in Eq. (1.3), which has, however, two variables that are not yet normalized, namely  $\omega$  and  $\dot{\omega}$ . The normalization is achieved in Eq. (1.4) when introducing an equivalent inertia constant  $M(t) = J(t)\omega_s^2/S_b$  in  $[\text{s}]$  and a damping coefficient  $D(t) = B(t)\omega_s^2/S_b$  in  $[\text{pu}]$ .

$$\frac{\omega}{S_b} J(t) \dot{\omega} = \frac{P_G(t, \omega)}{S_b} - \frac{P_L(t, \omega)}{S_b} - \frac{\omega}{S_b} B(t) (\omega - \omega_s) \quad (1.3)$$

$$xM(t)\dot{x} = u(t, x) - w(t, x) - xD(t)(x - 1) \quad (1.4)$$

Eq. (1.4) introduces a state-space representation that correlates the instantaneous active power unbalance in a synchronous machine to deviations in its angular speed, where  $x = \omega/\omega_s$ ,  $u(t, x)$  and  $w(t, x)$  are the normalized angular speed, power generation, and power consumption, respectively. This expression is referred to as the Swing Equation in literature and can represent the averaged dynamic behavior of synchronous machines connected in parallel and complex ac grids to a certain extent. The interested reader may find an extensive discussion about the limits of its applications in [5, 6].

Eq. (1.4) can also be obtained where Newton's second law is applied to the flywheel in Fig. 1.1, a procedure described in many classical power systems books [7–11]. The work-energy theorem provides, however, a more general and intuitive framework for thinking about complex power systems where there exist multiple energy carriers, ESDs, and power conversion equipment based on different principles. Work transfers energy from one place to another or one form to another, which is indeed the goal of any power conversion equipment. Work is also a scalar quantity; it has, accordingly, only magnitude and no direction and can be simply added in a closed system. These advantages will become clearer in Sec. 1.3 where a correlation between synchronous machines and PECs is derived. Before that, the next section uses Eq. (1.4) as a basis to summarize the frequency control mechanisms in traditional power systems.

## 1.2 FREQUENCY CONTROL AND POWER RESERVES IN POWER SYSTEMS

The dynamics of Eq. (1.4) could be better understood when rearranging it and defining a state centered at the rated angular speed, i.e.  $\tilde{x} = x - 1$ , as in Eq. (1.5). An inspection of this state-space equation shows that  $\tilde{x} = 0$  (i.e.  $\omega = \omega_s$ ) is an equilibrium point of the system, if  $D(t, \tilde{x}) > 0$ ,  $M(t) > 0$  and there is balance between power generation and demand (i.e.  $u(t, \tilde{x}) = w(t, \tilde{x})$ ). Eq. (1.5) also reveals that the dynamic behavior of  $\tilde{x}$  is governed by three terms:  $M(t)$ ,  $D(t, \tilde{x})$ , and  $u(t, \tilde{x}) - w(t, \tilde{x})$ , each associated to a strategy for control frequency in power systems.

$$M(t)\dot{\tilde{x}} = -D(t, \tilde{x})\tilde{x} + \frac{u(t, \tilde{x}) - w(t, \tilde{x})}{(\tilde{x} + 1)} \quad (1.5)$$

*Inertial control* is physically embedded in synchronous machines as their rotors are flywheels providing the inertial effect required to oppose frequency

variations.  $M(t)$  increases whenever a synchronous machine is directly connected to the power systems and can be seen as a derivative gain in frequency control, meaning that the higher the value of  $M(t)$ , the harder it is to change  $\tilde{x}$  when an active power disturbance occurs.

*Primary control* is offered by equipment that automatically adjusts its active power output proportionally to  $\tilde{x}$ , i.e. the deviation of the grid frequency from its rated value [12]. This scheme is known as frequency-droop control [13] or frequency sensitivity mode [14]. The proportional gain of each droop controller (slope of the frequency sensitivity mode curve) contributes to the value of  $D(t, \tilde{x})$ , where the higher the latter is, the lower  $\tilde{x}$  will be for a given active power disturbance.

*Secondary control* is responsible for reestablishing the balance between power generation and demand and it is typically implemented in a centralized fashion within a dispatch center where the reference of generators or loads are remotely modified after a large disturbance occurs to reestablish  $u(t, \tilde{x}) = w(t, \tilde{x})$  [12]. This process can be seen as an integral contribution that aims to maintain  $\tilde{x} \approx 0$ , making it, therefore, the only frequency control mechanism capable of restoring the kinetic energy of synchronous machines to its rated value and eliminating the steady-state error in  $\tilde{x}$  that activates primary control.

The implementation of frequency control mechanisms requires power reserves in the equipment providing them, in addition to their normal duties. The amount of power reserved by generation units or loads contributing to frequency control is, in Europe, called **frequency containment reserve (FCR)** for primary control and **frequency restoration reserve (FRR)** for secondary control [15]. The newly introduced **fast frequency reserve (FFR)** can be associated with inertial control, but its practical implementation may not correspond entirely to the synchronous machine's inertial effect described above [16].

Fig. 1.2 illustrates the typical dynamic behavior of  $x$  and the three frequency control mechanisms where a perturbation causing excess of demand ( $u < w$ ) occurs at  $t = 0$  and the system was previously in steady state at  $\tilde{x} \approx 0$ . The three distinct periods and the contribution of each control mechanism that follows a disturbance [12, 17] are described below.

The *arrest* period starts immediately after the active power disturbance occurs and lasts until  $x$  reaches its minimum value (nadir) where there is lack of generation ( $u < w$ ), or its maximum value (zenith) where there is excess of generation ( $u > w$ ). Inertial control provides most of the balancing power  $P_a$  initially required to stabilize the system, where primary control gradually delivers **FCR** as  $\tilde{x}$  increases. Important metrics of this period are the total time to reach the nadir/zenith  $t_a$  and the maximum  $\dot{x}$ , also known as the **rate of change of frequency (RoCoF)**.

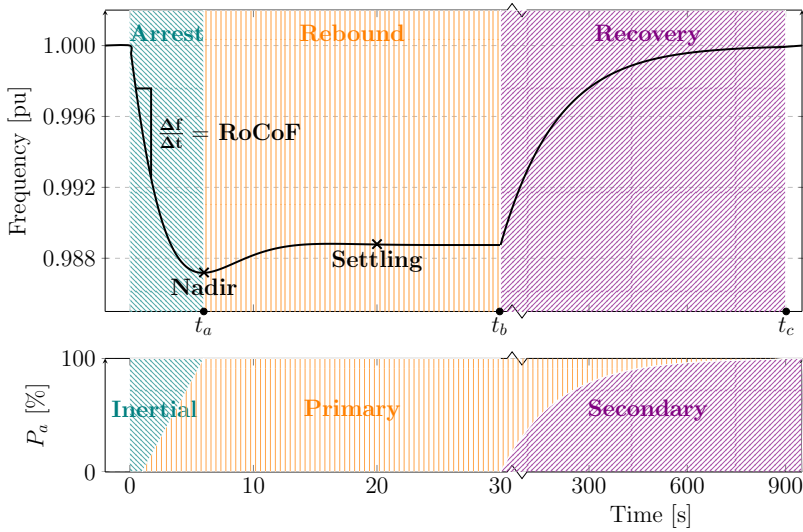


**FIGURE 1.2.** The typical periods of frequency variation (arrest, rebound and recovery) and control actions (inertial, primary and secondary) following a perturbation caused by lack of generation. © Erick F. Alves et al., 2021. [18]

The *rebound* period starts immediately after the nadir/zenith is reached and lasts until the secondary control is activated. **FCR** is fully active at this instant and brings  $x$  to a new equilibrium condition, being this settling point below 1 pu when  $u < w$  and above it when  $u > w$ . The balancing power  $P_a$  is, in general, provided only by the primary control in this period, although the inertial control can work against the frequency restoration process as the sign of  $\dot{x}$  may be inverted.<sup>1</sup> One of the important metrics of this period is the settling time  $t_b$ , i.e., the total time required to activate the secondary control after the nadir/zenith is achieved.<sup>2</sup>

The *recovery* period commences when the secondary control is activated. **FCR** is fully active at  $t_b$ , but **FRR** gradually takes over the balancing power  $P_a$  due to the secondary control action until the balance  $u(t) = w(t)$  is restored and **FCR** is fully deactivated. Tertiary control and generator rescheduling can later replace **FRR** using more optimal resources; this topic is discussed in [Ch. 2](#). One of the important metrics of this period is the recovery time  $t_c$ , i.e., the total time required to reestablish the rated frequency ( $\dot{x} \approx 0$ ).

Note that the demanded energy and power gradient are quite different for

<sup>1</sup>This negative effect can be counteracted where damper windings are added in the rotor of synchronous machines [10].

<sup>2</sup>Note that the rebound period can in theory be eliminated (i.e.,  $t_a = t_b$  and  $\dot{x}(t_a) = \dot{x}(t_b)$ ) where the secondary control action is fast. This is, in general, not the case in traditional, high-inertia power systems which typically have slow secondary control to avoid inertial counteraction and comply with restrictions and limitations of actuators, communication, and control systems.

each frequency control strategy; consequently, not all power units can deliver these ancillary services to the grid simultaneously. **FRR** is the reserve requiring the largest amount of **ES**, followed by **FCR** and **FFR**. **FRR** needs, nonetheless, modest power gradients, which increase dramatically in **FCR** and **FFR**.

Such constraints require the optimal sizing and allocation of reserves for frequency control, which is indeed a century-old problem in electrical power engineering [19, 20] but still timely, as it is being done on a continuous basis by system operators for planning and real-time operation of power systems. The required amount of inertia is, for instance, a design parameter influencing the rotor weight of a synchronous machine and, consequently, its construction costs. Nuclear, coal, and hydro power plants may not be able to deliver the steep power gradients required by **FCR** because of pressure limitations in boilers [21] and penstocks [22], while run-of-the-river hydro power plants may not be capable of delivering **FRR** due to the limited size of their reservoirs.

This problem achieves a new level of complexity when massive electrification and large penetration of **VRESs** occur simultaneously, as the inertia provided by synchronous machines is drastically reduced and, at the same time, instantaneous power imbalances may increase dramatically due to wind and solar units' variability and lack of dispatchability. Sizing and real-time allocation of generating units and **ESDs** to provide **FFR**, **FCR**, and **FRR** become critical tasks to pave the way for more sustainable power systems while ensuring stable and secure supply [23]. The next section presents the theoretical background for how **PECs** combined with **ESDs** could enable **VRESs** and flexible loads to deliver these ancillary services to the grid.

### 1.3 THE EQUIVALENCE BETWEEN POWER ELECTRONIC CONVERTERS AND SYNCHRONOUS MACHINES FOR FREQUENCY CONTROL

Power systems can no longer be represented by the flywheel model of a synchronous machine where power generation is interfaced via **PECs** as  $M(t) \approx 0$  [24]. It is, however, possible to represent the dynamics in Eq. (1.4) using **PECs** and **ESDs** augmented by additional control structures [25].

To achieve that, one can start by applying the work-energy theorem to the idealized voltage source converter represented in Fig. 1.3, assuming its resistances are negligible, and its current control is configured to keep the dc-link voltage  $U_{dc}$  in [V] at its rated value  $U_b^{dc}$  using a droop mechanism. This results in Eq. (1.6), which expresses the electrical energy change in the dc-link capacitor by the net work done on the system, where  $C_{dc}(t)$  is the capacitance in [F],  $K_{U_{dc}}(t)$  is the gain of the droop controller in [ $W V^{-1}$ ], and  $W_{dc}(t)$  and  $W_{ac}(t)$  in [J] are the work done by any device connected to the dc and ac side of the voltage source converter, respectively. Eq. (1.7) presents the time derivative



of Eq. (1.6) for  $\dot{C}(t) \approx 0$ , where  $P_{dc}(t)$  and  $P_{ac}(t)$  are in [W] and depict the active power delivered at the dc side and consumed at the ac side, respectively.

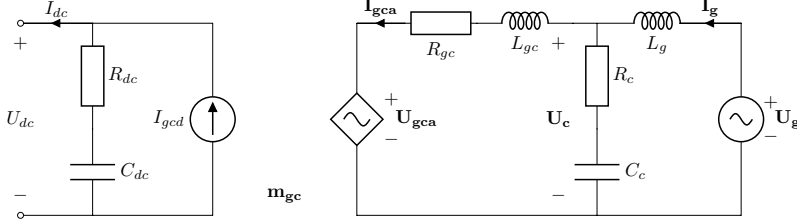


**FIGURE 1.3.** Idealized representation of a voltage source converter with a capacitor  $C_{dc}$  in its dc link and a LCL filter on the ac side. © Erick F. Alves et al., 2021 [18].

$$\frac{1}{2}C_{dc}(t)U_{dc}^2 = W_{dc}(t) - W_{ac}(t) - \int K_{U_{dc}}(t)(U_{dc} - U_b^{dc})dt \quad (1.6)$$

$$C_{dc}(t)U_{dc}\dot{U}_{dc} = P_{dc}(t) - P_{ac}(t) - K_{U_{dc}}(t)(U_{dc} - U_b^{dc}) \quad (1.7)$$

The voltage source converter's active power balance equation can then be normalized using  $U_b^{dc}$  and assuming  $S_b = (U_b^{dc})^2/Z_b^{dc}$ , as in Eq. (1.8), where  $Z_b^{dc}$  is the base impedance on the dc side of the voltage source converter. The normalization is achieved in Eq. (1.10) when introducing, in Eq. (1.9), an equivalent time constant  $N(t) = C(t)Z_b^{dc}$  in [s], where  $K_{u_{dc}} = K_{U_{dc}}Z_b^{dc}/U_b^{dc}$  is in [pu] and  $u_{dc}, p_{dc}(t), p_{ac}(t)$  are the normalized dc-link voltage, dc-side, and ac-side active powers in [pu], respectively.

$$\frac{U_{dc}}{S_b}C_{dc}(t)\dot{U}_{dc} = \frac{P_{dc}(t) - P_{ac}(t) - K_{U_{dc}}(t)(U_{dc} - U_b^{dc})}{S_b} \quad (1.8)$$

$$\frac{U_{dc}}{U_b^{dc}}C_{dc}(t)Z_b^{dc}\frac{\dot{U}_{dc}}{U_b^{dc}} = \frac{P_{dc}(t)}{S_b} - \frac{P_{ac}(t)}{S_b} - K_{U_{dc}}(t)\frac{Z_b^{dc}}{U_b^{dc}}\frac{(U_{dc} - U_b^{dc})}{U_b^{dc}} \quad (1.9)$$

$$u_{dc}N(t)\dot{u}_{dc} = p_{dc}(t) - p_{ac}(t) - K_{u_{dc}}(t)(u_{dc} - 1) \quad (1.10)$$

The similarities between Eqs. (1.4) and (1.10) might be more apparent at this point. The variable that indicates the balance of active power in each swing equation is  $x$  (normalized angular speed) for the synchronous machine and  $u_{dc}$  (normalized dc-link voltage) for the voltage source converter, while the amount of energy stored in these devices are linked to the normalized terms  $M$  and  $N$ , respectively. It is also possible to correlate  $u$  to  $p_{dc}$  and  $w$  to  $p_{ac}$  in these two equations.

A voltage source converter, however, does not deliver frequency control to the ac grid out-of-the-box; this functionality typically requires outer control

loops influencing  $p_{dc}$  or  $p_{ac}$ . Eq. (1.11) is the augmented version of Eq. (1.10) to achieve this goal<sup>3</sup>, where  $\underline{D}(t)$  is a “virtual damping” equivalent to the frequency sensitivity mode of a synchronous machine and  $\underline{M}(t)$  is the parameter of a controller, usually referred to as “virtual inertia” to differentiate it from the physical property provided by synchronous machines [26].

$$u_{dc}N(t)\dot{u}_{dc} = \underbrace{-\underline{M}(t)\dot{\hat{x}} - \underline{D}(t)\hat{x} + u(t)}_{p_{dc}} - \underbrace{w(t)}_{p_{ac}(t)} - K_{u_{dc}}(t)(u_{dc} - 1) \quad (1.11)$$

$$\underline{M}(t)\dot{\hat{x}} = -\underline{D}(t)\hat{x} + u(t) - w(t) \quad (1.12)$$

A crucial difference between Eqs. (1.4) and (1.11) is that  $\hat{x}$  is no longer a state of the system but an estimated input, which makes the performance of frequency control extremely dependent on the quality of the estimation algorithms. This becomes a challenge during the arrest period, where the transient behavior of **phase-locked loops (PLLs)** and frequency-locked loops may cause limitations for the implementation of inertial control [24, 26].

The state variable of a voltage source converter is indeed  $u_{dc}$ , and one valid alternative for dealing with this challenge is to assume that the  $\hat{x}$  dynamics are at least one order of magnitude slower than the  $u_{dc}$  dynamics, as is typically the case in power systems [12]. These two dynamics can, under this condition, be separated in a slow and fast manifold for the purposes of control design and stability analysis [27, Chapters 10 and 11], which, in practical terms, is equivalent to assuming: 1)  $\dot{\hat{x}} = 0$  for  $u_{dc}$  stability analysis of a specific voltage source converter, and 2)  $u_{dc} \approx 1$  for frequency stability analysis of an ac grid where many voltage source converters are present. The second assumption results in Eq. (1.12), which finally concludes the proof of the equivalence between **PECs** and synchronous machines for the purpose of frequency control.

Here it is important to highlight and discuss two major assumptions made to derive Eq. (1.12):

- the time scale separation between  $u_{dc}$  and  $\hat{x}$  dynamics.
- the existence of sufficient, dispatchable power sources connected to the dc link of a voltage source converter to implement the frequency control mechanisms described in **Sec. 1.2**.

The first assumption could be challenged in power systems where the penetration of **VRESs** with limited dispatch capability and interfaced by **PECs** gets close to 100%, considering that  $M(t)$  and  $N(t)$  might have the same order

<sup>3</sup>Eq. (1.11) presents the alternative of influencing  $p_{dc}$  to provide frequency control, although affecting  $p_{ac}$  is also possible.

of magnitude in these conditions. It is assumed, however, that  $M(t) \gg N(t)$  for the remainder of this document, as the presentation of a detailed analysis of the frequency control problem where this condition is no longer valid is regarded outside the scope of this thesis. The interested reader can find a deeper discussion of this topic in [12, 24–26, 28].

It is, on the other hand, the focus of this thesis to discuss and define boundaries for the second assumption, namely defining frameworks to properly size and operate ESDs that shall be connected to the dc link of PECs to provide different frequency control strategies.

## 1.4 REFERENCES

- [1] William James King. 3. The early arc light and generator. In *The Development of Electrical Technology in the 19th Century*. Contributions from the Museum of History and Technology Paper 30, United States National Museum Bulletin 228 pages 333–407. Smithsonian Institution Washington, D.C. (1962). Cited on p. 3.
- [2] Charles Proteus Steinmetz. Theory and Calculation of Alternating Current Phenomena. McGraw New York third edition (1900). URL <http://archive.org/details/in.ernet.dli.2015.261582>. Cited on p. 3.
- [3] André Blondel. Synchronous motors and converters: Theory and methods of calculation and testing. McGraw-Hill New York (1913). URL <https://archive.org/details/cu31924004687129>. Cited on p. 3.
- [4] R. E. Doherty and C. A. Nickle. Synchronous Machines III - Torque-Angle Characteristics Under Transient Conditions. *Transactions of the American Institute of Electrical Engineers XLVI*, 1–18 (January 1927). ISSN 0096-3860. doi: 10.1109/T-AIEE.1927.5061336. Cited on p. 3.
- [5] Sina Yamac Caliskan and Paulo Tabuada. Compositional Transient Stability Analysis of Multimachine Power Networks. *IEEE Transactions on Control of Network Systems* 1 (1), 4–14 (March 2014). ISSN 2325-5870. doi: 10.1109/TCNS.2014.2304868. Cited on p. 5.
- [6] Sina Y. Caliskan and Paulo Tabuada. Uses and abuses of the swing equation model. In *2015 54th IEEE Conference on Decision and Control (CDC)* pages 6662–6667 Osaka (December 2015). IEEE. ISBN 978-1-4799-7886-1. doi: 10.1109/CDC.2015.7403268. Cited on p. 5.
- [7] Charles Concordia. Synchronous machines, theory and performance. Number viii, 224 p. in *General Electric Series*. Wiley New York (1951). URL <//catalog.hathitrust.org/Record/001617157>. Cited on p. 5.
- [8] John J. Grainger and William D. Stevenson. Power system analysis. McGraw-Hill Series in Electrical and Computer Engineering. McGraw-Hill New York (1994). ISBN 978-0-07-061293-8. Cited on p. 5.
- [9] Edward Wilson Kimbark. Power system stability. IEEE Press Power Systems Engineering Series. IEEE Press New York (1995). ISBN 978-0-7803-1135-0. Cited on p. 5.
- [10] P. Kundur, Neal J. Balu, and Mark G. Lauby. Power system stability and control. The EPRI Power System Engineering. McGraw-Hill New York (1994). ISBN 978-0-07-035958-1. Cited on p. 5, 7.
- [11] Jan Machowski, Janusz W. Bialek, and J. R. Bumby. Power system dynamics: Stability and control. Wiley Chichester, U.K 2nd ed edition (2008). ISBN 978-0-470-72558-0. Cited on p. 5.

- [12] Nikos Hatziargyriou, *et al.* Stability definitions and characterization of dynamic behavior in systems with high penetration of power electronic interfaced technologies. Technical Report PES-TR77 IEEE Power System Dynamic Performance Committee (May 2020). URL [https://resourcecenter.ieee-pes.org/technical-publications/technical-reports/PES\\_TP\\_TR77\\_PSDP\\_stability\\_051320.html](https://resourcecenter.ieee-pes.org/technical-publications/technical-reports/PES_TP_TR77_PSDP_stability_051320.html). Cited on p. 6, 10, 11.
- [13] IEEE Std 1547-2018: IEEE Standard for Interconnection and Interoperability of Distributed Energy Resources with Associated Electric Power Systems Interfaces. 1547. IEEE New York, NY (2018). ISBN 978-1-5044-4639-6. URL <https://ieeexplore.ieee.org/servlet/opac?punumber=8332110>. Cited on p. 6.
- [14] Comission Regulation (EU). Network code on requirements for grid connection of generators (April 2016). URL <http://data.europa.eu/eli/reg/2016/631/oj>. Cited on p. 6.
- [15] Comission Regulation (EU). Guideline on electricity transmission system operation (August 2017). URL <http://data.europa.eu/eli/reg/2017/1485/oj>. Cited on p. 6.
- [16] ENTSO-E. Fast Frequency Reserve – Solution to the Nordic inertia challenge. Technical report ENTSO-E (December 2019). URL <https://www.e-pressi.com/media/userfiles/107305/1576157646/fast-frequency-reserve-solution-to-the-nordic-inertia-challenge-1.pdf>. Cited on p. 6.
- [17] Joseph H Eto, John Undrill, Ciaran Roberts, Peter Mackin, and Jeffrey Ellis. Frequency Control Requirements for Reliable Interconnection Frequency Response. Technical Report LBNL-2001103 Lawrence Berkeley National Laboratory Berkley, CA (February 2018). Cited on p. 6.
- [18] Erick Fernando Alves, Daniel dos Santos Mota, and Elisabetta Tedeschi. Sizing of Hybrid Energy Storage Systems for Inertial and Primary Frequency Control. *Frontiers in Energy Research* 9, 649200 (May 2021). ISSN 2296-598X. doi: 10.3389/fenrg.2021.649200. Cited on p. 7, 9.
- [19] Raymond Bailey. Fundamental Plan of Power Supply In the Philadelphia Area. *Transactions of the American Institute of Electrical Engineers* 49 (2), 605–612 (April 1930). ISSN 0096-3860. doi: 10.1109/T-AIEE.1930.5055543. Cited on p. 8.
- [20] First Report of Power System Stability. *Transactions of the American Institute of Electrical Engineers* 56 (2), 261–282 (February 1937). ISSN 0096-3860. doi: 10.1109/T-AIEE.1937.5057521. Cited on p. 8.
- [21] F.P. de Mello. Boiler models for system dynamic performance studies. *IEEE Transactions on Power Systems* 6 (1), 66–74 (Feb./1991). ISSN 08858950. doi: 10.1109/59.131048. Cited on p. 8.
- [22] Hongqing Fang, Long Chen, Nkosinathi Dlakavu, and Zuyi Shen. Basic Modeling and Simulation Tool for Analysis of Hydraulic Transients in Hydroelectric Power Plants. *IEEE Transactions on Energy Conversion* 23 (3), 834–841 (September 2008). ISSN 0885-8969. doi: 10.1109/TEC.2008.921560. Cited on p. 8.
- [23] Thomas Ackermann, Thibault Prevost, Vijay Vittal, Andrew J. Roscoe, Julia Matevosyan, and Nicholas Miller. Paving the Way: A Future Without Inertia Is Closer Than You Think. *IEEE Power and Energy Magazine* 15 (6), 61–69 (November 2017). ISSN 1540-7977. doi: 10.1109/MPE.2017.2729138. Cited on p. 8.
- [24] Federico Milano, Florian Dorfler, Gabriela Hug, David J. Hill, and Gregor Verbic. Foundations and Challenges of Low-Inertia Systems (Invited Paper). In *2018 Power Systems Computation Conference (PSCC)* pages 1–25 Dublin (June 2018). IEEE. ISBN 978-1-910963-10-4. doi: 10.23919/PSCC.2018.8450880. Cited on p. 8, 10, 11.
- [25] Alvaro Ortega and Federico Milano. Generalized Model of VSC-Based Energy Storage Systems for Transient Stability Analysis. *IEEE Transactions on Power Systems* 31 (5), 3369–3380 (September 2016). ISSN 0885-8950, 1558-0679. doi: 10.1109/TPWRS.2015.2496217. Cited on p. 8, 11.

- [26] Jingyang Fang, Hongchang Li, Yi Tang, and Frede Blaabjerg. On the Inertia of Future More-Electronics Power Systems. *IEEE Journal of Emerging and Selected Topics in Power Electronics* 7 (4), 2130–2146 (December 2019). ISSN 2168-6777, 2168-6785. doi: 10.1109/JESTPE.2018.2877766. Cited on p. 10, 11.
- [27] Hassan K. Khalil. *Nonlinear systems*. Always Learning. Pearson Harlow, England third edition edition (2015). ISBN 978-1-78449-013-3. Cited on p. 10.
- [28] Federico Milano and Alvaro Ortega. A Method for Evaluating Frequency Regulation in an Electrical Grid Part I: Theory. *IEEE Transactions on Power Systems* pages 1–1 (2020). ISSN 0885-8950, 1558-0679. doi: 10.1109/TPWRS.2020.3007847. Cited on p. 11.





## CHAPTER 2

### *The Active Power Balance Problem from an Economic Perspective*

---

This chapter describes the active power balance problem from an economic perspective. It introduces the role of tertiary frequency control and summarizes the typical objectives and constraints involved in the planning and operation of power systems. The chapter also highlights the differences between planning and operational problems, gives an overview of the general challenges to achieve optimal techno-economic decisions, defines tertiary control, and outlines the basic formulation of security-constrained active power flow problems.

#### **2.1 CHALLENGES IN THE OPTIMAL PLANNING AND OPERATION OF POWER SYSTEMS**

Electric power is an enabling technology in our modern world and cheap access to it has a strong correlation with economic development and social welfare. Reference [1] depicted that, on average, a 1% increase in the gross domestic product per capita was associated to a 1.3% increment in electricity use based on data from the World Bank Databank for 2014. The authors, moreover, revealed a strong positive association of electricity access and reliability with gross domestic product per capita by reviewing evidence of development dividends in several countries resulting from electrification success stories. Reference [2] also shows that an increase of 2.3 outages per month (one standard deviation) is associated with a reduction of 1.5% in the rate of annual economic growth in Sub-Saharan Africa. Such analyses provide an order of magnitude to the possible economic impact that good or bad decisions in planning and operation of power systems may have.

Making good decisions is, however, a complex task, which involves harmonization of competing objectives. Fig. 2.1, which is inspired by [3], presents typical costs that shall be minimized, divided in three main groups: **capital expenditure (CAPEX)**, **operational expenditures (OPEX)**, and penalties and subsidies. For interconnected power systems, it will also depend on the power market structure and regulations, as different market players and stakeholders

(e.g., government agencies, regulators, transmission system operators, production companies, distribution system operators, aggregators, end-users) can have different objectives. The focus of this thesis is, however, on autonomous power systems, where typically a single entity is responsible for generation, transmission, and distribution planning and operation. Therefore, a discussion about power markets is not included in this chapter.

The goal of planning problems is finding the optimal long-term (several years), least-cost plan for the construction or capacity expansion of a power system, where usually load scenarios are diverse and highly uncertain. For operational problems, on the other hand, the goal is finding the optimal short-term (next hours to one week), least-cost dispatch for an existing power system, where typically CAPEX is disregarded, and a less uncertain load scenario is available. One example of planning problem is the European ten-year development plan [4] published every two years by ENTSO-E, while the single day-ahead and intraday capacity allocation and congestion management in Europe [5] are examples of operational problems.

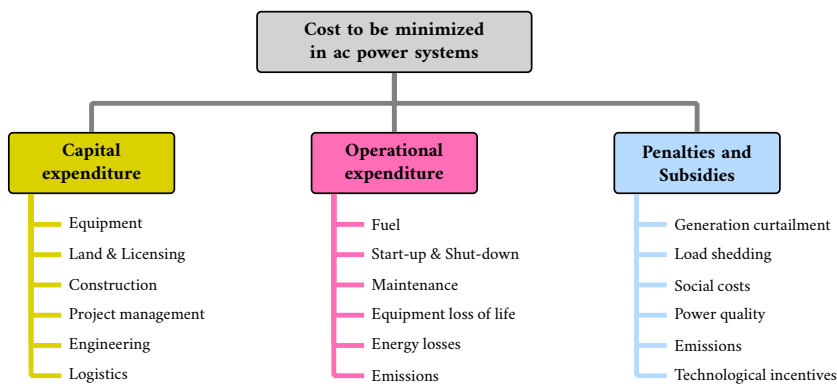


**FIGURE 2.1.** Typical costs to be minimized in power systems. © Erick F. Alves, 2022.

These problems are usually highly constrained, independent of their type (planning or operational), with the most typical limitations being:

- Generated and consumed electric power shall be balanced at every instant. Substantial amounts of electricity can only be stored in other energy forms, such as kinetic, potential, chemical, or thermal, where any conversion process is associated to losses and delays.
- Most power conversion equipment has operational limits, with the most common being maximum and minimum operating points, rate of set-point change, and minimum up and down time.



- Allocation of adequate power and energy reserves is necessary to ensure the system operates securely even under faults or large disturbances.
- Decisions are restricted by process limitations, regulations, guidelines, or market mechanisms.

If such constraints and the continuous differential formulations described in Ch. 1 are considered concurrently, huge computational resources and time-consuming calculations would be necessary to evaluate even small systems in time periods ranging from hours to years. The most common approach is, therefore, discretizing the problem and approximating the dynamic behavior of power systems by algebraic equations, which makes the application of extremely efficient algorithms used in mathematical optimization possible. Examples of such formulations include the generation expansion planning [6], the unit commitment [7], and the economic dispatch [8].

Such trade-offs between precision, accuracy, and computational tractability are key to allow convergence to an optimal solution in predefined time intervals, which in operational problems can be exceedingly small. Intraday capacity allocation and congestion management in Europe are, for instance, done in intervals of one hour [5], the imbalance settlement for FCR and FRR is done in gaps of fifteen minutes [9], while both dispatch and financial settlement of the physical market in Australia is done in five-minute intervals [10]. For autonomous power systems, there are no general industry standards to date setting requirements on time intervals for dispatch or allocation of frequency-control reserves. The decision intervals are, therefore, made at the discretion of the system owner or operator, depending on the capabilities and limitations of the installed equipment and the EMS. There is, however, some consensus that increasing the time granularity in dispatch decisions can reduce OPEX in large, integrated power systems with high penetration of VRES [11], meaning it is reasonable to extend these conclusions to autonomous systems as well.

Note that the solution of an operational optimization problem results in the dispatch of a set of units, which is the source of the *tertiary frequency control* and replaces via optimal sources the active reserves supplying secondary and primary frequency control at a specified time interval. The amount of power reserved to tertiary frequency control is, in Europe, called replacement reserve [12], typically considered a non-spinning reserve, which means that assigned equipment shall be first put in operation or shutdown to provide this ancillary service. From a control theory perspective, tertiary control can be understood as a feedforward contribution to the frequency control loop, while primary and secondary controls are feedback contributions. This concept is shown in Fig. 2.2, where  $w$  is a vector representing active disturbances to the power system, and  $u$  is a vector representing the dispatch of each unit.

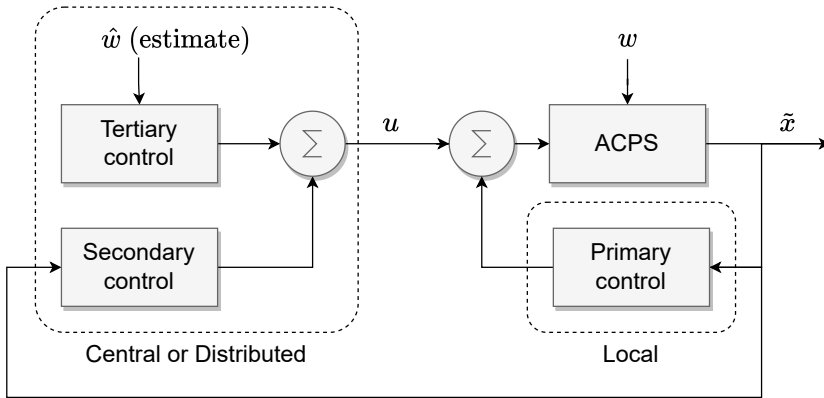


**FIGURE 2.2.** Overview of the traditional frequency control architecture in power systems. © Erick F. Alves, 2022.

The development of more advanced control architectures that allow real-time feedback optimization of autonomous power systems and integrate secondary and tertiary frequency control into a single controller has been an active area of research [13]. Those approaches are based on unified multiple-input, multiple-output control systems, which can tackle frequency control more efficiently than the parallel *single-input, single-output (SISO)* controllers shown in Fig. 2.2. Several questions remain, however, about how these strategies can be integrated into current planning practices, what the measurement and communication infrastructure required are, and the feasibility of decoupling the frequency stability parameters and dynamic response from market mechanisms. Such advanced architectures are excluded from the scope of this thesis, and the traditional architecture presented in Fig. 2.2 is assumed throughout the text.

## 2.2 SECURITY-CONSTRAINED ACTIVE POWER FLOW PROBLEMS

*Security-constrained* is a common qualifier used in the literature to refer to problems for planning and operation of power systems that consider frequency stability and allocation of spinning and non-spinning reserves in their formulation [14–16]. The term may also include other types of stability issues such as congestion of lines, voltage, and rotor angle stability [17], though those are not discussed in this thesis.

This section reviews the general formulation of security-constrained active power flow optimization problems in power systems, which is summarized in Eq. (2.1). Focus is given to discriminating typical constraints and explaining the logic behind them. Solution methods are not discussed in detail at this stage for

the sake of simplicity, although those may strongly affect results, convergence time, and strategies to implement practical algorithms. This topic will, however, be addressed in subsequent chapters.

$$\begin{aligned}
 \mathcal{P} : \min_{\mathbf{x}} \{ & \mathcal{F}(\mathbf{x}, \mathbf{w}) \} \\
 \text{where } \mathcal{F} := & \underbrace{\mathcal{J}_C(\mathbf{x}, \mathbf{w})}_{\text{CAPEX}} + \underbrace{\mathcal{J}_O(\mathbf{x}, \mathbf{w})}_{\text{OPEX}} + \underbrace{\mathcal{J}_{PS}(\mathbf{x}, \mathbf{w})}_{\text{Penalties \& Subsidies}} \\
 \text{subject to: } & \mathcal{G}(\mathbf{x}, \mathbf{w}) \leq 0 \\
 & \mathcal{H}(\mathbf{x}, \mathbf{w}) = 0
 \end{aligned} \tag{2.1}$$

In Eq. (2.1),  $\mathbf{x}$ ,  $\mathbf{w}$  are vectors of system states. Elements of  $\mathbf{x}$  include variables related to controllable elements, such as dispatchable sources and loads. They can be further subdivided into binary variables, such as on/off status or startup/shutdown indicators, and continuous variables, such as active power dispatch or amount of FCR. Elements of  $\mathbf{w}$  are related to non-controllable elements, such as contingencies, non-dispatchable sources and loads. They can also be separated into binary and continuous variables, examples being the status of circuit breakers, solar irradiance, or wind speed.

$\mathcal{F}$  depicts a cost function that can be decomposed into the three groups of costs represented in Fig. 2.1, where  $\mathcal{J}_C, \mathcal{J}_O$ , and  $\mathcal{J}_{PS}$  express CAPEX, OPEX, and penalties and subsidies, respectively. The description of these cost elements may be strongly affected by choice of technology, local conditions, regulations, and practices, which is a challenge when one would like to compare results for different generation options. It is a widespread practice, therefore, to compare distinct alternatives, projects, or systems based on their LCOE, which is defined as the ratio between the net present value of all expenses and estimated energy production during a predefined period, typically the system lifetime. Note that typically  $\mathcal{J}_C$  is not considered in operational problems. A description of cost functions for specific study cases will be provided in the next chapters, with a deeper discussion about the matter considered beyond the scope of this thesis. This topic, however, is well explored in the literature and the interested reader can find extensive reviews in, for instance, [3, 18].

$\mathcal{H}$  represents the set of equality constraints of the problem, the most important being the system static power balance presented in Eq. (2.10). The latter is derived from Eq. (1.4) assuming steady-state ( $\dot{\mathbf{x}} = 0$ ) and a perfect match between generation and consumption ( $u = w$ ). Where the dynamics of non-controllable loads and sources are considered, it is highly improbable that such assumptions will hold for the complete duration of a single step of the optimization problem, which may range from five minutes and up to one hour, as argued in the previous section. It is necessary, therefore, to properly allocate

spinning reserves, such as FFR, FCR, and FRR, to ensure that the values of  $\hat{x}$  and  $\dot{\hat{x}}$  are maintained at acceptable levels, as discussed earlier in Sec. 1.2.

$\mathcal{G}$  represents the set of inequality constraints of the problem, the most common being the operational limits of dispatchable elements (sources or loads) and the distribution of spinning reserves. Examples include, for each element, the maximum allowed FCR allocation (Eqs. (2.2) and (2.3)), the maximum and minimum operating points (Eq. (2.4)), and the rate of setpoint change (Eq. (2.5)). Other typical inequality constraints include restrictions for turning on or off controllable elements (Eqs. (2.6) and (2.7)) and for their minimum up (Eq. (2.8)) and down (Eq. (2.9)) time intervals.

The terms in these constraints are described below, where the subscript  $c$  indicates an element of the set  $C$  of controllable sources and loads and the subscript  $i$  indicates an element of the discrete set  $[t_0, t_0 + T_s, \dots, t_0 + NT_s]$ , with  $t_0$ ,  $T_s$ , and  $N$  representing the initial time, the time step, and the total number of steps of the optimization problem, respectively:

- $P_{c,i}^{FCR,up}, P_{c,i}^{FCR,dn}$ , the FCR allocated for upward and downward frequency regulation.
- $\rho_{c,i}$ , the on/off status.
- $D_c^{mx,up}, D_c^{mx,dn}$ , the maximum damping that can be allocated for upward and downward frequency regulation.
- $\hat{x}^{mx}, \hat{x}^{mn}$ , the maximum and minimum allowed frequency deviation from its rated value.
- $P_{c,i}, P_w$ , the active power dispatch and the power consumption.
- $P_c^{mx}, P_c^{mn}$ , the maximum and minimum setpoints.
- $R_c^{up}, R_c^{dn}$ , the maximum rate of setpoint change for upward and downward regulation.
- $\nu_{c,i}, \mu_{c,i}$ , the shutdown and the startup decisions.
- $T_c^{up}, T_c^{dn}$ , the minimum up and down time intervals.

$$\forall i, \forall c \quad P_{c,i}^{FCR,up} \leq -\rho_{c,i} D_c^{mx,up} \tilde{x}^{mn} \quad (2.2)$$

$$\forall i, \forall c \quad P_{c,i}^{FCR,dn} \leq \rho_{c,i} D_c^{mx,dn} \tilde{x}^{mx} \quad (2.3)$$

$$\forall i, \forall c \quad \rho_{c,i} P_c^{mn} + P_{c,i}^{FCR,dn} \leq P_{c,i} \leq \rho_{c,i} P_c^{mx} - P_{c,i}^{FCR,up} \quad (2.4)$$

$$\forall i, \forall c \quad T_s R_c^{dn} \leq P_{c,i+1} - P_{c,i} \leq T_o R_c^{up} \quad (2.5)$$

$$\forall i, \forall c \quad v_{c,i} - \mu_{c,i} \leq \rho_{c,i-1} - \rho_{c,i} \quad (2.6)$$

$$\forall i, \forall c \quad \mu_{c,i} - v_{c,i} \leq 1 \quad (2.7)$$

$$i \geq T_c^{up}, \forall c \quad \sum_{k=i-T_c^{up}}^{i-1} \rho_{c,k} \leq T_c^{up} v_{m,i} \quad (2.8)$$

$$i \geq T_c^{dn}, \forall c \quad \sum_{k=i-T_c^{dn}}^{i-1} \rho_{c,k} \leq T_c^{dn} (1 - \mu_{m,i}) \quad (2.9)$$

$$\forall i, \quad \sum_c P_{c,i} - P_w = 0 \quad (2.10)$$

Note that  $P_w$  is typically a stochastic variable and an input to the security-constrained active power flow optimization problem. It is assumed, in this formulation, that the contribution of VRES with limited dispatch capability is summed up and discounted from  $P_w$ . The problem is considered deterministic where values of  $P_w$  are a priori well defined, and probabilistic or stochastic where only the probability density function of  $P_w$  is known. This choice naturally affects the solution method of the problem, as addressed in the next chapters.

Where allocation of spinning reserves is considered, it is necessary to guarantee that  $\mathcal{G}$  includes system constraints, in addition to the restrictions for each element in  $\mathcal{C}$  described above. From a frequency stability perspective, the most important constraints are related to minimum values of the total system inertia  $M_{min}$  and damping  $D_{min}$ , so that thresholds for  $\tilde{x}^{mx}$ ,  $\tilde{x}^{mn}$ ,  $\dot{\tilde{x}}^{mx}$ , and  $\dot{\tilde{x}}^{mn}$  are observed. Note, however, that the system model represented in Eq. (1.4) is a nonlinear differential equation, which can transform the optimization into a non-convex or convex nonlinear problem depending on the choice of decision variables and drastically increase the solution time. The linearization of the model is a widespread approach to deal with this issue, which is made easier when assuming that  $\tilde{x}$  is typically small in a bulk power system [19, 20]. This procedure reduces the model to the linear differential equation presented in Eq. (2.11), which can be used to obtain the system inequality constraints related to FCR in Eqs. (2.12) and (2.13) where the dynamics of the arrest period (refer to Fig. 1.2) are ignored or, in other words, where  $\dot{\tilde{x}} = 0$  is assumed. The undefined terms in these equations are:

- $P_{sup,i}^{FCR} = \sup \{ \sum_c P_c(t) - P_w(t) : t_0 + T_s i \geq t \geq t_0 + T_s(i+1) \}$ , the least upper bound or *supremum* of the power imbalance between the current and the next decision interval.
- $P_{inf,i}^{FCR} = \inf \{ \sum_c P_c(t) - P_w(t) : t_0 + T_s i \geq t \geq t_0 + T_s(i+1) \}$ , the greatest lower bound or *infimum* of the power imbalance between the current and the next decision interval.

$$\overbrace{M(t)\dot{\tilde{x}}}^{FRR} = \overbrace{-D(t)\tilde{x}}^{FCR} + \overbrace{\sum_c P_c(t)}^{FRR} - P_w(t) \quad (2.11)$$

$$-P_{inf,i}^{FCR} \leq \sum_c P_{c,i}^{FCR,up} \quad (2.12)$$

$$P_{sup,i}^{FCR} \leq \sum_c P_{c,i}^{FCR,dn} \quad (2.13)$$

The values of  $P_{inf,i}^{FCR}$ ,  $P_{sup,i}^{FCR}$  are usually defined in a security assessment, a task whose complexity increases with the size of the power system. Disturbances included in this assessment are, for instance, the sudden disconnection of the largest load or source in the system, also known as the N-1 criteria, or the largest expected sudden variation of VRES [12]. Other threats to the power system may also be analyzed, such as incorrect operation of protection and control equipment, exceptional weather conditions, human failure, and cyber-attacks, just to name a few. Calculations of  $P_{inf,i}^{FCR}$ ,  $P_{sup,i}^{FCR}$  can usually be included as a subroutine in the optimization algorithm where a simplified security assessment is possible, such as fulfilling the N-1 criteria. More complex procedures are usually performed externally and fed back into the optimization algorithm. Security assessment is an involved topic and only simplified approaches are addressed in the next chapters, since complex procedures and their integration in the optimization problem are considered outside the scope of this thesis. The interested reader can find an example of a complex procedure in [21] and investigate further the topic in [22].

In security-constrained active power flow optimization problems, the allocation of FRR follows a process like FCR, i.e., quantification of the required reserves followed by ensuring via constraints that enough active power capacity is available in controllable sources and loads. The main difference is that FRR replaces FCR in the recovery period, as discussed in Sec. 1.2, therefore making it necessary to account for that in  $\mathcal{G}$ . FRR can also directly compensate smooth variations in  $P_w$ , in which the fast action of FCR and FFR is not required. This may require an analysis of power imbalances during several decision intervals, particularly if the recovery period can be larger than  $T_s$ , which

is a typical situation in operational problems. Eqs. (2.14) and (2.15) present the system inequality constraints related to FRR, taking the arguments above into consideration, where the newly introduced terms are:

- $P_{sup,i}^{FRR} = \sup \{ \sum_c P_c(t) - P_w(t) : t_0 + T_s i \geq t \geq t_0 + T_s(i + N_{FRR}) \}$ , the least upper bound or *supremum* of the power imbalance between the current and the next  $N_{FRR}$  decision intervals.
- $P_{inf,i}^{FRR} = \inf \{ \sum_c P_c(t) - P_w(t) : t_0 + T_s i \geq t \geq t_0 + T_s(i + N_{FRR}) \}$ , the greatest lower bound or *infimum* of the power imbalance between the current and the next  $N_{FRR}$  decision intervals.

$$- \min \left\{ P_{inf,i}^{FRR}, P_{inf,i}^{FCR} \right\} \leq \sum_c (P_c^{mx} - P_{c,i}) \quad (2.14)$$

$$\max \left\{ P_{sup,i}^{FRR}, P_{sup,i}^{FCR} \right\} \leq \sum_c (P_{c,i} - P_c^{mn}) \quad (2.15)$$

Where allocation of FFR is considered, the faster dynamics in the arrest period shall be considered to address limitations in  $\dot{\tilde{x}}^{mx}$ ,  $\dot{\tilde{x}}^{mn}$  and transient values of  $\tilde{x}^{mx}$ ,  $\tilde{x}^{mn}$  (a.k.a. frequency zenith and nadir). To achieve this goal, the model from Eq. (2.11) must be extended to include the dynamics of actuators, a procedure that transforms the power system model into a system of differential equations and complicates the linearization procedure. Eq. (2.16), for instance, presents a model extension, where the dynamics of actuators are approximated by a first-order time delay  $\epsilon_c$  and each element of set  $C$  can contribute with a damping  $D_c$  and an inertia  $M_c$ , either physical or virtual.

$$\begin{aligned} \Sigma_0 : \quad & \sum_c M_c(t) \dot{\tilde{x}} = \sum_c (P_c(t) + y_c) - P_w(t) \\ \Sigma_c : \quad & \epsilon_c \dot{y}_c = -y_c - D_c(t) \tilde{x} \end{aligned} \quad (2.16)$$

This topic has been an active area of research in recent years and several works in the literature proposed simplifications and analytical solutions of Eq. (2.16) to address this issue, such as [23–29]. These analytical approaches present, at the same time, a solution but also a challenge, as most of them introduce nonlinear relationships between  $D_c$ ,  $M_c$ ,  $\epsilon_c$  that can drastically increase the solution time of optimization algorithms. This issue has been addressed in large power systems considering  $D_{c,i}$  and  $M_{c,i}$  constants and controlling the total system inertia  $M_i$  and damping  $D_i$  at each iteration  $i$  using the binary decision variables  $\nu_{c,i}$ ,  $\mu_{c,i}$ , which allows a convex problem formulation. Note that, where set  $C$  is large enough, the transitions between possible discrete values of  $D_{c,i}$  and  $M_{c,i}$  may be sufficiently smooth, and such an approach can be

used for adapting the system parameters to achieve a particular performance during the arrest period.

Set  $C$ , on the other hand, can be small in autonomous power systems, such as isolated industrial plants, O&G platforms, ships, islands, and community microgrids, making a discrete control scheme hard to apply as a consequence. An offshore O&G platform, for instance, is typically equipped with two to five GTs in its power generation system and a small number of flexible loads. Where a high penetration of wind power and ES is allowed to reduce greenhouse gases (GHG) emissions, there is little margin to control  $D_{c,i}$  and  $M_{c,i}$  using binary decision variables, as the system has a small number of controllable sources and loads. The alternative, in such conditions, is including  $D_{c,i}$  and  $M_{c,i}$  as continuous decision variables in the optimization. An inspection of Eq. (2.11), nonetheless, will reveal that the dynamic response of the arrest period depends on the ratio between these decision variables, turning the optimization into a non-convex problem.

Another important discussion is the conditions where the linearization of the swing equation presented in Eq. (2.11) continues to be valid, as most of the constraints proposed in the literature relies on this model. Note that autonomous power systems may be subject to larger frequency variations than bulk power systems, as a tight frequency regulation is typically a challenge in low-inertia systems where time delays of actuators are in the same order of magnitude as  $M$ . Equipment in offshore O&G installations, for instance, must be designed to withstand frequency variations of up 5% continuously [30], but the assumptions used to derive Eq. (2.11) consider an upper bound of 1%.

The focus of this thesis is defining frameworks to properly size and operate ESDs that shall be connected to the dc link of PECs to provide different frequency control strategies, as stated in Ch. 1. To this end, these frameworks must be integrated into security-constrained active power flow optimization problems. This allows one to obtain a complete techno-economic perspective to optimally size equipment in planning problems or allocate their use in operational problems, minimizing, therefore, the LCOE of autonomous power systems or other alternative objectives.

## 2.3 REFERENCES

- [1] David I. Stern, Paul J. Burke, and Stephan B. Bruns. The Impact of Electricity on Economic Development: A Macroeconomic Perspective (December 2017). URL <https://escholarship.org/uc/item/7jb0015q>. Cited on p. 15.
- [2] Thomas Barnebeck Andersen and Carl-Johan Dalgaard. Power outages and economic growth in Africa. *Energy Economics* **38**, 19–23 (July 2013). ISSN 01409883. doi: 10.1016/j.eneco.2013.02.016. Cited on p. 15.



- [3] Aftab Ahmad Khan, Muhammad Naeem, Muhammad Iqbal, Saad Qaisar, and Alagan Anpalagan. A compendium of optimization objectives, constraints, tools and algorithms for energy management in microgrids. *Renewable and Sustainable Energy Reviews* **58**, 1664–1683 (May 2016). ISSN 13640321. doi: 10.1016/j.rser.2015.12.259. Cited on p. 15, 19.
- [4] ENTSO-E. Completing the map – Power system needs in 2030 and 2040. Technical Report TYNDP2020 ENTSO-E Brussels, Belgium (2030). URL [https://eepublicdownloads.blob.core.windows.net/public-cdn-container/tyndp-documents/TYNDP2020/FINAL/entso-e\\_TYNDP2020\\_IoSN\\_Main-Report\\_2108.pdf](https://eepublicdownloads.blob.core.windows.net/public-cdn-container/tyndp-documents/TYNDP2020/FINAL/entso-e_TYNDP2020_IoSN_Main-Report_2108.pdf). Cited on p. 16.
- [5] Comission Regulation (EU). Guideline on capacity allocation and congestion management (July 2015). URL <http://data.europa.eu/eli/reg/2015/1222/oj>. Cited on p. 16, 17.
- [6] Vishwamitra Oree, Sayed Z. Sayed Hassen, and Peter J. Fleming. Generation expansion planning optimisation with renewable energy integration: A review. *Renewable and Sustainable Energy Reviews* **69**, 790–803 (March 2017). ISSN 13640321. doi: 10.1016/j.rser.2016.11.120. Cited on p. 17.
- [7] Ying-Yi Hong and Gerard Francesco DG Apolinario. Uncertainty in Unit Commitment in Power Systems: A Review of Models, Methods, and Applications. *Energies* **14** (20), 6658 (January 2021). ISSN 1996-1073. doi: 10.3390/en14206658. Cited on p. 17.
- [8] X. Xia and A. M. Elaiw. Optimal dynamic economic dispatch of generation: A review. *Electric Power Systems Research* **80** (8), 975–986 (August 2010). ISSN 0378-7796. doi: 10.1016/j.epsr.2009.12.012. Cited on p. 17.
- [9] Comission Regulation (EU). Guideline on electricity balancing (November 2017). URL <http://data.europa.eu/eli/reg/2017/2195/oj/eng>. Cited on p. 17.
- [10] AEMC. Five Minute Settlement, final determination (November 2017). URL <https://www.aemc.gov.au/sites/default/files/content/97d09813-a07c-49c3-9c55-288baf8936af/ERC0201-Five-Minute-Settlement-Final-Determination.PDF>. Cited on p. 17.
- [11] IRENA. Increasing time granularity in electricity markets: Innovation landscape brief. Technical Report 978-92-9260-127-0 IRENA Abu Dhabi (2019). Cited on p. 17.
- [12] Comission Regulation (EU). Guideline on electricity transmission system operation (August 2017). URL <http://data.europa.eu/eli/reg/2017/1485/oj>. Cited on p. 17, 22.
- [13] Florian Dorfler, Saverio Bolognani, John W. Simpson-Porco, and Sergio Grammatico. Distributed Control and Optimization for Autonomous Power Grids. In *2019 18th European Control Conference (ECC)* pages 2436–2453 Naples, Italy (June 2019). IEEE. ISBN 978-3-907144-00-8. doi: 10.23919/ECC.2019.8795974. Cited on p. 18.
- [14] Baraa Mohandes, Mohamed Shawky El Moursi, Nikos Hatziargyriou, and Sameh El Khatib. A Review of Power System Flexibility With High Penetration of Renewables. *IEEE Transactions on Power Systems* **34** (4), 3140–3155 (July 2019). ISSN 0885-8950, 1558-0679. doi: 10.1109/TPWRS.2019.2897727. Cited on p. 18.
- [15] Joachim Steinkohl, Saeed Peyghami, Xiongfei Wang, Pooya Davari, and Frede Blaabjerg. Frequency security constrained control of power electronic-based generation systems. *IET Renewable Power Generation* **15** (10), 2246–2256 (July 2021). ISSN 1752-1416, 1752-1424. doi: 10.1049/rpg2.12159. Cited on p. 18.
- [16] Nan Yang, Zhenqiang Dong, Lei Wu, Lei Zhang, Xun Shen, Daojun Chen, Binxin Zhu, and Yikui Liu. A Comprehensive Review of Security-constrained Unit Commitment. *Journal of Modern Power Systems and Clean Energy* **10** (3), 562–576 (2022). ISSN 2196-5625. doi: 10.35833/MPCE.2021.000255. Cited on p. 18.
- [17] Florin Capitanescu. Critical review of recent advances and further developments needed in AC optimal power flow. *Electric Power Systems Research* **136**, 57–68 (July 2016). ISSN 03787796. doi: 10.1016/j.epsr.2016.02.008. Cited on p. 18.
- [18] Morteza Nazari-Heris, Somayeh Asadi, and Behnam Mohammadi-Ivatloo, editors. Plan-

- ning and Operation of Multi-Carrier Energy Networks. Power Systems. Springer International Publishing Cham (2021). ISBN 978-3-030-60085-3 978-3-030-60086-0. doi: 10.1007/978-3-030-60086-0. Cited on p. 19.
- [19] P. Kundur, Neal J. Balu, and Mark G. Lauby. Power system stability and control. The EPRI Power System Engineering. McGraw-Hill New York (1994). ISBN 978-0-07-035958-1. Cited on p. 21.
- [20] Jan Machowski, Janusz W. Bialek, and J. R. Bumby. Power system dynamics: Stability and control. Wiley Chichester, U.K 2nd ed edition (2008). ISBN 978-0-470-72558-0. Cited on p. 21.
- [21] Emanuele Ciapessoni, Diego Cirio, Gerd Kjolle, Stefano Massucco, Andrea Pitto, and Marino Sforna. Probabilistic Risk-Based Security Assessment of Power Systems Considering Incumbent Threats and Uncertainties. *IEEE Transactions on Smart Grid* 7 (6), 2890–2903 (November 2016). ISSN 1949-3053, 1949-3061. doi: 10.1109/TSG.2016.2519239. Cited on p. 22.
- [22] Goran Strbac, Daniel Kirschen, and Rodrigo Moreno. Reliability Standards for the Operation and Planning of Future Electricity Networks. Now Publishers Norwell, MA (2016). ISBN 978-1-68083-183-2. URL <http://public.eblib.com/choice/PublicFullRecord.aspx?p=6308989>. Cited on p. 22.
- [23] Vivek Prakash, Kailash Chand Sharma, Rohit Bhakar, Har Pal Tiwari, and Furong Li. Frequency Response Constrained Modified Interval Scheduling Under Wind Uncertainty. *IEEE Transactions on Sustainable Energy* 9 (1), 302–310 (January 2018). ISSN 1949-3029, 1949-3037. doi: 10.1109/TSTE.2017.2731941. Cited on p. 23.
- [24] Qingxin Shi, Fangxing Li, and Hantao Cui. Analytical Method to Aggregate Multi-Machine SFR Model With Applications in Power System Dynamic Studies. *IEEE Transactions on Power Systems* 33 (6), 6355–6367 (November 2018). ISSN 0885-8950, 1558-0679. doi: 10.1109/TPWRS.2018.2824823. Cited on p. 23.
- [25] Luis Badesa, Fei Teng, and Goran Strbac. Simultaneous Scheduling of Multiple Frequency Services in Stochastic Unit Commitment. *IEEE Transactions on Power Systems* 34 (5), 3858–3868 (September 2019). ISSN 0885-8950, 1558-0679. doi: 10.1109/TPWRS.2019.2905037. Cited on p. 23.
- [26] Vincenzo Trovato, Agnes Bialecki, and Anes Dallagi. Unit Commitment With Inertia-Dependent and Multispeed Allocation of Frequency Response Services. *IEEE Transactions on Power Systems* 34 (2), 12 (2019). Cited on p. 23.
- [27] Ziyang Zhang, Ershun Du, Fei Teng, Ning Zhang, and Chongqing Kang. Modeling Frequency Dynamics in Unit Commitment With a High Share of Renewable Energy. *IEEE Transactions on Power Systems* 35 (6), 4383–4395 (November 2020). ISSN 0885-8950, 1558-0679. doi: 10.1109/TPWRS.2020.2996821. Cited on p. 23.
- [28] Tao Ding, Ziyu Zeng, Ming Qu, Joao P. S. Catalao, and Mohammad Shahidehpour. Two-Stage Chance-Constrained Stochastic Thermal Unit Commitment for Optimal Provision of Virtual Inertia in Wind-Storage Systems. *IEEE Transactions on Power Systems* 36 (4), 3520–3530 (July 2021). ISSN 0885-8950, 1558-0679. doi: 10.1109/TPWRS.2021.3051523. Cited on p. 23.
- [29] Vincenzo Trovato. System Scheduling with Optimal Time-varying Delivery Intervals for Frequency Response. *IEEE Transactions on Power Systems* page 16 (February 2022). Cited on p. 23.
- [30] IEC 61892-2:2019 Mobile and fixed offshore units - Electrical installations - Part 2: System design. IEC Geneva, Switzerland (April 2019). ISBN 978-2-8322-6667-0. URL <https://webstore.iec.ch/publication/6083>. Cited on p. 24.





Part II

# RESULTS



## CHAPTER 3

### *Power quality in wind-powered oil and gas platforms*

---

Erick Alves<sup>1</sup>, Santiago Sanchez<sup>1</sup>, and Elisabetta Tedeschi<sup>1</sup>

Conference poster presented in: *EERA Deep Wind'19* - 16th Deep Sea Offshore Wind R&D conference (January 2019).

DOI: [10.13140/RG.2.2.11176.01289](https://doi.org/10.13140/RG.2.2.11176.01289)



**Open Access** This work is licensed under a Creative Commons Attribution 4.0 International License. It means that unrestricted use, sharing, adaptation, distribution, and reproduction in any medium or format are allowed, as long as the original author(s) and the source are appropriately credited, a link to the Creative Commons license is provided, and any changes made are indicated. To view a copy of this license, please visit <http://creativecommons.org/licenses/by/4.0/>.

© Alves, Sanchez and Tedeschi, 2019.

#### **Author Contributions**

Conceptualization, E.A. and E.T.; methodology, E.A. and S.S.; software, E.A. and S.S.; validation, E.A.; formal analysis, E.A.; investigation, E.A.; resources, S.S. and E.T.; data curation, E.A.; writing—original draft preparation, E.A.; writing—review and editing, S.S., and E.T.; visualization, E.A.; supervision, S.S. and E.T.; project administration, E.T.; funding acquisition, E.T.

---

<sup>1</sup>Department of Electric Power Engineering, NTNU, 7034 Trondheim, Norway.



# POWER QUALITY IN WIND-POWERED OIL AND GAS PLATFORMS

ERICK F. ALVES, SANTIAGO S. ACEVEDO, ELISABETTA TEDESCHI  
Department of Electric Power Engineering

## RESEARCH QUESTIONS



In offshore platforms with high penetration of wind power:

1. Which power quality problems in the time-scale of seconds appear with no power from shore?
2. How energy storage can improve power quality?
3. What influences the sizing of the energy storage?

## CONTACT INFORMATION

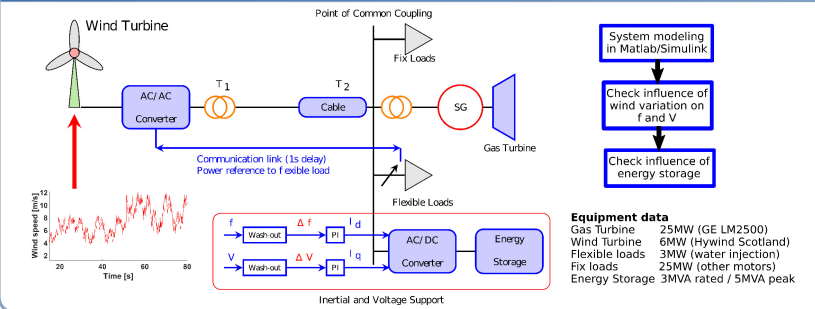


<https://tinyurl.com/HES-OFF>



erick.f.alves@ntnu.no  
santiago.sanchez@ntnu.no  
elisabetta.tedeschi@ntnu.no

## METHOD



## RESULTS

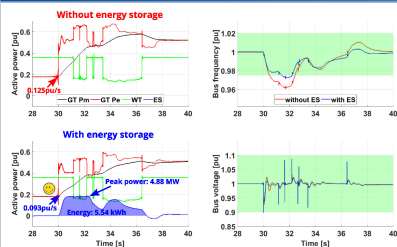


Figure 1: 10 MW load is switched on (1 pu = 25 MVA)

Electrical power quality problems:  
 $\uparrow \Delta f \Rightarrow \uparrow$  governor actuation  $\Rightarrow \uparrow$  wear and tear ☹️  
 $\uparrow \Delta V \Rightarrow \uparrow (P_m - P_e) \Rightarrow \uparrow$  mechanical stresses ☹️

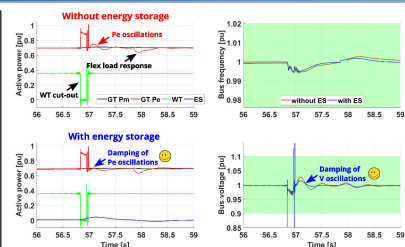


Figure 2: Wind power stops due to cut-out (1 pu = 25 MVA)

Energy storage as inertial and voltage support:  
 $\downarrow \Delta f$  oscillations  $\Rightarrow \downarrow$  wear and tear ☺️  
 Shorten  $\Delta V / \Delta P_e$  oscillations  $\Rightarrow \downarrow$  mechanical stresses ☺️

## CONCLUSIONS

- |   |                             |  |   |
|---|-----------------------------|--|---|
| 1 | $\uparrow$ wind penetration | $\Rightarrow \downarrow$ power quality                             | $\Rightarrow \uparrow$ maintenance + $\downarrow$ reliability |
| 2 | Energy storage              | $\Rightarrow f$ and $V$ support                                    | $\Rightarrow \uparrow$ power quality                          |
| 3 | Energy storage MW           | $\propto \max(\text{wind penetration}) + \max(\text{load on/off})$ |   |
| 4 | Energy storage kWh          | $\propto$ control parameters                                       | $\Rightarrow$ frequency droop                                 |

FIGURE 3.1. Conference poster presented at the EERA Deep Wind'19 - 16th Deep Sea Offshore Wind R&D conference (January 2019). © Erick F. Alves et al., 2019.



**EERA DeepWind'2019**  
**Best Poster Award**  
The Poster Award Committee recognizes

**Best communication**

**Erick F. Alves, Santiago S. Acevedo,  
Elisabetta Tedeschi**  
**NTNU, Department of Electric Power  
Engineering**

Selection criteria are  
relevance, quality and originality.

*John Olav Glæver Tande*  
John Olav Glæver Tande  
Chairman EERA DeepWind'2019

*Trond Kvamsdal*  
Trond Kvamsdal  
CO-Chairman EERA DeepWind'2019

*Michael Muskulus*  
Michael Muskulus  
CO-Chairman EERA DeepWind'2019

**EERA DeepWind'2019**  
Trondheim 18 January 2019

**EERA**  
European Energy Research Alliance

**NTNU**

**SINTEF**

**FIGURE 3.2.** Recognition from the Poster Award Committee at the EERA Deep Wind'19 - 16th Deep Sea Offshore Wind R&D conference (January 2019). © Erick F. Alves et al., 2019.



## CHAPTER 4

### *Smart Load Management with Energy Storage for Power Quality Enhancement in Wind-Powered Oil and Gas Applications*

---

Erick Alves<sup>1</sup>, Santiago Sanchez<sup>1</sup>, Danilo Brandao<sup>2</sup>, and Elisabetta Tedeschi<sup>1</sup>

Journal paper published in: *Energies* **12** (15), 2985 (August 2019).

DOI: [10.3390/en12152985](https://doi.org/10.3390/en12152985)



**Open Access** This work is licensed under a Creative Commons Attribution 4.0 International License. It means that unrestricted use, sharing, adaptation, distribution, and reproduction in any medium or format are allowed, as long as the original author(s) and the source are appropriately credited, a link to the Creative Commons license is provided, and any changes made are indicated. To view a copy of this license, please visit <http://creativecommons.org/licenses/by/4.0/>.

© Alves, Sanchez, Brandao and Tedeschi, 2019.

#### **Author Contributions**

Conceptualization, E.A. and E.T.; methodology, E.A. and S.S.; software, E.A. and S.S.; validation, E.A.; formal analysis, E.A.; investigation, E.A.; resources, S.S., D.B. and E.T.; data curation, E.A.; writing - original draft preparation, E.A.; writing - review and editing, S.S., D.B. and E.T.; visualization, E.A.; supervision, D.B. and E.T.; project administration, E.T.; funding acquisition, E.T.

---

<sup>1</sup>Department of Electric Power Engineering, NTNU, 7034 Trondheim, Norway.

<sup>2</sup>Graduate Program in Electrical Engineering, UFMG, 31270-901 Belo Horizonte, Brazil.

## ABSTRACT

This paper investigates power quality issues in a wind-powered offshore oil and gas platform operating in island mode. Topics of interest are the negative effects that load and wind power variability have on the electrical system frequency and voltage; and how those influence the gas turbine operation. The authors discuss how smart load management together with energy storage can mitigate those effects, and propose a control algorithm for that. Simulations in MATLAB/Simulink demonstrate that the proposed energy storage controller reduces frequency and voltage variations in a case study. Moreover, the paper presents a methodology to derive a simplified model of the hybrid energy system that reduces simulation time in at least two orders of magnitude. The latter can be a useful tool for optimization algorithms evaluating a huge number of scenarios, especially those dealing with economical dispatch of generators or sizing of energy storage systems.

#### 4.1 INTRODUCTION

Offshore oil and gas platforms are energy-intensive environments, where power demand is typically larger than 30 MW and natural gas is widely used to fuel equipment in the production, gathering and processing of gas and conventional crude oil [1]. Hence, in many countries, they contribute greatly to the emission of greenhouse gases (GHGs). For instance, the petroleum sector is the main contributor to GHG emissions in Norway, making up 27.8% of the total in 2017 [2].

This fact led to an increased interest in wind power integration into offshore oil and gas platforms in parallel to GTs [3–5], especially where power from shore is not feasible, either technically or economically [6]. Also, the industry has a strong interest in this concept, and pilot installations in the Norwegian Continental Shelf are already planned [7, 8].

From an electrical point of view, intermittent wind resources introduce challenges for the stable and efficient operation of this hybrid energy system. In an offshore oil and gas platform, load variations can be sharp and represent a significant part of the total generation capacity. On top of that, stochastic variations are added on the generation side when wind power is integrated. This raises concerns not only about insufficient amount of inertia, but also excessive frequency and voltage variations during operation that might negatively affect the electrical power quality and the GT operation [9, 10]. Hence, during the design phase of a wind-powered offshore oil and gas platform, it is

important not only to meet the power balance between generation and loads, but also consider system dynamics that may affect voltage and frequency in the electrical grid.

From this perspective, energy storage is an enabling technology that can provide proper frequency and voltage regulation, and can then increase frequency and voltage stability in such hybrid energy system [11, 12]. The literature provides several approaches to the problem of optimally designing an ESS for an hybrid energy system [13–17], the majority based on solving the unit commitment and economic dispatch problems associating a cost function to the ESS.

However, a common simplification when solving the unit commitment problem is assuming steady-state equations to obtain the active power balance in the system. While valid for an hybrid energy system connected to a strong grid, this assumption becomes questionable in islanded mode operation or when connected to a weak grid. In those conditions, the ESS is expected to contribute to frequency regulation [11, 18], and considerable amounts of energy during a short period of time might be used for this purpose [19]. Furthermore, previous works [20–22] demonstrated that control and energy management strategies might affect substantially the ESS sizing in a stand-alone system.

Within this context, the present work investigates power quality issues in an offshore oil and gas platforms operating in islanded mode where the wind turbine is rated at 36% of the GT nominal power. It is an extension of [10], which combines the previously proposed smart load management strategy with an ESS to mitigate the effects of wind variability. For that, the detailed dynamic model presented in this previous work is used as benchmark, extended to include an ESS, and then compared to the proposed simplified dynamic model in Sec. 4.4. The main contributions of this work are:

1. a demonstration of the benefits to power quality that a smart load management together with an ESS can provide in a wind-powered offshore oil and gas platform;
2. a control strategy for the ESS that provides inertial and voltage support to the electrical grid during transients and reduces frequency and voltage variations significantly;
3. a simplified dynamic model of the hybrid energy system that can be used to optimally design an ESS and dispatch available power sources.

From a control and modeling perspective, there are no large differences in the mathematical tools and techniques applied in the EMS of a wind-powered offshore oil and gas platform when compared to a typical onshore system. Hence, the proposed simplified model and energy storage system controller

can be generally applied to any hybrid energy system. However, boundary conditions and constraints may differ significantly. For instance, GTs should supply both electrical and heat power in an offshore oil and gas platform and comply with additional technical and environmental limitations. Typically, poor power quality (i.e., excessive frequency and voltage deviations) can negatively influence the performance of the process. Consequently, the problem formulation and objective functions for economical dispatch and energy storage sizing should be affected.

This paper is organized in the following manner: Sec. 4.2 introduces the case study and highlights the main additions compared to the previous contribution [10]; Sec. 4.3 presents the negative effects that power fluctuations have on the frequency and voltage of the studied hybrid energy system in a time scale of seconds. It also demonstrates how those can be counteracted by an ESS providing inertial and voltage support; Sec. 4.4 introduces the simplified model of the hybrid energy system, explains why it is necessary, and compares its results with the detailed model developed with MATLAB/Simulink using the Simscape Electrical library; finally, Sec. 4.5 presents a discussion of the obtained results and recommendations for further work.

## 4.2 THE CASE STUDY

Fig. 4.1 presents the main elements of the electric power system for the wind-powered offshore oil and gas platforms which is used as case study in this paper. Specifically, they are: a floating wind turbine with its associated ac/ac converter and transformer ( $T_1$ ); the transmission line cable; fixed loads; a GT with its associated synchronous generator and transformer ( $T_2$ ); flexible loads; and an ESS with its associated ac/dc converter. An extensive description of this model without the ESS is provided in [10], and a summary of the system parameters required for modeling is available in table 4.1.

The input for the wind turbine model is the wind speed, which is interpolated with the power curve to obtain the wind turbine output power. The wind speed is a time series from high-resolution measurements of the Sleipner weather station in the North Sea and is based on data from MET Norway [23]. This time series is filtered before interpolation by a low-pass filter representing the inertia constant of the turbine. The power curve is based on a cut-in speed of 4 m/s, nominal speed of 12 m/s, cut-out speed of 25 m/s and is available in [24]. The wind turbine side converter operates in maximum power point tracking, and no active power curtailment is applied to regulate the grid frequency. The grid side converter controls the dc link voltage.

To simplify the representation of fixed loads in the model, they are lumped

in two single loads representing the following groups: (1) loads that have minor variation in consumption during operation, such as low-voltage motors and pumps from the process, and auxiliary services (e.g., illumination and housing of personnel); (2) loads that have large, short time variations during operation, such as medium-voltage motors responsible for pumping oil or compressing gas. Please note that for the sake of simplicity, Fig. 4.1 shows only one fixed load representing both groups.

On the other hand, flexible loads represent large, medium-voltage motors interfaced with variable speed drives. They are different from group 2 because their active and reactive power can be controlled by the EMS to provide inertial and voltage support to the grid without affecting the process performance. In this case study, the flexible load is the water injection system, which is responsible to maintain overall and hydrostatic reservoir pressures and force the oil toward the production wells [1]. This type of load is flexible because reservoir pressures can vary within a certain range, and the time constant of the system is large (i.e., minutes) when compared to the electrical system dynamics (i.e., seconds). Hence, the EMS can actively change active and reactive power of the flexible loads during a short period without affecting the overall process performance.

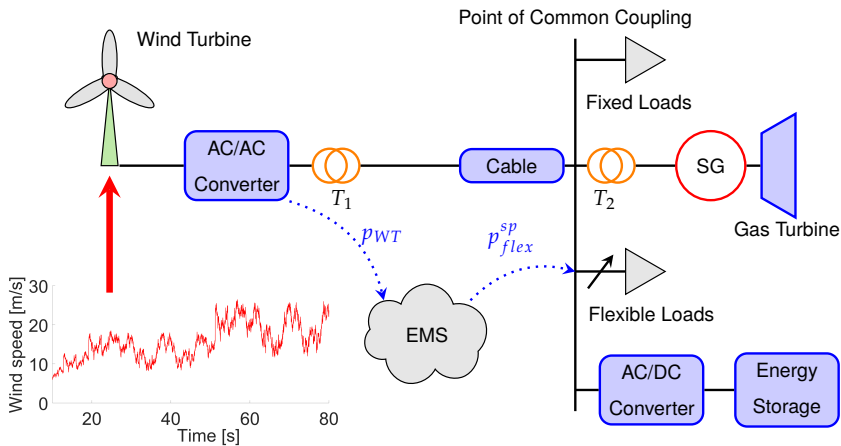


**FIGURE 4.1.** Main elements of the electric power system for a wind-powered OOGPs. © Erick Alves et al, 2019.

The smart load management proposed in [10] is also applied to this case study, i.e., the EMS dynamically adjusts the flexible load setpoint according to the wind turbine production with a 1 s delay. In other words, if the instantaneous wind turbine power output is 0.4 pu of the wind turbine rated value, then the EMS will set the flexible load setpoint to 0.4 pu of the flexible load rated value. If a wind gust increases the instantaneous wind turbine output to

0.6 pu, then the EMS will change the flexible load setpoint to 0.6 pu after 1 s. For modeling purposes, the flexible load setpoint ( $p_{flex}$ ) is represented by:

$$p_{flex}^{sp} = - \left( \frac{S_{WT}^{rated}}{S_{flex}^{rated}} \right) \left( \frac{1}{T_{comm} s + 1} \right) p_{WT} \quad (4.1)$$

where  $p_{flex}^{sp}$  is the flexible load active power setpoint [pu];  $p_{WT}$  is the wind turbine active power [pu];  $S_{flex}^{rated}$ ,  $S_{WT}^{rated}$  are the converter rated apparent power of the flexible load and the wind turbine respectively; and  $T_{comm}$  is the time constant of a low-pass filter. The latter is an approximation of: (1) a filter to remove measurement noise; (2) the communication delay required for interaction of the wind turbine and flexible load with the EMS through a communication link.

It is assumed the EMS can forecast the day-ahead average wind power production ( $p_{WT}$ ) and average load consumption ( $p_{fix}$ ,  $p_{flex}$ ) with an error of a few percent of the rated load capacity during short time intervals (>15 min and <1 h). The literature provides several examples of such forecasting algorithms: [25–27]. Accordingly, tertiary control [28] is not considered in the simulations, the EMS algorithm for optimal dispatch is not executed in real time and setpoints for the GT and ESS are assumed constant during the simulations.

The remaining of this section will focus on describing the ESS model and its proposed controller.

#### 4.2.1 Energy Storage System

A model identical to the wind turbine grid side and flexible load converters is adopted for the ESS ac/dc converter, i.e., a voltage source converter connected to the grid through a L filter. More details about modeling of this converter and tuning of its internal control loops can be obtained in [30].

To simplify the ESS model and make it technology-independent, the following assumptions are made:

- the storage device provides a constant voltage to the dc link of the voltage source converter;
- the EMS can change the setpoint of the GT to charge or discharge the ESS;
- the state of charge is ignored, as it is assumed the EMS can maintain a minimum state of charge to guarantee inertial support to the electrical grid.



The control for the **ESS** is designed to provide frequency and voltage support to the electrical grid, also referred as primary control [28]. Taking this into consideration, Eqs. (4.2) and (4.3) present the proposed closed-loop transfer functions in the Laplace domain for the external controller of the **ESS**:

$$I_{dref}(s) = - \left( \frac{1}{T_{flp}s + 1} \right) \left[ \left( \frac{T_{fr}s}{T_{fr}s + 1} \right) K_{ft} + \frac{K_{fi}}{s} \right] \Delta F_{PCC}(s) \quad (4.2)$$

$$I_{qref}(s) = - \left( \frac{1}{T_{ulp}s + 1} \right) \left[ \left( \frac{T_{ur}s}{T_{ur}s + 1} \right) K_{ut} + \frac{K_{ui}}{s} \right] \Delta U_{PCC}(s) \quad (4.3)$$

where  $I_{dref}$  is the voltage source converter reference current in the d-axis [pu],  $\Delta F_{PCC}$  is the point of common coupling frequency deviation from its reference value [pu],  $T_{flp}$  is the time constant of the frequency low-pass filter [s],  $T_{fr}$  is the reset time of the frequency wash-out filter [s],  $K_{ft}$  is the transient frequency droop [pu·s/pu],  $K_{fi}$  is the integral gain of the frequency controller [pu/(pu·s)],  $I_{qref}$  is the converter reference current in the q-axis [pu],  $\Delta U_{PCC}$  is the point of common coupling voltage deviation from its reference value [pu],  $T_{ulp}$  is the time constant of the voltage low-pass filter [s],  $T_{ur}$  is the reset time of the voltage wash-out filter [s],  $K_{ut}$  is the voltage transient droop [pu·s/pu], and  $K_{ui}$  is the integral gain of the voltage controller [pu/(pu·s)]. point of common coupling frequency and voltage references are assumed as 1 pu.

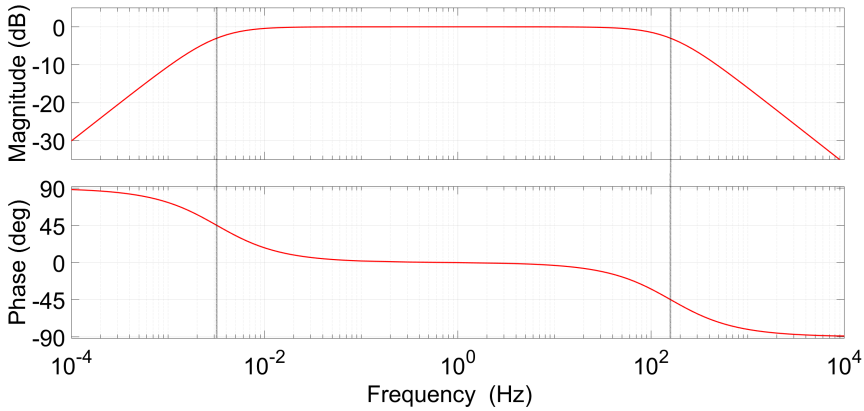


**FIGURE 4.2.** Frequency response of the low-pass filter combined with the wash-out filter when  $K_t = 1$ ,  $T_{lp} = 0.001$  s,  $T_r = 50$  s. This combination is equivalent to a band-pass filter. © Erick Alves et al, 2019.

The low-pass and wash-out filters combined are equivalent to a band-pass filter that eliminates the DC and high-frequency/noise values from measurements. Its frequency response can be seen in Fig. 4.2. Their effect together with the gain  $K_t$  is momentarily increasing the system damping when a transient

occurs, hence the name transient droop. Furthermore, the integral action of the controller takes care of bringing frequency and voltage to their rated values.

When implementing these control laws, it is important to consider some non-linearities. First, the control signal output must be limited to the rated values of the equipment. Second, whenever this occurs, an anti-windup logic must be activated in the integral part of the controller ([31] sec 9.3.1). Fig. 4.3 presents a complete block diagram of the controller considering these non-linear effects.

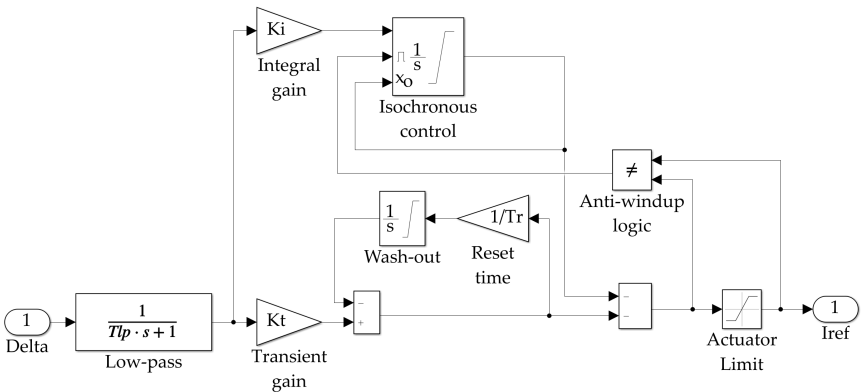


**FIGURE 4.3.** Block diagram of the proposed controller considering non-linear effects. © Erick Alves et al, 2019.

While transient droop is not a new topic in power system stability and has been explored for decades [32], the use of an ESS interfaced by a voltage source converter provides the bandwidth required to effectively implement it. The following section provides results corroborating this affirmation.

**4.3 SIMULATION RESULTS**

The purpose of this section is to demonstrate that power quality can be improved with the smart load management combined with the proposed ESS controller. For that, the system is simulated in MATLAB/Simulink with and without the ESS for a period of 80 s. Fixed loads are represented as constant impedances and flexible loads as constant power loads. The wind turbine is started at  $t = 10$  s and two transients are considered: the largest motor in fixed load group 2 (10 MW, 0.4 pu) is switched on at  $t = 30$  s, and then switched off at  $t = 65$  s.

To evaluate the simulation results, some metrics are introduced:

$$f_{RMSE} = \sqrt{\frac{\sum_{n=1}^N (f - 1)^2}{N}} \quad (4.4)$$

$$u_{RMSE} = \sqrt{\frac{\sum_{n=1}^N (u - 1)^2}{N}} \quad (4.5)$$

$$u/f_{RMSE} = \sqrt{\frac{\sum_{n=1}^N \left(\frac{u}{f} - 1\right)^2}{N}} \quad (4.6)$$

$$p_{RMSE} = \sqrt{\frac{\sum_{n=1}^N (p_m - p_e)^2}{N}} \quad (4.7)$$

where  $N$  is the number of samples for the entire simulation,  $f$ ,  $u$  are respectively the point of common coupling instantaneous frequency and voltage,  $p_m$ ,  $p_e$  are respectively the instantaneous mechanical and electrical power of the GT. In summary, the proposed metrics compare the measured variables to their setpoints and do not account for the error sign. The root mean square error compares the accuracy of models [33] and its values vary between  $\pm\infty$  (bad fit) and 0 (perfect fit).

Fig. 4.4 presents an overview of the simulation results, while Figs. 4.5 and 4.6 present details of the transients and table 4.2, the metrics. For the point of common coupling frequency, voltage and  $u/f$  curves, the area highlighted in green is the range allowed for continuous operation by typical industry standards [18, 34–36]. The regions outside this area are allowed for transient operation. The domain where protection schemes are usually activated [37, 38] lies beyond the y-axis limits.

Some interesting observations from the simulation results are:

- When analyzing  $f_{max}$ ,  $f_{min}$  values, one will notice that the proposed controller is not able to substantially improve these indicators. This can be justified by the fact that the ESS has a relatively small power capacity (0.18 pu) when compared to the rated power of the wind turbine (0.36 pu) and GT (1 pu);
- When considering  $f_{RMSE}$  values, the proposed controller reduces frequency deviations considerably (−23.1%). This is visually confirmed in Fig. 4.4 when comparing the amount of time outside the continuous operation range in both cases;
- When analyzing  $u_{max}$ ,  $u_{min}$ ,  $u/f_{max}$ ,  $u/f_{min}$  values, one will notice that the proposed controller is not able at all to improve these indicators.

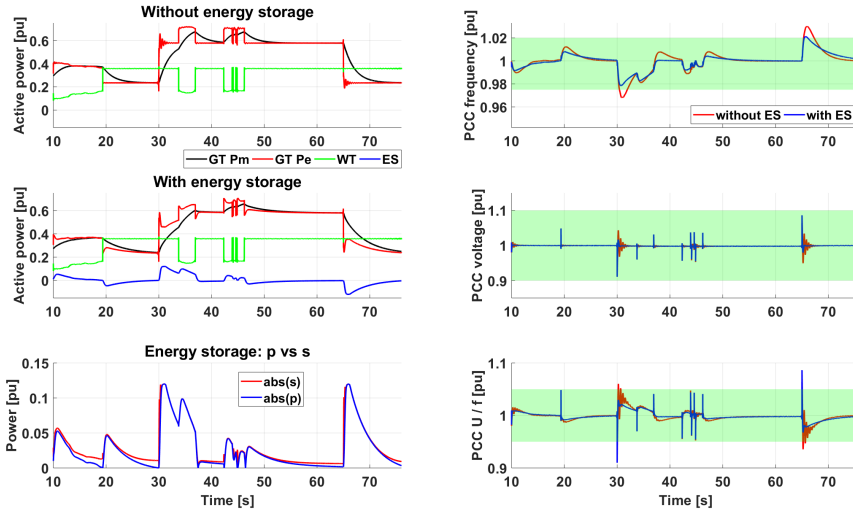


**FIGURE 4.4.** Active power, ESS active ( $p$ ) versus apparent ( $s$ ) power, PCC frequency and voltage for  $10 < t < 76$  s. © Erick Alves et al, 2019.

This is justified by the fact that the controller bandwidth is not large enough to counteract the voltage spikes induced by abrupt power flow changes;

- When referring to  $u_{RMSE}$  values, the proposed controller reduces voltage oscillations dramatically ( $-37.6\%$ ). This is visually confirmed in Figs. 4.5 and 4.6 when comparing the required time for damping oscillations in both cases.
- Improvements in  $u_{RMSE}$ ,  $f_{RMSE}$  with the ESS are also reflected in  $u/f_{RMSE}$ ;
- Figs. 4.5 and 4.6 indicate that the damping of voltage oscillations has also a positive effect on the reduction of active power oscillations. This confirms the controller efficacy in voltage support and suggests that such control scheme also provides a power system stabilizer functionality;
- For the case without ESS, the peak rate of change of the GT mechanical power  $\frac{dp_{mGT}}{dt}max$  is very close to the maximum allowed value for a typical GT used in offshore oil and gas platform (e.g., 0.15 pu/s for GE LM2500 [39]). This is greatly alleviated with the ESS ( $-26.2\%$ ), which confirms the controller efficacy in transient inertial support;
- For the case with ESS, the ESS energy throughput is 4.96 kWh during the 10 MW load switch on (with wind variations), and 4.17 kWh during the 10 MW load switch off (no wind variations). It is interesting to notice

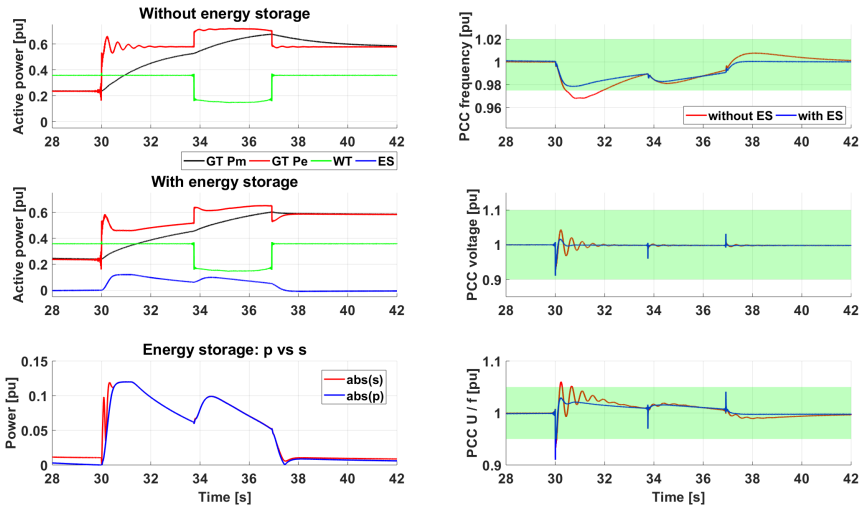


**FIGURE 4.5.** Detail of the period where a 10 MW load is switched on. © Erick Alves *et al*, 2019.

that wind variability affects considerably (+18.9%) the energy throughput during a disturbance;

- The difference between absolute values of the **ESS** active (p) and apparent (s) power are minimal ( $RMSE = 0.0065pu$ ).

#### 4.4 SIMPLIFIED MODEL

For assessment and early design purposes, the impact of a given **ESS** in an hybrid energy system should be easy and fast to evaluate. In particular, given a specific **ESS** configuration and the forecast of renewable sources (e.g., wind speed, solar irradiance, sea state) and load consumption, it should be straight to obtain the expected power production of all generators, and the **ESS** peak apparent power, power flow and energy throughput. Those are key input variables for the state-of-the-art optimization procedures tackling the **ESS** sizing problem [13–17]. As described earlier in [Sec. 4.1](#), a common simplification in those optimization procedures is assuming steady-state equations to obtain the active power balance in the system. This means that point of common coupling frequency variations and power quality requirements are currently ignored.

On one hand, an **ESS** can play a significant role in improving power quality, as shown in [Sec. 4.3](#). On the other hand, the model developed in [Sec. 4.2](#) is very detailed, and many of its parameter values are not available during the assessment and early design phases of an hybrid energy system. Not least, its total

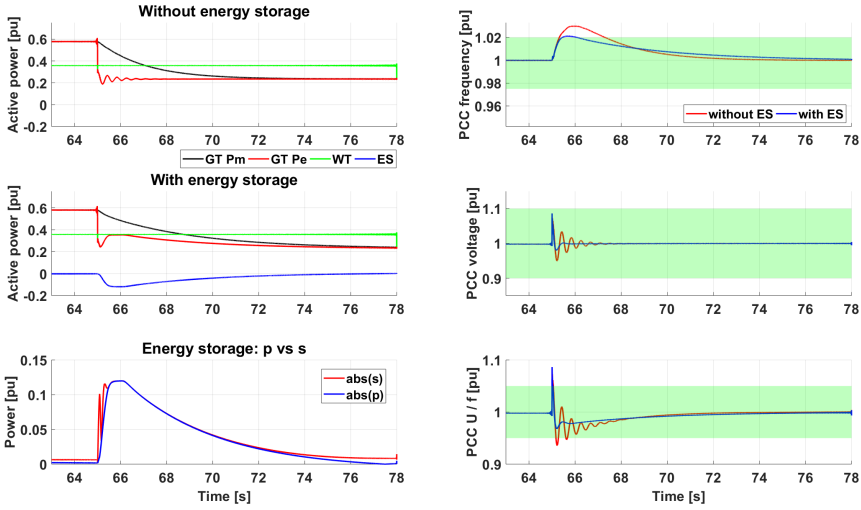


**FIGURE 4.6.** Detail of the period where a 10 MW load is switched off. © Erick Alves et al, 2019.

execution time on standard office computers can make its application impractical in current optimization algorithms, which are based on the evaluation of thousands of different scenarios.

Keeping this context in mind, the authors derives a simplified model for the hybrid energy system using a procedure similar to those outlined in [40]. The frequency dynamics are evaluated using the equations of motion from a synchronous generator ([41] ch.5):

$$\frac{2H}{\omega_m} \frac{d\omega_m}{dt} = \Delta p \tag{4.8}$$

$$\Delta p = p_m - p_e - p_d \tag{4.9}$$

$$p_d = \omega_m k_d \Delta \omega_m \tag{4.10}$$

$$\Delta \omega_m = \omega_{mref} - \omega_m \tag{4.11}$$

where  $H$  is the equivalent inertia constant of the system [s],  $\omega_m$  is the equivalent mechanical angular speed [pu],  $\Delta p$  is the instantaneous accelerating power [pu],  $p_m$ ,  $p_e$ ,  $p_d$  are respectively the equivalent mechanical power [pu], electrical power [pu] and power provided by the damper windings [pu],  $k_d$  is the damping constant [pu/pu],  $\omega_{mref}$  is the reference or rated angular speed [pu], assumed as 1 pu for all simulations. Fig. 4.7 presents a block diagram of this subsystem.

The voltage dynamics are not evaluated in the simplified model because they have negligible impact on the ESS sizing problem. When analyzing the voltage regulation law (Eq. (4.3)), one will notice that it influences  $I_q$  of the voltage source converter and, as so, the reactive power of the ESS. As seen in



where  $\|$  indicates the Euclidean or  $L^2$  norm of a vector, and the reference is the detailed model. The normalized mean square error is an estimator of the overall deviations between a reference model ( $x_{ref}$ ) and the measured values ( $x$ ), and its values vary between  $-\infty$  (bad fit) to 1 (perfect fit) [33].

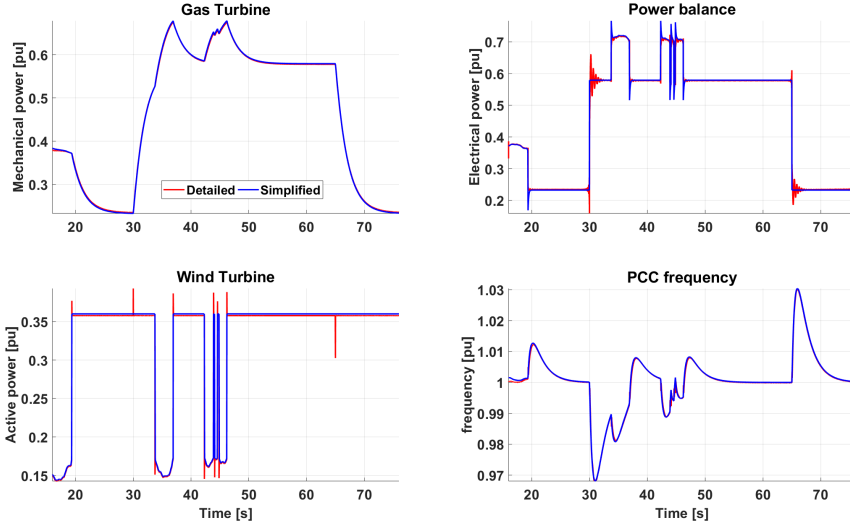


**FIGURE 4.8.** Detailed versus simplified model without energy storage system. © Erick Alves et al, 2019.

Some relevant observations emerge from the comparison:

- For both scenarios, some steady-state errors are observed. This is clearly seen in Fig. 4.8 in the offset of the  $p_{WT}$ , and in Fig. 4.9 in the offset of the  $p_{ES}$  curves. Those also affect  $p_e, p_{GT}$ , as they are correlated by Eq. (4.12). This is expected, as the simplified model considers only power flows and ignores ohmic losses;
- The simplified model approximates frequency dynamics really well for both scenarios, as seen by the negligible values of  $\Delta f_{max}, \Delta f_{min}$ , as well as  $f_{NMSE}$  very close to 1;
- The simplified model gives considerable absolute errors in both scenarios for variables that are influenced by the voltage dynamics, namely  $p_e, p_{WT}$ . This is seen on the metrics  $\Delta p_{emax}, \Delta p_{emin}, \Delta p_{WTmax}, \Delta p_{WTmin}$ . This is expected, as the simplified model ignores voltage dynamics, hence voltage spikes and power oscillations are not captured. However,  $p_{eNMSE}, p_{WTNMSE}$  are close to 1, which shows that the goodness of fit of the simplified model for those variables is accurate;



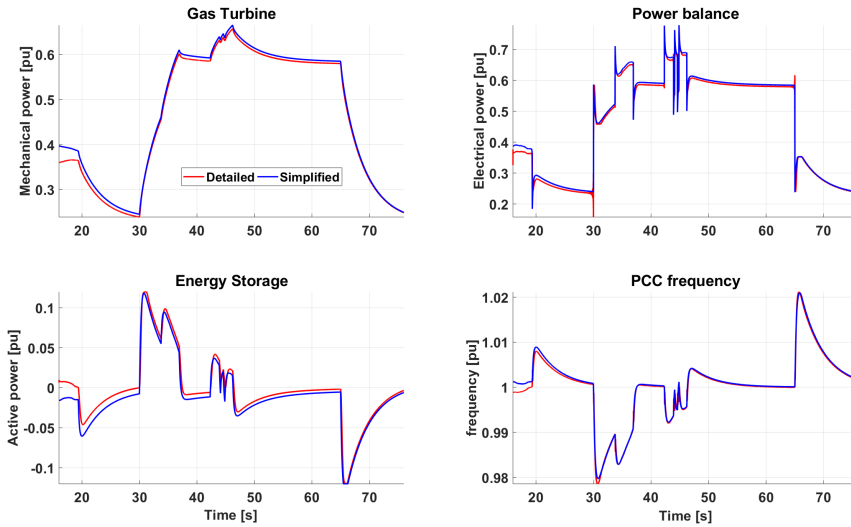


**FIGURE 4.9.** Detailed versus simplified model with energy storage system. © Erick Alves et al, 2019.

- The GT mechanical power and ESS active power are very well captured by the simplified model. Absolute errors present small values, i.e.,  $\Delta p_{GTmax}$ ,  $\Delta p_{GTmin}$ ,  $\Delta p_{ESmax}$ ,  $\Delta p_{ESmin}$ . On the other hand, while  $p_{GTNMSE}$  gives an almost perfect goodness of fit,  $p_{ESNMSE}$  is penalized by the steady-state error;
- For the scenario with ESS, the ESS energy throughput is 4.51 kWh during the 10 MW load switch on, and 4.53 kWh during the 10 MW load switch off. This represents respectively errors of  $-9.1\%$  and  $+8.6\%$  when compared to the detailed model. The reason for those large deviations is the steady-state error between  $p_{ES}$  in both models;
- The required simulation steps are  $20 \mu s$  for the detailed model and 1ms for the simplified model. Moreover, the latter has no VSCs and their associated control loops, what reduces dramatically the model complexity and total simulation time. For reference purposes, the detailed and simplified model run respectively in 694 and 1.1 s in a laptop equipped with MATLAB 2018a, an Intel Core i7-8650U CPU at 2.11 GHz, and 16 GB of RAM.

## 4.5 DISCUSSION AND FURTHER WORK

As seen in Sec. 4.3, an ESS with the proposed controllers effectively contributes to increase power quality in the hybrid energy system studied. For a wind-

powered offshore oil and gas platform in islanded mode, this brings some advantages.

Firstly, the **ESS** may help to reduce the negative impact of intermittent energy sources on the maintenance and reliability of other equipment. Reduced frequency deviations translate into less actuation of the **GT** governor and thus less wear and tear of electromechanical actuators. Furthermore, the **ESS** provides inertial support that reduces the peak rate of change of the **GT** power. The latter may not only contribute to less mechanical stresses but also to the reduction of **GHG** emissions. Finally, the voltage support provided by the **ESS** damps active power oscillations. This in turn reduces torque pulsations not only at the shaft of the **GT**, but also in motors connected to the grid without a motor drive.

Secondly, the additional inertial support provided by the **ESS** may allow the operation of only one **GT** in a wind-powered offshore oil and gas platform meeting the power quality limits required by industry standards. This opens the possibility to review redundant hot-standby schemes of **GTs** that are typical in traditional offshore oil and gas platform, by either operating the second **GT** in cold-standby or even eliminating it at all. This allows operation of the active **GT** in better efficiency points, and consequently a reduction of **GHG** emissions, especially if combined with waste heat recovery units.

In this context, topics to be further developed are a more detailed investigation about reliability and maintenance issues of **GT** and motors affected by intermittent energy sources in hybrid energy system, and the best control strategies to reduce **GHG** in a hybrid energy system.

However, the operation of the **ESS** providing inertial support requires additional energy throughput that is proportional to the frequency variations in the hybrid energy system. Therefore, an efficient simplified model that can estimate frequency variations with accuracy is necessary to provide key input variables for optimization procedures tackling the **ESS** sizing and economical dispatch problems. **Sec. 4.4** provides a procedure to derive such model for the offshore oil and gas platform case study described in **Sec. 4.2**. It is worth emphasizing that the methods presented can be easily extended to other types of hybrid energy system, despite the focus on the offshore oil and gas platform application.

The results presented in **Sec. 4.4.1** suggest that the proposed simplified model serves its purpose, i.e. it captures the frequency dynamics of the hybrid energy system with a high level of accuracy when compared to a detailed model developed with Matlab/Simulink using the Simscape Electrical library. It also provides estimations of the **ESS** peak power and energy throughput that are accurate enough for design purposes, with a total simulation time at least two orders of magnitude lower than the detailed model. This allows the proposed

model to be incorporated in optimization algorithms evaluating a huge number of scenarios.

Hence, a natural step further in future research may be to incorporate new constraints based on power quality requirements in the state-of-the-art ESS sizing procedures. This may also involve the optimization of the ESS sizing based on constraints such as apparent power peak rate of change, and the application of distinct storage technologies for different needs.

Nevertheless, the proposed simplified model has also drawbacks. First, it does not capture voltage dynamics and power oscillations of the electrical grid. While these may not be so critical in an offshore oil and gas platform, they will certainly be relevant to evaluate the stability of a hybrid energy system connected to distribution grids with high impedance and limited power transfer capacity. Moreover, steady-state errors of the proposed model generate significant errors in the estimated energy throughput of the ESS. Therefore, the ability of this model to provide a reliable state of charge estimation may be compromised, especially for very long periods.

#### ACKNOWLEDGMENTS

This research was funded by the Research Council of Norway under the program PETROMAKS2, grant number 281986, project “Innovative Hybrid Energy System for Stable Power and Heat Supply in Offshore Oil & Gas Installation (HES-OFF)”.

Danilo Brandao and Elisabetta Tedeschi were supported by the Research Council of Norway under the grant number 261735, project “Norwegian-Brazilian collaboration on Power Theories and Cooperative Control for Renewable Energy Integration (NB\_POCCREI)”.

## 4.6 REFERENCES

- [1] Håvard Devold. Oil and gas production handbook: An introduction to oil and gas production, transport, refining and petrochemical industry. ABB Oslo (2013). ISBN 978-82-997886-3-2. URL [https://library.e.abb.com/public/34d5b70e18f7d6c8c1257be500438ac3/Oil%20and%20gas%20production%20handbook%20ed3x0\\_web.pdf](https://library.e.abb.com/public/34d5b70e18f7d6c8c1257be500438ac3/Oil%20and%20gas%20production%20handbook%20ed3x0_web.pdf). Cited on p. 36, 39.
- [2] Trude Melby Bothner and Henning Høie. Table 1: Emissions to Air of Greenhouse Gases. Technical report Statistisk Sentralbyrå (August 2018). URL <http://www.ssb.no/natur-og-miljo/statistikker/klimagassn/>. Cited on p. 36.
- [3] Magnus Korpås, Leif Warland, Wei He, and John Olav Giæver Tande. A Case-Study on Offshore Wind Power Supply to Oil and Gas Rigs. *Energy Procedia* 24, 18–26 (2012). doi: 10.1016/j.egypro.2012.06.082. Cited on p. 36.

- [4] Wei He, Kjetil Uhlen, Mahesh Hadiya, Zhe Chen, Gang Shi, and Emilio del Rio. Case Study of Integrating an Offshore Wind Farm with Offshore Oil and Gas Platforms and with an Onshore Electrical Grid. *Journal of Renewable Energy* **2013**, 1–10 (2013). ISSN 2314-4386, 2314-4394. doi: 10.1155/2013/607165. Cited on p. 36.
- [5] Magne Lorentzen Kolstad, Atle Rygg Årdal, Kamran Sharifabadi, and Tore Marvin Undeland. Integrating offshore wind power and multiple oil and gas platforms to the onshore power grid using VSC-HVDC technology. *Marine Technology Society Journal* **48** (2), 31–44 (2014). Cited on p. 36.
- [6] Luca Riboldi and Lars O. Nord. Concepts for lifetime efficient supply of power and heat to offshore installations in the North Sea. *Energy Conversion and Management* **148**, 860–875 (September 2017). ISSN 01968904. doi: 10.1016/j.enconman.2017.06.048. Cited on p. 36.
- [7] Irati Legorburu, Kate R. Johnson, and Sandy A. Kerr. Multi-use maritime platforms - North Sea oil and offshore wind: Opportunity and risk. *Ocean & Coastal Management* **160**, 75–85 (June 2018). ISSN 09645691. doi: 10.1016/j.ocecoaman.2018.03.044. Cited on p. 36.
- [8] Elin A. Isaksen. Wind farm being considered at Snorre and Gullfaks (August 2018). URL <https://www.equinor.com/en/news/27aug2018-hywind-tampen.html>. Cited on p. 36.
- [9] Jorun I. Marvik, Eirik V. Øyslebø, and Magnus Korpås. Electrification of offshore petroleum installations with offshore wind integration. *Renewable Energy* **50**, 558–564 (February 2013). ISSN 09601481. doi: 10.1016/j.renene.2012.07.010. Cited on p. 36.
- [10] Santiago Sanchez, Elisabetta Tedeschi, Jesus Silva, Muhammad Jafar, and Alexandra Marichalar. Smart load management of water injection systems in offshore oil and gas platforms integrating wind power. *IET Renewable Power Generation* **11** (9), 1153–1162 (July 2017). ISSN 1752-1416, 1752-1424. doi: 10.1049/iet-rpg.2016.0989. Cited on p. 36, 37, 38, 39.
- [11] IEEE Std 1547.4-2011: IEEE Guide for Design, Operation, and Integration of Distributed Resource Island Systems with Electric Power Systems. Number 4 in 1547. IEEE New York, NY (2011). ISBN 978-0-7381-6687-2. URL <http://ieeexplore.ieee.org/servlet/opac?punumber=6006493>. Cited on p. 37.
- [12] IEEE Std 2030.2-2015: IEEE guide for the interoperability of energy storage systems integrated with the electric power infrastructure. Number 2 in 2030. IEEE New York, NY (2015). ISBN 978-0-7381-9638-1. URL <http://ieeexplore.ieee.org/servlet/opac?punumber=7140713>. Cited on p. 37.
- [13] S. X. Chen, H. B. Gooi, and M. Q. Wang. Sizing of Energy Storage for Microgrids. *IEEE Transactions on Smart Grid* **3** (1), 142–151 (March 2012). ISSN 1949-3053, 1949-3061. doi: 10.1109/TSG.2011.2160745. Cited on p. 37, 45.
- [14] Shaghayegh Bahramirad, Wanda Reder, and Amin Khodaei. Reliability-Constrained Optimal Sizing of Energy Storage System in a Microgrid. *IEEE Transactions on Smart Grid* **3** (4), 2056–2062 (December 2012). ISSN 1949-3053, 1949-3061. doi: 10.1109/TSG.2012.2217991. Cited on p. 37, 45.
- [15] Jiaojiao Dong, Feng Gao, Xiaohong Guan, Qiaozhu Zhai, and Jiang Wu. Storage-Reserve Sizing With Qualified Reliability for Connected High Renewable Penetration Micro-Grid. *IEEE Transactions on Sustainable Energy* **7** (2), 732–743 (April 2016). ISSN 1949-3029, 1949-3037. doi: 10.1109/TSTE.2015.2498599. Cited on p. 37, 45.
- [16] Juan P. Fossati, Ainhoa Galarza, Ander Martín-Villate, and Luis Fontán. A method for optimal sizing energy storage systems for microgrids. *Renewable Energy* **77**, 539–549 (May 2015). ISSN 09601481. doi: 10.1016/j.renene.2014.12.039. Cited on p. 37, 45.
- [17] Ling Ai Wong, Vigna K. Ramachandaramurthy, Phil Taylor, J.B. Ekanayake, Sara L. Walker, and Sanjeevikumar Padmanaban. Review on the optimal placement, sizing and control of an energy storage system in the distribution network. *Journal of Energy Storage* **21**, 489–504 (February 2019). ISSN 2352152X. doi: 10.1016/j.est.2018.12.015. Cited on p. 37, 45.

- [18] IEEE Std 1547-2018: IEEE Standard for Interconnection and Interoperability of Distributed Energy Resources with Associated Electric Power Systems Interfaces. 1547. IEEE New York, NY (2018). ISBN 978-1-5044-4639-6. URL <https://ieeexplore.ieee.org/servlet/opac?punumber=8332110>. Cited on p. 37, 43.
- [19] Mohammad Reza Aghamohammadi and Hajar Abdolahinia. A new approach for optimal sizing of battery energy storage system for primary frequency control of islanded Microgrid. *International Journal of Electrical Power & Energy Systems* **54**, 325–333 (January 2014). ISSN 01420615. doi: 10.1016/j.ijepes.2013.07.005. Cited on p. 37.
- [20] Øystein Ulleberg. The importance of control strategies in PV–hydrogen systems. *Solar Energy* **76** (1-3), 323–329 (January 2004). ISSN 0038092X. doi: 10.1016/j.solener.2003.09.013. Cited on p. 37.
- [21] Rodolfo Dufo-López, José L. Bernal-Agustín, and Javier Contreras. Optimization of control strategies for stand-alone renewable energy systems with hydrogen storage. *Renewable Energy* **32** (7), 1102–1126 (June 2007). ISSN 09601481. doi: 10.1016/j.renene.2006.04.013. Cited on p. 37.
- [22] José L. Bernal-Agustín and Rodolfo Dufo-López. Simulation and optimization of stand-alone hybrid renewable energy systems. *Renewable and Sustainable Energy Reviews* **13** (8), 2111–2118 (October 2009). ISSN 13640321. doi: 10.1016/j.rser.2009.01.010. Cited on p. 37.
- [23] MET Norway. Frost API (July 2019). URL <https://frost.met.no/index.html>. Cited on p. 38.
- [24] Finn Gunnar Nielsen. Hywind – From idea to world’s first wind farm based upon floaters (2018). URL [https://www.uib.no/sites/w3.uib.no/files/attachments/hywind\\_energy\\_lab.pdf](https://www.uib.no/sites/w3.uib.no/files/attachments/hywind_energy_lab.pdf). Cited on p. 38.
- [25] V.S. Pappala, I. Erlich, K. Rohrig, and J. Dobschinski. A Stochastic Model for the Optimal Operation of a Wind-Thermal Power System. *IEEE Transactions on Power Systems* **24** (2), 940–950 (May 2009). ISSN 0885-8950, 1558-0679. doi: 10.1109/TPWRS.2009.2016504. Cited on p. 40.
- [26] Elizaveta Kuznetsova, Yan-Fu Li, Carlos Ruiz, and Enrico Zio. An integrated framework of agent-based modelling and robust optimization for microgrid energy management. *Applied Energy* **129**, 70–88 (September 2014). ISSN 03062619. doi: 10.1016/j.apenergy.2014.04.024. Cited on p. 40.
- [27] Spyridon Chapaloglou, Athanasios Nesiadis, Petros Iliadis, Konstantinos Atsonios, Nikos Nikolopoulos, Panagiotis Grammelis, Christos Yiakopoulos, Ioannis Antoniadis, and Emmanuel Kakaras. Smart energy management algorithm for load smoothing and peak shaving based on load forecasting of an island’s power system. *Applied Energy* **238**, 627–642 (March 2019). ISSN 03062619. doi: 10.1016/j.apenergy.2019.01.102. Cited on p. 40.
- [28] Josep M. Guerrero, Juan C. Vasquez, José Matas, Luis García de Vicuna, and Miguel Castilla. Hierarchical Control of Droop-Controlled AC and DC Microgrids—A General Approach Toward Standardization. *IEEE Transactions on Industrial Electronics* **58** (1), 158–172 (January 2011). ISSN 0278-0046, 1557-9948. doi: 10.1109/TIE.2010.2066534. Cited on p. 40, 41.
- [29] IEEE. IEEE Std 421.5-2016: IEEE Recommended Practice for Excitation System Models for Power System Stability Studies. Number 5 in 421. IEEE New York 2016 edition (August 2016). ISBN 978-1-5044-0855-4. URL <https://ieeexplore.ieee.org/document/7553421/>. Cited on p. 55.
- [30] Jon Are Suul, Marta Molinas, Lars Norum, and Tore Undeland. Tuning of control loops for grid connected voltage source converters. In *2008 IEEE 2nd International Power and Energy Conference* pages 797–802 Johor Bahru, Malaysia (December 2008). IEEE. ISBN 978-1-4244-2404-7. doi: 10.1109/PECON.2008.4762584. Cited on p. 40.
- [31] Gene F. Franklin, J. David Powell, and Abbas Emami-Naeini. Feedback control of dynamic systems. Pearson Upper Saddle River, NJ 6. ed., internat. ed edition (2010). ISBN 978-0-

- 13-500150-9. Cited on p. 42.
- [32] Ramnarayan Patel, T. S. Bhatti, and D. P. Kothari. Improvement of Power System Transient Stability Using Fast Valving: A Review. *Electric Power Components and Systems* **29** (10), 927–938 (October 2001). ISSN 1532-5008, 1532-5016. doi: 10.1080/15325000152646532. Cited on p. 42.
- [33] Colin Lewis-Beck and Michael Lewis-Beck. *Applied Regression: An Introduction*. SAGE Publications, Inc 2455 Teller Road, Thousand Oaks California 91320 (2016). ISBN 978-1-4833-8147-3 978-1-4833-9677-4. doi: 10.4135/9781483396774. Cited on p. 43, 48.
- [34] NORSOK E-001:2016 Electrical systems. NTS Oslo. Norway sixth edition (December 2016). Cited on p. 43.
- [35] IEC 61892:2015 Mobile and fixed offshore units - Electrical installations. IEC Geneva, Switzerland 3.0 edition (July 2015). URL <https://webstore.iec.ch/publication/6083>. Cited on p. 43.
- [36] IEEE Std C50.13-2014: IEEE Standard for Cylindrical-Rotor 50 Hz and 60 Hz Synchronous Generators Rated 10 MVA and Above. Number 13 in C50. IEEE. S.I. (2014). ISBN 978-0-7381-9068-6. URL <http://ieeexplore.ieee.org/lpdocs/epic03/wrapper.htm?arnumber=6811137>. Cited on p. 43.
- [37] IEEE Std C37.102: IEEE Guide for AC Generator Protection. Number 102 in C37. IEEE New York, NY (2006). ISBN 0-7381-5250-29. doi: 10.1109/IEEESTD.2006.320495. Cited on p. 43.
- [38] IEEE Std C37.106: IEEE Guide for Abnormal Frequency Protection for Power Generating Plants. Number 106 in C37. IEEE New York, NY (February 2004). ISBN 0-7381-3733-2. doi: 10.1109/IEEESTD.2004.94434. Cited on p. 43.
- [39] G. H. Badeer. GE Aeroderivative Gas Turbines - Design and Operating Features (October 2000). URL [https://www.ge.com/content/dam/gepower-pgdp/global/en\\_US/documents/technical/ger/ger-3695e-ge-aero-gas-turbine-design-op-features.pdf](https://www.ge.com/content/dam/gepower-pgdp/global/en_US/documents/technical/ger/ger-3695e-ge-aero-gas-turbine-design-op-features.pdf). Cited on p. 44.
- [40] M.S. Mahmoud, S. Azher Hussain, and M.A. Abido. Modeling and control of microgrid: An overview. *Journal of the Franklin Institute* **351** (5), 2822–2859 (May 2014). ISSN 00160032. doi: 10.1016/j.jfranklin.2014.01.016. Cited on p. 46.
- [41] Jan Machowski, Janusz W. Bialek, and J. R. Bumby. *Power system dynamics: Stability and control*. Wiley Chichester, U.K 2nd ed edition (2008). ISBN 978-0-470-72558-0. Cited on p. 46, 47.



**TABLE 4.1.** Summary of the model parameters for the case study.

| Parameter                       | Value  | Unit  | Parameter                         | Value              | Unit  |
|---------------------------------|--------|-------|-----------------------------------|--------------------|-------|
| <i>Base values</i>              |        |       | <i>Simulink configurations</i>    |                    |       |
| Apparent power                  | 25     | MVA   | Simulink solver                   | Fixed-step ode4    | -     |
| Line voltage                    | 11     | kV    | powergui discrete solver          | TBE                | -     |
| Frequency                       | 50     | Hz    |                                   |                    |       |
| <i>SG</i>                       |        |       | <i>Exciter</i>                    |                    |       |
| Apparent power                  | 1      | pu    | IEEE421.5 [29] Type               | AC1C               | -     |
| Number of poles                 | 2      | pairs | Ka                                | 20                 | pu/pu |
| Shunt resistance                | 0.002  | pu    | Ke                                | 0.8                | pu/pu |
| Shunt reactance                 | 0.3    | pu    | Kf                                | 0.01               | pu/pu |
| Inertia constant                | 1.85   | s     | Ta                                | 0.02               | s     |
| Damping factor                  | 7.04   | pu/pu | Tb                                | 0.2                | s     |
|                                 |        |       | Tc                                | 1.2                | s     |
|                                 |        |       | Te                                | 0.5                | s     |
|                                 |        |       | Tf                                | 0.35               | s     |
| <i>Turbine governor</i>         |        |       | <i>Fixed loads rated power</i>    |                    |       |
| Permanent droop                 | 0.8222 | pu/pu | Load 1                            | (0.4727 + j0.0834) | pu    |
| Actuator delay                  | 2.25   | s     | Load 2                            | (0.3464 + j0.2000) | pu    |
| <i>Wind speed</i>               |        |       | <i>Flexible load setpoint</i>     |                    |       |
| Low-pass filter time constant   | 1.2    | s     | Low-pass filter time constant     | 1                  | s     |
| <i>WT VSC</i>                   |        |       | <i>ESS and flexible load VSCs</i> |                    |       |
| Apparent power                  | 0.36   | pu    | Apparent power                    | 0.18               | pu    |
| Filter inductance               | 12.6   | mH    | Filter inductance                 | 25.2               | mH    |
| Filter shunt resistance         | 121    | mΩ    | Filter shunt resistance           | 242                | mΩ    |
| Filter capacitance              | 4      | μF    |                                   |                    |       |
| Filter parallel resistance      | 13.2   | Ω     |                                   |                    |       |
| dq current                      |        |       | dq current                        |                    |       |
| proportional gain               | 0.5556 | pu/pu | proportional gain                 | 0.5556             | pu/pu |
| dq current                      |        |       | dq current                        |                    |       |
| integral gain                   | 5.3333 | pu/s  | integral gain                     | 5.3333             | pu/s  |
| <i>ESS frequency controller</i> |        |       | <i>ESS voltage controller</i>     |                    |       |
| Transient droop                 | 50     | pu/pu | Transient droop                   | 20                 | pu/pu |
| Transient reset time            | 50     | s     | Transient reset time              | 50                 | pu/pu |
| Low-pass filter time            | 0.001  | s     | Low-pass filter time              | 0.001              | s     |
| Integral gain                   | 0.2    | s     | Integral gain                     | 0.2                | pu/s  |

**TABLE 4.2.** Metrics obtained from the detailed model simulation results.

| Metric                   | Without ESS | With ESS   | Difference |
|--------------------------|-------------|------------|------------|
| $f_{max}$                | 1.030 pu    | 1.021 pu   | -0.9%      |
| $f_{min}$                | 0.968 pu    | 0.979 pu   | 1.1%       |
| $\hat{f}_{RMSE}$         | 0.009 pu    | 0.007 pu   | -23.1%     |
| $u_{max}$                | 1.086 pu    | 1.086 pu   | 0%         |
| $u_{min}$                | 0.910 pu    | 0.910 pu   | 0%         |
| $u_{RMSE}$               | 0.005 pu    | 0.003 pu   | -37.6%     |
| $u/f_{max}$              | 1.086 pu    | 1.086 pu   | 0%         |
| $u/f_{min}$              | 0.910 pu    | 0.910 pu   | 0%         |
| $u/\hat{f}_{RMSE}$       | 0.010 pu    | 0.007 pu   | -26.9%     |
| $p_{RMSE}$               | 0.071 pu    | 0.056 pu   | -21.8%     |
| $\frac{p_{mGT}}{dt} max$ | 0.130 pu/s  | 0.096 pu/s | -26.2%     |

**TABLE 4.3.** Metrics comparing the detailed and simplified models.

| Metric             | Without ESS |      | With ESS |      |
|--------------------|-------------|------|----------|------|
|                    | [pu]        | [%]  | [pu]     | [%]  |
| $\Delta p_{GTmax}$ | 0.003       | 0.4  | 0.008    | 1.2  |
| $\Delta p_{GTmin}$ | -0.002      | -0.8 | 0.006    | 2.7  |
| $p_{GTNMSE}$       | 0.999       | -    | 0.996    | -    |
| $\Delta p_{emax}$  | 0.044       | 6.1  | 0.071    | 10.0 |
| $\Delta p_{emin}$  | 0.009       | 6.0  | 0.026    | 16.7 |
| $p_{eNMSE}$        | 0.997       | -    | 0.995    | -    |
| $\Delta p_{WTmax}$ | -0.017      | -4.4 | -0.017   | -4.4 |
| $\Delta p_{WTmin}$ | 0.014       | 10.8 | 0.014    | 10.8 |
| $p_{WTNMSE}$       | 0.998       | -    | 0.998    | -    |
| $\Delta p_{ESmax}$ | -           | -    | -0.002   | -1.3 |
| $\Delta p_{ESmin}$ | -           | -    | 0.000    | 0    |
| $p_{ESNMSE}$       | -           | -    | 0.955    | -    |
| $\Delta f_{max}$   | 0.001       | 0.1  | 0.000    | 0    |
| $\Delta f_{min}$   | 0.000       | 0    | 0.001    | 0.1  |
| $f_{NMSE}$         | 0.998       | -    | 0.993    | -    |



## CHAPTER 5

### *Innovative hybrid energy system for stable power and heat supply in offshore oil & gas installation (HES-OFF): System design and grid stability*

---

Luca Riboldi<sup>1</sup>, Erick F. Alves<sup>2</sup>, Marcin Pilarczyk<sup>1</sup>, Elisabetta Tedeschi<sup>2</sup>, and Lars O. Nord<sup>1</sup>

Conference paper published in: *Proceedings of the 30th European Symposium on Computer Aided Process Engineering (ESCAPE30)* volume A, pages 211–216, Milano, Italy (May 2020).

DOI: [10.1016/B978-0-12-823377-1.50036-7](https://doi.org/10.1016/B978-0-12-823377-1.50036-7)



The title and content of this chapter are based on the accepted manuscript version of the paper that has been published in the aforementioned proceedings. This accepted manuscript is licensed under a Creative Commons Attribution NonCommercial NoDerivatives 4.0 International License. It means that any non-commercial use and distribution are allowed, as long as no modifications are made, and proper credit is given to the the original author(s) as well as the source. To view a copy of this license, please visit <https://creativecommons.org/licenses/by-nc-nd/4.0/>.

© Elsevier, 2020.

#### **Author Contributions**

Conceptualization, L.R. and L.N.; methodology, L.R. and E.A.; software, L.R., M.P., and E.A.; validation, L.R., M.P., and E.A.; formal analysis, L.R. and E.A.; investigation, L.R., M.P., and E.A.; resources, L.N. and E.T.; data curation, L.R. and E.A.; writing - original draft preparation, L.R., E.A., and M.P.; writing - review and editing, E.T. and L.N.; visualization, L.R. and E.A.; supervision, E.T. and L.N.; project administration, L.N.; funding acquisition, L.R., L.N., and E.T.

---

<sup>1</sup>Department of Energy and Process Engineering, NTNU, 7034 Trondheim, Norway.

<sup>2</sup>Department of Electric Power Engineering, NTNU, 7034 Trondheim, Norway.

## ABSTRACT

This paper presents an innovative **Innovative Hybrid Energy System for Stable Power and Heat Supply in Offshore Oil & Gas Installation (HES-OFF)**. The hybrid concept integrates offshore wind power with gas turbines and a  $H_2$  energy storage solution based on **proton exchange membrane fuel cells** and **electrolysers**. The objectives are: 1) improve the environmental performance of offshore installations by maximizing the exploitation of offshore wind and partially decarbonizing the **gas turbines** by co-feeding  $H_2$ ; 2) minimize the negative effects that wind power variability has on the electrical grid frequency stability. This study presents a first assessment of the **HES-OFF** concept performance using an offshore platform in the North Sea as case study. The results show that the **HES-OFF** concept: 1) cuts  $CO_2$  emissions by up to 40 % when compared to the reference case but requires large  $H_2$  storage capacity to fully exploit wind power throughout the year; 2) allows higher wind power penetration without infringing the grid frequency requirements.

## 5.1 INTRODUCTION

Due to the long-term character of the energy transition and the many technical limitations to replace fossil fuels with **renewable energy sources (RESs)**, **hybrid energy systems (HESs)** with **energy storage (ES)** can be affordable alternatives. The choice of the hybrid energy system configuration and its specification depends on the availability of renewable energy sources and the general purpose of the system. Optimum design can be achieved through comprehensive analyses and optimization of layouts and the size of system components.

Offshore **oil and gas (O&G)** production is likely to increase in the near future and thus its related  $CO_2$  emissions. In Norway, the petroleum sector is the main contributor to greenhouse gas emissions, making up 27% of the total emissions in 2018 [1]. Several options to reduce the carbon footprint of the **O&G** sector have been investigated [2], including the electrification of offshore facilities [3]. The utilization of renewable energy sources is a very promising opportunity, though there are challenges for their efficient exploitation offshore.

This article presents the concept of an innovative **Innovative Hybrid Energy System for Stable Power and Heat Supply in Offshore Oil & Gas Installation (HES-OFF)**, which considers wind energy along with  $H_2$  ES using a **proton exchange membrane (PEM) fuel cell (FC)** and **electrolyser (EL)** system.

## 5.2 THE HES-OFF HYBRID CONCEPT

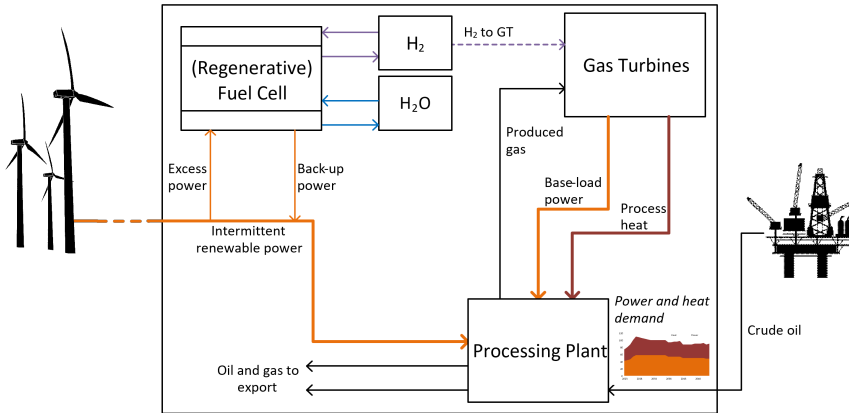


**FIGURE 5.1.** Schematic of the Innovative Hybrid Energy System for Stable Power and Heat Supply in Offshore Oil & Gas Installation system proposed. © Elsevier, 2020.

The HES-OFF concept consists of a hybrid energy system integrating an offshore wind farm, stacks of proton exchange membrane fuel cell and gsel for ES and back-up power supply, and a gas turbine (GT). The ES is further integrated with the GT, where the possibility to co-feed  $H_2$  is envisioned. Fig. 5.1 depicts the HES-OFF system layout.

Within this energy system, the GT operation meets the process heat demand and supplies base-load power to a processing plant. Wind turbines (WTs) provide the remaining load. The fuel cell and electrolyser stacks smooth out the intermittent wind power output by: 1) storing excess power in the form of gaseous  $H_2$  when production is larger than demand; 2) providing back-up power on the contrary. This hybrid energy system is expected to reduce  $CO_2$  emissions from an offshore facility due to: 1) enhanced exploitation of GTs; 2) clean fuel to GTs; 3) improved operational strategy of the GTs.

## 5.3 MODELING FRAMEWORK

Two main areas of the modelling activity are distinguished, namely (1) process components and (2) offshore grid modelling. The general intention is to pre-screen the feasibility of the HES-OFF concept and to assess the potential reduction of  $CO_2$  emissions.

### 5.3.1 Process components

The HES-OFF process components are modeled in MATLAB and are presented below.

**GTs:** Two types of GTs are considered for the study, namely a GE LM2500+G4 (rated power 32.2 MW) and a GE LM6000 PF (rated power 41.9 MW). To simulate the GTs, two data-defined models are used. Those are based on performance curves retrieved from tabulated data and assess the effect of changing working conditions as well as off-design operation. The models were validated against Thermoflow Inc.'s Thermoflex Version 26.0. The performance of the LM2500+G4 model was further checked against real operational data by Riboldi and Nord [4], showing good agreement, and used in previous publications (e.g., [5]).

**fuel cells&electrolysers stacks:** The models used in this study are based on zero-dimensional, static models of proton exchange membrane fuel cell and electrolyser stacks, which describe the electrical domain of cells. The fuel cell stack model is based on Spiegel [6], improved and tuned according to Dicks and Rand [7]. The electrolyser stack model is based on Zhang *et al.* [8] with further improvements based on Millet [9]. The output of the model is the overall performance of the fuel cell and electrolyser stacks as a function of load expressed in MJ/kgH<sub>2</sub> and kgH<sub>2</sub>/MJ, respectively. The obtained results reflect the state-of-the-art for high capacity PEM systems on the market.

**wind turbine:** The conversion of wind speed into power was simulated through the power curve of the Hywind Scotland wind turbine [10]. The wind speed distribution throughout a year was based on the measurements from a platform in the North Sea made available by the Norwegian Meteorological Institute (reported in [11]).

### 5.3.2 Offshore grid

A surrogate model of the electrical grid [12] was developed in Simulink. It evaluates frequency dynamics using Eq. (5.1):

$$\dot{\omega} = \frac{P_a - k_d \omega^2}{2H_{GT} \omega} \quad (5.1)$$

$$P_a = P_{GT} + P_{FC} + P_{WT} - P_{EL} - P_{LD} \quad (5.2)$$

where  $\omega$  is the frequency in per unit (pu), the model state and output;  $P_a$  is the net accelerating power in pu and the model input;  $H_{GT}$  and  $k_d$  are model

---

per unit (pu) is a system for expressing values in terms of a reference or base quantity.

parameters, defined as the equivalent inertia constant in s and the equivalent damping constant of the plant in pu/pu. Base values are:  $\omega_b = 2\pi 60 \text{ rad s}^{-1}$ ;  $P_b = 44.7 \text{ MW}$ .

$P_a$  is defined by Eq. (5.2) where  $P_{GT}$ ,  $P_{FC}$ ,  $P_{WT}$ ,  $P_{EL}$ ,  $P_{LD}$  are respectively the power in pu of GT, fuel cell, wind turbine, electrolyser and loads. The model from Eq. (5.1) is extended to include PID controllers for the GT, fuel cell and electrolyser [12, 13]. Those keep the grid frequency at its rated value. The choice of controller parameters follows the magnitude optimum criteria as outlined by Papadopoulos [14].

## 5.4 RESULTS

The developed methodology was tested on a case study: an offshore facility in the North Sea, for which an estimation of the energy requirements throughout its lifetime was made available by the operator (18 years). To ease the analysis, the power and heat supply demand was discretized:

1. *Peak (2 years)*: 43.6 MW electrical power, 14.0 MW heat power;
2. *Mid-life (4 years)*: 35.2 MW electrical, 11.0 MW heat;
3. *Tail (12 years)*: 32.9 MW electrical, 8.0 MW heat.

### 5.4.1 Long-term system design

The long-term analysis sizes the components of the hybrid energy system by:

1. ensuring that power and heat demand is always met;
2. maximizing the reduction of  $CO_2$  emissions;
3. removing one GT;
4. avoiding waste of wind power.

The discretized lifetime energy demand of the offshore installation is considered, where each year is simulated with an hourly resolution. Table 5.1 reports the input parameters varied to define a design.

The storage strategy adopted ensures a net-zero balance of  $H_2$  at the end of the year and the storage size is determined by the largest variation in the storage level. At first the design is tested over one year without ES.

In case of a net deficit of power (typical of peak years), the strategy: 1) evaluates total  $H_2$  needed; 2) when possible, increases GT load and uses extra

**TABLE 5.1.** Input parameters for the long-term system design.

| INPUT PARAMETERS    |                     |
|---------------------|---------------------|
| GT type             | GE LM2500 or LM6000 |
| Max. GT load        | 95 %                |
| Min. GT load        | 40 %                |
| Max. $H_2$ in GT    | 20 % vol.           |
| Wind turbine        | Hywind Scotland     |
| Wind farm size (MW) | 12-18-24            |

power to produce  $H_2$ ; 3) stops when reaching a maximum storage level; 4) stops when reaching overall  $H_2$  needed. In case of a net surplus of power (typical of tail years), the strategy: 1) evaluates total  $H_2$  produced due to surplus power; 2) when possible, decreases GT load and use fuel cells to produce power; 3) when the level of  $H_2$  storage reaches a maximum, uses  $H_2$  in the GT; 4) if some  $H_2$  is still unused, sends  $H_2$  to the GT. Tables 5.2 and 5.3 shows results obtained for the small and large GTs, respectively.

The designs of the HES-OFF concept reduce  $CO_2$  emissions both compared to the reference case (only GT) and to the basic integration of wind power (GT+WIND). The lowest cumulative  $CO_2$  emissions are obtained by the HES-OFF designs based on the small GT (LM2500). However, those are also characterized by extremely large (possibly unfeasible) sizes of the  $H_2$  storage and fail to remove one GT. Conversely, the HES-OFF design based on the large GT obtain a more limited  $CO_2$  emission reduction but with more acceptable sizes of the  $H_2$  storage and with a single GT.

The size of the  $H_2$  storage is given in kg of  $H_2$  as the storage technology is not specified. Cryogenic option has been ruled out because of the significant energy requirements.  $H_2$  storage in gaseous form has been considered as more appropriate for this application. The very large volumes connected with this option would require a storage on the seabed. Some technologies have been qualitatively investigated such as the utilization of gas balloons [15], gas pipes and underground formations [16]. Additional analyses are planned to identify the most promising option.

#### 5.4.2 Short-term grid stability analysis

This step verifies if each proposed design of the long-term analysis: 1) is stable from the frequency stability perspective [17]; 2) complies with industry requirements [18] for frequency deviations ( $\pm 2\%$ ) during normal operation conditions; 3) complies with technical specifications of GT ramp rates.

For that, it simulates the offshore grid model presented in Sec. 5.3.2. Inputs are obtained as following: 1)  $P_{GT}$ ,  $P_{FC}$ , and  $P_{EL}$  are results from the long-term

**TABLE 5.2.** Output results of the HES-OFF concept based on the LM2500 GT

| INPUTS  | Only GT | GT + WIND |        |        |        | HES-OFF |        |        |
|---|---------|-----------|--------|--------|--------|---------|--------|--------|
|   |         | LM2500    | LM2500 | LM2500 | LM2500 | LM2500  | LM2500 | LM2500 |
| <b>GT type</b>                                | LM2500  | LM2500    | LM2500 | LM2500 | LM2500 | LM2500  | LM2500 |        |
| <b>No. GT</b>                                 | 2       | 2         | 2      | 2      | 2      | 2       | 2      |        |
| <b>Max. GT load</b> %                         | 90      | 90        | 90     | 90     | 95     | 95      | 95     |        |
| <b>Min. GT load</b> %                         | 40      | 40        | 40     | 40     | 40     | 40      | 40     |        |
| <b>Wind farm size</b> MW                      | -       | 12        | 18     | 24     | 12     | 18      | 24     |        |
| <b>OUTPUTS</b>                                |         |           |        |        |        |         |        |        |
| <b>Size H<sub>2</sub> storage</b> kg          | -       | -         | -      | -      | 175334 | 81605   | 71062  |        |
| <b>Size EL stacks</b> MW                      | -       | -         | -      | -      | 6      | 6       | 6      |        |
| <b>Size FC stacks</b> MW                      | -       | -         | -      | -      | 4      | 4       | 4      |        |
| <b>CO<sub>2</sub> emissions</b> Mt            | 3.51    | 2.71      | 2.42   | 2.25   | 2.50   | 2.27    | 2.09   |        |
| <b>Max. frequency</b> Hz                      | 60.00   | 60.15     | 60.23  | 60.31  | 60.12  | 60.19   | 60.25  |        |
| <b>Min. frequency</b> Hz                      | 59.22   | 59.02     | 58.91  | 58.79  | 59.13  | 59.04   | 58.95  |        |
| <b>Max. <math>\frac{dP}{dt}</math> GT</b> %/s | 1.52    | 1.88      | 2.11   | 2.33   | 1.68   | 1.86    | 2.03   |        |

**TABLE 5.3.** Output results of the HES-OFF concept based on the LM6000 GT

| INPUTS  | Only GT | GT + WIND |        |        |        | HES-OFF |        |        |
|---|---------|-----------|--------|--------|--------|---------|--------|--------|
|   |         | LM6000    | LM6000 | LM6000 | LM6000 | LM6000  | LM6000 | LM6000 |
| <b>GT type</b>                                | LM6000  | LM6000    | LM6000 | LM6000 | LM6000 | LM6000  | LM6000 |        |
| <b>No. GT</b>                                 | 2       | 2         | 2      | 2      | 1      | 1       | 1      |        |
| <b>Max. GT load</b> %                         | 90      | 90        | 90     | 90     | 95     | 95      | 95     |        |
| <b>Min. GT load</b> %                         | 40      | 40        | 40     | 40     | 40     | 40      | 40     |        |
| <b>Wind farm size</b> MW                      | -       | 12        | 18     | 24     | 12     | 18      | 24     |        |
| <b>OUTPUTS</b>                                |         |           |        |        |        |         |        |        |
| <b>Size H<sub>2</sub> storage</b> kg          | -       | -         | -      | -      | 10010  | 8014    | 11824  |        |
| <b>Size EL stacks</b> MW                      | -       | -         | -      | -      | 4.0    | 4.0     | 6.6    |        |
| <b>Size FC stacks</b> MW                      | -       | -         | -      | -      | 1.1    | 1.1     | 1.1    |        |
| <b>CO<sub>2</sub> emissions</b> Mt            | 2.92    | 2.36      | 2.48   | 2.30   | 2.45   | 2.32    | 2.23   |        |
| <b>Max. frequency</b> Hz                      | 60.00   | 60.15     | 60.23  | 60.31  | 60.14  | 60.22   | 60.30  |        |
| <b>Min. frequency</b> Hz                      | 59.21   | 59.02     | 58.90  | 58.78  | 59.06  | 58.92   | 58.75  |        |
| <b>Max. <math>\frac{dP}{dt}</math> GT</b> %/s | 1.05    | 1.30      | 1.46   | 1.61   | 2.49   | 2.88    | 3.32   |        |

analysis of the process model and are assumed as constants; 2)  $P_{WT}$  and  $P_{LD}$  are results from analyses of 1-year long datasets of wind speeds and loads sampled every minute and are assumed as variables. These datasets are stored in an NTNU repository and are not publicly available. To reduce total simulation time, two synthetic time series reflect the worst-case scenarios of operation during the offshore platform lifetime. Those are 3-minutes long and contain the most sharp and common positive and negative variations of  $P_{WT}$  and  $P_{LD}$ . Parameters for the short-term grid stability analysis are reported in table 5.4.

The bottom part of tables 5.2 and 5.3 presents the obtained results. Note that as the wind farm size increases: 1) the frequency deviations increase and, in the extreme cases (24 MW wind farm), the minimum frequency limit (58.8 Hz) is always violated, except for the LM2500 HES-OFF concept; 2) the rate of change of power ( $\frac{dP}{dt}$ ) of the GT increases, which translates into increased actuation of the governor and consequently additional wear and tear. The HES-OFF concept contributes to decrease frequency deviations and GT ramp rates. Note that, in the LM6000 HES-OFF concept with 24 MW wind farm, the

**TABLE 5.4.** Input parameters for the short-term grid stability analysis.

| INPUT PARAMETERS                         |  |
|--|--|
| $H_{GT}$                                 | 1.85s for LM2500<br>1.8s for LM6000            |
| $k_d$                                    | 7 pu/pu  |
| GT PID controller                        | $K_p = 3.8, K_i = 1.6$<br>$K_d = 0, T_d = 100$ |
| electrolyser / fuel cell PID controllers | $K_p = 0, K_i = 0$<br>$K_d = 6, T_d = 50$      |

minimum frequency limit can be respected if the fuel cell increases to 1.6 MW. This shows the importance of considering grid requirements in the design phase of a hybrid energy system.

## 5.5 CONCLUSIONS

The HES-OFF concept was presented and tested on a case study. Six configurations were assessed using two GTs of different rated power. Long- and short-term analyses verified the hybrid energy system potential to reduce  $CO_2$  emissions and to provide a stable offshore grid. The HES-OFF concept demonstrated the ability to reduce the cumulative  $CO_2$  emissions of an O&G platform not only compared to a reference case using only GTs but also compared to a concept integrating GTs and WTs without ES. The designs based on the small GT return the highest  $CO_2$  emission reductions (between 29% and 40% depending on the wind farm size) but are unable to remove one of the GTs and involve very large  $H_2$  storage capacity. Conversely, the designs based on the large GT return lower  $CO_2$  emission reductions (between 16% and 24% depending on the wind farm size) but use a single GT and more limited  $H_2$  storage capacity.

It is also shown that the addition of ES helps reducing the frequency variations in the offshore grid. The minimum frequency specification is generally met by the HES-OFF solutions but at 24 MW wind capacity for the large GT. However, an increase in the fuel cell stack size would allow the frequency to be within the required limits. Not least, GTs ramp rates are reduced as well, with potential advantages in terms of decreased wear, tear and maintenance requirements. Further work in this ongoing research project envisions the development of more complex models, optimization of the hybrid energy system and validation by means of hardware-in-the-loop simulation.



## 5.6 REFERENCES

- [1] Trude Melby Bothner and Henning Høie. Table 1: Emissions to Air of Greenhouse Gases. Technical report Statistisk Sentralbyrå (August 2018). URL <http://www.ssb.no/natur-og-miljo/statistikker/klimagassn/>. Cited on p. 58.
- [2] Luca Riboldi and Lars O. Nord. Concepts for lifetime efficient supply of power and heat to offshore installations in the North Sea. *Energy Conversion and Management* **148**, 860–875 (September 2017). ISSN 01968904. doi: 10.1016/j.enconman.2017.06.048. Cited on p. 58.
- [3] Luca Riboldi, Steve Völler, Magnus Korpås, and Lars O. Nord. An Integrated Assessment of the Environmental and Economic Impact of Offshore Oil Platform Electrification. *Energies* **12** (11), 2114 (June 2019). ISSN 1996-1073. doi: 10.3390/en12112114. Cited on p. 58.
- [4] Luca Riboldi and Lars Nord. Offshore Power Plants Integrating a Wind Farm: Design Optimisation and Techno-Economic Assessment Based on Surrogate Modelling. *Processes* **6** (12), 249 (December 2018). ISSN 2227-9717. doi: 10.3390/pr6120249. Cited on p. 60.
- [5] Luca Riboldi and Lars Nord. Lifetime Assessment of Combined Cycles for Cogeneration of Power and Heat in Offshore Oil and Gas Installations. *Energies* **10** (6), 744 (May 2017). ISSN 1996-1073. doi: 10.3390/en10060744. Cited on p. 60.
- [6] Colleen Spiegel. PEM fuel cell modeling and simulation using Matlab. Academic Press Amsterdam first edition (2008). ISBN 978-0-12-374259-9. URL <https://www.elsevier.com/books/pem-fuel-cell-modeling-and-simulation-using-matlab/spiegel/978-0-12-374259-9>. Cited on p. 60.
- [7] Andrew Dicks and D. A. J. Rand. Fuel cell systems explained. Wiley Hoboken, NJ, USA third edition edition (2018). ISBN 978-1-118-61352-8. Cited on p. 60.
- [8] Houcheng Zhang, Shanhe Su, Guoxing Lin, and Jincan Chen. Efficiency Calculation and Configuration Design of a PEM Electrolyzer System for Hydrogen Production. *Int. J. Electrochem. Sci.* **7**, 4143–4157 (2012). URL <http://www.electrochemsci.org/papers/vol7/7054143.pdf>. Cited on p. 60.
- [9] Pierre Millet. PEM Water Electrolysis. In Agata Godula-Jopek, editor, *Hydrogen Production* pages 63–116. Wiley-VCH Verlag GmbH & Co. KGaA Weinheim, Germany (February 2015). ISBN 978-3-527-67650-7 978-3-527-33342-4. doi: 10.1002/9783527676507.ch3. Cited on p. 60.
- [10] Finn Gunnar Nielsen. Hywind – From idea to world’s first wind farm based upon floaters (2018). URL [https://www.uib.no/sites/w3.uib.no/files/attachments/hywind\\_energy\\_lab.pdf](https://www.uib.no/sites/w3.uib.no/files/attachments/hywind_energy_lab.pdf). Cited on p. 60.
- [11] Magnus Korpås, Leif Warland, Wei He, and John Olav Giæver Tande. A Case-Study on Offshore Wind Power Supply to Oil and Gas Rigs. *Energy Procedia* **24**, 18–26 (2012). doi: 10.1016/j.egypro.2012.06.082. Cited on p. 60.
- [12] Erick Alves, Santiago Sanchez, Danilo Brandao, and Elisabetta Tedeschi. Smart Load Management with Energy Storage for Power Quality Enhancement in Wind-Powered Oil and Gas Applications. *Energies* **12** (15), 2985 (August 2019). ISSN 1996-1073. doi: 10.3390/en12152985. Cited on p. 60, 61.
- [13] Santiago Sanchez, Elisabetta Tedeschi, Jesus Silva, Muhammad Jafar, and Alexandra Marichalar. Smart load management of water injection systems in offshore oil and gas platforms integrating wind power. *IET Renewable Power Generation* **11** (9), 1153–1162 (July 2017). ISSN 1752-1416, 1752-1424. doi: 10.1049/iet-rpg.2016.0989. Cited on p. 61.
- [14] Konstantinos G. Papadopoulos. PID Controller Tuning Using the Magnitude Optimum Criterion. Springer International Publishing Cham (2015). ISBN 978-3-319-07262-3 978-3-319-07263-0. doi: 10.1007/978-3-319-07263-0. Cited on p. 61.
- [15] Andrew J. Pimm, Seamus D. Garvey, and Maxim de Jong. Design and testing of Energy

- Bags for underwater compressed air energy storage. *Energy* **66**, 496–508 (March 2014). ISSN 03605442. doi: 10.1016/j.energy.2013.12.010. Cited on p. 62.
- [16] Olaf Kruck, Fritz Crotogino, Ruth Prelicz, and Tobias Rudolph. Overview on all Known Underground Storage Technologies for Hydrogen. Technical Report 303417-D3.1 Project HyUnder (August 2013). URL [http://www.hyunder.eu/wp-content/uploads/2016/01/D3.1\\_Overview-of-all-known-underground-storage-technologies.pdf](http://www.hyunder.eu/wp-content/uploads/2016/01/D3.1_Overview-of-all-known-underground-storage-technologies.pdf). Cited on p. 62.
- [17] Prabha Kundur, *et al.* Definition and Classification of Power System Stability. *IEEE Transactions on Power Systems* **19** (3), 1387–1401 (August 2004). ISSN 0885-8950. doi: 10.1109/TPWRS.2004.825981. Cited on p. 62.
- [18] IEC 61892:2015 Mobile and fixed offshore units - Electrical installations. IEC Geneva, Switzerland 3.0 edition (July 2015). URL <https://webstore.iec.ch/publication/6083>. Cited on p. 62.



## CHAPTER 6

### *Optimal Design of a Hybrid Energy System for the Supply of Clean and Stable Energy to Offshore Installations*

---

Luca Riboldi<sup>1</sup>, Erick F. Alves<sup>2</sup>, Marcin Pilarczyk<sup>1</sup>, Elisabetta Tedeschi<sup>2</sup>, and Lars O. Nord<sup>1</sup>

Journal paper published in: *Frontiers in Energy Research*, 8:326 (December 2020).  
DOI: [10.3389/fenrg.2020.607284](https://doi.org/10.3389/fenrg.2020.607284)



**Open Access** This work is licensed under a Creative Commons Attribution 4.0 International License. It means that unrestricted use, sharing, adaptation, distribution, and reproduction in any medium or format are allowed, as long as the original author(s) and the source are appropriately credited, a link to the Creative Commons license is provided, and any changes made are indicated. To view a copy of this license, please visit <http://creativecommons.org/licenses/by/4.0/>.

© Riboldi, Alves, Pilarczyk, Tedeschi and Nord, 2020.

#### **Author Contributions**

Conceptualization, L.R. and L.N.; methodology, L.R. and E.A.; software, L.R., M.P., and E.A.; validation, L.R., M.P., and E.A.; formal analysis, L.R. and E.A.; investigation, L.R., M.P., and E.A.; resources, L.N. and E.T.; data curation, L.R. and E.A.; writing - original draft preparation, L.R. and E.A.; writing - review and editing, M.P., E.T. and L.N.; visualization, L.R. and E.A.; supervision, E.T. and L.N.; project administration, L.N.; funding acquisition, L.R., L.N., and E.T.

---

<sup>1</sup>Department of Energy and Process Engineering, NTNU, 7034 Trondheim, Norway.

<sup>2</sup>Department of Electric Power Engineering, NTNU, 7034 Trondheim, Norway.

## ABSTRACT

This paper presents an innovative hybrid energy system for stable power and heat supply in offshore oil and gas installations. The proposed concept integrates offshore wind power, onsite gas turbines and an energy storage system based on fuel cell and electrolyzer stacks. It is expected to be an effective option to decarbonize the offshore petroleum sector as it allows a more extensive exploitation of the offshore wind resource by means of energy storage. To ascertain its potential, an integrated model was developed. The integrated model allows to simulate the process and electric grid performances. The inclusion of both domains provides a comprehensive picture of a given design operational performance. The feasibility of the proposed concept was first investigated through a parametric analysis where an understanding of its potential and limitations was gained. A rigorous optimization was then implemented to identify the designs resulting in the best performances and ultimately to obtain a comprehensive picture of the suitability of the concept. It is shown that a well-designed system can reduce carbon emissions compared, not only to a standard concept based on gas turbines (almost 1300 kt less  $CO_2$  emissions, making up for a relative 36% reduction), but also to the integration of a wind farm alone (more than 70 kt less  $CO_2$  emissions, making up for a relative 3% reduction, but complying with grid dynamics requirements). Moreover, the energy storage system brings benefits to the electric grid stability and allows the integration of large wind power capacity without overpassing the 2% maximum frequency variation (as it is the case without energy storage). Not least, the optimization showed that the definition of an optimal design is a complex task, with little margin to further gains in terms of carbon emissions, likely due to technological limitations.

## 6.1 INTRODUCTION

Global warming is among the biggest challenges facing the world today, something clearly reflected in efforts made by governments, industries and academia to reduce GHG emissions and provide sustainable energy for all. The general roadmap to reach these goals includes country-specific paths depending on the national energy and industrial system. For instance, in Norway, the petroleum sector is currently a key element of the socio-economic development but, simultaneously, accounts for 28% of the total GHG emissions [1].

Konkraft [2] presents possible emission-reduction technologies for the energy industry on the Norwegian continental shelf. The target is decreasing

GHG emissions by 40% in 2030 compared with 2005 and reaching near zero in 2050. The 40% drop by 2030 corresponds to an absolute reduction of 5.4 Mt of CO<sub>2</sub> equivalents compared with 2005. Feasible approaches include design optimization of the platform [3], energy efficiency measures [4], carbon capture and storage [5] and electrification [6].

Within this context, renewable energy sources appear to be applicable to various projects. Choi *et al.* [7] presents 11 different cases of onshore and offshore oil and gas production sites at which different technologies were incorporated including PV, wind, solar and geothermal energy. Nonetheless, in this study, offshore facilities were connected only with wind power technology. The potential installation of dedicated PV arrays on an offshore rig would be probably much more challenging and costly than the equivalent wind turbine installation, especially in areas such as the North sea where wind power is abundant compared to solar energy. For instance, in 2005, Shell constructed and installed two monotower platforms with two small wind turbines and two arrays of PV panels on the deck [8]. However, these platforms are small unmanned facilities for well drilling at shallow waters. Also, MacDonald [9] evaluated solutions based on wave energy and other renewables to cover the electrical demand in living quarters of offshore platforms. Although all sources could accomplish the required energy demand, some form of energy storage is needed. All in all, the author considered two deep-sea wave energy devices as promising solutions in hybrid system. But they still have to demonstrate their commercial and technical maturity to be applied in the oil and gas industry. Not least, Hanssen *et al.* [10] analyzed a hybrid offshore renewable energy platform which comprises wind turbines and arrays of wave energy converters. The investigation yielded promising technical results and economic performance for the North Sea area. However, there are no more works dedicated to this installation. Finally, Rafiee and Khalilpour [11] offers a good overview of the various applications of renewable energy sources in the oil and gas sector. The authors focused on the hybridization of upstream and downstream processes in oil and gas supply chains and found that not only the integration of clean energy sources with the oil and gas industry decreases its emission intensity, but may also reduce production costs.

In this sense, a mitigation option for the oil and gas industry which made significant progress in recent years is offshore wind power. Offshore wind displays advantageous characteristics in comparison to onshore, for instance higher average wind speed, lower turbulence intensity and wind shear [12]. The Norwegian Sea and the northern end of the North Sea were regarded as extremely promising for the combination of oil, gas and offshore wind, when evaluating technical, environmental and market aspects [13].

Wind is obviously an irregular power source, which poses inherent chal-

lenges to match the power demand from a stand-alone user such as an offshore installation. The solution proposed so far has been to couple offshore wind farms with GTs [14]. However, this approach has invariably led to the under-design of wind farms or the dissipation of excess wind power.

Another challenge that arises from this standard solution is the grid stability for large wind installed capacity. For example, Orlandini *et al.* [15] showed that a maximum wind power of 10 MW was feasible considering an installed electrical load of 30 MW to comply with frequency requirements. Conservative operating strategies are often applied to achieve the requested level of reliability and flexibility, leading to poor performance and increased emissions. A smart load management of flexible loads interfaced by variable speed drives, such as water injection systems, shows to be beneficial, as discussed by Sanchez *et al.* [16].

Not least, all the challenges outlined increase costs and make the integration of wind power into offshore installations an intricate business case. Riboldi and Nord [17] demonstrated that the economic viability of wind power integration needs to be supported by favorable conditions in terms of gas and CO<sub>2</sub> prices and improves if large offshore projects are considered.

In summary, the studies available in the literature show a significant potential for emission cuts in the oil and gas extraction sector by exploiting the offshore wind resources. However, multiple technical and economical issues must be addressed to effectively harness wind power. A typical technical issue is to efficiently couple the intermittent nature of renewable sources with the reliable power supply requested by oil and gas platforms. Adding the possibility of energy storage to the equation could be extremely helpful to smooth the irregular contribution of wind power. Alves *et al.* [18] corroborated this hypothesis by investigating power quality issues in a wind-powered offshore oil and gas platform operating in island mode with energy storage.

Hybrid electric power systems could offer the opportunity to improve safety, reliability and operational efficiency when compared to traditional electrical power systems [19]. Several storage techniques have been proposed for systems with different characteristics. Despite the maturity of some of those techniques, their application offshore would introduce a set of additional challenges, such as space and weights constraints, difficulty of storage and harsh operating conditions. This paper introduces an innovative and efficient technological solution to curb emissions while not endangering the economics of offshore operations.

To this end, the proposed HES-OFF concept combines a renewable energy source with an ESS and conventional GTs. The underlying idea is to exploit the full potential of the wind offshore resource and typical equipment of offshore installations by introducing an ESS consisting of stacks of proton exchange

membrane fuel cells and electrolysers together with a subsea  $H_2$  storage system. The proton exchange membrane technology was chosen as the most appropriate for this concept due to its fast-dynamic response, good efficiency and relative maturity. This HES-OFF is expected to offer significant advantages:

- *Full exploitation of renewable energy sources:* the ESS allows the storage of excessive wind energy that otherwise would have been immediately converted into heat to avoid grid overloading.
- *Removal of redundant GTs:* back-up power is guaranteed by the fuel cell stack thus it might be possible to remove redundant GTs.
- *Increased security of power supply:* a properly designed ESS helps to cope with unforeseen variations of wind power and demand allowing a more flexible operation of the plant.
- *Improved operation of the GT:* use of a cleaner fuel ( $H_2$ ) and a more efficient operational strategy that do not directly respond to wind fluctuations.
- *Additional electric grid stability:* the ESS acts as a buffer smoothing out the fluctuations of the wind power system.

The paper aims to ascertain that the HES-OFF system is capable to deliver the listed advantages and so decarbonise the offshore petroleum sector. For this purpose an integrated model was developed to simulate the process and electric grid performances. Such model is used to perform a parametric analysis followed by a rigorous design optimization, and gain a full understanding of the potential of this hybrid concept.

## 6.2 MATERIALS AND METHODS

### 6.2.1 Principles of the proposed concept

The proposed HES-OFF operates in the following manner. The GT provides base-load power while the waste heat available in its exhaust gas is harvested to supply process heat to the installation. The wind farm supplies the remaining power demand, while the ESS helps to cope with its intermittency by providing backup power. In the case of excess wind power, the electrolyser stack absorbs this surplus and produces hydrogen. The latter can be stored or used in the GT where the possibility to blend it with natural gas is envisioned. Conversely, in the case of lack of wind power, the fuel cell stack provide backup power using the hydrogen stored. Fig. 6.1 presents a schematic of the proposed system.

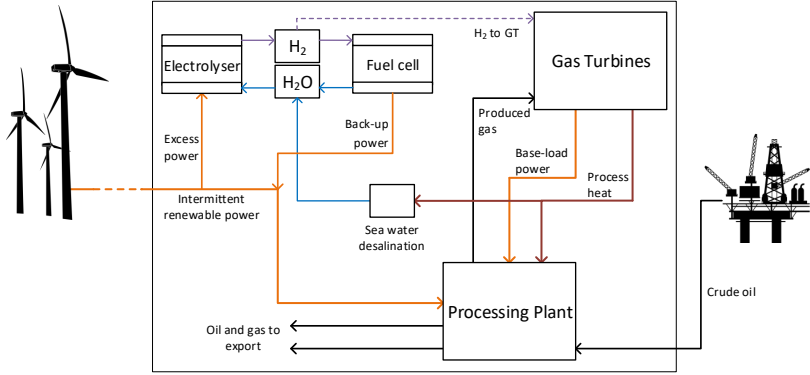


**FIGURE 6.1.** Schematic representation of the proposed **Innovative Hybrid Energy System for Stable Power and Heat Supply in Offshore Oil & Gas Installation (HES-OFF)**. © Luca Riboldi et al, 2020.

### 6.2.2 Integrated model

An integrated model of the proposed system was developed combining sub-models of the process and the electric grid components. This integrated model allows designing the hybrid energy system for maximum process performance, while simultaneously verifying the stable operation of the offshore grid. This approach not only helps avoiding designs that would prove operationally unfeasible, but actively directs the design process towards optimal solutions by considering the mutual influence of the process and the electric domains.

Fig. 6.2 gives an overview of the design approach based on the integrated model. More details are presented in the following sections.

### 6.2.3 Process models

In this section, the sub-models simulating the main process components of the hybrid system are described. The process components contribute to meet the heat and power demands of the offshore installation:

$$Power\ demand = P_W + P_{GT} + P_{FC} - P_{EL} - P_{Wdiss} \quad (6.1)$$

$$Heat\ demand = Q_{WHRU} \quad (6.2)$$

where  $P_W$  is wind power,  $P_{GT}$  is gas turbine power,  $P_{FC}$  is fuel cell power,  $P_{EL}$  is electrolyzer power,  $P_{Wdiss}$  is wind power dissipated and  $Q_{WHRU}$  is heat harvested from the waste heat recovery unit.



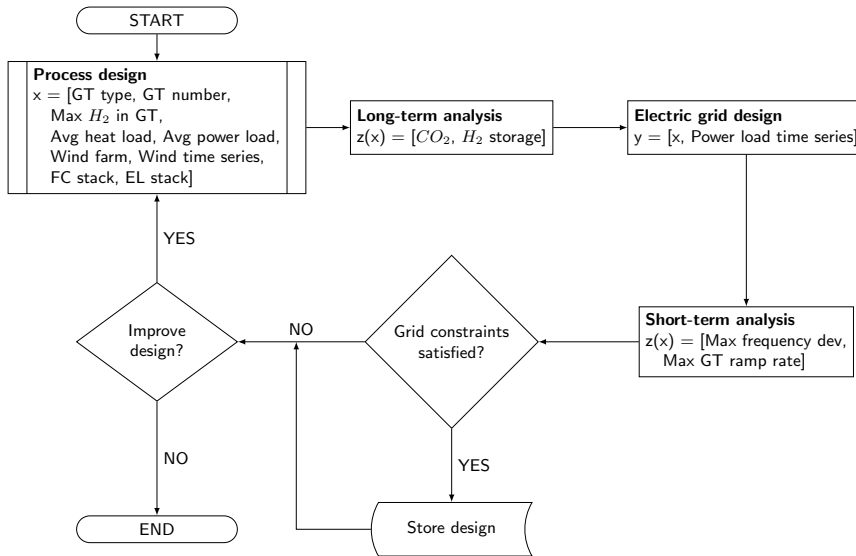


**FIGURE 6.2.** Flowchart of the proposed design methodology combining models of the process and electric domains. © Luca Riboldi *et al.*, 2020.

In the current study, the hydrogen storage technology has not been explicitly defined, with the size of the storage simply given in kg  $H_2$ . Preliminary analyses showed that gaseous storage as the preferable option compared to liquid storage. The additional energy requirements of a cryogenic process would indeed be detrimental for achieving an acceptable roundtrip energy efficiency. Given the large volumes associated with gaseous hydrogen storage, subsea storage solutions are envisaged. Potential storage technologies exist, such as the utilization of gas balloons (Pimm *et al.* [20]), gas pipes and underground formations (Kruck *et al.* [21]). More detailed analyses will be made to identify the optimal technological solutions. Another limitation of this study is that it does not model seawater desalination that is needed to produce the make up water used by the electrolyzer stack. The inherent assumption is that the residual thermal energy from the GT flue gas is sufficient to supply the necessary thermal energy for the desalination process. Preliminary calculations showed that this assumption holds true even in the worst case scenario where all water required by the electrolyzer stack would need to be produced by a designated unit (i.e., no water made available from the fuel cell stack). However, further analyses are needed to ensure the energy balance and to address the practical challenges to introduce another unit onto the offshore installation.

## Gas turbines

The GTs are simulated through a data-defined model based on the curves provided by the manufacturer. Data for the entire operating range of the engines (10–100%) were retrieved for the two GTs modelled, a GE LM2500+G4 (rated power 33.3 MW) and a GE LM6000 PF (rated power 44.7 MW). Those are aeroderivative gas turbines, typically used for offshore applications. More details on the models and their validation can be found in [6].

The proposed concept includes the possibility to co-feed a certain amount of  $H_2$  to the GT. The maximum concentration of  $H_2$  that can be used depends on the type of GT considered, particularly on the type of combustor. A white paper by the manufacturer of the modelled GTs [22] reports that aeroderivative models with a single annular combustor can handle hydrogen concentrations from 30 vol% up to 85 vol%. However, dry low emission and dry low  $NO_x$  combustors must operate with more limited amounts of hydrogen in the fuel, down to 5 vol% in certain cases. In this analysis, a conservative upper threshold of 20 vol% was selected.

Moreover, a simplified approach was considered to model the effect of  $H_2$  in the fuel. The strategy implemented keeps a constant chemical energy entering the GT combustor. That implies changes in the mass flow rate of fuel because of the different heating values at different fuel compositions. This is an approximation as it is known that the presence of a significant amount of  $H_2$  in the fuel might have profound effects in the operation of a GT [23]. However, the approximation may be considered acceptable given the limited maximum  $H_2$  concentration considered and the nature of this analysis.

## Waste heat recovery unit

A model of a waste heat recovery unit was developed and the physical hardware was designed to resemble that of an actual waste heat recovery unit from an offshore installation. More details about this model and its validation can be found in Riboldi and Nord [24]. In the integrated model of the proposed concept, the waste heat recovery unit model is not directly included. However, some input data from its model are necessary. First, an estimation of the pressure drops, to determine the outlet pressure from the GT. Second, a way to evaluate the relation between the exhaust gas from the GT and the heat that can be harvested. This allows the estimation of the heat available at each operating condition. Polynomial correlations, obtained by interpolating simulation outputs, were developed to make this information available to the integrated model.

### Fuel cell stack

As stated earlier, proton exchange membrane fuel cell stacks are foreseen in the proposed concept. Based on preliminary analyses, the expected output power was in the order of 1–4 MW. Such systems contains a few modules, each of them comprised by several stacks. The whole system is equipped with necessary components and auxiliaries commonly referred as balance of plant equipment, namely fuel and water management system, heat exchangers, sensors and controls.

The strategy adopted to model the complete proton exchange membrane fuel cell system was simulating a singular stack of 125 kW rated power and scaling it up to a full-scale system. A simple steady-state, zero-dimensional model of the fuel cell stack was prepared to assess the part-load performance of the stack. For this purpose, the scripts published in [25] were used and supplemented by additional in-house scripts for scaling-up the system. The outputs, including polarization curves and performance characteristic, have been calculated based on updated technical data of modern commercial stacks, where the main reference for parameters and tuning was the PowerCell model S3 125 kW [26]. Considering the standard operating conditions specified by manufacturer, the highest performance of this stack is 64 MJ/kgH<sub>2</sub> (electrical energy per kg of consumed hydrogen) at the 20–25 kW range. Then, the stack performance drops linearly to 56 MJ/kgH<sub>2</sub> at full load. The calculated performance curve has been used in scaling-up the system to the multi-megawatt output and used in the integrated model. The fuel cell stack degradation is neglected in the analysis.

### Electrolyzer stack

In the proposed concept, a proton exchange membrane electrolyser system is used to convert electricity and water into hydrogen and oxygen. The anticipated rated power of this system is in the 2–6 MW range, and its partial-load performance has been considered in the integrated model. A dedicated model for a 500 kW stack was prepared based on Zhang *et al.* [27] and additional in-house scripts for scaling-up the system. The 500 kW commercial stack NEL Hydrogen model M100 [28] served as reference for parameters and tuning of the model. The determined performance characteristic shows that the electrolyzer part-load performance is higher than at full load as it is in the case of the fuel cell stack. According to the performed calculations and respecting standard operating conditions specified by the manufacturer, the electrolyser stack's performance at 500 kW load is 4.9 gH<sub>2</sub>/MJ, then increases almost linearly to 5.5 gH<sub>2</sub>/MJ at 250 kW, thereafter exponentially reaches value of 6.4 gH<sub>2</sub>/MJ at 50 kW. Similarly to the fuel cell system, the degradation process is neglected

in the analysis. The presented electrolyzer performance characteristic has been used in scaling-up the system to the multi-megawatt output and used in the integrated model.

### Wind power

To calculate the offshore wind power available, wind data must be first retrieved. Appropriate wind speed time series are necessary to understand the potential of a given geographical location. A one year wind speed time series with 20-minutes resolution served as basis for our analysis [14]. The dataset refers to measurements from an oil platform in the North Sea by The Norwegian Meteorological Institute [17]. The wind speed raw data were corrected with a factor to consider the wind speed at turbine hub height:

$$k = \left( \frac{h_{hub}}{h_{ref}} \right)^{\frac{1}{7}} = \left( \frac{90}{14} \right)^{\frac{1}{7}} = 1.304 \quad (6.3)$$

where  $k$  is the wind correction factor and  $h_{hub}$ ,  $h_{ref}$  are the height of the wind turbine hub and reference data, respectively. An average wind speed of  $10.2 \text{ m s}^{-1}$  at the turbine hub height was calculated, in line with the expected range of  $9\text{--}11 \text{ m s}^{-1}$  for offshore applications on the Norwegian Continental Shelf [29]. Refer to the Supplementary Material for the probability density function of this dataset.

An additional dataset was retrieved for comparison from an open-source database of scientific-quality weather and energy data. The methods on which the database is developed are described in [30]. The weather data are taken from global reanalysis models and satellite observations [31]. The additional dataset refers to the weather conditions of an offshore area in the North Sea in 2017 and have a resolution of one hour. An average wind speed of  $10.9 \text{ m s}^{-1}$  is calculated.

For both data series, the conversion from wind speed to wind power is based on the power curve of the Siemens Gamesa SWT 6.0-154 wind turbine, a commercial 6 MW three-bladed floating turbine concept.

#### 6.2.4 Electric grid model

In electric grids, deviations of the average system frequency  $\omega$  [ $\text{rad s}^{-1}$ ] from its rated value  $\omega_s$  are proportional to the mismatch between power generation and demand. In other words, if power generation exceeds the demand, frequency increases beyond its rated value, until energy balance is achieved. Conversely, the frequency decreases if there is power generation deficit. This concept

is better understood if one considers all generators in a power system as an equivalent mass rotating around a shaft with damping at rated angular speed  $\omega_s$  [rad s<sup>-1</sup>], as seen in Fig. 6.3.

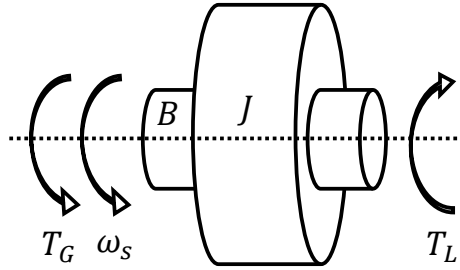


**FIGURE 6.3.** Ideal representation of the electric grid as a rotating mass with inertia and damping. © Luca Riboldi *et al*, 2020.

If Newton's second law of motion is applied to this system, Eq. (6.4) is obtained:

$$J(t, \omega)\dot{\omega} = T_G(t, \omega) - T_L(t, \omega) - B(t, \omega)(\omega - \omega_s) \quad (6.4)$$

where  $J(t, \omega)$ ,  $B(t, \omega)$  represent the equivalent inertia [kg m] and damping coefficient [N m s rad<sup>-1</sup>] of the system and are functions of the time  $t$  [s] and  $\omega$ ;  $T_G(t, \omega)$  and  $T_L(t, \omega)$  are the equivalent torques from generators and loads [N m], also functions of  $t$  and  $\omega$ .

From the electric power engineering perspective, one of the main challenges of the HES-OFF is guaranteeing frequency stability in the electric grid. Stability here is seen in the sense of keeping frequency values within an acceptable range for changes in power generation and demand [32]. Due to the stochastic nature of wind power, the interconnection of an offshore windfarm to an oil-and-gas platform may cause instabilities if the system is not properly designed. Moreover, as discussed in [33–35], integration of renewable energy sources and increased frequency and voltage deviations can increase maintenance, reduce reliability and affect performance of process and electric equipment. Therefore, the proposed integrated model includes a stability assessment of the electric grid and produces designs that satisfy minimum conditions for stable operation, as shown in Fig. 6.2.

To achieve that, the average frequency dynamics of the system is evaluated

using the normalized state-space realization of Eq. (6.4)'s model:

$$\dot{\tilde{x}} = -\frac{D(t, \tilde{x})}{M(t, \tilde{x})}\tilde{x} + \frac{u(t, \tilde{x}) - w(t, \tilde{x})}{(\tilde{x} + 1)M(t, \tilde{x})} \quad (6.5)$$

where  $x = \frac{\omega}{\omega_s}$  and  $\tilde{x} = x - 1$  are the normalized angular speed and the angular speed deviation from  $\omega_s$  [pu];  $M(t, \tilde{x}) = \frac{J(t, \omega)\omega_s^2}{S_b}$  and  $D(t, \tilde{x}) = \frac{B(t, \omega)\omega_s^2}{S_b}$  are the normalized equivalent moment of inertia [s] and damping coefficient [pu] with  $S_b$  [W] being the rated power of the system;  $u(t, \tilde{x})$  and  $w(t, \tilde{x})$  are the normalized total active power from generators and loads [pu]. In this surrogate model implemented in MATLAB Simulink, the wind farm, the turbo generator sets, and the fuel cell stacks are seen as generators, while motors of the platform and electrolyser stacks are seen as loads.

Not least, the wind farm is modeled similarly to the process model described in Sec. 6.2.3, i.e. interpolating a time series of average wind speeds with the wind turbine power curve. However, the effect of wind turbulence is added in the electric grid model according to the recommendations in industry standards for offshore turbines [36]. The Kaimal spectrum is applied with a length scale of  $\frac{1}{5}$  of the rotor diameter (25.2 m) and a turbulence intensity of 6%, as suggested in [37].

Note that voltage stability is ignored in this surrogate model. This is justified by the following facts: 1) in offshore installations, voltage dynamics typically have a negligible effect on the sizing of the process equipment [18]; 2) voltage stability can be improved by control strategies [16, 18, 38]; 3) voltage stability analysis requires complex dynamic simulations with long solve times, what may render the overall optimization procedure intractable [18].

### 6.2.5 Long-term analysis

The long-term analysis deals with the design of the HES-OFF considering the various stages of life of the offshore installation: peak, mid-life and tail. For each stage of life, an annual time span is considered, where the year is discretized with an hourly resolution, i.e. 8760 instances. While the power and heat demands are constant throughout the year, the wind speed profiles lead to varied hourly wind powers. Depending on the operational strategy, different contributions from the fuel cell and electrolyser stack will be requested and the storage level will change consequently. The analysis must ensure that the HES-OFF is able to meet the power and heat demands in each instance of the year and that a net-zero balance of stored  $H_2$  is achieved at the end of the year. The main objective is to minimize  $CO_2$  emissions. Secondary objectives are to remove one GT and maximize the exploitation of the offshore wind resource.

The following solution strategy is implemented. Once a design is defined, it is first tested over one year without considering energy storage. At the end of the year, either a net deficit of power (typical of peak years) or a net surplus of power (typical of tail years) is obtained. In the case of a net deficit of power, the next step implemented by the solution algorithm is to evaluate in which instances during the year it is possible to increase GT load and to use extra power for  $H_2$  production by the electrolyser stack. The production is stopped when either the maximum storage level or the  $H_2$  output target is reached. In the case of a net surplus of power (typical of tail years), the solution algorithm decreases the GT load and use the fuel cell stack to cover the related decrease of power output whenever possible during the year. When the level of storage reaches a maximum, a fraction of the  $H_2$  is co-fed to the GT in order to constrain the size of the storage. If this measure is not enough to handle the amount of  $H_2$  available because of excess power, some wind power is dissipated and the  $H_2$  production is therefore reduced. If at the end of the iteration throughout the year, some  $H_2$  is still unused, additional  $H_2$  is co-fed to the GT whenever possible throughout the year.

### 6.2.6 Short-term analysis

The main goal of the short-term analysis is checking the feasibility of the offshore grid design from an operational perspective. This step is performed based on the outputs of the long-term analysis described earlier in Sec. 6.2.5. It checks the robustness of a proposed solution to electrical transients in a time scale of minutes. Examples of such transients are load variations in pumps and compressors and wind power production. It can be considered one of the innovations of this work compared to the state-of-the-art design techniques for HES-OFFs reported in the literature.

The short-term analysis tries to answer the following questions: *can the electrical frequency of the electric grid be maintained within the allowed range specified in industry standards for offshore installations [39]? Will the allowed ramp rates of GTs be respected during typical load and wind power transients?*

To achieve that, the following procedure is executed:

1. Equipment sizes are obtained from the long-term analysis results, namely: number and type of GTs, number of wind turbines, size of the fuel cells and electrolysers stacks.
2. Average load and wind power and their possible variations are obtained from historical data.

3. This data is parametrized into a MATLAB Simulink model of the offshore grid, as described in [Sec. 6.2.4](#).
4. The Simulink model is executed for two 180-seconds simulations. The first time with the maximum positive variation of wind power, the second with the minimum negative variation. During these two executions, the maximum positive load variation is introduced at 60s and the minimum negative load variation at 120s.
5. At the end of these executions, the following values are obtained from the time series of the simulation: maximum and minimum frequency of the offshore grid, maximum ramp rate of the [GTs](#).
6. The dynamic constraints of the offshore grid are considered satisfied if all these values are below their specified limits. Otherwise, the long-term analysis is re-executed changing the size of equipment as described below:
  - If the minimum frequency limit was reached, the fuel cell stack is increased.
  - If the maximum frequency limit is reached, the electrolyser stack is increased.
  - If the [GT](#) ramp rate is reached, the number of wind turbine is reduced.

### 6.2.7 Optimization framework

An optimization framework was developed to identify the optimal designs for the [HES-OFF](#). The input parameters for the optimization problem (i.e., the decision variables) are those deemed having the largest impact on the performances. They are illustrated in [table 6.1](#) with their selected lower and upper bounds.

**TABLE 6.1.** Input parameters for the optimization problem

| Decision variables              | Unit | Lower bound | Upper bound |
|---------------------------------|------|-------------|-------------|
| <a href="#">GT</a> type         | -    | LM2500      | LM6000      |
| <a href="#">GT</a> number       | -    | 1           | 2           |
| Max $H_2$ in <a href="#">GT</a> | vol% | 0           | 20          |
| Wind farm size                  | MW   | 12          | 24          |
| fuel cell stack size            | MW   | 1           | 5           |
| electrolyser stack size         | MW   | 2           | 8           |



The metrics selected to analyze the performance of a design (i.e., the objective functions) are the cumulative  $CO_2$  emissions and the  $H_2$  storage size. Both objectives are to be minimized by the optimizer. To explore only the space considered of interest, an additional constraint was established, that is to discard designs leading to an  $H_2$  storage size larger than 50,000 kg. A multi-objective constrained optimization problem is so defined. A meta-heuristic approach was selected to solve the optimization problem. The genetic algorithm using the MATLAB Global Optimisation Toolbox [40] was implemented, with the following characteristics:

- Population size: 500
- Maximum number of generations = 10
- Function tolerance =  $10^{-3}$
- Number of stall generations: 5
- Crossover fraction: 0.8

## 6.3 RESULTS

### 6.3.1 Case study

An offshore facility located in the Norwegian sector of the North Sea is used as case study. The power and heat are supplied to the processing block which delivers export oil and gas and additionally fuel to the GTs. Electrical power is consumed primarily by pumps (i.e. circulation of cooling water, water injection, oil export) and compressors (i.e. gas export, gas lift, gas re-injection) [24]. All electrically driven equipment is connected to the grid. Crude oil separation and stabilization makes up for a large share of the heat requirement, with the remaining part supplied to other processing requirements and utility demands. For the long-term analysis, the power and heat supply demands were based on estimations provided by the platform operator and discretized as follows:

- Peak demand (2 years): 43.6 MW power, 14.0 MW heat
- Mid-life demand (4 years): 35.2 MW power, 11.0 MW heat
- Tail demand (12 years): 32.9 MW power, 8.0 MW heat

For the short-term analysis, historical data of the power demand was compiled from the supervisory control and data acquisition system of the platform.

A data set covering a time interval of one week with one second interval between samples was extracted and fit by a normal distribution. From the latter, it was obtained an average load demand of 44.6 MW and maximum load variation of 3 MW with 99.9% of probability.

### 6.3.2 Parametric analysis

First, a parametric analysis was performed aiming not only to preliminarily evaluate the potential of the HES-OFF concepts, but also to identify parameters that influence significantly the performances and in which ranges they can be varied. This information is essential to appropriately define the subsequent optimization problem. The results of this parametric analysis have been partially reported in Riboldi *et al.* [41].

The following parameters were kept constant in this analysis:

- Maximum GT load: 95% (with energy storage), 90% (without energy storage)
- Minimum GT load: 40% (to ensure the heat demand is met in every instance)
- Maximum fraction of  $H_2$  in GT: 20 vol%
- Wind turbine size: 6 MW

The parameters that have been investigated are (with the default values when the focus is on another parameter):

- Type and number of GTs
- Number of wind turbines
- Maximum  $H_2$  storage size – 50,000 kg default
- Maximum electrolyser stack size – 6.0 MW default
- Maximum fuel cell stack size – 3.6 MW default

The main findings are only qualitatively described in this section. The complete set of results obtained is available in the Supplementary Material.

### Maximum storage size

The designs based on the large GT (LM6000) return, on average, smaller sizes of  $H_2$  storage than those obtained when using the small GT (LM2500), not larger than about 10,000 kg. On the other hand, the large GT does not allow to constrain the maximum size of the storage below a certain threshold. The small GT can meet those constraints in most cases but to the cost of wind power dissipation. With respect to  $CO_2$  emissions, allowing large sizes of storage leads to reduction in emissions, as expected. However, these reductions saturate after a certain storage size. It should also be highlighted that the designs based on the small GT must rely on two units, otherwise very large storage is required. On the contrary, it is always possible to operate the system with a single unit when the large GT is considered.

### Maximum electrolyzer stack size

Decreasing the electrolyser stack size results in a slight increase of the  $CO_2$  emissions. However, the negative impact is very limited. A maximum increase of cumulative emissions of 0.5–0.6% was registered for the cases based on the small and large GTs, respectively. In the first case, the size of the stack was varied between 2.5 and 7 MW, in the second case between 4 and 7 MW. The sizing of the electrolyser stack might have a role in constraining the storage size necessary, mainly when the small GT is considered.

### Maximum fuel-cell stack size

The fuel cell stack size appears not particularly relevant for the large GT, while showing a slightly larger influence for the cases based on the small GT. The data suggests that the main design challenge is to store enough  $H_2$  rather than being able to instantaneously consume the  $H_2$  produced. In other words, the storage rated energy capacity in MJ seems to play a larger role than its rated power capacity in MW. With regard to the large GT, increasing the fuel cell stack size does not affect the  $CO_2$  emissions significantly. A limited positive effect is noted on the cumulative emissions but mainly on the storage size, when large wind farms (i.e. excess of wind power) are considered. In such cases, the storage size is influenced by the ability to quickly consume  $H_2$  and a larger fuel cell stack might have a positive effect.

### Discussion of the parametric analysis

Overall, the following can be argued from the parametric analysis of the case study. The design parameters investigated (i.e. the  $H_2$  storage, the electrolyser

and fuel cell stack sizes) seem to have little effect on the cumulative  $CO_2$  emissions. This might suggest that it is not useful to pursue an optimal technical design in terms of minimum possible emissions, considering that those might offer relatively low environmental advantages and might not be justified economically. Hence, it could be more convenient to keep those design parameters at a level that ensure reliable operation. To confirm this hypothesis, the optimization framework described in Sec. 6.2.7 was applied and its results are presented in the following section.

### 6.3.3 *Integrated results using the optimization framework*

#### **Benchmark scenarios**

Based on the insights gained through the parametric analysis, a first set of designs were defined and tested and those constitute the benchmark scenarios. The results obtained by these proposed HES-OFF designs were compared against two other concepts: a standard design relying solely on GTs (GTs), and designs involving GTs and wind turbines without any storage (GTs+wind turbines). These two additional concepts were simulated using the same models previously described.

For all concepts, the maximum allowed frequency deviation in the electric grid was  $\pm 2\%$  from its rated value (60 Hz) and the maximum GT ramp rate 14.7 %/s. In the proposed HES-OFF designs, the maximum GT load was set to 95% rather than 90% to account for the decreased contribution of GTs to operational reserves, which is also ensured by the ESS. The size of the fuel cell and electrolyser stacks are set at their default values, i.e. 3.6 MW and 6 MW respectively. Not least, the proposed designs selected constrained the  $H_2$  storage size to about 5,000 kg for the small GT, and to the minimum possible for the large GT.

Tables 6.2 and 6.3 report the results of this comparative analysis. These results suggest that the proposed concept reduces  $CO_2$  emissions compared both to the GTs and the GTs+wind turbines concepts. If the design based on the small GT in a simple cycle is taken as reference, a maximum  $CO_2$  emissions reduction of about 40% can be achieved by the HES-OFF system. The improvements compared to the standard integration of wind power lie in a range between 1% and 7%. The lowest cumulative  $CO_2$  emissions are obtained by the proposed design based on the small GT coupled with the largest size of wind farm tested (24 MW), reaching a cumulative  $CO_2$  emissions cut of over 1400 kt compared to the standard solution based on the same GT. However, such design fails to constrain the  $H_2$  storage and to remove one GT. At smaller sizes of the wind farm size (18 and 12 MW), the proposed designs using the LM6000 GT gain in

**TABLE 6.2.** Designs based on the LM2500 GT - Comparative analysis between a standard concept on GTs only (GTs), a concept involving GTs and wind turbines (GTs+wind turbines), and the proposed concept (HES-OFF)

| INPUTS                                 | GTs    |        |        |        | GTs+wind turbines |        |        | HES-OFF |        |        |
|--|--------|--------|--------|--------|-------------------|--------|--------|---------|--------|--------|
|  | LM2500 | LM2500 | LM2500 | LM2500 | LM2500            | LM2500 | LM2500 | LM2500  | LM2500 | LM2500 |
| <b>GT type</b>                         | LM2500 | LM2500 | LM2500 | LM2500 | LM2500            | LM2500 | LM2500 | LM2500  | LM2500 | LM2500 |
| <b>GT number</b>                       | 2      | 2      | 2      | 2      | 2                 | 2      | 2      | 2       | 2      | 2      |
| <b>Max. GT load</b>                    | 95 %   | 90 %   | 90 %   | 90 %   | 95 %              | 95 %   | 95 %   | 95 %    | 95 %   | 95 %   |
| <b>Min. GT load</b>                    | 40 %   | 40 %   | 40 %   | 40 %   | 40 %              | 40 %   | 40 %   | 40 %    | 40 %   | 40 %   |
| <b>Wind farm size [MW]</b>             | -      | 12     | 18     | 24     | 12                | 18     | 24     | 12      | 18     | 24     |
| <b>Max. electrolyser size [MW]</b>     | -      | -      | -      | -      | 6.0               | 6.0    | 6.0    | 6.0     | 6.0    | 6.0    |
| <b>Max. fuel cell size [MW]</b>        | -      | -      | -      | -      | 3.6               | 3.6    | 3.6    | 3.6     | 3.6    | 3.6    |
| <b>Max. storage [kg]</b>               | -      | -      | -      | -      | 5000              | 5000   | 5000   | 5000    | 5000   | 5000   |
| <b>OUTPUTS</b>                         |        |        |        |        |                   |        |        |         |        |        |
| <b>H<sub>2</sub> storage size [kg]</b> | -      | -      | -      | -      | 5034              | 5038   | 25245  | 5034    | 5038   | 25245  |
| <b>electrolyser size [MW]</b>          | -      | -      | -      | -      | 6.0               | 6.0    | 6.0    | 6.0     | 6.0    | 6.0    |
| <b>fuel cell size [MW]</b>             | -      | -      | -      | -      | 3.6               | 3.6    | 3.6    | 3.6     | 3.6    | 3.6    |
| <b>CO<sub>2</sub> emission [Mt]</b>    | 3.51   | 2.71   | 2.42   | 2.25   | 2.53              | 2.28   | 2.10   | 2.53    | 2.28   | 2.10   |
| <b>Max. frequency [Hz]</b>             | 60.77  | 60.84  | 60.88  | 60.92  | 60.74             | 60.77  | 60.80  | 60.74   | 60.77  | 60.80  |
| <b>Min. frequency [Hz]</b>             | 59.22  | 59.02  | 58.91  | 58.79  | 59.13             | 59.04  | 58.95  | 59.13   | 59.04  | 58.95  |
| <b>Max. freq. dev. [%]</b>             | 1.30   | 1.63   | 1.82   | 2.02   | 1.45              | 1.6    | 1.75   | 1.45    | 1.6    | 1.75   |
| <b>Max. GT ramp [%/s]</b>              | 1.52   | 1.88   | 2.11   | 2.33   | 1.68              | 1.86   | 2.03   | 1.68    | 1.86   | 2.03   |

**TABLE 6.3.** Designs based on the LM6000 GT - Comparative analysis between a standard concept on GTs only (GTs), a concept involving GTs and wind turbines (GTs+wind turbines), and the proposed concept (HES-OFF)

| INPUTS                                 | GTs    |        |        |        | GTs+wind turbines |        |        | HES-OFF |        |        |
|--|--------|--------|--------|--------|-------------------|--------|--------|---------|--------|--------|
|  | LM6000 | LM6000 | LM6000 | LM6000 | LM6000            | LM6000 | LM6000 | LM6000  | LM6000 | LM6000 |
| <b>GT type</b>                         | LM6000 | LM6000 | LM6000 | LM6000 | LM6000            | LM6000 | LM6000 | LM6000  | LM6000 | LM6000 |
| <b>GT number</b>                       | 2      | 2      | 2      | 2      | 1                 | 1      | 1      | 1       | 1      | 1      |
| <b>Max. GT load</b>                    | 95 %   | 90 %   | 90 %   | 90 %   | 95 %              | 95 %   | 95 %   | 95 %    | 95 %   | 95 %   |
| <b>Min. GT load</b>                    | 40 %   | 40 %   | 40 %   | 40 %   | 40 %              | 40 %   | 40 %   | 40 %    | 40 %   | 40 %   |
| <b>Wind farm size [MW]</b>             | -      | 12     | 18     | 24     | 12                | 18     | 24     | 12      | 18     | 24     |
| <b>Max. electrolyser size [MW]</b>     | -      | -      | -      | -      | 6.0               | 6.0    | 6.0    | 6.0     | 6.0    | 6.0    |
| <b>Max. fuel cell size [MW]</b>        | -      | -      | -      | -      | 3.6               | 3.6    | 3.6    | 3.6     | 3.6    | 3.6    |
| <b>Max. storage [kg]</b>               | -      | -      | -      | -      | 5000              | 5000   | 5000   | 5000    | 5000   | 5000   |
| <b>OUTPUTS</b>                         |        |        |        |        |                   |        |        |         |        |        |
| <b>H<sub>2</sub> storage size [kg]</b> | -      | -      | -      | -      | 9876              | 7449   | 6221   | 9876    | 7449   | 6221   |
| <b>electrolyser size [MW]</b>          | -      | -      | -      | -      | 6.0               | 6.0    | 6.0    | 6.0     | 6.0    | 6.0    |
| <b>fuel cell size [MW]</b>             | -      | -      | -      | -      | 1.1               | 3.6    | 3.6    | 1.1     | 3.6    | 3.6    |
| <b>CO<sub>2</sub> emissions [Mt]</b>   | 2.92   | 2.48   | 2.36   | 2.30   | 2.45              | 2.32   | 2.24   | 2.45    | 2.32   | 2.24   |
| <b>Max. frequency [Hz]</b>             | 60.77  | 60.85  | 60.88  | 60.92  | 60.83             | 60.82  | 60.85  | 60.83   | 60.82  | 60.85  |
| <b>Min. frequency [Hz]</b>             | 59.21  | 59.02  | 58.90  | 58.78  | 59.06             | 58.95  | 58.85  | 59.06   | 58.95  | 58.85  |
| <b>Max. freq. dev. [%]</b>             | 1.32   | 1.63   | 1.83   | 2.03   | 1.56              | 1.75   | 1.92   | 1.56    | 1.75   | 1.92   |
| <b>Max. GT ramp [%/s]</b>              | 1.05   | 1.30   | 1.45   | 1.61   | 2.49              | 2.78   | 3.06   | 2.49    | 2.78   | 3.06   |

competitiveness compared to those based on the LM2500. Overall, the small GT designs can be characterized as high-risk high-gain concepts, where the challenges to implement them are larger but the potential positive effects on  $CO_2$  emissions are larger as well. Conversely, use of the large GT results in easier to implement designs and stable performance, but lower potentials to cut  $CO_2$  emissions.

In addition, the proposed designs contribute to decrease frequency deviations of the offshore grid when compared to the GTs+wind turbines ones. Note that the the minimum frequency limit and hence the maximum frequency deviation can be respected in the proposed concept relying on the LM6000 GT with the 18 and 24 MW wind farms. This shows the importance of considering grid requirements in the design phase of a HES-OFF. Not least, the use of only one LM6000 GT in the proposed designs comes at the price of increased GT ramp rates. While these values are well below the critical ramp rate informed by the manufacturer, it is important to highlight that additional efforts by the GT governor may be required due to the continuous compensation of the wind power variation. Such operation could lead to premature failure of actuators by wear and tear and, consequently, additional maintenance of the GT as discussed in Troy *et al.* [42].

### Investigation of the optimal designs

The optimization framework allowed to further investigate the proposed HES-OFF designs and to fully understand the potential of this concept. The following sections present how some of the constraints imposed in the optimization procedure affect the objective functions to be minimized, namely the  $CO_2$  emissions and the  $H_2$  storage size.

**Reference case** The optimization process was initially implemented using only the long-term analysis, thus not including considerations on the grid stability. The Pareto fronts illustrated in Fig. 6.4 were obtained by the optimizer using the reference wind data series from The Norwegian Meteorological Institute. Table 6.4 shows the two optimal designs resulting in minimum cumulative  $CO_2$  emissions (Min  $CO_2$ ) and minimum size of the  $H_2$  storage (Min  $H_2$  storage).

The optimization process seems to have worked satisfactorily as a lower value for cumulative  $CO_2$  emissions and for  $H_2$  storage size were obtained when compared to the results of the parametric analysis. The optimal solutions cut  $CO_2$  emissions up to 1300 kt compared to the standard GT-based concept, making up for a 36% reduction. However, Fig. 6.4A shows that the reduction of  $CO_2$  emissions is somewhat limited for a large increase in the storage size. The range between the maximum and minimum level of  $CO_2$  emissions in the

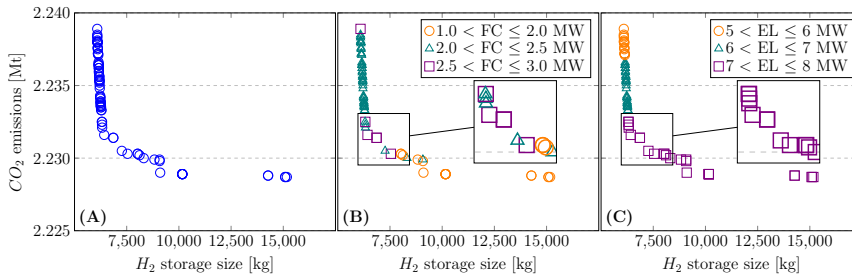


**FIGURE 6.4.** Pareto front 1 - the reference case, (A) shows a limited reduction of  $CO_2$  emissions, (B) highlights the different fuel cell stack size ranges, and (C) the different electrolyser stack size ranges. © Luca Riboldi et al, 2020.

**TABLE 6.4.** Optimal designs of the reference case - Pareto 1

| Decision variables              |      | Min $CO_2$ | Min $H_2$ storage |
|---------------------------------|------|------------|-------------------|
| GT type                         | -    | LM6000     | LM6000            |
| GT number                       | -    | 1          | 1                 |
| Max. $H_2$ in GT                | vol% | 13.9       | 15.3              |
| Size of wind farm               | MW   | 24         | 24                |
| Max. size of fuel cell stack    | MW   | 1.4        | 3.0               |
| Max. size of electrolyser stack | MW   | 7.8        | 5.7               |
| <b>Objective functions</b>      |      |            |                   |
| Cumulative $CO_2$ emissions     | Mt   | 2.229      | 2.239             |
| $H_2$ storage size              | kg   | 15170      | 6089              |

Pareto front is slightly higher than 10 kt. An analysis of the optimal solutions shows that only designs relying on the LM6000 GT were selected and only the largest possible size of the wind farm. This indicates that the  $H_2$  storage size is not strongly affected by the GT or wind farm sizes, while a large wind farm allows to cut more emissions. It is also interesting to note that the Pareto front displays a knee, after which emissions decrease only marginally while the size of the  $H_2$  storage increases significantly. The designs around the knee are consequently strong candidates to be the most relevant.

Moreover, effects of other input parameters were not so obvious. Fig. 6.4B presents fuel cell stack sizes for different Pareto designs. The designs resulting in the lowest emissions rely on relatively small fuel cell stacks. This might indicate that the optimizer pointed towards the utilization of  $H_2$  not only in the fuel cell but also in the GT, as much as possible. Therefore, it may be convenient to have the minimum fuel cell stack size that ensures reliable operation and utilize the extra  $H_2$  in the GT. On the other hand, larger stacks are required when the priority is to reduce the  $H_2$  storage. Yet a maximum fuel cell stack of 3

MW was obtained, quite below the maximum size allowed in the optimization (i.e. 5 MW). The results around the Pareto knee shows optimal fuel cell sizes between 1.5 and 3 MW.

Fig. 6.4C shows electrolyser stack sizes for different Pareto designs. Large electrolyser stacks are necessary to obtain the lowest possible  $CO_2$  emissions. However, the  $CO_2$  emissions reductions are rather limited while large electrolyser stacks seem to be connected to large  $H_2$  storage. If a design in the vicinity of the Pareto knee is targeted, electrolyser stacks of at least 7 MW should be envisaged.

### Constant performance of fuel cell and electrolyser stacks

A possible explanation of the limited range of  $CO_2$  emissions cuts obtained may be related to the relatively low round-trip efficiency of the ESS. To verify this, an optimization problem was defined in which a constant and relatively high efficiency was configured in fuel cell and electrolyser stacks, namely  $66 \text{ MJ kg}^{-1}$  and  $0.007 \text{ kg MJ}^{-1}$ . The Pareto front obtained (Pareto 1B) was compared to Pareto 1 and results are illustrated in Fig. 6.5. In addition, table 6.5 shows the two optimal designs resulting in minimum cumulative  $CO_2$  emissions (Min  $CO_2$ ) and minimum  $H_2$  storage size of the (Min  $H_2$  storage) for Pareto 1B.

**TABLE 6.5.** Optimal designs of the constant fuel cell and electrolyser performance case - Pareto 1B

| Decision variables              |      | Min $CO_2$ | Min $H_2$ storage |
|---------------------------------|------|------------|-------------------|
| GT type                         | -    | LM2500     | LM6000            |
| GT number                       | -    | 2          | 1                 |
| Max. $H_2$ in GT                | vol% | 19.2       | 15.3              |
| Size of wind farm               | MW   | 24         | 24                |
| Max. size of fuel cell stack    | MW   | 4.4        | 3.2               |
| Max. size of electrolyser stack | MW   | 4.5        | 2.2               |
| <b>Objective functions</b>      |      |            |                   |
| Cumulative $CO_2$ emissions     | Mt   | 2.074      | 2.250             |
| $H_2$ storage size              | kg   | 52909      | 5566              |

With these adaptations, also optimal designs based on the smaller GT are obtained. Indeed, those designs reached the lowest cumulative  $CO_2$  emissions and are placed in the right bottom corner of Fig. 6.5A. As expected, the better efficiency of the ESS resulted in a larger potential to reduce  $CO_2$  emissions. Nevertheless, the range of emission cuts is still limited, suggesting that there might be a hard limit to emissions reduction achievable by the proposed HES-OFF.

Fig. 6.5B and C show the fuel cell and electrolyser stacks size ranges for the optimal designs identified in Pareto 1B. It can be observed that the larger



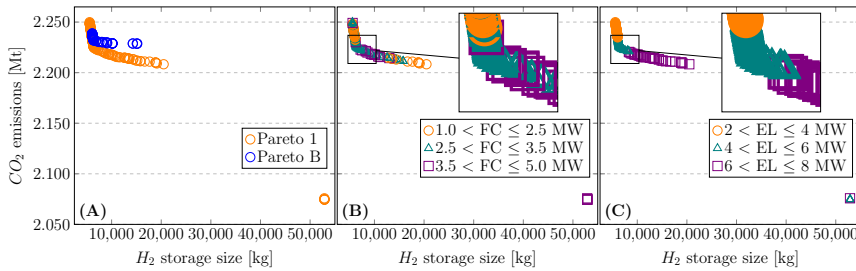


**FIGURE 6.5.** Pareto front 1B - constant performance of fuel cell and electrolyser stacks, (A) shows a larger reduction of  $CO_2$  emissions when compared to Pareto 1, (B) highlights the different fuel cell stack size ranges, and (C) the different electrolyser stack size ranges. © Luca Riboldi *et al*, 2020.

efficiency led to a more intensive utilization of the fuel cell, with optimal designs using up to 5 MW stacks. The influence on the optimal electrolyser stack size is less apparent.

### Alternative wind data

The wind speed data set used is expected to have a strong influence on the results. To this end, the optimization problem was run for an alternative wind data series, as described earlier in [Sec. 6.2.3](#). The Pareto front obtained (Pareto 2) was compared to Pareto 1 and results are illustrated in [Fig. 6.6A](#). [Table 6.6](#) shows the two optimal designs resulting in minimum cumulative  $CO_2$  emissions (Min  $CO_2$ ) and minimum  $H_2$  storage size of the (Min  $H_2$  storage). The reference wind data series appears to be more challenging for the design of the hybrid system. The alternative wind dataset resulted in a performance improvement of the proposed HES-OFF, with cumulative  $CO_2$  emissions decreasing by about 10%, while a similar range of  $H_2$  storage size is obtained.

**TABLE 6.6.** Optimal designs of the alternative wind data case - Pareto 2

| Decision variables              |      | Min $CO_2$ | Min $H_2$ storage |
|---------------------------------|------|------------|-------------------|
| GT type                         | -    | LM2500     | LM6000            |
| GT number                       | -    | 2          | 1                 |
| Max. $H_2$ in GT                | vol% | 19.2       | 11.1              |
| Size of wind farm               | MW   | 18         | 12                |
| Max. size of fuel cell stack    | MW   | 4.3        | 4.4               |
| Max. size of electrolyser stack | MW   | 7.7        | 6.2               |
| <b>Objective functions</b>      |      |            |                   |
| Cumulative $CO_2$ emissions     | Mt   | 2.024      | 2.330             |
| $H_2$ storage size              | kg   | 49998      | 4991              |

### Accounting for electric grid dynamics

The last analysis makes use of the whole integrated model illustrated in Fig. 6.2. The optimizer first tests the long-term performance of each design in terms of cumulative  $CO_2$  emissions and  $H_2$  storage size. The outputs of this analysis are then utilized as inputs to test the short-term grid stability. If a design is found not to comply with the grid dynamics criteria as reported, it is discarded. This integrated approach, composed of two consecutive steps, allows to direct the optimization towards process designs that are operationally feasible from the electric grid perspective.

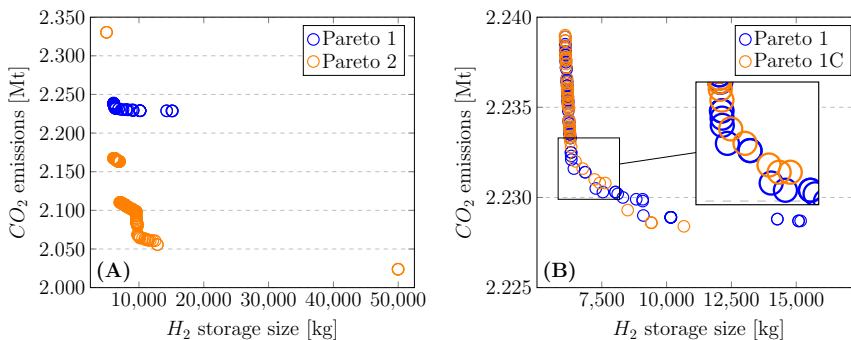


**FIGURE 6.6.** (A) Pareto front 2 shows a larger reduction of  $CO_2$  emissions when compared to Pareto 1, while (B) Pareto front 1C has fewer feasible solutions when compared to Pareto 1. © Luca Riboldi et al, 2020.

The Pareto front obtained (Pareto 1C) is illustrated in Fig. 6.6-B and compared to Pareto 1, while table 6.7 shows, for each of them, the two optimal designs resulting in minimum cumulative  $CO_2$  emissions (Min  $CO_2$ ) and minimum  $H_2$  storage size (Min  $H_2$  storage). It can be observed that the two Pareto fronts nearly overlap in large part of the solution space. That was expected as the same optimization problem was solved. The notable difference is Pareto 1C has fewer feasible solutions, because the optimizer rejected all designs that do not fulfill the dynamic criteria imposed. Those include the designs which returned the minimum  $CO_2$  emissions but the larger  $H_2$  storage size in the reference case.

## 6.4 CONCLUSIONS

This paper compared the performances of three concepts for stable power and heat supply in offshore oil and gas installations: a standard design relying solely on GTs, a state-of-the-art solution involving GTs and wind turbines without

**TABLE 6.7.** Optimal designs accounting for grid dynamics - Pareto 1C

| <b>Decision variables</b>            |      | <b>Min CO<sub>2</sub></b> | <b>Min H<sub>2</sub> storage</b> |
|--------------------------------------|------|---------------------------|----------------------------------|
| GT type                              | -    | LM6000                    | LM6000                           |
| GT number                            | -    | 1                         | 1                                |
| Max. H <sub>2</sub> in GT            | vol% | 18.0                      | 18.3                             |
| Size wind farm                       | MW   | 24                        | 24                               |
| Max. size fuel cell stack            | MW   | 1.3                       | 3.1                              |
| Max. size electrolyser stack         | MW   | 7.8                       | 5.6                              |
| <b>Objective functions</b>           |      |                           |                                  |
| Cumulative CO <sub>2</sub> emissions | Mt   | 2.228                     | 2.239                            |
| H <sub>2</sub> storage size          | kg   | 10666                     | 6086                             |

any storage, and a novel **HES-OFF** in which a H<sub>2</sub>-based **ESS** was integrated with **GTs** and wind turbines. The performances have been obtained through an integrated model, consisting of two macro-models representing the power unit and the offshore electric grid. Those are in turn constituted by sub-models properly developed to represent the various components of the system. The analyses carried out include the two domains embedded in the modelling – i.e., process and grid dynamics – and, therefore, involve different time scales – i.e., hours and seconds. They were therefore labeled long-term and short-term.

The long-term analysis is used to size the main process components of the system and to understand the effect of different design choices on the energy and environmental performance. The short-term analysis takes as input one given design and verifies the robustness of the proposed solution to electrical transients. Both domains are necessary to correctly evaluate the potentials and the limitations of the **HES-OFF**.

The proposed integrated model was then used to perform several analyses on the case study defined, an oil and gas platform in the North Sea. The proposed **HES-OFF** concept was first assessed by means of a parametric analysis, aiming to identify the key design parameters influencing the system performance. The effect of the type and number of gas turbines, the size of the wind farm, the size of the fuel cell and electrolyzer stacks, and the size of the hydrogen storage were tested. The outputs obtained were then compared to standard and state-of-the-art concepts to supply energy offshore. The main findings from the parametric analysis are:

- The proposed concept can significantly curb CO<sub>2</sub> emissions compared to the standard concept based solely on gas turbines. A potential for CO<sub>2</sub> emissions reduction of up to 40%, corresponding to around 1400 kt of CO<sub>2</sub>, was observed.
- The proposed concept can as well further decrease CO<sub>2</sub> emissions com-

pared to the state-of-the-art concept as the energy storage system allows to more extensively exploit the offshore wind resource. In this case the emissions reduction is predictably more limited, ranging between 1% and 7%.

- For the parameters investigated, little effect was noted on the achievable  $CO_2$  emissions reductions. Those seem to be more constrained by technological limitations (e.g., roundtrip efficiency of the energy storage system, amount of  $H_2$  that can be fed to the gas turbine) than by design considerations.
- The obtained size of the underwater  $H_2$  storage appears to be reasonable if the designs are developed with proper constraints and a minor dissipation of wind power is allowed when necessary.
- The proposed designs improve the grid stability and allow a successful integration of larger wind power capacity in the offshore electric grid without overpassing the 2% frequency variation as in the case of standard integration of the wind farm.

While the parametric analysis gave a first picture of the feasibility of the proposed concept, the developed optimization framework produced a more comprehensive insight into the performance of the novel hybrid energy system. A multi-objective optimization based on a genetic algorithm was defined, where the two minimization objectives were the cumulative  $CO_2$  emissions and the hydrogen storage size. The optimizer provided Pareto front of optimal designs, outlining what is the best performance that can be expected by the proposed **HES-OFF** system. Moreover, the optimization results provide new important insights to understand the performance obtained and identify directions for further improvements. The main findings from the optimization are:

- The optimizer indicated a maximum  $CO_2$  emissions cut of almost 1300 kt (i.e. 36% reduction) compared to the standard **GT**-based concept. The reduction compared to a standard integration of wind power and **GT** is limited to around 70 kt (i.e. 3% reduction). The emissions reductions achievable might be constrained by technological limitations.
- The optimizer generally selected the larger gas turbine (LM6000) as the best compromise for simultaneously constraining emissions and the hydrogen storage size.
- Relatively small fuel cell stacks (a maximum of 3 MW in the reference case) were obtained for the optimal designs. This might indicate that the fuel cell stack is designed to constrain the storage size and further

increases are not advantageous for curbing emissions. It is rather preferable to increase the amount of hydrogen used in the gas turbine, than reconverting the storage into electricity.

- The wind dataset selected for the analysis has a strong influence on the results.' An alternative dataset resulted in a performance improvement of the HES-OFFs system, with a increase of emissions savings of 10%. This source of uncertainty must be properly addressed in the design of HES-OFFs.
- The designs targeting the minimum possible  $CO_2$  emissions might be critical in terms of electric grid stability and, accordingly, should be screened out by the short-term analysis.

Finally, it is worth highlighting that the two types of analyses allowed by the integrated model – long-term and short-term – were successfully included in the optimization problem. This is an innovative approach for the design of a HES-OFF where the optimizer is evaluating simultaneously the performance in terms of process metrics (energy efficiency,  $CO_2$  emissions etc.) as well as the robustness of the proposed solution to electrical transients and security of power supply.

#### CONFLICT OF INTEREST STATEMENT

The authors declare that the research was conducted in the absence of any commercial or financial relationships that could be construed as a potential conflict of interest.

#### FUNDING

This research was funded by the Research Council of Norway under the program PETROMAKS2, grant number 281986, project “Innovative Hybrid Energy System for Stable Power and Heat Supply in Offshore Oil & Gas Installation (HES-OFF)”.

## 6.5 REFERENCES

- [1] Trude Melby Bothner, Eirik Knutsen, and Mona Irene Andersen Engedal. Emissions to air, 2019. Technical report Statistics Norway Oslo, Norway (June 2020). URL <https://www.ssb.no/en/natur-og-miljo/statistikker/klimagassn/aar/2020-06-08>. Cited on p. 68.

- [2] Konkraft. The Energy Industry Of Tomorrow On The Norwegian Continental Shelf: Climate Strategy Towards 2030 and 2050. Technical Report 2020-1 Konkraft (February 2020). URL <https://konkraft.no/wp-content/uploads/2020/02/The-energy-industry-on-the-NCS.-climate-strategy-towards-2030-and-2050.pdf>. Cited on p. 68.
- [3] Tuong-Van Nguyen, Yuri M. Barbosa, Julio A.M. da Silva, and Silvio de Oliveira Junior. A novel methodology for the design and optimisation of oil and gas offshore platforms. *Energy* **185**, 158–175 (October 2019). ISSN 03605442. doi: 10.1016/j.energy.2019.06.164. Cited on p. 69.
- [4] Tuong-Van Nguyen, Mari Voldsund, Peter Breuhaus, and Brian Elmegaard. Energy efficiency measures for offshore oil and gas platforms. *Energy* **117**, 325–340 (December 2016). ISSN 03605442. doi: 10.1016/j.energy.2016.03.061. Cited on p. 69.
- [5] S. Roussanaly, *et al.* Offshore power generation with carbon capture and storage to decarbonise mainland electricity and offshore oil and gas installations: A techno-economic analysis. *Applied Energy* **233–234**, 478–494 (January 2019). ISSN 03062619. doi: 10.1016/j.apenergy.2018.10.020. Cited on p. 69.
- [6] Luca Riboldi, Steve Völler, Magnus Korpås, and Lars O. Nord. An Integrated Assessment of the Environmental and Economic Impact of Offshore Oil Platform Electrification. *Energies* **12** (11), 2114 (June 2019). ISSN 1996-1073. doi: 10.3390/en12112114. Cited on p. 69, 74.
- [7] Yosoon Choi, Chaeyoung Lee, and Jinyoung Song. Review of Renewable Energy Technologies Utilized in the Oil and Gas Industry. *International Journal of Renewable Energy Research* (v7i2) (2017). ISSN 13090127. doi: 10.20508/ijrer.v7i2.5460.g7034. Cited on p. 69.
- [8] K Mundheim. Monotower Production Platforms With Renewable Energy. In *Proceedings of the Offshore Mediterranean Conference and Exhibition* page 12 Ravenna, Italy (March 2007). OnePetro. ISBN 978-88-940436-2-4. Cited on p. 69.
- [9] Jamie Stewart MacDonald. Providing Scope for Reducing the Carbon Footprint of an Offshore Oil Rig. *Master's thesis*. Strathclyde Glasgow, UK (June 2014). URL [https://www.esru.strath.ac.uk/Documents/MSc\\_2014/MacDonald.pdf](https://www.esru.strath.ac.uk/Documents/MSc_2014/MacDonald.pdf). Cited on p. 69.
- [10] Jan Erik Hanssen, *et al.* Design and performance validation of a hybrid offshore renewable energy platform. In *2015 Tenth International Conference on Ecological Vehicles and Renewable Energies (EVER)* pages 1–8 Monte Carlo (March 2015). IEEE. ISBN 978-1-4673-6785-1. doi: 10.1109/EVER.2015.7113017. Cited on p. 69.
- [11] Ahmad Rafiee and Kaveh Rajab Khalilpour. Renewable Hybridization of Oil and Gas Supply Chains. In *Polygeneration with Polystorage for Chemical and Energy Hubs* pages 331–372. Elsevier (2019). ISBN 978-0-12-813306-4. doi: 10.1016/B978-0-12-813306-4.00011-2. Cited on p. 69.
- [12] Wei He, Gunnar Jacobsen, Tiit Anderson, Freydar Olsen, Tor D. Hanson, Magnus Korpås, Trond Toftevaag, Jarle Eek, Kjetil Uhlen, and Emil Johansson. The Potential of Integrating Wind Power with Offshore Oil and Gas Platforms. *Wind Engineering* **34** (2), 125–137 (March 2010). doi: 10.1260/0309-524X.34.2.125. Cited on p. 69.
- [13] Irati Legorburu, Kate R. Johnson, and Sandy A. Kerr. Multi-use maritime platforms - North Sea oil and offshore wind: Opportunity and risk. *Ocean & Coastal Management* **160**, 75–85 (June 2018). ISSN 09645691. doi: 10.1016/j.ocecoaman.2018.03.044. Cited on p. 69.
- [14] Magnus Korpås, Leif Warland, Wei He, and John Olav Giæver Tande. A Case-Study on Offshore Wind Power Supply to Oil and Gas Rigs. *Energy Procedia* **24**, 18–26 (2012). doi: 10.1016/j.egypro.2012.06.082. Cited on p. 70, 76.
- [15] Valentina Orlandini, Leonardo Pierobon, Signe Schløer, Andrea De Pascale, and Fredrik Haglind. Dynamic performance of a novel offshore power system integrated with a wind farm. *Energy* **109**, 236–247 (August 2016). ISSN 03605442. doi: 10.1016/j.energy.2016.04.073. Cited on p. 70.

- [16] Santiago Sanchez, Elisabetta Tedeschi, Jesus Silva, Muhammad Jafar, and Alexandra Marichalar. Smart load management of water injection systems in offshore oil and gas platforms integrating wind power. *IET Renewable Power Generation* **11** (9), 1153–1162 (July 2017). ISSN 1752-1416, 1752-1424. doi: 10.1049/iet-rpg.2016.0989. Cited on p. 70, 78.
- [17] Luca Riboldi and Lars Nord. Offshore Power Plants Integrating a Wind Farm: Design Optimisation and Techno-Economic Assessment Based on Surrogate Modelling. *Processes* **6** (12), 249 (December 2018). ISSN 2227-9717. doi: 10.3390/pr6120249. Cited on p. 70, 76.
- [18] Erick Alves, Santiago Sanchez, Danilo Brandao, and Elisabetta Tedeschi. Smart Load Management with Energy Storage for Power Quality Enhancement in Wind-Powered Oil and Gas Applications. *Energies* **12** (15), 2985 (August 2019). ISSN 1996-1073. doi: 10.3390/en12152985. Cited on p. 70, 78.
- [19] Milton Korn, Shilpa Mesineni, and Weiguang Hu. Offshore Powering with a Closed Loop and Bus: Coupling Energy Storage for Maritime Electrical Networks. *IEEE Industry Applications Magazine* **24** (5), 43–51 (September 2018). ISSN 1077-2618, 1558-0598. doi: 10.1109/MIAS.2017.2740443. Cited on p. 70.
- [20] Andrew J. Pimm, Seamus D. Garvey, and Maxim de Jong. Design and testing of Energy Bags for underwater compressed air energy storage. *Energy* **66**, 496–508 (March 2014). ISSN 03605442. doi: 10.1016/j.energy.2013.12.010. Cited on p. 73.
- [21] Olaf Kruck, Fritz Crotogino, Ruth Prelicz, and Tobias Rudolph. Overview on all Known Underground Storage Technologies for Hydrogen. Technical Report 303417-D3.1 Project HyUnder (August 2013). URL [http://www.hyunder.eu/wp-content/uploads/2016/01/D3.1\\_Overview-of-all-known-underground-storage-technologies.pdf](http://www.hyunder.eu/wp-content/uploads/2016/01/D3.1_Overview-of-all-known-underground-storage-technologies.pdf). Cited on p. 73.
- [22] Dr Jeffrey Goldmeer. Power to Gas: Hydrogen for Power Generation - Fuel Flexible Gas Turbines as Enablers for a Low or Reduced Carbon Energy Ecosystem (February 2019). URL [https://www.ge.com/content/dam/gepower/global/en\\_US/documents/fuel-flexibility/GEA33861%20Power%20to%20Gas%20-%20Hydrogen%20for%20Power%20Generation.pdf](https://www.ge.com/content/dam/gepower/global/en_US/documents/fuel-flexibility/GEA33861%20Power%20to%20Gas%20-%20Hydrogen%20for%20Power%20Generation.pdf). Cited on p. 74.
- [23] Paolo Chiesa, Giovanni Lozza, and Luigi Mazzocchi. Using Hydrogen as Gas Turbine Fuel. *Journal of Engineering for Gas Turbines and Power* **127** (1), 73–80 (January 2005). ISSN 0742-4795, 1528-8919. doi: 10.1115/1.1787513. Cited on p. 74.
- [24] Luca Riboldi and Lars O. Nord. Concepts for lifetime efficient supply of power and heat to offshore installations in the North Sea. *Energy Conversion and Management* **148**, 860–875 (September 2017). ISSN 01968904. doi: 10.1016/j.enconman.2017.06.048. Cited on p. 74, 81.
- [25] Colleen Spiegel. PEM fuel cell modeling and simulation using Matlab. Academic Press Amsterdam first edition (2008). ISBN 978-0-12-374259-9. URL <https://www.elsevier.com/books/pem-fuel-cell-modeling-and-simulation-using-matlab/spiegel/978-0-12-374259-9>. Cited on p. 75.
- [26] PowerCell. PowerCell S3 Product Datasheet (December 2018). URL <https://www.powercell.se/wordpress/wp-content/uploads/2018/12/S3-Produktblad-190430.pdf>. Cited on p. 75.
- [27] Houcheng Zhang, Shanhe Su, Guoxing Lin, and Jincan Chen. Efficiency Calculation and Configuration Design of a PEM Electrolyzer System for Hydrogen Production. *Int. J. Electrochem. Sci.* **7**, 4143–4157 (2012). URL <http://www.electrochemsci.org/papers/vol7/7054143.pdf>. Cited on p. 75.
- [28] NEL Hydrogen. M Series Containerized Datasheet. Technical Report PD-0600-0136 NEL Hydrogen (March 2020). URL <https://nelhydrogen.com/wp-content/uploads/2020/03/M-Series-Containerized-Spec-Sheet-Rev-B.pdf>. Cited on p. 75.
- [29] Erik Berge, Øyvind Byrkjedal, Yngve Ydersbond, and Detlef Kindler. Modelling of offshore wind resources. Comparison of a meso- scale model and measurements from FINO 1

- and North Sea oil rigs. In European Wind Energy Association, editor, *Proceedings of EWEC 2009* volume 4 pages 2327–34 Marseille, France (March 2009). Curran Associates, Inc. ISBN 978-1-61567-746-7. URL <https://pdfs.semanticscholar.org/7889/5f8949019e013143927bab369b0db2c7afc1.pdf>. Cited on p. 76.
- [30] Iain Staffell and Stefan Pfenninger. Using bias-corrected reanalysis to simulate current and future wind power output. *Energy* **114**, 1224–1239 (November 2016). ISSN 03605442. doi: 10.1016/j.energy.2016.08.068. Cited on p. 76.
- [31] Ronald Gelaro, *et al.* The Modern-Era Retrospective Analysis for Research and Applications, Version 2 (MERRA-2). *Journal of Climate* **30** (14), 5419–5454 (July 2017). ISSN 0894-8755, 1520-0442. doi: 10.1175/JCLI-D-16-0758.1. Cited on p. 76.
- [32] Prabha Kundur, *et al.* Definition and Classification of Power System Stability. *IEEE Transactions on Power Systems* **19** (3), 1387–1401 (August 2004). ISSN 0885-8950. doi: 10.1109/TPWRS.2004.825981. Cited on p. 77.
- [33] R. Fadaeinedjad, G. Moschopoulos, and M. Moallem. The Impact of Tower Shadow, Yaw Error, and Wind Shears on Power Quality in a Wind–Diesel System. *IEEE Transactions on Energy Conversion* **24** (1), 102–111 (March 2009). ISSN 0885-8969. doi: 10.1109/TEC.2008.2008941. Cited on p. 77.
- [34] A. Honrubia-Escribano, E. Gómez-Lázaro, A. Molina-García, and J.A. Fuentes. Influence of voltage dips on industrial equipment: Analysis and assessment. *International Journal of Electrical Power & Energy Systems* **41** (1), 87–95 (October 2012). ISSN 01420615. doi: 10.1016/j.ijepes.2012.03.018. Cited on p. 77.
- [35] Xiaodong Liang. Emerging Power Quality Challenges Due to Integration of Renewable Energy Sources. *IEEE Transactions on Industry Applications* **53** (2), 855–866 (March 2017). ISSN 0093-9994, 1939-9367. doi: 10.1109/TIA.2016.2626253. Cited on p. 77.
- [36] International Electrotechnical Commission. IEC 61400-3:2019 Wind energy generation systems - Part 3: Design requirements for floating offshore wind turbines. International Electrotechnical Commission Geneva, Switzerland (2019). URL <https://webstore.iec.ch/publication/29360>. Cited on p. 78.
- [37] Mark Kelly. From standard wind measurements to spectral characterization: Turbulence length scale and distribution. *Wind Energy Science* **3** (2), 533–543 (August 2018). ISSN 2366-7451. doi: 10.5194/wes-3-533-2018. Cited on p. 78.
- [38] Atle Rygg Årdal, Tore Undeland, and Kamran Sharifabadi. Voltage and Frequency Control in Offshore Wind Turbines Connected to Isolated Oil Platform Power Systems. *Energy Procedia* **24**, 229–236 (2012). ISSN 18766102. doi: 10.1016/j.egypro.2012.06.104. Cited on p. 78.
- [39] IEC 61892:2015 Mobile and fixed offshore units - Electrical installations. IEC Geneva, Switzerland 3.0 edition (July 2015). URL <https://webstore.iec.ch/publication/6083>. Cited on p. 79.
- [40] MathWorks. Global Optimization Toolbox. Technical report (2020). URL <https://se.mathworks.com/products/global-optimization.html>. Cited on p. 81.
- [41] Luca Riboldi, Erick F Alves, Marcin Pilarczyk, Elisabetta Tedeschi, and Lars O. Nord. Innovative hybrid energy system for stable power and heat supply in offshore oil & gas installation (HES-OFF): System design and grid stability. In *Proceedings of the 30th European Symposium on Computer Aided Process Engineering (ESCAPE30)* volume A pages 211–216 Milano, Italy (May 2020). Elsevier. doi: 10.1016/B978-0-12-823377-1.50036-7. Cited on p. 82.
- [42] Niamh Troy, Damian Flynn, Michael Milligan, and Mark O’Malley. Unit Commitment With Dynamic Cycling Costs. *IEEE Transactions on Power Systems* **27** (4), 2196–2205 (November 2012). ISSN 0885-8950, 1558-0679. doi: 10.1109/TPWRS.2012.2192141. Cited on p. 86.







## CHAPTER 7

### *Sufficient conditions for robust frequency stability of isolated ac power systems*

---

Erick Alves<sup>1</sup>, Gilbert Bergna-Diaz<sup>1</sup>, Danilo Brandao<sup>2</sup>, and Elisabetta Tedeschi<sup>1,3</sup>

Journal paper published in: *IEEE Transactions on Power Systems* **36** (3), 2684–2692 (May 2021).

DOI: [10.1109/TPWRS.2020.3039832](https://doi.org/10.1109/TPWRS.2020.3039832)



**Open Access** This work is licensed under a Creative Commons Attribution 4.0 International License. It means that unrestricted use, sharing, adaptation, distribution, and reproduction in any medium or format are allowed, as long as the original author(s) and the source are appropriately credited, a link to the Creative Commons license is provided, and any changes made are indicated. To view a copy of this license, please visit <http://creativecommons.org/licenses/by/4.0/>.

© Alves, Bergna-Diaz, Brandao and Tedeschi, 2021.

#### **Author Contributions**

Conceptualization, E.A. and G.B.; methodology, E.A. and G.B.; software, E.A.; validation, E.A.; formal analysis, E.A. and G.B.; investigation, E.A. and G.B.; resources, E.T.; data curation, E.A.; writing - original draft preparation, E.A.; writing - review and editing, G.B., D.B. and E.T.; visualization, E.A.; supervision, G.B., D.B. and E.T.; project administration, E.T.; funding acquisition, E.T.

---

<sup>1</sup>Department of Electric Power Engineering, NTNU, 7034 Trondheim, Norway.

<sup>2</sup>Graduate Program in Electrical Engineering, UFMG, 31270-901 Belo Horizonte, Brazil.

<sup>3</sup>Department of Industrial Engineering, University of Trento, 38123 Trento, Italy.

## ABSTRACT

This paper analyses the frequency stability of ac grids in the presence of non-dispatchable generation and stochastic loads. Its main goal is to evaluate conditions in which the system is robust to large, persistent active power disturbances without recurring to time-domain simulations. Considering the ongoing energy transition to more renewable sources, defining robustness boundaries is a key topic for power system planning and operation. However, much of the research on long-term studies has not dealt with robust dynamic constraints, while short-term analyses usually depend on time-consuming simulations to evaluate nonlinearities. To bridge this gap, the authors derive an algebraic equation that provides sufficient conditions for robust frequency stability in ac power systems and a relationship among four key quantities: the maximum active power perturbation, the minimum system damping, the steady-state and the transient frequency limits. To achieve this goal, it uses a nonlinear average-model of the ac grid and Lyapunov's direct method extended by perturbation analysis requiring only limited knowledge of the system parameters. The algebraic calculations are validated using time-domain simulations of the IEEE 39-bus test system and results are compared to the traditional Swing Equation model.

## 7.1 INTRODUCTION

Any modern society requires an energy system that is affordable, accessible, secure and sustainable. However, recent technological advancements and social changes have been challenging the limits of this balance and pushing for a complete rethinking of energy systems. Electric power generation is now: 1) becoming more decentralized; 2) taking place closer to final users; 3) undergoing a technological transformation that comprehends more diversified primary sources, new forms of energy storage and power electronics [1, 2].

In this new paradigm, planning and operation of electrical ac grids are becoming more involved. For instance, conversion from primary sources and storage is performed using not only synchronous machines but also converter-interfaced generators. The latter can supply up to 50% of the annual demand and 100% of the hourly demand in places such as Colorado, Denmark, Hawai'i, Ireland, Tasmania, Texas and South Australia [3, 4]. This introduces new dynamics into the electric power system that are "yet to be fully understood" [5] and blurry the boundaries to which well-established models can be applied [6].

Moreover, groups of interconnected loads and distributed energy resources,

also known as microgrids [7, 8], can form islands and operate independently from the bulk power system. However, this desired feature is only achieved when primary sources, storage units, power converters and control systems are properly planned, designed and operated.

From this perspective, one of the main challenges is defining sufficient conditions for stable operation of low-inertia systems in islanded mode [2]. Stability here is seen in the sense of system states remaining within acceptable ranges for given changes in inputs, i.e. input-to-state stability. In recent years, this topic has been an active area of research and references [5, 9] present extensive reviews on it. Providing proper models and clear stability criteria is essential for tasks, such as: 1) setting proper controller gains [10, 11]; 2) establishing technical constraints for dispatching [12]; 3) deciding about load shedding or generation curtailment [13].

Specifically, guaranteeing frequency stability of low-inertia systems can be a major challenge and requires proper sizing of dispatchable power sources and energy storage. Nevertheless, an inspection of recent literature reviews on ac microgrid planning [14, 15] shows that conditions for frequency stability are largely overlooked in the problem formulation. Specifically, most optimization algorithms assume that matching power demand with production is the only required dynamic constraint, without imposing minimum requirements on system damping or FCR. While such results may be optimal from the affordability point of view, they could be questionable from the security aspect and may be operationally unfeasible.

On the other hand, an inspection of the literature reveals that methods for designing low-inertia power systems in the presence of stochastic loads and non-dispatchable generation considering frequency stability constraints have been proposed lately. Some time ago, [16] introduced a method to optimally size and operate an energy storage system that provides FCR in an isolated power system with wind, hydraulic, gas turbines and stochastic loads. Results were validated using a dynamic model in Matlab Simulink. In addition, [17] demonstrated how a fast-acting energy storage can increase the frequency stability of the Guadalupe archipelago in the Caribbean and reduce the actuation of automatic load shedding using power-hardware-in-the-loop simulations. In [18], the authors also used time-domain simulations to study how the size and controller settings of an energy storage based on ultracapacitors impacted the frequency stability and the performance of the automatic load shedding scheme in the isolated power system of La Palma, Spain. Later, the same authors extended this work with field-tests results in [19]. Not least, [20] solved the unit commitment problem including FCR constraints for an isolated power system using mixed-integer linear programming. For that, it determined the minimum system damping empirically relying on the load-frequency sensitivity index. Moreover,

frequency stability constraints have been proposed in planning and operation studies, such as optimal power flow problems [21–24].

Note that, in the different approaches discussed above, there is a heavy reliance on time-domain simulations and/or model linearization to establish key boundaries for frequency stability. Time-domain simulations provide the most accurate results but are hard to integrate in optimization problems such as optimum power flow, while linearizations around an operation point do not give realistic values for frequency deviations during large active power disturbances. Taking into account this background, the main contribution of this paper is the derivation of sufficient conditions for frequency stability of an ac power system where sources and loads are subject to non-vanishing, bounded perturbations. Using a nonlinear average-model of the ac grid, Lyapunov’s direct method and perturbation analysis, an algebraic equation is derived and provides a relationship among four boundaries: the maximum active power disturbance, the minimum system damping, the steady-state and the transient frequency limits. The main goal is providing a framework to implement frequency stability constraints in optimization algorithms without recurring to time-consuming simulations or unnecessary linearizations of the power balance equations.

The text is organized as follows: [Sec. 7.2](#) introduces a nonlinear, average model of the ac grid that is appropriate for frequency stability analysis during large active power disturbances; [Sec. 7.3](#) presents the main proposition of this work followed by its mathematical proof; [Sec. 7.4](#) validates the proposition using time-domain simulations of the IEEE 39-bus test system [25] and compares its results to the linear Swing Equation model; [Sec. 7.5](#) discusses applications of the proposition, its main limitations and directions for future research; finally, [Sec. 7.6](#) presents the concluding remarks.

## 7.2 NONLINEAR AVERAGE MODEL OF AN AC POWER SYSTEM

When omitting network topology and voltage dynamics, the average behavior of an ac grid angular speed can be modeled using first principles as an equivalent rotating mass using Newton’s second law of motion [5, 26]:

$$J\dot{\omega} = T_S(t, \omega) - T_L(t, \omega) - B(t)(\omega - \omega_s) \quad (7.1)$$

where  $J$  is the equivalent moment of inertia [ $\text{kg m}^2$ ] of the system and  $B(t)$  is a time-varying function representing the equivalent damping coefficient [ $\text{N m s rad}^{-1}$ ] of the system;  $T_S(t, \omega)$  and  $T_L(t, \omega)$  are the equivalent torques from sources and loads [ $\text{N m}$ ], functions of the time  $t$  [ $\text{s}$ ] and the center of inertia angular speed  $\omega$  [ $\text{rad s}^{-1}$ ];  $\omega_s$  is a constant representing the synchronous angular speed [ $\text{rad s}^{-1}$ ].

**Proposition 1.** *The nonlinear system in Eq. (7.1) can be expressed as:*

$$\dot{\tilde{x}} = f(t, \tilde{x}) + g(t, \tilde{x})$$

where  $\tilde{x}$  is the state variable of the system,  $f(t, \tilde{x})$  is piecewise continuous in  $t$  and represents the dynamics of the system,  $g(t, \tilde{x})$  is a perturbation term that results from uncertainties and disturbances.

*Proof.* Eq. (7.1) can be rearranged into the desired form when multiplying it by  $\omega$  and normalizing it with the system base power ( $S_b$ ) [W]:

$$\begin{aligned} \omega J \dot{\omega} &= \omega T_S(t, \omega) - \omega T_L(t, \omega) - \omega B(t)(\omega - \omega_s) \\ &= P_S(t, \omega) - P_L(t, \omega) - \omega B(t)(\omega - \omega_s) \\ \frac{\omega J}{S_b} \dot{\omega} &= \frac{P_S(t, \omega)}{S_b} - \frac{P_L(t, \omega)}{S_b} - \omega \frac{B(t)(\omega - \omega_s)}{S_b} \\ xM\dot{x} &= u(t, x) - w(t, x) - xD(t)(x - 1) \\ \dot{x} &= -\frac{D(t)}{M}(x - 1) + \frac{u(t, x) - w(t, x)}{xM} \\ \dot{\tilde{x}} &= \underbrace{-\frac{D(t)}{M}\tilde{x}}_{f(t, \tilde{x})} + \underbrace{\frac{u(t, \tilde{x}) - w(t, \tilde{x})}{(\tilde{x} + 1)M}}_{g(t, \tilde{x})} \end{aligned} \quad (7.2)$$

where  $x = \frac{\omega}{\omega_s}$  and  $\tilde{x} = x - 1$  are the normalized center of inertia angular speed and the center of inertia angular speed deviation from the synchronous speed [pu];  $M = \frac{J\omega_s^2}{S_b}$  and  $D(t) = \frac{B(t)\omega_s^2}{S_b}$  are the normalized equivalent moment of inertia [s] and damping coefficient [pu];  $P_S(t, \omega)$  and  $P_L(t, \omega)$  are the total active power from sources and loads [W];  $u(t, \tilde{x})$  and  $w(t, \tilde{x})$  are the normalized total active power from sources and loads [pu]. ■

### 7.3 SUFFICIENT CONDITIONS FOR ROBUST FREQUENCY STABILITY

This section introduces the main proposition of this paper, which is an algebraic expression relating four key boundaries in an ac power system: the maximum active power disturbance  $\|u(t, \tilde{x}) - w(t, \tilde{x})\| < P_b$  [pu], the minimum system damping  $D_{min}$  [pu], the steady-state  $r_{ss}$  and the transient  $r_{tr}$  frequency limits [pu]. Once three of these boundaries are set, the fourth can be unequivocally defined. While the involved mathematical proof of this proposition is presented in detail below, there will be no loss of understanding by proceeding directly to Eq. (7.4), which summarizes the relationship between these quantities.

**Proposition 2.** Let  $\|u(t, \tilde{x}) - w(t, \tilde{x})\| < P_b$  be the maximum active power disturbance of the system defined in Eq. (7.2) in which  $M$  is a positive constant,  $D(t)$  is piecewise continuous in the time  $t$  and lower-bounded by a positive constant  $D_{min}$ .

If  $P_b = D_{min}r_{ss}(1 - r_{tr})$ ,  $\forall t \geq 0$ ,  $\tilde{x} \in \mathbb{D} = \{\tilde{x} \in \mathbb{R} \mid \|\tilde{x}\| \leq r_{tr}, 0 < r_{tr} < 1\}$  where  $r_{tr}, r_{ss}$  are the maximum allowed values of  $\tilde{x}$  during the transient and steady-state periods, respectively.

Then, for all  $\|\tilde{x}(t_0)\| < r_{ss}$  and  $r_{ss} < r_{tr}$ , the solution  $\tilde{x}$  of Eq. (7.2) satisfies

$$\begin{aligned} \|\tilde{x}\| &\leq \exp[-\gamma(t - t_0)]r_{tr}, \quad t_0 \leq t < t_0 + T \\ \|\tilde{x}\| &\leq r_{ss}, \quad \forall t \geq t_0 + T \end{aligned}$$

for  $\gamma = (1 - \frac{r_{ss}}{r_{tr}})\frac{D_{min}}{M}$  and some finite  $T$  that represents the duration of the transient period.

*Proof.* Let  $\mathcal{V}(\tilde{x}) = \frac{M}{2}\tilde{x}^2$  be an input-to-state Lyapunov function candidate for the system in Eq. (7.2). Note that  $\mathcal{V}(\tilde{x})$  is: 1) a piecewise, continuous differentiable function on  $\mathbb{R}$ ; 2) class  $\mathcal{K}_\infty$  according to definition 4.2 in [27]; 3) upper- and lower-bounded by  $\frac{M}{2}\|\tilde{x}\|^2$ . Moreover, its time derivative is given by:

$$\begin{aligned} \dot{\mathcal{V}}(t, \tilde{x}) &= \tilde{x}^\top M \dot{\tilde{x}} \\ &= -D(t)\tilde{x}^2 + \frac{\tilde{x}}{\tilde{x} + 1}(u(t, \tilde{x}) - w(t, \tilde{x})) \end{aligned} \quad (7.3)$$

Assuming that  $\tilde{x} \in \mathbb{D}$  and using the Cauchy-Schwarz's inequality, it holds that:

$$\begin{aligned} \dot{\mathcal{V}}(t, \tilde{x}) &\leq -D_{min}\|\tilde{x}\|^2 + \frac{\|\tilde{x}\|}{1 - r_{tr}}(\|u(t, \tilde{x}) - w(t, \tilde{x})\|) \\ &\leq -D_{min}(1 - \theta)\|\tilde{x}\|^2 \\ &\quad - \|\tilde{x}\| \left( D_{min}\theta\|\tilde{x}\| - \frac{\|u(t, \tilde{x}) - w(t, \tilde{x})\|}{1 - r_{tr}} \right) \\ &\leq -W_3(\tilde{x}), \quad \forall \|\tilde{x}\| \geq \rho(\|u(t, \tilde{x}) - w(t, \tilde{x})\|) > 0 \end{aligned}$$

where  $0 < \theta < 1$ ,  $D_{min} > 0$ ,  $W_3(\tilde{x}) = D_{min}(1 - \theta)\|\tilde{x}\|^2$  and  $\rho(\|z\|) = \frac{\|z\|}{(1 - r_{tr})D_{min}\theta}$ .

As  $W_3(\tilde{x})$  is a continuous positive definite function on  $\mathbb{R}$  and  $\rho(\|z\|)$  is class  $\mathcal{K}$ , all conditions of the input-to-state theorem in Appendix 7.9 are fulfilled. Hence, the system defined in Eq. (7.2) is input-to-state stable on  $\mathbb{D}$ .

Now, let us analyze the unforced system, i.e. the case where  $\|u(t, \tilde{x}) -$



$w(t, \tilde{x})\| = 0$ . The inequalities:

$$\begin{aligned} c_1 \|\tilde{x}\|^2 &\leq \mathcal{V}(t, \tilde{x}) \leq c_2 \|\tilde{x}\|^2 \\ \dot{\mathcal{V}}(t, \tilde{x}) &\leq -c_3 \|\tilde{x}\|^2 \\ \left\| \frac{\delta \mathcal{V}}{\delta \tilde{x}} \right\| &\leq c_4 \|\tilde{x}\| \end{aligned}$$

are derived directly from Eq. (7.3) and the assumptions in Proposition 2 where  $c_1 = c_2 = \frac{M}{2}$ ,  $c_3 = D_{min}$ ,  $c_4 = M$  are positive constants. These are valid for all  $(t, x) \in [0, \infty) \times \mathbb{D}$ . Consequently, the unforced system fulfills all conditions from Theorem 4.10 in [27] and  $\tilde{x} = 0$  is exponentially stable on  $\mathbb{D}$ .

With the previous results, it is possible to apply lemma 9.2 in [27]. In this context, when assuming that:

1.  $g(t, \tilde{x}) = \frac{u(t, \tilde{x}) - w(t, \tilde{x})}{(\tilde{x} + 1)M}$  is the perturbation term of the system in Eq. (7.2)
2.  $\|\tilde{x}(t)\|$  must be bounded by  $r_{ss}$ , i.e.  $b = \frac{c_4}{c_3} \sqrt{\frac{c_2}{c_1}} \frac{\delta}{\theta} = r_{ss}$
3.  $r_{ss} = r_{tr} \theta$

it follows that:

$$\begin{aligned} \|g(t, \tilde{x})\| &\leq \delta < \frac{c_3}{c_4} \sqrt{\frac{c_1}{c_2}} r_{tr} \theta \\ \left\| \frac{u(t, \tilde{x}) - w(t, \tilde{x})}{M(\tilde{x} + 1)} \right\| &< \frac{D_{min}}{M} r_{tr} \theta \\ \frac{\|u(t, \tilde{x}) - w(t, \tilde{x})\|}{M \|\tilde{x} + 1\|} &< \frac{D_{min}}{M} r_{ss} \\ \|u(t, \tilde{x}) - w(t, \tilde{x})\| &< \underbrace{D_{min} r_{ss} (1 - r_{tr})}_{P_b} \end{aligned}$$

for all  $t \geq 0$ , all  $\tilde{x} \in \mathbb{D}$  and  $0 < r_{ss} < r_{tr}$ .

Hence, if the maximum active power disturbance satisfies the upper-bound:

$$P_b = D_{min} r_{ss} (1 - r_{tr}) \quad (7.4)$$

Then, for all  $\|\tilde{x}(t_0)\| < r_{ss}$  and for some finite  $T$ , the solution  $\tilde{x}(t)$  of Eq. (7.2) satisfies:

$$\begin{aligned} \|\tilde{x}\| &\leq \exp[-\gamma(t - t_0)] r_{tr}, \quad t_0 \leq t < t_0 + T \\ \|\tilde{x}\| &\leq r_{ss}, \quad \forall t \geq t_0 + T \end{aligned}$$

where the minimum convergence rate of  $\|\tilde{x}\|$  is:

$$\gamma = \left(1 - \frac{r_{ss}}{r_{tr}}\right) \frac{D_{min}}{M} \quad (7.5)$$

In summary, the steps of the proof are the following:

1. Show that the system in Eq. (7.2) is input-to-state stable on  $\mathbb{D}$  using the input-to-state theorem in Appendix 7.9.
  - Use  $\mathcal{V}(\tilde{x}) = \frac{M}{2}\tilde{x}^2$  as Lyapunov function candidate.
  - Use the Cauchy-Schwarz's inequality to show that  $\frac{1}{\|\tilde{x}+1\|} \leq \frac{1}{1-r_{tr}}$  when  $\tilde{x} \in \mathbb{D}$ .
2. Using Theorem 4.10 in [27], show that  $\tilde{x} = 0$  is an exponentially stable equilibrium point of the unforced system, i.e.  $g(t, \tilde{x}) = 0$  in Eq. (7.2).
3. Apply Lemma 9.2 in [27] assuming that:
  - $g(t, \tilde{x}) = \frac{u(t, \tilde{x}) - w(t, \tilde{x})}{(\tilde{x}+1)M}$  is the perturbation term of the system in Eq. (7.2)
  - The state must be bounded by  $r_{ss}$ , i.e.  $b = \frac{c_d}{c_3} \sqrt{\frac{c_2}{c_1} \frac{\delta}{\theta}} = r_{ss}$
  - $r_{ss} = r_{tr}\theta$

■

**Remark 2.1.** The time intervals from Proposition 2 can be divided in:

- $t < t_0$  is the steady-state period before the active power disturbance  $\|u(t, \tilde{x}) - w(t, \tilde{x})\| < P_b$  appears at  $t = t_0$ . The system is in an equilibrium point  $\tilde{x}(t_0)$  whose norm is upper-bounded by  $r_{ss}$ .
- $t_0 \leq t < t_0 + T$  is the transient period after the active power disturbance is applied to the system at  $t = t_0$  in which the state norm  $\|\tilde{x}(t)\|$  is upper-bounded by  $\exp[-\gamma(t - t_0)]r_{tr}$ , where  $\gamma = \left(1 - \frac{r_{ss}}{r_{tr}}\right) \frac{D_{min}}{M}$  is the minimum convergence rate from  $\tilde{x}(t_0)$  to  $\tilde{x}(t_0 + T)$ .
- $t \geq t_0 + T$  is the steady-state period after the system settles down on the new equilibrium point  $\tilde{x}(t_0 + T)$ , whose norm is upper-bounded by  $r_{ss}$ .

**Remark 2.2.** The proof assumes that  $\tilde{x}$  always remains in  $\mathbb{D}$ . In other words, Proposition 2 is only valid when  $\tilde{x}$  lies between  $-r_{tr}$  and  $r_{tr}$ . Though, note that this is a reasonable assumption. In ac power systems, when  $\tilde{x} \notin \mathbb{D}$ , load shedding or generation curtailment will take place to reduce the power imbalance and bring it back to  $\mathbb{D}$ .

**Remark 2.3.** The inequality  $\frac{1}{\|\bar{x}+1\|} \leq \frac{1}{1-r_{tr}}$  and, hence, [Proposition 2](#) are valid when  $0 < r_{tr} < 1$ , i.e.  $0 < \omega < 2\omega_s$ . For most ac power systems, this is a reasonable assumption.

**Remark 2.4.** As seen in [Eq. \(7.5\)](#),  $\gamma$  and hence the maximum rate of change of frequency is dependent on  $D_{min}$  and  $M$ . However, the equilibrium point of the system is independent of  $M$ , as highlighted in [Eq. \(7.4\)](#). This statement is formally justified with an equilibrium analysis in [Appendix 7.7](#).

**Remark 2.5.** From a practical perspective,  $\theta = \frac{r_{ss}}{r_{tr}}$  is a safety margin. The closer to 1 its value is, the closer to marginal stability the system will be after an active power disturbance of amplitude  $P_b$ . When ignoring the term  $(1 - r_{tr})$ , [Eq. \(7.4\)](#) reduces to  $P_b = D_{min}r_{ss}$  which is the expression retrieved from the linear Swing Equation [[28](#), [29](#)].

**Remark 2.6.** In the problem formulation, time delays in actuators of primary frequency controllers are neglected. While they affect the dynamics of the system and important benchmarks such as the rate of change of frequency, the frequency nadir and zenith, time delays have no influence in the new equilibrium point of the system after a large active power disturbance. [Appendix 7.8](#) formally justifies this statement.

## 7.4 VALIDATION USING THE IEEE 39-BUS TEST SYSTEM

At first, the advantages of the proposed model over the linear Swing Equation model may not be obvious. Therefore, this section presents study cases of large active power disturbances in the IEEE 39-bus test system [[25](#)]. The aim is to compare results of rms time-domain simulations in DIgSILENT PowerFactory 2020 SP2 with algebraic calculations using [Eq. \(7.4\)](#) and the reference equation  $P_b = D_{min}r_{ss}$  derived from the linear Swing Equation model.

[Fig. 7.1](#) shows the single-line diagram of the IEEE 39-bus test system and [tables 7.1](#) and [7.2](#) introduce relevant system parameters used in the calculations. For all simulations and calculations presented herein,  $S_b = 100$  MW. Further details required to reproduce the results in this section are available in [[30](#)], which is an open data repository containing the model file and its thorough documentation including a description of modeling differences when compared to [[25](#)].

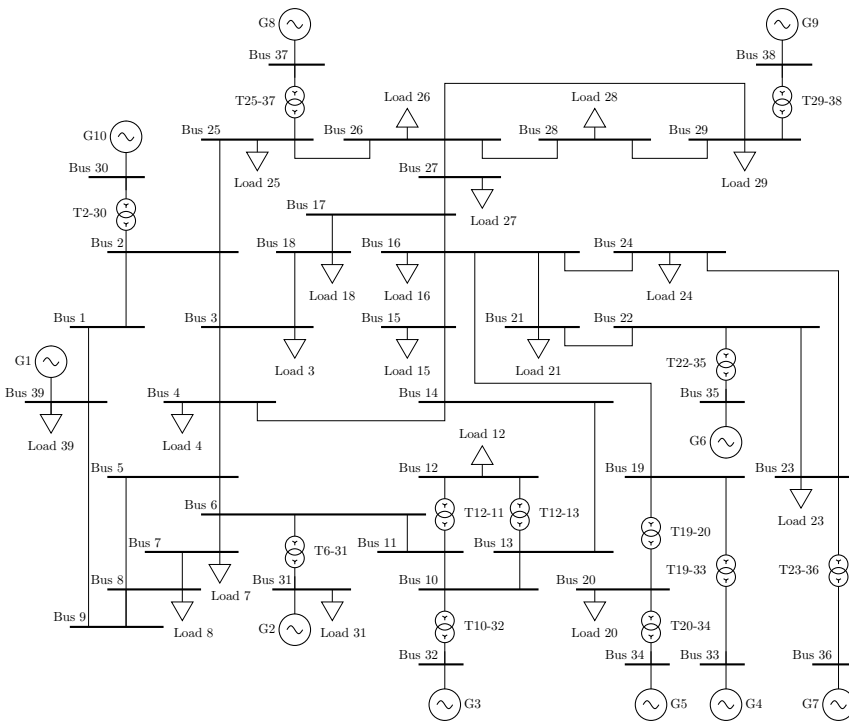


**FIGURE 7.1.** Single-line diagram of the IEEE 39-bus test system. © Erick Alves et al, 2021.

**TABLE 7.1.** Initial conditions of the study-case.

| Load     | Demand [MW] | Gen.      | Injection [MW] | Up-regulation capacity [MW] |
|----------|-------------|-----------|----------------|-----------------------------|
| 3        | 322         | 1         | 1000           | 0                           |
| 4        | 500         | (slack) 2 | 520.8          | 74.2                        |
| 7        | 233.8       | 3         | 650            | 30                          |
| 8        | 522         | 4         | 632            | 48                          |
| 12       | 7.5         | 5         | 508            | 2                           |
| 15       | 320         | 6         | 650            | 30                          |
| 16       | 329         | 7         | 560            | 35                          |
| 18       | 158         | 8         | 540            | 55                          |
| 20       | 628         | 9         | 830            | 20                          |
| 21       | 274         | 10        | 250            | 600                         |
| 23       | 247.5       | $\Sigma$  | 6140.8         | 894.2                       |
| 24       | 308.6       |           |                |                             |
| 25       | 224         |           |                |                             |
| 26       | 139         |           |                |                             |
| 27       | 281         |           |                |                             |
| 28       | 206         |           |                |                             |
| 29       | 283.5       |           |                |                             |
| 31       | 9.2         |           |                |                             |
| 39       | 1104        |           |                |                             |
| $\Sigma$ | 6097.1      |           |                |                             |

**TABLE 7.2.** Relevant data of each generator and its primary frequency controller when  $S_b = 100$  MW.

| Gen.     | Rated active power [MW] | D [pu] (gen. base) | D [pu] (sys. base) | M [s] (sys. base) |
|----------|-------------------------|--------------------|--------------------|-------------------|
| 1        | 1000                    | 0                  | 0                  | 500.0             |
| 2        | 595                     | 5                  | 29.75              | 30.3              |
| 3        | 680                     | 5                  | 34                 | 35.8              |
| 4        | 680                     | 5                  | 34                 | 28.6              |
| 5        | 510                     | 5                  | 25.5               | 26.0              |
| 6        | 680                     | 5                  | 34                 | 34.8              |
| 7        | 595                     | 5                  | 29.75              | 26.4              |
| 8        | 595                     | 5                  | 29.75              | 24.3              |
| 9        | 850                     | 5                  | 42.5               | 34.5              |
| 10       | 850                     | 25                 | 212.5              | 42.0              |
| $\Sigma$ |                         |                    | 471.75             | 782.7             |

### 7.4.1 Load Damping

The damping coefficient  $D$  introduced in Eq. (7.2) can be subdivided into:

$$D = D_L + \sum_i D_i \quad (7.6)$$

where  $D_L$  is the load damping and  $\sum_i D_i$  is the sum of the frequency droop of all primary frequency controllers. In real systems,  $D_L$  is typically defined either introducing active power disturbances or applying statistical methods such as system identification to historical data [20].

For the study case, the term  $\sum_i D_i = 471.75$  is directly retrieved from table 7.2. However, for the initial conditions shown in table 7.1, the up-regulation capacity of  $G5$  is extremely limited and this unit will saturate for very small net-load increases. Therefore, its damping is ignored, i.e.  $\sum_i D_i = 446.25$ , and  $G5$  is considered a constant active power source at rated capacity during a net-load increase. To maintain the energy balance, the up-regulation capacity of  $G5$  is subtracted from the active power disturbance for all calculations.

With the assumptions above,  $D_L$  is obtained by suddenly increasing bus 4 load by 100 MW (20% step) and analyzing the load-frequency sensitivity index. Fig. 7.2 shows the center of inertia frequency deviation of the time-domain simulation in PowerFactory and a new equilibrium at  $-0.002017$  pu. Substituting its absolute value as  $r_{ss}$  in the linear and Eq. (7.4) models, assuming that  $r_{ss} = r_{tr}$  (i.e. no safety margin) and  $P_b = \frac{100-2}{100} = 0.98$  pu:

$$\begin{aligned} D_L^l &= \frac{P_b}{r_{ss}} - \sum_i D_i \\ &= \frac{0.98}{0.002017} - (446.25) = 39.62 \\ D_L^p &= \frac{P_b}{r_{ss}(1 - r_{tr})} - \sum_i D_i \\ &= \frac{0.98}{0.002017(1 - 0.002017)} - (446.25) = 40.60 \end{aligned}$$

where  $D_L^l$  is the load damping calculated using the linear model and  $D_L^p$  using Eq. (7.4). Note that  $D_L^p$  is almost 2.5% higher than  $D_L^l$ .

### 7.4.2 Generator 10 outage

Next, let us compare the results of time-domain simulation with the linear Swing Equation and proposed models for an outage of  $G10$ , which is a hydro

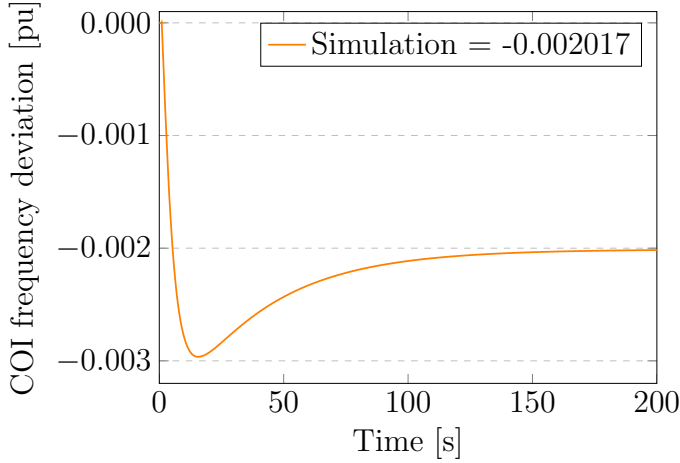


**FIGURE 7.2.** Center of inertia (COI) frequency after increasing bus 4 load by 100 MW. © Erick Alves et al, 2021.

unit providing most of the FCR. For that, let assume that  $r_{tr} = 0.02$  pu, which is the value for maximum instantaneous frequency deviation allowed in the Nordic system, as defined in article 127 and annex III of the European grid code [31]. The latter also imposes a maximum steady-state frequency deviation of 0.01 pu, which will be considered the target for  $r_{ss}$ .

Under these assumptions, let us consider that G10's initial injection of 250 MW and damping of 212.5 pu are lost. Hence,  $P_b = \frac{250-2}{100} = 2.48$  pu and  $\sum_i D_i = 446.25 - 212.5 = 233.75$ . Substituting in the linear and Eq. (7.4) models:

$$\begin{aligned} r_{ss}^l &= \frac{P_b}{(D_L + \sum_i D_i)} \\ &= \frac{2.48}{39.62 + 233.75} = 0.009072 \\ r_{ss}^p &= \frac{P_b}{(D_L + \sum_i D_i)(1 - r_{tr})} \\ &= \frac{2.48}{(40.60 + 233.75)(1 - 0.02)} = 0.009224 \end{aligned}$$

where  $r_{ss}^l$  is the steady-state frequency calculated using the linear model and  $r_{ss}^p$  using Eq. (7.4). Fig. 7.3 compares the two calculated limits with the time-domain simulation and shows that the linear Swing Equation model gives optimistic results which are 0.82% below the time-domain simulation's new equilibrium at  $-0.009147$  pu. On the other hand, Eq. (7.4) model provides pessimistic results which are 0.84% above the new equilibrium. Regardless, the three obtained

references are below the adopted target for  $r_{ss}$  and the test system can robustly operate for net-load variations of up to 250 MW without  $G10$ .

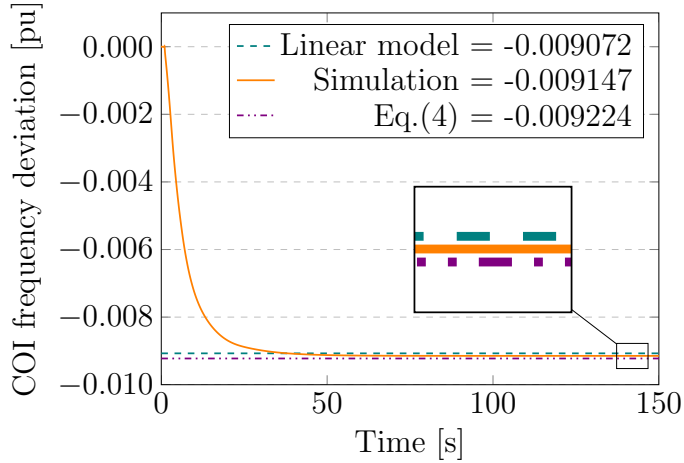


**FIGURE 7.3.** Center of inertia (COI) frequency after the outage of generator 10. © Erick Alves et al, 2021.

### 7.4.3 Islanding

In this time-domain simulation, the test system is islanded from the bulk grid by disconnecting  $G1$ . As before, results are compared to the proposed and linear models.

Under the same assumptions from Sec. 7.4.2, consider that  $G1$ 's initial injection is lost. Note that no damping is provided by the interconnection. Thus,  $\sum_i D_i = 446.25$  and  $P_b = \frac{1000-2}{100} = 9.98$  pu. Substituting in the linear and Eq. (7.4) models:

$$\begin{aligned} r_{ss}^l &= \frac{P_b}{(D_L + \sum_i D_i)} \\ &= \frac{9.98}{39.62 + 446.25} = 0.02054 \\ r_{ss}^p &= \frac{P_b}{(D_L + \sum_i D_i)(1 - r_{tr})} \\ &= \frac{9.98}{(40.60 + 446.25)(1 - 0.02)} = 0.02092 \end{aligned}$$

Fig. 7.4 compares the two calculated limits with the time-domain simulation and shows that the linear model gives optimistic values which are 2% below



the time-domain simulation's new equilibrium at  $-0.02096$ , while the proposed model provides optimistic values which are 0.2% below the time-domain simulation result. Though, Eq. (7.4) discrepancy occurs because  $r_{ss} > r_{tr}$ , which invalidates the assumptions from Proposition 2. This indicates that additional measures for frequency stability are required, such as reducing the initial injection of  $G1$  or increasing FCR. The reader is invited to recalculate  $r_{ss}^p$  using  $r_{tr}$  larger than the new equilibrium to confirm that the proposed model will produce pessimistic values as long as  $r_{ss} < r_{tr}$ .

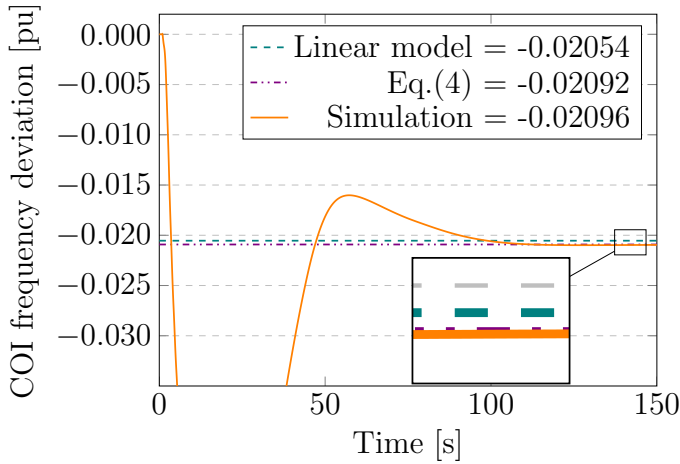


**FIGURE 7.4.** Center of inertia (COI) frequency after the system is islanded. © Erick Alves et al, 2021.

Note that a recalculation of  $D$  or  $P_b$  using the linear model does not guarantee frequency stability, as it produces optimistic values. On the contrary, Eq. (7.4) produces pessimistic values whenever  $r_{ss} < r_{tr}$  and provides a stability certificate against the nonlinearities introduced in Eq. (7.2).

## 7.5 DISCUSSION

At this point, the utility of Proposition 2 may be more apparent. By deriving sufficient conditions for robust frequency stability of ac power systems operating under large active power disturbances, it defines an algebraic relationship between four system boundaries: the maximum active power disturbance  $P_b$ , the minimum equivalent damping coefficient  $D_{min}$ , the transient  $r_{tr}$  and  $r_{ss}$  steady-state frequency limits. This relationship is summarized in Eq. (7.4) and allows calculation of one of these boundaries once the other three are predefined without resorting to time-consuming time-domain simulations.

As shown in [Sec. 7.4](#), the proposed algebraic equation produces more realistic forecasts of the center of inertia frequency deviation under large active power disturbances than the linear Swing Equation model. The proposed boundary is robust to nonlinearities and includes a safety factor that depends on the relationship between the maximum instantaneous and steady-state frequency deviations allowed by grid codes or industry standards. One may argue that deviations corrected by [Eq. \(7.4\)](#) are minimal in large ac grids, where frequency deviations and nonlinearities are minimal. Though, that might not be the case in low-inertia systems, where frequency excursions could be considerable under large active power disturbances. Therefore, the use of [Eq. \(7.4\)](#) may be preferred when an algebraic equation must evaluate the frequency stability of generalized ac grids. Note the model described in [Sec. 7.2](#) and the theory applied in [Sec. 7.3](#) can be used to study frequency stability of microgrids dominated by converter-interfaced generator if primary controllers use droop control or equivalent strategies [32].

Naturally, time-domain simulations still provides the most accurate results and includes assessment of voltage and rotor angle stability, which are ignored in the proposed model. However, the algebraic expression given in [Eq. \(7.4\)](#) allows easy integration of frequency stability criteria in long-term optimization algorithms, such as sizing of primary sources and energy storage, uncertain unit commitment and economic dispatch. For instance, some of the authors are contributing to the project [HES-OFF](#) [33] in which a software tool is being developed to reduce greenhouse gases emissions of offshore oil and gas installations by integrating a wind farm and hydrogen-based energy storage in their power generation systems. In [HES-OFF](#), [Eq. \(7.4\)](#) is integrated into a multi-objective, long-term optimization procedure that considers frequency stability criteria in the design stage of the ac power system. The procedure is described in detail in [34, 35]. The proposed model reduced the total optimization time by one order of magnitude when compared to the algorithm recurring to time-domain simulations.

Once again, it is important to emphasize that while criteria offered by [Proposition 2](#) are sufficient from a frequency stability perspective, they are only required conditions for the overall stability of an ac power system. The model developed in [Sec. 7.2](#) ignores network topology and voltage dynamics, therefore rotor angle and voltage stability criteria are not considered. Evidently, analysis of these dynamics requires detailed models of synchronous machines and converter-interfaced generators, as described in [36]. To make the problem more tractable, it might be interesting to apply the standard singular perturbation model described in [27] and divide the analysis in two time scales: slow (frequency) and fast (rotor angle and voltage) dynamics. This approach is one possible direction for future research.

Another limitation of this work is assuming that  $r_{tr}$  is not violated. As commented in [remark 2.6](#), time delays of primary frequency controllers influence the rate of change of frequency, the frequency nadir and zenith. In low-inertia systems, this might require the reduction of controller delays, as discussed in [Sec. 7.8](#). On one hand, the time-delay of FCR is a variable that typically cannot be influenced. On the other hand, this scenario is changing by the introduction of FFR. For instance, in the Nordic synchronous areas, market solutions for the procurement of FFR have been recently introduced [[37](#), [38](#)]. Consequently, how to optimally size FFR and FCR simultaneously to achieve frequency stability at a limit  $r_{ss}$  without infringing a limit  $r_{tr}$  during transients is another interesting topic for future research, in which the framing presented in this paper might be useful.

## 7.6 CONCLUSION

Using Lyapunov's direct method extended by perturbation theory, this article proposed sufficient conditions for frequency stability in ac power systems in the presence of active power disturbances originated by non-dispatchable sources and stochastic loads. By doing that, it defined a clear relationship between four system boundaries: the maximum active power disturbance, the minimum equivalent damping coefficient, the transient and steady-state frequency limits. Hence, when three of these boundaries are defined, the fourth is obtained without recurring to time-consuming simulations. The latter feature allows its integration into long-term optimization algorithms such as sizing of primary sources and energy storage, uncertain unit commitment and economic dispatch. The proposition is validated using time-domain simulations of the IEEE 39-bus test system and compared to the results of the linear Swing Equation model. Moreover, limitations and possible directions for future research are also discussed.

### DATA AVAILABILITY STATEMENT

The models and datasets presented in this study can be found in online repositories. The names of the repository/repositories and accession number(s) can be found at [[30](#)].

## ACKNOWLEDGMENT

The authors would like to thank Prof. Jan Tommy Gravdahl and Prof. Francisco Gonzalez-Longatt for the initial revision of the manuscript and their valuable feedback.

## 7.7 APPENDIX A: EQUILIBRIUM ANALYSIS

Let us define the admissible equilibrium set of the system in Eq. (7.2) as

$$\mathcal{E} \triangleq \left\{ \tilde{x} \in \mathbb{D} \mid 0 = -\frac{D}{M}\tilde{x} + \frac{u - w}{(\tilde{x} + 1)M} \right\}$$

Solving in  $x^*$ ,  $u^*$ ,  $w^*$ :

$$\begin{aligned} \frac{D}{M}x^* &= \frac{u^* - w^*}{(x^* + 1)M} \\ x^{*2} + x^* - \left( \frac{u^* - w^*}{D} \right) &= 0 \\ x^* &= -\frac{1}{2} \pm \sqrt{\frac{1}{4} + \left( \frac{u^* - w^*}{D} \right)} \end{aligned} \quad (7.7)$$

Note that if  $u^* = w^*$  (i.e. no active power imbalance), Eq. (7.7) has two solutions:  $x^* = 0$  and  $x^* = -1$ . The latter is not in  $\mathbb{D}$ , so only the former is valid. In conclusion, the equilibrium around  $x^* = 0$  is independent of  $M$  and affected only by  $D$  and  $u^* - w^*$ , as highlighted in Eqs. (7.4) and (7.7).

## 7.8 APPENDIX B: THE EFFECTS OF TIME DELAYS

Let us assume that primary frequency controllers are affected by time delay in their actuators and/or measurement and these can be approximated by a first-order system as suggested in [39]. In this case, the average model of an ac power system can be modeled by the following cascade system:

$$\begin{aligned} \Sigma_0 : (\tilde{x} + 1) M \dot{\tilde{x}} &= -D_L \tilde{x} (\tilde{x} + 1) + u - w + (\tilde{x} + 1) \sum_i y_i \\ \Sigma_i : \quad \epsilon_i \dot{y}_i &= -y_i - D_i \tilde{x} \end{aligned}$$

where  $D_L$  is the load damping [pu],  $i = 1, \dots, n$ , and  $y_i, \epsilon_i, D_i$  are the active power output [pu], time delay [s] and frequency droop [pu] of the  $i$ -th primary frequency controller. All other variables are as defined in Sec. 7.2.

The admissible equilibrium set of the cascade system is

$$\mathcal{E} \triangleq \left\{ X \in \mathbb{R}^{(n+1)} \mid \dot{X} = 0 \right\}, X = [\tilde{x} \quad y_1 \quad \cdots \quad y_n]^\top$$

In the equilibrium (i.e.  $\dot{y}_i = 0$ ), the output of primary frequency controllers is  $y_i = -D_i \tilde{x}$ . As consequence, the equilibrium analysis of the complete system is reduced to solving in  $x^*$ ,  $u^*$ ,  $w^*$  the following equation:

$$0 = u^* - w^* - (x^* + 1)x^* \left( D_L + \sum_i D_i \right)$$

which produces the same results from Appendix 7.7 when considering  $D = D_L + \sum_i D_i$ . In conclusion, the equilibrium around  $x^* = 0$  is independent of the time delays  $\epsilon_i$  and affected only by the total system damping  $D$  and the active power imbalance  $u^* - w^*$ . By induction, it is also possible to realize that time delays modeled by higher-order functions such as those presented in [40] will render the same results.

On the other hand, time delays may affect the stability of the cascade system. Let us consider:

$$\mathcal{V}(X) = \frac{1}{2} X^\top \begin{bmatrix} M & 0 & \cdots & 0 \\ 0 & \epsilon_1 & \cdots & 0 \\ \vdots & \vdots & \ddots & \vdots \\ 0 & 0 & \cdots & \epsilon_n \end{bmatrix} X$$

as a Lyapunov function candidate. Its time derivative for the unperturbed system (i.e.  $u - w = 0$ ) is given by:

$$\dot{\mathcal{V}} = - \begin{bmatrix} M\tilde{x} \\ \epsilon_1 y_1 \\ \vdots \\ \epsilon_n y_n \end{bmatrix}^\top \underbrace{\begin{bmatrix} \frac{D_L}{M} & -\frac{1}{\epsilon_1} & \cdots & -\frac{1}{\epsilon_n} \\ \frac{D_1}{M} & \frac{1}{\epsilon_1} & \cdots & 0 \\ \vdots & \vdots & \ddots & \vdots \\ \frac{D_n}{M} & 0 & \cdots & \frac{1}{\epsilon_n} \end{bmatrix}}_Q \begin{bmatrix} M\tilde{x} \\ \epsilon_1 y_1 \\ \vdots \\ \epsilon_n y_n \end{bmatrix}$$

Note that  $\dot{\mathcal{V}}$  is a quadratic form, hence  $\dot{\mathcal{V}} < 0 \iff Q > 0$ , which is indeed the condition for exponential stability of the cascade system. Using the argument that  $Q_{sym} = \frac{1}{2}(Q + Q^\top)$  and Kron reduction, it is possible to show that the cascade system is stable if and only if  $\epsilon_{max} < \frac{M}{D}$ .

However, a proper stability analysis must also consider local and inter-area active power oscillations and rotor angle stability, which is assumed as pre-requisite here. This demands a proper distribution of damping and inertia among primary frequency controllers. An extensive discussion about this topic is found in [36].

## 7.9 APPENDIX C: INPUT-TO-STATE STABILITY THEOREM

**Theorem 4.19 in [27].** Let  $\mathcal{V} : [0, \infty) \times \mathbb{R}^n \rightarrow \mathbb{R}$  be a continuously differentiable function such that

$$\alpha_1(\|x\|) \leq \mathcal{V}(t, x) \leq \alpha_2(\|x\|)$$

$$\frac{\delta \mathcal{V}}{\delta t} + \frac{\delta \mathcal{V}}{\delta x} f(t, x, u) \leq -W_3(x), \quad \forall \|x\| \geq \rho(\|u\|) > 0$$

$\forall (t, x, u) \in [0, \infty) \times \mathbb{R}^n \times \mathbb{R}^m$ , where  $\alpha_1, \alpha_2$  are class  $\mathcal{K}_\infty$  functions,  $\rho$  is a class  $\mathcal{K}$  function, and  $W_3(x)$  is a continuous positive definite function on  $\mathbb{R}^n$ . Then, the system

$$\dot{x} = f(t, x, u)$$

is input-to-state stable with  $\gamma = \alpha_1^{-1} \circ \alpha_2 \circ \rho$ , where  $f : [0, \infty) \times \mathbb{R}^n \times \mathbb{R}^m \rightarrow \mathbb{R}^n$  is piecewise continuous in  $t$  and locally Lipschitz in  $x$  and  $u$ , and the input  $u(t)$  is a piecewise continuous, bounded function of  $t$  for all  $t \geq 0$ .

## 7.10 REFERENCES

- [1] H. Farhangi. The path of the smart grid. *IEEE Power and Energy Magazine* **8** (1), 18–28 (January 2010). ISSN 1540-7977. doi: 10.1109/MPE.2009.934876. Cited on p. 100.
- [2] Goran Strbac, Nikos Hatzigiorgiou, Joao Pecos Lopes, Carlos Moreira, Aris Dimeas, and Dimitrios Papadaskalopoulos. Microgrids: Enhancing the Resilience of the European Megagrid. *IEEE Power and Energy Magazine* **13** (3), 35–43 (May 2015). ISSN 1540-7977. doi: 10.1109/MPE.2015.2397336. Cited on p. 100, 101.
- [3] Debra Lew, Derek Stenclik, Drake Bartlett, Andrew Groom, Peter Jorgensen, Jon O’Sullivan, Ryan Quint, Bruce Rew, Brad Rockwell, and Sandip Sharma. Secrets of Successful Integration: Operating Experience With High Levels of Variable, Inverter-Based Generation. *IEEE Power and Energy Magazine* **17** (6), 24–34 (November 2019). ISSN 1540-7977, 1558-4216. doi: 10.1109/MPE.2019.2930855. Cited on p. 100.
- [4] Julia Matevosyan, et al. Grid-Forming Inverters: Are They the Key for High Renewable Penetration? *IEEE Power and Energy Magazine* **17** (6), 89–98 (November 2019). ISSN 1540-7977, 1558-4216. doi: 10.1109/MPE.2019.2933072. Cited on p. 100.
- [5] Federico Milano, Florian Dorfler, Gabriela Hug, David J. Hill, and Gregor Verbic. Foundations and Challenges of Low-Inertia Systems (Invited Paper). In *2018 Power Systems Computation Conference (PSCC)* pages 1–25 Dublin (June 2018). IEEE. ISBN 978-1-910963-10-4. doi: 10.23919/PSCC.2018.8450880. Cited on p. 100, 101, 102.
- [6] Sina Y. Caliskan and Paulo Tabuada. Uses and abuses of the swing equation model. In *2015 54th IEEE Conference on Decision and Control (CDC)* pages 6662–6667 Osaka (December 2015). IEEE. ISBN 978-1-4799-7886-1. doi: 10.1109/CDC.2015.7403268. Cited on p. 100.
- [7] IEEE Std 1547-2018: IEEE Standard for Interconnection and Interoperability of Distributed Energy Resources with Associated Electric Power Systems Interfaces. 1547. IEEE New York, NY (2018). ISBN 978-1-5044-4639-6. URL <https://ieeexplore.ieee.org/servlet/opac?punumber=8332110>. Cited on p. 101.

- [8] IEEE Std 2030.8-2018: IEEE Standard for the Testing of Microgrid Controllers. IEEE New York, NY (2018). ISBN 978-1-5044-5050-8. URL <https://ieeexplore.ieee.org/servlet/opac?punumber=8444945>. Cited on p. 101.
- [9] Johannes Schiffer, Daniele Zonetti, Romeo Ortega, Aleksandar M. Stanković, Tevfik Sezi, and Jörg Raisch. A survey on modeling of microgrids—From fundamental physics to phasors and voltage sources. *Automatica* **74**, 135–150 (December 2016). ISSN 00051098. doi: 10.1016/j.automatica.2016.07.036. Cited on p. 101.
- [10] Ali Bidram and Ali Davoudi. Hierarchical Structure of Microgrids Control System. *IEEE Transactions on Smart Grid* **3** (4), 1963–1976 (December 2012). ISSN 1949-3053, 1949-3061. doi: 10.1109/TSG.2012.2197425. Cited on p. 101.
- [11] Ebrahim Rokrok, Miadreza Shafie-khah, and João P.S. Catalão. Review of primary voltage and frequency control methods for inverter-based islanded microgrids with distributed generation. *Renewable and Sustainable Energy Reviews* **82**, 3225–3235 (February 2018). ISSN 13640321. doi: 10.1016/j.rser.2017.10.022. Cited on p. 101.
- [12] P P Varaiya, F F Wu, and J W Bialek. Smart Operation of Smart Grid: Risk-Limiting Dispatch. *Proceedings of the IEEE* **99** (1), 40–57 (January 2011). ISSN 0018-9219, 1558-2256. doi: 10.1109/JPROC.2010.2080250. Cited on p. 101.
- [13] J.A. Laghari, H. Mokhlis, A.H.A. Bakar, and Hasmaini Mohamad. Application of computational intelligence techniques for load shedding in power systems: A review. *Energy Conversion and Management* **75**, 130–140 (November 2013). ISSN 01968904. doi: 10.1016/j.enconman.2013.06.010. Cited on p. 101.
- [14] Carlos Gamarra and Josep M. Guerrero. Computational optimization techniques applied to microgrids planning: A review. *Renewable and Sustainable Energy Reviews* **48**, 413–424 (August 2015). ISSN 13640321. doi: 10.1016/j.rser.2015.04.025. Cited on p. 101.
- [15] Mohammad A.A. Al-Jaafreh and Geev Mokryani. Planning and operation of LV distribution networks: A comprehensive review. *IET Energy Systems Integration* **1** (3), 133–146 (September 2019). ISSN 2516-8401. doi: 10.1049/iet-esi.2019.0013. Cited on p. 101.
- [16] P. Mercier, R. Cherkaoui, and A. Oudalov. Optimizing a Battery Energy Storage System for Frequency Control Application in an Isolated Power System. *IEEE Transactions on Power Systems* **24** (3), 1469–1477 (August 2009). ISSN 0885-8950, 1558-0679. doi: 10.1109/TPWRS.2009.2022997. Cited on p. 101.
- [17] Gauthier Delille, Bruno Francois, and Gilles Malarange. Dynamic Frequency Control Support by Energy Storage to Reduce the Impact of Wind and Solar Generation on Isolated Power System’s Inertia. *IEEE Transactions on Sustainable Energy* **3** (4), 931–939 (October 2012). ISSN 1949-3029, 1949-3037. doi: 10.1109/TSTE.2012.2205025. Cited on p. 101.
- [18] Lukas Sigrüst, Ignacio Egido, Enrique Lobato Miguez, and Luis Rouco. Sizing and Controller Setting of Ultracapacitors for Frequency Stability Enhancement of Small Isolated Power Systems. *IEEE Transactions on Power Systems* **30** (4), 2130–2138 (July 2015). ISSN 0885-8950, 1558-0679. doi: 10.1109/TPWRS.2014.2356721. Cited on p. 101.
- [19] I. Egido, L. Sigrüst, E. Lobato, L. Rouco, and A. Barrado. An ultra-capacitor for frequency stability enhancement in small-isolated power systems: Models, simulation and field tests. *Applied Energy* **137**, 670–676 (January 2015). ISSN 03062619. doi: 10.1016/j.apenergy.2014.08.041. Cited on p. 101.
- [20] Gary W. Chang, Ching-Sheng Chuang, Tai-Ken Lu, and Ching-Chung Wu. Frequency-regulating reserve constrained unit commitment for an isolated power system. *IEEE Transactions on Power Systems* **28** (2), 578–586 (May 2013). ISSN 0885-8950, 1558-0679. doi: 10.1109/TPWRS.2012.2208126. Cited on p. 101, 110.
- [21] Yunfeng Wen, Wenyuan Li, Gang Huang, and Xuan Liu. Frequency Dynamics Constrained Unit Commitment With Battery Energy Storage. *IEEE Transactions on Power Systems* **31** (6), 5115–5125 (November 2016). ISSN 0885-8950, 1558-0679. doi: 10.1109/TPWRS.2016.

2521882. Cited on p. 102.
- [22] Shrirang Abhyankar, Guangchao Geng, Mihai Anitescu, Xiaoyu Wang, and Venkata Dinavahi. Solution techniques for transient stability-constrained optimal power flow – Part I. *IET Generation, Transmission & Distribution* **11** (12), 3177–3185 (August 2017). ISSN 1751-8687, 1751-8695. doi: 10.1049/iet-gtd.2017.0345. Cited on p. 102.
- [23] Guangchao Geng, Shrirang Abhyankar, Xiaoyu Wang, and Venkata Dinavahi. Solution techniques for transient stability-constrained optimal power flow – Part II. *IET Generation, Transmission & Distribution* **11** (12), 3186–3193 (August 2017). ISSN 1751-8687, 1751-8695. doi: 10.1049/iet-gtd.2017.0346. Cited on p. 102.
- [24] Nga Nguyen, Saleh Almasabi, Atri Bera, and Joydeep Mitra. Optimal Power Flow Incorporating Frequency Security Constraint. *IEEE Transactions on Industry Applications* **55** (6), 6508–6516 (November 2019). ISSN 0093-9994, 1939-9367. doi: 10.1109/TIA.2019.2938918. Cited on p. 102.
- [25] IEEE PES Task Force on Benchmark Systems for Stability Controls. Benchmark Systems for Small-Signal Analysis and Control. Technical Report PES-TR18 IEEE Power System Dynamic Performance Committee (August 2015). URL <https://resourcecenter.ieee-pes.org/technical-publications/technical-reports/PESTR18.html>. Cited on p. 102, 107.
- [26] Carlos Tavora and Otto M. Smith. Characterization of Equilibrium and Stability in Power Systems. *IEEE Transactions on Power Apparatus and Systems* **PAS-91** (3), 1127–1130 (May 1972). ISSN 0018-9510. doi: 10.1109/TPAS.1972.293468. Cited on p. 102.
- [27] Hassan K. Khalil. Nonlinear systems. Prentice Hall Upper Saddle River, NJ 3rd ed edition (2002). ISBN 978-0-13-067389-3. Cited on p. 104, 105, 106, 114, 118.
- [28] P. Kundur, Neal J. Balu, and Mark G. Lauby. Power system stability and control. The EPRI Power System Engineering. McGraw-Hill New York (1994). ISBN 978-0-07-035958-1. Cited on p. 107.
- [29] Jan Machowski, Janusz W. Bialek, and J. R. Bumby. Power system dynamics: Stability and control. Wiley Chichester, U.K 2nd ed edition (2008). ISBN 978-0-470-72558-0. Cited on p. 107.
- [30] Erick F. Alves. Efantnu/ips-freq-stability: As submitted after Review 1 in IEEE TPWRS. Zenodo (November 2020). Cited on p. 107, 115.
- [31] Comission Regulation (EU). Guideline on electricity transmission system operation (August 2017). URL <http://data.europa.eu/eli/reg/2017/1485/oj>. Cited on p. 111.
- [32] John W. Simpson-Porco, Florian Dörfler, and Francesco Bullo. Synchronization and power sharing for droop-controlled inverters in islanded microgrids. *Automatica* **49** (9), 2603–2611 (September 2013). ISSN 00051098. doi: 10.1016/j.automatica.2013.05.018. Cited on p. 114.
- [33] Lars O. Nord. Innovative Hybrid Energy System for Stable Power and Heat Supply in Offshore Oil & Gas Installation (HES-OFF) (June 2018). URL <https://www.ntnu.edu/ept/hes-off/>. Cited on p. 114.
- [34] Luca Riboldi and Lars Nord. Offshore Power Plants Integrating a Wind Farm: Design Optimisation and Techno-Economic Assessment Based on Surrogate Modelling. *Processes* **6** (12), 249 (December 2018). ISSN 2227-9717. doi: 10.3390/pr6120249. Cited on p. 114.
- [35] Luca Riboldi, Erick F Alves, Marcin Pilarczyk, Elisabetta Tedeschi, and Lars O. Nord. Innovative hybrid energy system for stable power and heat supply in offshore oil & gas installation (HES-OFF): System design and grid stability. In *Proceedings of the 30th European Symposium on Computer Aided Process Engineering (ESCAPE30)* volume A pages 211–216 Milano, Italy (May 2020). Elsevier. doi: 10.1016/B978-0-12-823377-1.50036-7. Cited on p. 114.
- [36] Florian Dörfler and Francesco Bullo. Synchronization and Transient Stability in Power Networks and Nonuniform Kuramoto Oscillators. *SIAM Journal on Control and Optimization*



- 50 (3), 1616–1642 (January 2012). ISSN 0363-0129, 1095-7138. doi: 10.1137/110851584. Cited on p. 114, 117.
- [37] Niklas Modig, Robert Eriksson, Lisa Haarla, Mikko Kuivaniemi, Knut Styve Hornnes, Per Arne Vada, Soroush Afkhami Meybodi, and Daniel Karlsson. Technical Requirements for Fast Frequency Reserve Provision in the Nordic Synchronous Area. Technical report ENTSO-E (May 2019). URL <https://www.svk.se/siteassets/aktorsportalen/tekniska-riktlinjer/ovriga-instruktioner/technical-requirements-for-fast-frequency-reserve-provision-in-the-nordic-synchronous-area-1.pdf>. Cited on p. 115.
- [38] ENTSO-E. Fast Frequency Reserve – Solution to the Nordic inertia challenge. Technical report ENTSO-E (December 2019). URL <https://www.epressi.com/media/userfiles/107305/1576157646/fast-frequency-reserve-solution-to-the-nordic-inertia-challenge-1.pdf>. Cited on p. 115.
- [39] I. Egidio, F. Fernandez-Bernal, P. Centeno, and L. Rouco. Maximum Frequency Deviation Calculation in Small Isolated Power Systems. *IEEE Transactions on Power Systems* 24 (4), 1731–1738 (November 2009). ISSN 0885-8950, 1558-0679. doi: 10.1109/TPWRS.2009.2030399. Cited on p. 116.
- [40] IEEE Task Force on Turbine-Governor Modeling. Dynamic Models for Turbine-Governors in Power System Studies. Technical Report PES-TR1 IEEE New York, NY (August 2013). URL <https://resourcecenter.ieee-pes.org/publications/technical-reports/PESTR1.html>. Cited on p. 117.





## CHAPTER 8

### *Sizing of Hybrid Energy Storage Systems for Inertial and Primary Frequency Control*

---

Erick Fernando Alves<sup>1</sup>, Daniel dos Santos Mota<sup>1</sup>, and Elisabetta Tedeschi<sup>1,2</sup>

Journal paper published in: *Frontiers in Energy Research*, 9:649200 (May 2021).

DOI: [10.3389/fenrg.2021.649200](https://doi.org/10.3389/fenrg.2021.649200)



**Open Access** This work is licensed under a Creative Commons Attribution 4.0 International License. It means that unrestricted use, sharing, adaptation, distribution, and reproduction in any medium or format are allowed, as long as the original author(s) and the source are appropriately credited, a link to the Creative Commons license is provided, and any changes made are indicated. To view a copy of this license, please visit <http://creativecommons.org/licenses/by/4.0/>.

© Alves, Mota and Tedeschi, 2021.

#### **Author Contributions**

Conceptualization, E.A. and E.T.; methodology, E.A.; software, E.A. and D.M.; validation, E.A.; formal analysis, E.A. and D.M.; investigation, E.A. and D.M.; resources, E.T.; data curation, E.A.; writing - original draft preparation, E.A.; writing - review and editing, D.M. and E.T.; visualization, E.A.; supervision, E.T.; project administration, E.T.; funding acquisition, E.T.

---

<sup>1</sup>Department of Electric Power Engineering, NTNU, 7034 Trondheim, Norway.

<sup>2</sup>Department of Industrial Engineering, University of Trento, 38123 Trento, Italy.

## ABSTRACT

The exponential rise of renewable energy sources and microgrids brings about the challenge of guaranteeing frequency stability in low-inertia grids through the use of energy storage systems. This paper reviews the frequency response of ac power systems, highlighting its different time scales and control actions. Moreover, it pinpoints main distinctions among high-inertia interconnected systems relying on synchronous machines and low-inertia systems with high penetration of converter-interfaced generation. Grounded on these concepts and with a set of assumptions, it derives algebraic equations to rate an energy storage system providing inertial and primary control. The equations rely on parameters typically defined by system operators, industry standards or network codes, are independent from the energy storage technology and robust to system nonlinearities. Using these results, the authors provide a step-by-step procedure to size the main components of a converter-interfaced hybrid energy storage system. Finally, a case study of a wind-powered oil and gas platform in the North Sea demonstrates with numerical examples how the proposed methodology: 1) can be applied in a practical problem; 2) allows the system designer to take advantage of different technologies and set specific requirements for each storage device and converter according to the type of frequency control provided.

## 8.1 INTRODUCTION

Planning, design and operation of ac power systems are becoming more involved. For instance, conversion from primary sources and storage is performed using not only synchronous machines but also converter-interfaced generators. Moreover, groups of interconnected loads and distributed energy resources, also known as microgrids [1, 2], can form islands and operate independently from the interconnected power system.

From this perspective, ESSs can help to balance demand and supply, and control frequency, voltage and power flows in isolated power systems or microgrids operating in islanded mode. These features increase not only the stability and security of the system, but also its efficiency and assets utilization [3, 4]. Nonetheless, these desired features can be achieved only with the proper sizing of ESSs.

In particular, sizing the components of a converter-interfaced ESS is one of the main challenges in microgrids and large ac power systems with high penetration of converter-interfaced generators. The main reason being the

trade-off among key technical characteristics in storage solutions, where no single technology stands out [5–7]. For instance, ultracapacitors and flywheels are appropriate for inertia simulation as they offer high power density and efficiency. However, their low energy density and high cost per kWh make them unsuitable for primary and secondary control. Further examples are the several types of batteries and fuel cell technologies. These solutions are well-suited for secondary control because they offer reasonable power and energy densities and cost per kWh. Nevertheless, their life time can be extremely reduced if applied in inertia simulation and primary control due to the abrupt current changes and number of charge and discharge cycles required. In summary, there is no one-size-fits-all technology for ESSs, so hybrid solutions are currently becoming the preferred choice not only in transportation, but also in ac power systems applications [8].

When considering all that, sizing an ESS to provide inertial and primary frequency control becomes an intricate task. Many researchers have been devoting time to untangle this problem. For microgrids, Aghamohammadi and Abdolahinia [9] optimally size a battery ESS for primary frequency control considering overloading characteristics and limitation of the state of charge. For that, the authors propose an iterative procedure based on time-domain simulations that considers the battery permissible overload coefficient and duration. In [10, 11], the authors present a control-based approach applying the Hamiltonian Surface Shaping and Power Flow Control to size the ESS and to address how communication and controller bandwidth can affect the sizing and filtering requirements. For large ac power systems with high penetration of converter-interfaced generators, Knap *et al.* [12] introduce a methodology to size ESSs for the provision of inertial response and primary frequency regulation. In this work, a linearized version of the swing equation is applied to determine the ESS rated power and energy capacity and it is shown that this converter-interfaced system can achieve similar performance to a conventional peak power plant. In [13], the authors focus on primary control and propose a more broad three-stage methodology, that evaluates not only the battery dynamic response and provision of frequency reserves, but also its lifetime and economic assessment.

From a system operator or developer point of view, the main limitations in these previous works are: 1) the extensive use of time-domain simulations to support their sizing methodology; 2) the assumption that the required ESS technology and model parameters are well-known beforehand; 3) the linearization of the swing equation to study the frequency control problem.

For the first limitation, it must be noted that defining the rated active power and energy capacity of an ESS is a multi-stage process involving a techno-economical evaluation as emphasized by Sandelic *et al.* [13], Riboldi *et al.* [14].

Hence, the analysis of the ESS dynamic response is only one step of the problem, which requires integration into a broad optimization involving several time scales. Nonetheless, an inspection of recent literature reviews on ac microgrid planning [15, 16] reveals that conditions for frequency stability are largely overlooked in the problem formulation and most optimization algorithms consider that matching power demand with generation is the only required dynamic constraint, without imposing minimum requirements on system damping or frequency reserves. This is typically justified by the argument that frequency stability analysis in ac power systems requires computationally demanding simulation models that can turn the optimization into an intractable problem. Therefore, ESS sizing models should be efficient and, if possible, algebraic to be directly incorporated as constraints in larger optimization algorithms.

For the second limitation, system operators of ac power systems are fundamentally interested in specifying the minimum equivalent inertia, damping, deadband and time delay of equipment supplying inertial response and primary frequency regulation [17]. Indeed, in many regulated ac power systems, such as transmission and distribution grids, system operators avoid requiring specific technologies and prefer to limit specifications to functionalities to be provided [18]. For instance, Chang *et al.* [19] solved the unit commitment problem for islanded ac power systems with high penetration of converter-interfaced generators including constraints on frequency reserves using mixed-integer linear programming. For that, the authors determined the minimum system damping empirically relying on the load-frequency sensitivity index. Moreover, frequency stability constraints have also been proposed in planning and operation studies of large ac power systems, such as optimal power flow problems, by Wen *et al.* [20], Abhyankar *et al.* [21], Geng *et al.* [22], Nguyen *et al.* [23].

For the third limitation, it is reported in the literature that the linearized swing equation may underestimate frequency variations during transients [24] and, as consequence, the required damping of ac power systems [25]. Accordingly, a certain level of robustness must be considered when sizing an ESS to account for nonlinear effects, especially in low-inertia systems.

Considering this context, the contributions of this work are threefold: 1) it offers an updated literature review of the frequency response of ac power systems, highlighting the different time scales of the frequency control problem and the main distinctions among traditional systems, large systems with high penetration of converter-interfaced generator and microgrids; 2) based on the type of frequency control being supplied by a converter-interfaced ESS, it proposes an algebraic method to calculate the rated energy of its ES devices and the rated power of its converters. The proposed method is robust to system nonlinearities and based on parameters typically defined by system operators, industry standards or network codes; 3) it provides a step-by-step systematic

procedure to size the main components of hybrid ESSs independently from the technologies used in the ES devices and requiring knowledge of few ac power systems parameters.

## 8.2 MATERIALS AND METHODS

### 8.2.1 Frequency Control in AC Power Systems

The principles of frequency control in ac power systems can be understood by analysing a simplified model of a flywheel spinning at a rated angular frequency  $\omega_s$  [rad s<sup>-1</sup>]. The rotating masses of all synchronous generators and motors connected to ac power systems are represented by an equivalent moment of inertia  $J$ . On the driving end of the shaft, all generators deliver energy to the flywheel via a torque  $T_G$ , whereas the consumers remove energy through  $T_L$ . The natural and controlled damping of the system are represented by a coefficient  $B$ .

Eq. (8.1) is obtained by applying Newton's second law of motion to this simplified flywheel model. The moment of inertia  $J(t, \omega)$  is in [kg m<sup>2</sup>], the damping coefficient  $B(t, \omega)$  is in [N m s rad<sup>-1</sup>], the average (center of inertia) angular speed  $\omega$  is in [rad s<sup>-1</sup>], and the equivalent torques  $T_G(t, \omega)$  and  $T_L(t, \omega)$  are the in [N m].

$$J(t, \omega)\dot{\omega} = T_G(t, \omega) - T_L(t, \omega) - B(t, \omega)(\omega - \omega_s) \quad (8.1)$$

The representation of ac power systems as an equivalent rotating mass and Eq. (8.1), also referred as the Swing Equation, was already applied in the interwar period by Doherty and Nickle [26] and reported in many classical power systems books such as Concordia [27], Grainger and Stevenson [28], Kimbark [29], Kundur *et al.* [30], Machowski *et al.* [31]. Moreover, limitations of this model have been discussed in the last 40 years [24, 32]. Mainly, a proper transient analysis of ac power systems must include voltage dynamics, which requires very detailed models and knowledge of the network topology and characteristics, time delays of controllers and so on [33]. This level of detail is often not available during the planning phases of ac power systems and the Swing Equation model is still today an useful concept to evaluate the frequency response in the early design of a project [34–36] or in operation planning [19, 20, 37].

It is convenient to normalize and express the balance of torques in Eq. (8.1) as a balance of power. The normalization starts by dividing Eq. (8.1) by the

rated apparent power of the system  $S_b$  [VA], whereas the balance of power requires a multiplication by the angular frequency  $\omega$ , as shown in Eq. (8.2).

$$\frac{\omega}{S_b} J(t, \omega) \dot{\omega} = \frac{P_G(t, \omega)}{S_b} - \frac{P_L(t, \omega)}{S_b} - \frac{\omega}{S_b} B(t, \omega) (\omega - \omega_s). \quad (8.2)$$

Eq. (8.2) contains two variables that are not yet normalized, namely  $\omega$  and  $\dot{\omega}$ . The normalization can be performed by introducing an equivalent inertia constant  $M(t, \omega) = \frac{J(t, \omega) \omega_s^2}{S_b}$  in [s] and a damping coefficient  $D(t, \omega) = \frac{B(t, \omega) \omega_s^2}{S_b}$  in [pu]. Furthermore, one can obtain a state-space representation by defining the state  $x = \frac{\omega}{\omega_s}$ , as in Eq. (8.3), where  $u(t, x)$  and  $w(t, x)$  are the normalized power generation  $\frac{P_G}{S_b}$  and power consumption  $\frac{P_L}{S_b}$  from Eq. (8.2).

$$xM(t, x)\dot{x} = u(t, x) - w(t, x) - xD(t, x)(x - 1), \quad (8.3)$$

The dynamics from Eq. (8.3) is better understood when rearranging it and defining a state centered at the rated angular frequency, i.e.  $\tilde{x} = x - 1$ , which results in Eq. (8.4).

$$\dot{\tilde{x}} = -\frac{D(t, \tilde{x})}{M(t, \tilde{x})} \tilde{x} + \frac{u(t, \tilde{x}) - w(t, \tilde{x})}{(\tilde{x} + 1)M(t, \tilde{x})}. \quad (8.4)$$

When inspecting Eq. (8.4) and assuming that  $D(t, \tilde{x}) > 0$  and  $M(t, \tilde{x}) > 0$ , it becomes clear that  $\tilde{x} = 0$  (i.e.  $\omega = \omega_s$ ) is an equilibrium point of the system whenever there is balance between power generation and consumption (i.e.  $u(t, \tilde{x}) = w(t, \tilde{x})$ ). Moreover, the dynamics of  $\tilde{x}$  are governed by three terms:  $M(t, \tilde{x})$ ,  $D(t, \tilde{x})$ , and  $u(t, \tilde{x}) - w(t, \tilde{x})$ . Each of them is affected by the strategies for frequency control in ac power systems, namely: inertial, primary and secondary control.

In traditional interconnected ac power systems with high inertia ( $M > 10$  s) and centralized power generation and dispatch, these control strategies are implemented as following:

- *Inertial control* is physically embedded in synchronous machines, because their rotors are flywheels providing the inertial effect required to oppose frequency variations. In other words,  $M(t, \tilde{x})$  increases whenever a synchronous machine is directly connected to the power system. Conversely, it reduces if a synchronous machine is disconnected. The inertial control is offered by both generators and motors with a practically instantaneous reaction time, as the rotor of a synchronous machine is electromagnetically coupled to ac power systems.



- *Primary control* is offered by generators or loads sensing frequency deviations from the rated value and automatically adjusting their active power accordingly. This control scheme is known as frequency-droop control [1] or frequency sensitivity mode [38]. The slope of the frequency sensitivity mode curve (solid black line) shown in Fig. 8.1 represents the value of  $D(t, \tilde{x})$ . Note that, for a specific generator, the damping coefficient  $D(t, \tilde{x})$  is equal to zero within the dead band (solid orange line), if the power reaches the maximum level (solid teal line), or if it reaches a minimum level (solid violet line). The primary control reaction time is in the order of seconds, and it is directly connected to the actuation delay of turbines and their governors [18, 39]. In Europe, the set of generators and loads offering primary control is called FCR [40].
- *Secondary control* is provided by a central controller typically in a dispatch center and requires communication infrastructure. When a frequency deviation is detected in the system and after a pre-defined time delay, this controller remotely changes the active power setpoint of generators or loads to match the power demand, i.e. make  $u(t, \tilde{x}) = w(t, \tilde{x})$ . This process can be done by an automatic controller or manually by an operator. In general, the secondary control reaction time is in the order of minutes. In Europe, the set of generators and loads offering secondary control is called FRR [40].

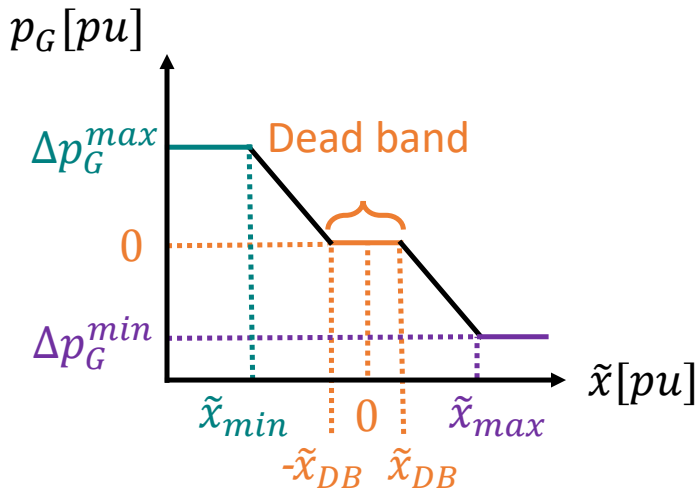


**FIGURE 8.1.** Frequency-droop, the main mechanism for primary frequency control. © Erick Alves et al, 2021.

In microgrids and ac power systems with high penetration of converter-

interfaced generators, where inertia may be low ( $M < 5$  s) and power generation is typically more distributed, the alternatives are the following:

- *Inertial control* is usually implemented in grid-forming units [41] using virtual inertia emulation [42, 43]. In this case, the value of  $M(t, \tilde{x})$  is a parameter of the inertia emulator. The inertial control reaction time is not instantaneous and will depend heavily on the frequency measurement algorithm and filtering techniques applied [44]. Furthermore, it may consume part of the FCR when activated, as grid-forming units typically provide primary control [18]. In Europe, the set of converter-interfaced generators offering inertial control is called FFR [18].
- *Primary control* is provided by grid-forming and grid-following units using the frequency-droop mechanism [41] akin to interconnected ac power systems. However, the reaction time is a fraction of a second, because the bandwidth of a converter-interfaced generator controller is at least one order of magnitude larger than traditional turbine governors and motor drives [43].
- *Secondary control* is provided by grid-following units [41]. Considering that a microgrid may contain a large number of small units, manual operation can become unfeasible and automatic dispatch coordinated by a central unit, such as a microgrid controller, may be necessary. The reaction time of secondary control is typically faster than in traditional ac power systems, from a couple of minutes in a large system with high penetration of converter-interfaced generators [18], to a couple of seconds in a microgrid [45, 46].

The dynamic behavior of the average system frequency after an active power imbalance is similar for high- and low-inertia ac power systems, despite their differences, and can be divided in three periods [39]:

1. *Arrest*: it starts immediately after the imbalance occurs. If there is lack of generation ( $u < w$ ), the frequency will decrease until it reaches its minimum value (nadir). If there is excess of generation ( $u > w$ ), the frequency will increase until it reaches its maximum value (zenith). At first, most of the balancing power  $P_a$  required to stabilize the system is provided by the inertial control. Then, primary controllers gradually take over  $P_a$  as the frequency deviation  $\tilde{x}$  increases. Important metrics of this period are the rate of change of frequency and the total time required to reach the nadir/zenith  $t_a$ .

2. *Rebound*: it starts immediately after the nadir/zenith is reached. During this period, the primary control is fully activated, and will bring the frequency to a new equilibrium condition. This settling point is below the rated value when  $u < w$  and above the rated value when  $u > w$ . In general, the balancing power  $P_a$  is provided only by the primary control. However, the inertial control may work against the frequency restoration, as the sign of the frequency derivative can be inverted. In synchronous machines, this negative effect is counteracted by adding damper windings in the rotor [30]. The same result can be obtained in converter-interfaced generators by applying adaptive virtual inertia emulation [43]. One of the important metrics of this period is the settling time  $t_b$ , i.e. the total time required to reach the settling point.
3. *Recovery*: it starts after the settling point is reached and secondary control is activated. Primary control does not have the capacity to restore the frequency to its rated value after an imbalance. Hence, the system frequency remains at the settling point until the secondary control is activated. In traditional high-inertia systems, the frequency is often restored to its rated value slowly due to practical limitations and to avoid counteraction of inertial control. Although, when secondary control is fast, the rebound period can be considerably shortened and even eliminated (i.e.  $t_a = t_b$  and  $\tilde{x}(t_a) = \tilde{x}(t_b)$ ). In the recovery period, the primary control is still active, but the secondary control gradually takes over the balancing power  $P_a$ , until the balance  $u(t) = w(t)$  is restored. One of the important metrics of this period is the recovery time  $t_c$ , i.e. the total time required to reestablish the rated frequency.

Fig. 8.2 illustrates the three control actions and the three periods following a perturbation caused by lack of generation. Even though the three periods following an active power imbalance are similar for both high- and low-inertia ac power systems, their energy management strategies for frequency control may differ considerably.

During the arrest period, a high-inertia system relies on the rotating masses of synchronous machines as its main energy buffer. In other words, kinetic energy is drained from or stored into the rotor of synchronous machines limiting the rate of change of frequency and bounding the nadir or zenith. This energy exchange happens “automatically” without any dedicated power or control equipment, because the rotor of a synchronous machine is electromagnetically coupled to its stator and hence ac power systems. For low-inertia systems, on the other hand, the energy buffer formed by rotating masses may not be large enough to guarantee the stable operation after a large power imbalance. In such cases, converter-interfaced generators must participate as FFR and support the

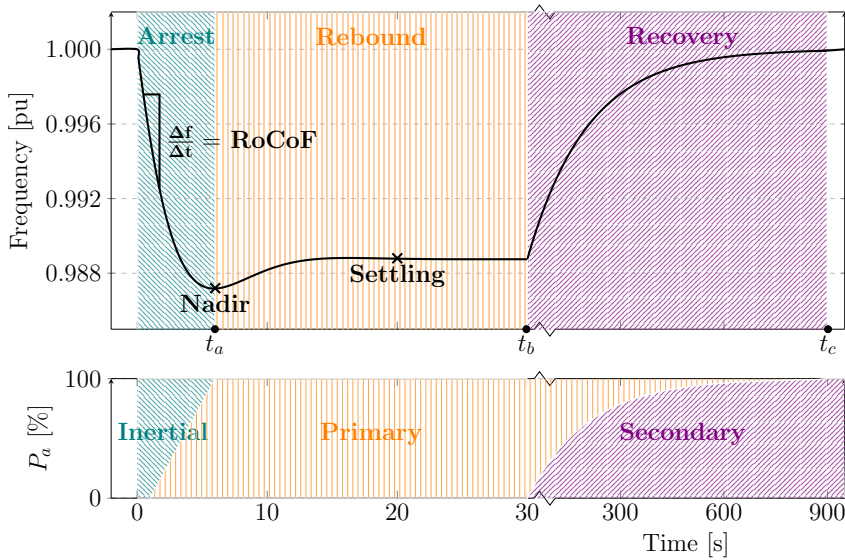


**FIGURE 8.2.** The three periods of frequency variation (arrest, rebound and recovery) and the control actions (inertial, primary and secondary) following a perturbation caused by lack of generation. © Erick Alves et al, 2021.

system by either supplying or absorbing energy during the arrest period. The dc-link capacitor of converter-interfaced generators could be considered an obvious candidate for storing the additional FFR energy. However, for power systems applications in the MW range, the required capacitance or voltage values become so high, that this solution becomes unfeasible with current technology. Therefore, an additional ESS must be sized specifically for this purpose [47].

As mentioned earlier, primary reserves are responsible for bringing the frequency from its extreme values to an acceptable settling point during the rebound phase. In traditional high-inertia systems, some generators are selected to operate with spare up- and down power capacity and form the FCR. Commonly, those are dispatchable and fast-acting generating units, such as those in gas and hydro plants, and have a large energy buffer in the form of chemical or potential energy. However, low-inertia systems may not have the necessary power or energy reserves for primary frequency control. This is because converter-interfaced generators are typically connected to renewable energy sources operating in maximum power point tracking. Those have no available power up capacity and have limited down capacity. Moreover, as is the case with FFR, the dc-link capacitor of converter-interfaced generators is not designed to store the energy amount required by FCR. In summary, an ESS must be sized to provide the energy and power capacity demanded by FCR in

low-inertia systems.

The main goal of this paper is, thus, establishing a procedure for sizing an ESS power and energy capacities according to its expected use (inertial control or FFR, primary control or FCR, or both) based on parameters that are: 1) typically defined by system operators, industry standards or network codes; 2) independent from the energy storage technology; 3) robust to system nonlinearities. It is worth mentioning, though, that sizing the ESS for secondary control or FRR is outside the scope of this paper. Also, the procedure presented in the following sections assumes that a thorough stability analysis was carried out beforehand in the ac power systems where the ESS will perform frequency control. This stability analysis must include measurement and actuation time delays, nonlinearities and, as result, select or at least restrict the possible values of  $M$  and  $D$ . This type of assessment is typically a task of the Transmission System Operator in large and regulated ac power systems. However, this responsibility might be debatable in smaller and unregulated systems such as microgrids. A detailed discussion about this topic is outside the scope of this paper, but it is worth highlighting that if  $\epsilon_{max} < \frac{M}{D}$ , where  $\epsilon_{max}$  is the maximum time delay of all active power sources in ac power systems, then this system can be frequency stable in the presence of time delays. For details and proofs, refer to appendix B of [25] and [33]. Though, this single criterion does not guarantee global stability of the ac power systems, and other aspects such as voltage, load-angle and phase-locked loop stability must be carefully investigated.

Additional information about frequency control in high-inertia ac power systems is discussed by Kundur *et al.* [30], Machowski *et al.* [31], Sauer *et al.* [48]. The main characteristics and challenges of low-inertia systems can be reviewed in Eto *et al.* [39], Vandoorn *et al.* [41], Fang *et al.* [43], dos Santos Alonso *et al.* [45], Milano *et al.* [47], Brandao *et al.* [49].

Lastly, tertiary control and generator rescheduling are further alternatives for frequency control. They are long-term, slow-response strategies based on communication infrastructure and/or electricity markets that are outside the scope of this paper. A throughout description of the European approach to these strategies is given by [50], while the North-American approach is summarized by Eto *et al.* [39].

### 8.2.2 Sizing of the Converter-Interfaced ESS Elements

This section includes the proposed procedure to size the energy capacity of the ES device and the rated power of an ES converter providing inertial or primary frequency control. Based on this initial estimation and selected references

from the literature, it describes a methodology to dimension the remaining ESS power unit components.

Fig. 8.3 presents an overview of the main elements of a converter-interfaced ESS, namely the power and control units. In general terms, the power unit can be further subdivided in: the ES device and its converter, the dc link, the grid converter and its LC filter.

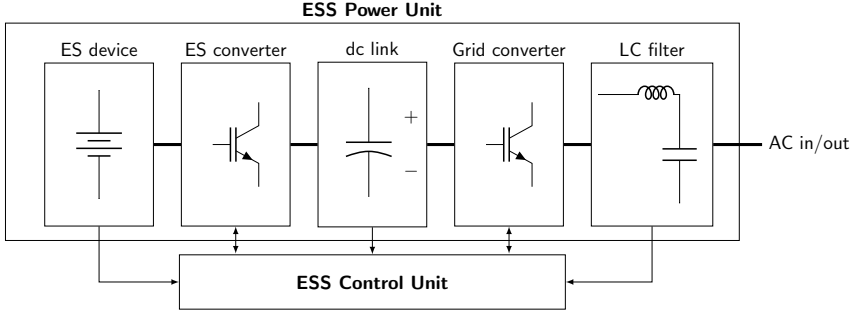


**FIGURE 8.3.** Elements of a converter-interfaced energy-storage system. © Erick Alves et al, 2021.

### The ES Device and its Converter

This section proposes a method to calculate the ES converter rated power  $P_{es}$  [W] and the ES device storage capacity  $E_{es}$  [J] according to the type of frequency control being provided. These variables are chosen as the starting point of the sizing procedure because they are the key drivers for the ESS equipment cost [51].

The calculation of  $P_{es}$ ,  $E_{es}$  starts by categorizing the terms of Eq. (8.3) in three sub-components according to the type of frequency control required to keep the power balance in the ac power systems, as in Eq. (8.5), where  $p_{iner}$ ,  $p_{pri}$  and  $p_{sec}$  are respectively the amount of power in pu required for inertial, primary and secondary control.

$$\underbrace{(\tilde{x} + 1)M(t, \tilde{x})\dot{\tilde{x}}}_{P_{iner}} = \underbrace{u(t, \tilde{x}) - w(t, \tilde{x})}_{-P_{sec}} - \underbrace{(\tilde{x} + 1)D(t, \tilde{x})\tilde{x}}_{P_{pri}} \quad (8.5)$$

Using this framework, algebraic expressions for  $P_{es}$  and  $E_{es}$  can be obtained with the following assumptions.

*Assumption 1.* Constant inertia and damping during the interval  $0 \leq t < t_c$ :

$M(t, \tilde{x})$  and  $D(t, \tilde{x})$  are constant throughout the power imbalance.

*Assumption 2. Primary control linearly takes over the inertial control during the interval  $0 \leq t < t_a$ :*

during the arrest period, the primary control linearly takes over the balancing power from the inertial control and the contributions of the secondary control are minimal compared to the overall balancing power required. Possible time delays of controllers are ignored for the energy calculations. In addition, the rate of change of frequency upper bound during this period can be approximated by  $\dot{\tilde{x}}_{0a} = \frac{\tilde{x}(t_a)}{t_a}$ .

*Assumption 3. Frequency nadir or zenith are bounded:*

the frequency nadir and zenith are enforced either by a proper combination of inertia, damping and primary control delays or the actuation of extreme control actions such as automatic generation curtailment or load shedding [39, 40].

In this case, the normalized angular speed error  $\tilde{x}(t_a)$  is upper and lower bounded by  $\tilde{x}_{tr}^{max}$  and  $\tilde{x}_{tr}^{min}$  respectively. In other words, if  $u < w$ , then the frequency nadir is greater than  $\tilde{x}_{tr}^{min}$ . Conversely, if  $u > w$ , then the frequency zenith is lower than  $\tilde{x}_{tr}^{max}$ . Hence, if the transient frequency limit is defined as  $r_{tr} = \max(\tilde{x}_{tr}^{max}, \tilde{x}_{tr}^{min})$ , then  $\|\tilde{x}(t_a)\| \leq r_{tr}$ .

*Assumption 4. Only primary control is active during the interval  $t_a \leq t < t_b$ :*

during the rebound period, only the primary control is active and the contributions of the inertial control and secondary control are minimal compared to the overall balancing power required. Moreover, the rate of change of frequency lower bound during this period can be approximated by  $\dot{\tilde{x}}_{ab} = \frac{\tilde{x}(t_b) - \tilde{x}(t_a)}{t_b - t_a}$ .

*Assumption 5. The settling point is bounded:*

after a power imbalance, the primary control is capable of driving the angular frequency back from the frequency zenith or nadir to within an acceptable steady-state frequency deviation  $r_{ss}$ .

The normalized angular speed error at the settling point  $\tilde{x}(t_b)$  is upper and lower bounded by  $\tilde{x}_{ss}^{max}$  and  $\tilde{x}_{ss}^{min}$  respectively. In other words, if  $u < w$ , then  $\tilde{x}(t_b) > \tilde{x}_{ss}^{min}$ . Conversely, if  $u > w$ , then  $\tilde{x}(t_b) < \tilde{x}_{ss}^{max}$ . Hence, if the steady-state frequency limit is defined as  $r_{ss} = \max(\tilde{x}_{ss}^{max}, \tilde{x}_{ss}^{min})$ , then  $\|\tilde{x}(t_b)\| \leq r_{ss}$ .

*Assumption 6. Secondary control linearly takes over during the interval  $t_b \leq t < t_c$ :*

during the recovery period, the secondary control linearly takes over the balancing power from the primary control and the contributions

of the inertial control are minimal. In addition, the rate of change of frequency lower bound during this period can be approximated by  $\dot{x}_{bc} = \frac{x(t_c) - x(t_b)}{t_c - t_b}$ .

Using [Assumption 2](#),  $P_{es}$  can be defined as the maximum between the components  $p_{iner}$  and  $p_{pri}$  in [Eq. \(8.5\)](#), as presented in [Eq. \(8.6\)](#). Using [Assumption 3](#), the bounds for  $p_{iner}$  are given by [Eq. \(8.7\)](#). However, obtaining a bound to  $p_{pri}$  requires an involved mathematical analysis, which is described in [\[25\]](#), and [Eq. \(8.8\)](#) presents only the main result of this analysis.

$$P_{es} = S_b \max(p_{es}^{iner}, p_{es}^{pri}) \quad (8.6)$$

$$p_{es}^{iner} = S_b \|(\tilde{x} + 1)M\dot{\tilde{x}}\| \leq S_b(1 + r_{tr})M\|\dot{\tilde{x}}\| \quad (8.7)$$

$$P_{es}^{pri} \leq S_b D r_{ss}(1 - r_{tr}) \quad (8.8)$$

The energy required by the inertial control  $E_{iner}$  and the primary control  $E_{pri}$  can be calculated as the time integral of their power components defined in [Eq. \(8.2\)](#), as seen in [Eqs. \(8.9\)](#) and [\(8.10\)](#). To solve these integrals analytically, it is necessary to: 1) remember that  $\dot{\tilde{x}} = \dot{x} = \frac{dx}{dt}$ ; 2) use [Assumption 2](#), [Assumption 4](#) and [Assumption 6](#). In [Eqs. \(8.10\)](#) to [\(8.13\)](#), the terms  $E_{pri}^{arr}$ ,  $E_{pri}^{reb}$  and  $E_{pri}^{rec}$  are respectively the energy required by the primary control during the arrest, rebound and recovery periods.

$$\begin{aligned} E_{iner} &= S_b \int_0^{t_a} (\tilde{x} + 1)M\dot{\tilde{x}}dt \\ &= S_b \int_{\tilde{x}(0)}^{\tilde{x}(t_a)} (\tilde{x} + 1)Md\tilde{x} \\ &= S_b M \left[ \frac{\tilde{x}^2(t_a)}{2} + \tilde{x}(t_a) \right] \end{aligned} \quad (8.9)$$

$$E_{pri} = \underbrace{\frac{S_b}{2} \int_0^{t_a} (\tilde{x} + 1)D\tilde{x}dt}_{E_{pri}^{arr}} + \underbrace{S_b \int_{t_a}^{t_b} (\tilde{x} + 1)D\tilde{x}dt}_{E_{pri}^{reb}} + \underbrace{\frac{S_b}{2} \int_{t_b}^{t_c} (\tilde{x} + 1)D\tilde{x}dt}_{E_{pri}^{rec}} \quad (8.10)$$

$$\begin{aligned} E_{pri}^{arr} &= \frac{S_b D}{2\dot{\tilde{x}}_{0a}} \left( \frac{\tilde{x}^3}{3} + \frac{\tilde{x}^2}{2} \right) \Big|_0^{t_a} \\ &= \frac{S_b D}{2} (t_a - t_0) \left[ \frac{\tilde{x}^2(t_a)}{3} + \frac{\tilde{x}(t_a)}{2} \right] \end{aligned} \quad (8.11)$$



$$\begin{aligned}
E_{pri}^{reb} &= \frac{S_b D}{\dot{\tilde{x}}_{ab}} \left( \frac{\tilde{x}^3}{3} + \frac{\tilde{x}^2}{2} \right) \Big|_{t_a}^{t_b} \\
&= S_b D \left[ \frac{t_b - t_a}{\tilde{x}(t_b) - \tilde{x}(t_a)} \right] \left[ \frac{\tilde{x}^3(t_b) - \tilde{x}^3(t_a)}{3} + \frac{\tilde{x}^2(t_b) - \tilde{x}^2(t_a)}{2} \right]
\end{aligned} \tag{8.12}$$

$$\begin{aligned}
E_{pri}^{rec} &= \frac{S_b D}{2\dot{\tilde{x}}_{bc}} \left( \frac{\tilde{x}^3}{3} + \frac{\tilde{x}^2}{2} \right) \Big|_{t_b}^{t_c} \\
&= \frac{S_b D}{2} (t_c - t_b) \left[ \frac{\tilde{x}^2(t_b)}{3} + \frac{\tilde{x}(t_b)}{2} \right]
\end{aligned} \tag{8.13}$$

To define the worst-case value for  $E_{es}$ , the bounds defined in [Assumption 3](#) and [Assumption 5](#) can be applied in [Eqs. \(8.9\) and \(8.11\) to \(8.13\)](#), leading to [Eqs. \(8.14\) to \(8.19\)](#).

$$E_{es} \geq E_{es}^{iner} + E_{es}^{pri} \tag{8.14}$$

$$E_{es}^{iner} \leq \frac{S_b M}{2} r_{tr} (r_{tr} + 2) \tag{8.15}$$

$$E_{es}^{pri} \leq E_{pri}^{arr} + E_{pri}^{reb} + E_{pri}^{rec} \tag{8.16}$$

$$E_{pri}^{arr} \leq \frac{S_b D}{12} (t_a - t_0) (2r_{tr}^2 + 3r_{tr}) \tag{8.17}$$

$$E_{pri}^{reb} \leq \frac{S_b D}{6} (t_b - t_a) \left( \frac{2r_{tr}^3 + 3r_{tr}^2 - 2r_{ss}^3 - 3r_{ss}^2}{r_{tr} - r_{ss}} \right) \tag{8.18}$$

$$E_{pri}^{rec} \leq \frac{S_b D}{12} (t_c - t_b) (2r_{ss}^2 + 3r_{ss}) \tag{8.19}$$

In short, a bound for  $P_{es}$  and the rated power of the ES converter can be obtained with [Eqs. \(8.6\) to \(8.8\)](#), whereas [Eqs. \(8.14\) to \(8.19\)](#) can be employed for bounding  $E_{es}$  and calculating the rated capacity of the ES device.

Notice that  $r_{tr}$ ,  $r_{ss}$ ,  $t_a$ ,  $t_b$ ,  $t_c$  are typically defined in industry standards and network codes such as [\[1, 38\]](#). Likewise, boundaries for  $M$ ,  $\|\tilde{x}\|$ , and  $D$  can be specified based on system operator requirements or power system stability and protection coordination studies. The latter can also be used to define less conservative values of  $\tilde{x}(t_a)$  and  $\tilde{x}(t_b)$ . In doing so, [Eqs. \(8.9\) and \(8.10\)](#) can be applied to calculate  $E_{es}$ . Not least, the use of normalized terms  $M, D$  allows system operators to specify inertia and damping requirements on a system level without knowing the installed power of a specific subsystem or installation.

## The DC Link

The main goal of this section is to define the rated capacitance  $C_{dc}$  [F] of the dc link. The dc link capacitor is a required energy source that provides balance between the ES converter and the grid converter, allowing them to be decoupled and controlled independently. Its capacitance is defined by Eq. (8.20) [52] where  $U_{dc}$  [V] is the dc-link rated voltage and  $\Delta U_{dc}^{max}$  is its maximum tolerable variation [V];  $T_r$  [s] represents the total time delay of the  $U_{dc}$  controller;  $\Delta P_{dc}^{max}$  is the maximum power variation in the dc link [W].

$$C_{dc} \geq \frac{T_r \Delta P_{dc}^{max}}{2U_{dc} \Delta U_{dc}^{max}} \quad (8.20)$$

Typically,  $U_{dc}$ ,  $\Delta U_{dc}^{max}$  are parameters associated with: 1) the capacitor material and technology [53]; 2) the voltage class of the power switch [54]; 3) network codes and requirements, because variations in  $U_{dc}$  will influence the maximum voltage that can be delivered by the grid converter.

The value of  $T_r$  will be affected by the parameters of the  $U_{dc}$  controller. If the latter is modeled as a transport-delay, an estimate is given by Eq. (8.21) where  $T_m$ ,  $T_c$ ,  $T_a$  are the  $U_{dc}$  measurement, the controller, and the actuator (i.e. the ES converter) delays, respectively.

$$T_r = T_m + T_c + T_a \quad (8.21)$$

Finally,  $\Delta P_{dc}^{max}$  can be approximated by the active power step applied immediately after the inertial or primary controllers leave their deadband zones, as seen in Eqs. (8.23) and (8.24), where  $x_{DB}^{iner}$ ,  $x_{DB}^{pri}$  [pu] are the dead band bounds of the inertial and primary control, respectively.

$$\Delta P_{dc}^{max} = \max(P_{iner}^{DB}, P_{pri}^{DB}) \quad (8.22)$$

$$P_{iner}^{DB} = 2S_b \bar{x}_{DB}^{iner} M \dot{\bar{x}} \quad (8.23)$$

$$P_{pri}^{DB} = 2S_b D \bar{x}_{DB}^{pri} \quad (8.24)$$

In the approximation of Eqs. (8.22) to (8.24), it is assumed that  $\bar{x}$  is a smooth function. Though, this assumption will not hold in an ac power systems where all generators and loads are interfaced by converters because  $M \rightarrow 0$  in Eq. (8.4) and the model and analysis presented in Sec. 8.2.2 will no longer be valid.

## The Grid Converter and its LC Filter

This section discusses briefly the sizing of the grid converter and recommends references for the design of the LC filter. Fig. 8.4 shows a schematic representation of the grid converter, the dc link and the LC filter.

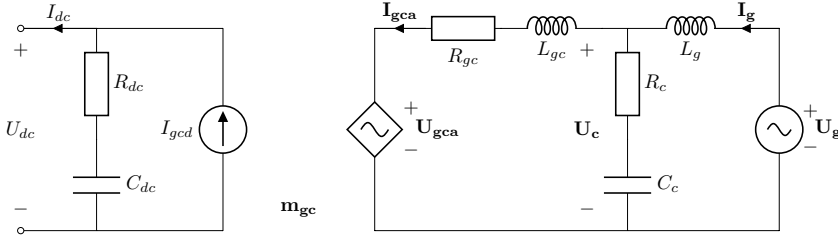


**FIGURE 8.4.** Schematic representation of the dc link, the grid converter and its LC filter. © Erick Alves et al, 2021.

Contractual and grid code requirements have to be taken into consideration when defining the rated apparent power of the grid converter. Among those requirements, one can mention minimum reactive power injection capacity, short-term overload, and low-voltage ride through capability [1, 38]. However, a relative simple and common practice in the industry is adopted in this paper. It uses a defined or required power factor  $\lambda$ . The rated apparent power of the converter,  $S_{gc}$  [VA], is then calculated as in Eq. (8.25).

$$S_{gc} = \frac{P_{gc}}{\lambda} \quad (8.25)$$

This practice generally limits the equipment size and cost. Nevertheless, it does not necessarily guarantee unsaturated operation for systems with high penetration of converter-interfaced generators and microgrid applications. In such cases, the grid converter sizing may have to consider the compensation of harmonic distortions and the definition of  $S_{gc}$  will become more involved. More information about this topic can be obtained in [55].

Once  $S_{gc}$  is defined, the design of the grid converter LC filter can start. For grid-connected converters, the LCL configuration is preferred as it limits the influence of the switching frequency harmonics in other equipment and reduces the filter size and cost [56]. Typically, the second inductance of the LCL configuration is provided by the series inductance of a step-up transformer between the ESS and the grid. The design of an LCL filter is an iterative procedure well documented in the literature, see [56–59]. It can be summarized in the following steps.

1. Calculate the converter side inductance  $L_{gc}$  based on the desired maximum current ripple  $\Delta I_{gca}$  on the ac side of the converter, its switching frequency  $f_{sw}$  and dc link voltage  $V_{dc}$ .
2. Choose the step-up transformer series inductance  $L_g$  upper-bounding the total inductance  $L_T = L_{gc} + L_g$  to avoid excessive voltage drop across

the inductors. Note that  $L_g$  is usually higher than 0.04 pu for medium-voltage transformers [60, 61]. When  $5 \text{ kHz} \leq f_{sw} \leq 10 \text{ kHz}$ , it is usually possible to adopt  $L_T \leq 0.1$  pu. On the contrary, a lower  $f_{sw}$  may demand a higher  $L_T$ .

3. Select the filter capacitance  $C_c$  upper-bounding its value to 0.05 pu (with converter rated power and voltage as base).
4. Check if the filter resonance frequency  $f_{res}$  lies between 0.2 and 0.5 times  $f_{sw}$ .
5. Calculate the filter damping resistance  $R_c$  based on the optimal quality factor  $Q$  and maximum power losses, limiting it to  $R_c^{min} = \frac{1}{10\pi f_{res} C_c}$  to avoid instabilities.

For that, the following equations can be used as guidelines:

$$L_{gc} = \frac{U_{dc}}{24 * f_{sw} * \Delta I_{gca}} \quad (8.26)$$

$$L_g = 0.1 * L_b - L_{gc} \quad (8.27)$$

$$C_c = \frac{L_{gc}}{Z_b^2} \quad (8.28)$$

$$f_{res} = \frac{Z_b}{2\pi L_{gc}} \sqrt{\frac{L_T}{L_g}} \quad (8.29)$$

$$R_c = Q \sqrt{\frac{L_{gc} L_g}{L_T C_c}} \quad (8.30)$$

where  $L_b = \frac{Z_b}{\omega_s}$ ,  $Z_b = \frac{U_{2n}^2}{S_{gc}}$  are the base inductance and impedance of the grid-side converter,  $U_{2n}$  is the rated line voltage on the low-voltage side of the step-up transformer.

It is worth emphasizing that the design of an LCL filter is iterative. Failure to comply with requirements implies restarting the whole process and changing the initial assumptions, i.e.  $\Delta I_{gca}$ ,  $f_{sw}$ , and  $U_{dc}$ . Moreover, additional optimization objectives and constraints may require the use of high-order filters or active damping. These topics are outside the scope of this paper, but can be further explored in [62–67].

Finally, alternative topologies to the one presented in Fig. 8.3 and Fig. 8.4 are possible. Nonetheless, the principles discussed earlier in this section can also be applied to more complex solutions. For instance, ES devices using different technologies may be connected in parallel, such as ultracapacitors and batteries. The hybridization is possible because the requirements for each type

of frequency control (inertial and primary) are set independently, as discussed in Sec. 8.2.2. This also allows control strategies to operate in parallel and ES converters to share the same dc link, grid converter and LC filter in a hybrid solution, which may help to reduce equipment costs, volume and weight [68]. Not least, ESSs may require more complex and robust configurations for the grid converter and consider aspects such as operating costs, efficiency, reliability, power quality and others, as discussed in [69]. However, note that these considerations will not affect the rated energy of ES devices nor the rated power of their converters, which are the variables being focused in the procedure presented in this paper.

### 8.3 RESULTS

This section presents a case study with numerical examples demonstrating how the method and equations presented in the previous section are applied to size the main components of a hybrid, converter-interfaced ESS supplying primary and secondary frequency control to an ac power systems, supported by inertial control of traditional synchronous generators.

#### 8.3.1 Case study: a wind-powered offshore platform in the North Sea

The system used as reference is depicted in Fig. 8.6 and represents an isolated ac power systems of an offshore oil and gas platform in the North Sea.

This installation operates at 60 Hz ( $\omega_s = 377 \text{ rad s}^{-1}$ ) and is equipped with two turbo-generators composed of a LM2500+ gas turbine from GE and an AMS 1250LG synchronous generator from ABB. Their combined active power is 70 MW, which is the value adopted for  $S_b$ . The normalized moment of inertia for these turbo-generators  $M_{GT}$  is equal to 5.1 s. This offshore installation must comply with IEC [70] which requires equipment to withstand frequency variations of up 5% continuously. However, it is a goal to keep frequency variations below 2% to limit excessive overheating of electrical machines and transformers. Therefore,  $r_{ss} = 0.02 \text{ pu}$  and  $r_{tr} = 0.05 \text{ pu}$ .

An initial techno-economical study of this installation [36] suggests that a reduction of up to 30% of its annual CO<sub>2</sub> emissions is possible when connecting it to a 12 MW offshore wind farm and employing an ESS based on 4 MW of proton exchange membrane fuel cells and 6 MW of proton exchange membrane electrolyzers. The main goal of this hydrogen-based ESS is to stabilize the wind farm output, allowing turbo-generators to operate with optimized setpoints and, hence, attaining higher efficiencies and lower emissions. From a frequency control perspective, the turbo-generators provide inertial control

and the ESS is responsible for primary and secondary control in normal operational conditions. To limit the size of the ESS, the turbo-generators contribute with additional primary and secondary control when the ESS saturates during occasional large frequency excursions.

Nevertheless, high number of start-stop and load-change cycles are known to be the main drivers for proton exchange membrane devices deterioration and performance decay [71]. To avoid that, proton exchange membrane fuel cells and electrolyzers are assigned to secondary control only and their load ramp rate is restricted to 0 to 100% in 120 s. The latter is also the value assumed for the recovery period ( $t_c - t_b$ ). Hence, an additional ES device must be considered to provide primary frequency control and to allow operation of the proton exchange membrane fuel cells and electrolyzers in more favorable conditions.

Further on the topic primary control, it is important to mention that electric loads of this platform are divided in two groups: fixed ( $P_{fix} = 37$  MW) and flexible ( $P_{flex} = 7.6$  MW). The first group represents equipment that cannot be influenced by the EMS, because changes in their set point are not possible or would affect negatively the oil and gas extraction and processing. Meanwhile, the second group represents loads whose set point can be temporarily raised or lowered by the EMS or primary control. An example of flexible load is the water injection system, which is responsible to maintain overall and hydrostatic reservoir pressures and force the oil toward the production wells [72]. This type of load is flexible because reservoir pressures can vary within a certain range without considerable impacts to production. In addition, this system time constant is large (minutes) when compared to the electrical system dynamics (seconds). This concept is explored in detail by DNV-GL [73], Sanchez *et al.* [74], Alves *et al.* [75].

Hence, the water injection system can also be considered a short-term ESS that is capable of offering primary frequency control to the ac power systems. When assuming that 20% of the installed flexible load can be used for primary frequency control, the following damping coefficient is obtained:

$$\begin{aligned} D_{flex} &= \frac{P_{flex}^{pri}}{S_b r_{ss}} \\ &= \frac{0.2 \times 7.6}{70 \times 0.02} = 1.09 \text{ pu} \end{aligned}$$

Finally, the load demand was obtained from the platform's supervisory control and data acquisition system for one representative week with a sampling period of one second. Fig. 8.5 presents the histogram of this data set, which is fit by a normal distribution when ignoring outliers below 0.6 pu. The distribution

gives a load variation of 0.0428 pu or 3 MW in normal operational conditions with 99.9% of probability, which should be covered by primary control. Using Eq. (8.8):

$$\begin{aligned} D_{min} &\geq \frac{P_{es}^{pri}}{r_{ss}(1-r_{tr})} \\ &\geq \frac{0.0428}{0.02 \times (1-0.05)} = 2.25 \text{ pu} \end{aligned}$$

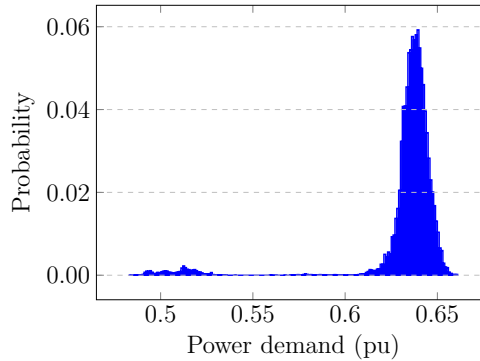


**FIGURE 8.5.** Histogram of the platform active power demand showing an average load of 0.6377 pu and maximum variation of 0.0428 pu with 99.9% of probability when outliers below 0.6 pu are ignored. © Erick Alves et al, 2021.

Thus, the ES device responsible for primary control should provide the following additional damping:  $D_{es} = D_{min} - D_{flex} = 1.16$  pu. With these parameters, initial simulations of the case study installation for a 3 MW load perturbations gives an arrest period ( $t_a - t_0$ ) = 11 s and a rebound period ( $t_b - t_a$ ) = 18 s.

Table 8.1 presents a summary of the installation parameters and the ESS requirements listed above.

### 8.3.2 Sizing of the Energy Storage System

Applying Eqs. (8.8) and (8.16) using the values from table 8.1, the rated power  $P_{es1}$  and energy capacity  $E_{es1}$  of the ES device providing primary control can be defined as  $P_{es1} = 1.54$  MW and  $E_{es1} = 108$  MJ or 30 kW h. Note, however, that the primary control must be bidirectional, i.e., it must compensate either lack or excess of power in the system. Therefore, a 50% state of charge for the ESS in normal operation should be considered. Hence,  $E_{es1} = \frac{108}{0.5} = 219$  MJ or 60 kW h.

**TABLE 8.1.** Parameters of the ac power systems of an offshore oil and gas platform in the Norwegian Continental Shelf and the requirements for its converter-interfaced ESS.

| Param.        | Value   | Param.        | Value                   |
|---------------|---------|---------------|-------------------------|
| $S_b$         | 70 MW   | $\omega_s$    | 377 rad s <sup>-1</sup> |
| $r_{tr}$      | 0.05 pu | $r_{ss}$      | 0.02 pu                 |
| $M_{GT}$      | 5.1 s   | $D_{min}$     | 2.25 pu                 |
| $D_{flex}$    | 1.09 pu | $D_{es}$      | 1.16 pu                 |
| $P_{ELY}$     | 6 MW    | $P_{FC}$      | 4 MW                    |
| $(t_a - t_0)$ | 11 s    | $(t_b - t_a)$ | 18 s                    |
| $(t_c - t_b)$ | 120 s   |               |                         |

The most suitable ES device is chosen based on the calculated  $P_{es1}$  and  $E_{es1}$ , on the parameters in table 8.1, and on a techno-economical evaluation. The latter is not covered in this paper. It is assumed, however, that a commercial lithium-ion system such as Saft Intensium Max+ 20P [76] is selected. This system incorporates ES device and converter in one assembly with two regulated dc output voltages of  $771 \pm 96$  V that can be connected in series or parallel and losses of about 25 kW at rated conditions. Considering the requirements of commercial grid converters such as Siemens SINACON PV [77], the ES device is assumed to have its two outputs connected in series and the following characteristics:  $U_{dc} = 1500$  V,  $\Delta U_{dc}^{max} = 150$  V,  $P_{losses}^{es1} = 25$  kW, and  $T_r = 2.1$  ms (one eighth of a grid cycle).

To define  $\Delta P_{dc}^{max}$ , the value  $x_{DB}^{pri} = 0.0025$  pu or 150 mHz is obtained from industry standards or grid codes such as [1, 38]. Then,  $\Delta P_{dc}^{max} = 360.5$  kW is attained when applying Eqs. (8.22) and (8.24). With these values defined, the dc-link capacitor is calculated using Eq. (8.20) and  $C_{dc} \geq 1.7$  mF is retrieved.

The next step in the procedure is defining  $S_{gc}$ . Assuming that all ES devices share the same dc link and that fuel cell and electrolyzer do not operate simultaneously, the active power bound will be defined by  $P_{ELY} + P_{es1} + P_{losses}^{es1} = 7.57$  MW, where  $P_{ELY}$  denotes the electrolyzer rated power. To have a buffer for the grid converter and LC filter losses, a safety margin of 2% is added to this value resulting in  $P_{gc} = 7.72$  MW. Additionally,  $\lambda = 0.8$  is adopted to limit the size of the grid converter. It then follows that  $S_{gc} = 9.65$  MVA.

The final step is calculating the components of the LC filter. For the sake of brevity, this design is not presented in this paper. The recommended procedure and references are listed in Sec. 8.2.2. Nonetheless, the algorithm for calculating the LC filter is available for the reader in [78]. The grid converter switching frequency is adopted as  $f_{sw} = 5.4$  kHz and its maximum current ripple as  $\Delta I_{gca} = 0.25$  pu. This results in the following values for the filter components:  $L_{gc} = 5.61$   $\mu$ H,  $L_g = 6.92$   $\mu$ H,  $C_c = 2.5$  mF, and  $R_c = 0.189$  m $\Omega$ . Refer to Fig. 8.4 for the placement of each filter element. It is worth mentioning that  $R_c$



yields an over-damped characteristic at the filter's resonance frequency, which is  $f_{res} = 1.80$  kHz or 0.334 times  $f_{sw}$ .

### 8.3.3 Sizing validation

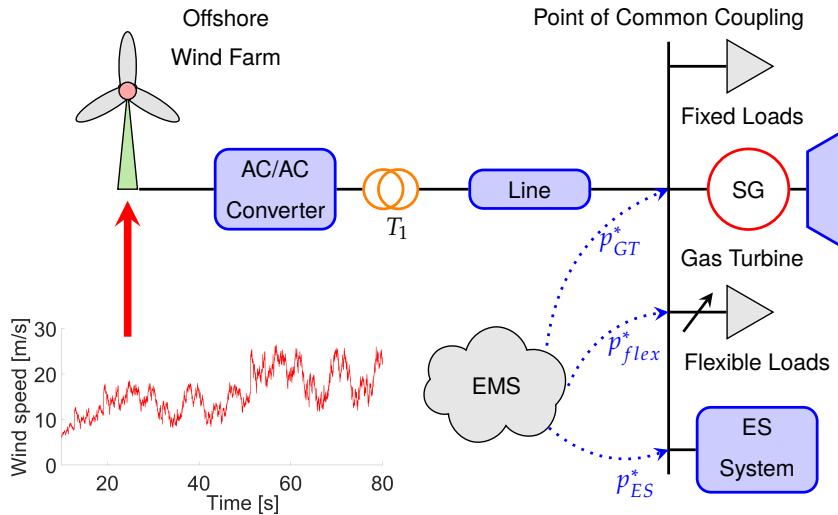


**FIGURE 8.6.** Schematic representation of the case study ac power systems. © Erick Alves et al, 2021.

To validate the calculations presented in [Sec. 8.3.2](#), a surrogate model of the case study installation was implemented in MATLAB Simulink R2018a. It has the level of details required to represent the frequency dynamics of the installation and to validate the proposed sizing of the ES device responsible for primary frequency control. It includes all main elements represented in [Fig. 8.6](#), namely: the turbo-generators, the fixed and flexible loads, the wind farm and its transmission line, the ESS and the EMS. [Fig. 8.7](#) gives an overview of these elements in Simulink.

The model was implemented using blocks of the Simscape Electrical Specialized Power Systems Toolbox complemented by an open library developed by the authors [79]. The latter includes a generalized nonlinear droop controller that is presented in [Fig. 8.8](#). This block is used as the main primary frequency controller in the turbo-generators, ESS and flexible load subsystems with their parameters as presented in [table 8.2](#). Moreover, the secondary control is implemented in the EMS subsystem using a nonlinear integral controller from the open library with anti-windup and hold functionalities. To minimize CO<sub>2</sub> emissions, the EMS gives priority for changes in the ESS setpoint when

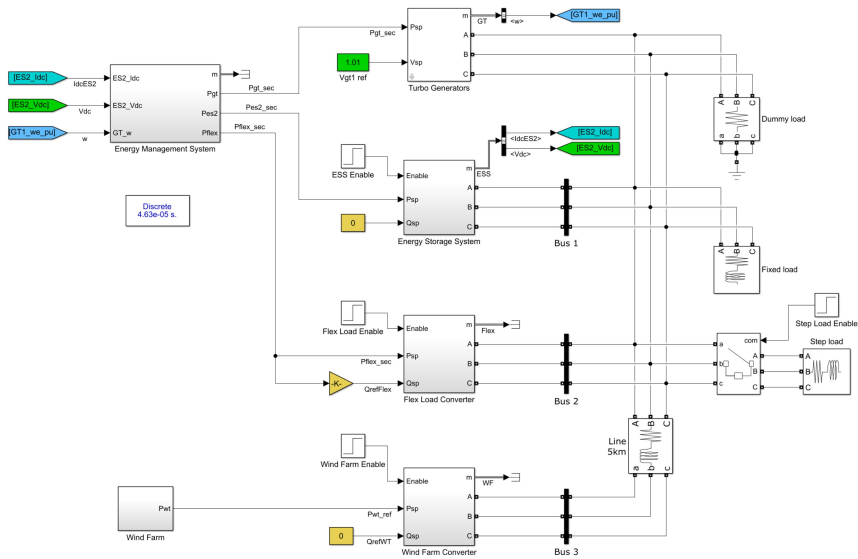


**FIGURE 8.7.** Overview of the MATLAB Simulink model used to validate the proposed sizing of the energy storage device responsible for primary control in the case study. © Erick Alves *et al*, 2021.

the secondary control is active. The re-dispatch of turbo-generators happens only when the limits of fuel cell or electrolyzers are reached and those may be considered a supplementary FRR.

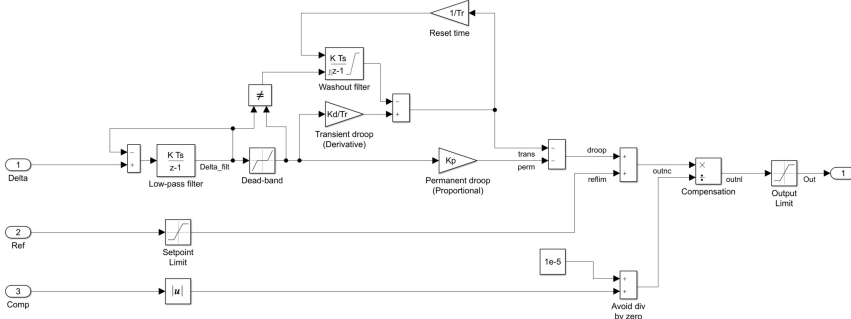


**FIGURE 8.8.** Generalized nonlinear droop controller with deadband, permanent droop (proportional gain), transient droop (derivative gain), output compensation, setpoint and output limitation. © Erick Alves *et al*, 2021.

It should be emphasized that it is not the goal of this model to validate the design of the grid converter, its controllers or its LC filter, nor to evaluate harmonics or possible power quality problems. Moreover, the validation of the fuel cell and electrolyzer stacks size, and their required  $H_2$  storage is presented by Riboldi *et al*. [14]. For the sake of brevity, the validation model is not

**TABLE 8.2.** Parameters of the primary controllers used during the validation.

| Parameter [Unit]                    | Turbo-gen             | ESS              | Flex               |
|-------------------------------------|-----------------------|------------------|--------------------|
| Permanent droop [pu]                |                       |                  |                    |
| Case 1: 3 MW load step without ESS  | $\frac{0.0214}{0.02}$ | 0                | $\frac{0.2}{0.02}$ |
| Case 2: 3 MW load step with ESS     | $\frac{0.1714}{0.02}$ | $\frac{1}{0.02}$ | $\frac{0.2}{0.02}$ |
| Case 3: 12 MW load step without ESS | $\frac{0.0857}{0.02}$ | 0                | $\frac{0.2}{0.02}$ |
| Case 4: 12 MW load step with ESS    | $\frac{0.1714}{0.02}$ | $\frac{1}{0.02}$ | $\frac{0.2}{0.02}$ |
| Transient droop [pu]                | 0                     | 0                | 0                  |
| Reset time [s]                      | 0.1                   | 0.1              | 0.1                |
| Low-pass frequency [Hz]             | 10                    | 450              | 30                 |
| Deadband [pu]                       | 0.025                 | 0.0025           | 0.0025             |

described further in this section. However, the interested reader can inspect it and find all necessary details, parameters and simulation files to reproduce the results presented below in [78].

To create the power imbalance required for checking the ESS sizing, a load of 3 MW (Step Load) is connected to the system at  $t_0 = 2$  s. As presented earlier in Sec. 8.3.1, this is the expected maximum load variation under normal operational conditions with 99.9% of probability. Fig. 8.9 shows the results of two simulations of the case study behavior during a load increase of 3 MW: Case 1 does not include the ESS in the installation, while Case 2 does include it.

From a frequency-control standpoint, a closer look at Fig. 8.9-(A) and (B) reveals that the angular speed behaves similarly in both cases, i.e. with and without ESS. The minor deviations among the cases are explained by the different deadbands and actuation delays of the turbo-generator and the ESS. Indeed, the smaller deadband and actuation delay of the converter-interfaced ESS makes its performance slightly superior, achieving a higher nadir (0.9796 pu) than the turbine governor (0.9787 pu) and a smaller steady-state error (0.25% versus 0.28%) after secondary control is deactivated. This better performance is reflected in the results seen in Fig. 8.9-(E) and (F), which show a marginal reduction of the flexible-load active power deviation from its original setpoint while the primary control is active. Foremost, Fig. 8.9-(C) and (D) corroborate the idea proposed in Sec. 8.3.2, i.e. a properly sized battery ESS would allow turbo-generators to operate at a constant setpoint when a 3 MW load variation happens suddenly, while respecting the load ramp-rate limit of the proton exchange membrane fuel cell, as shown in Fig. 8.9-(E) and (F).

From a sizing perspective, the ES device responsible for primary control (battery system) delivered a peak active power of 0.0197 pu or 1.38 MW and consumed 29.4 kW h of energy. The latter was calculated by trapezoidal numer-

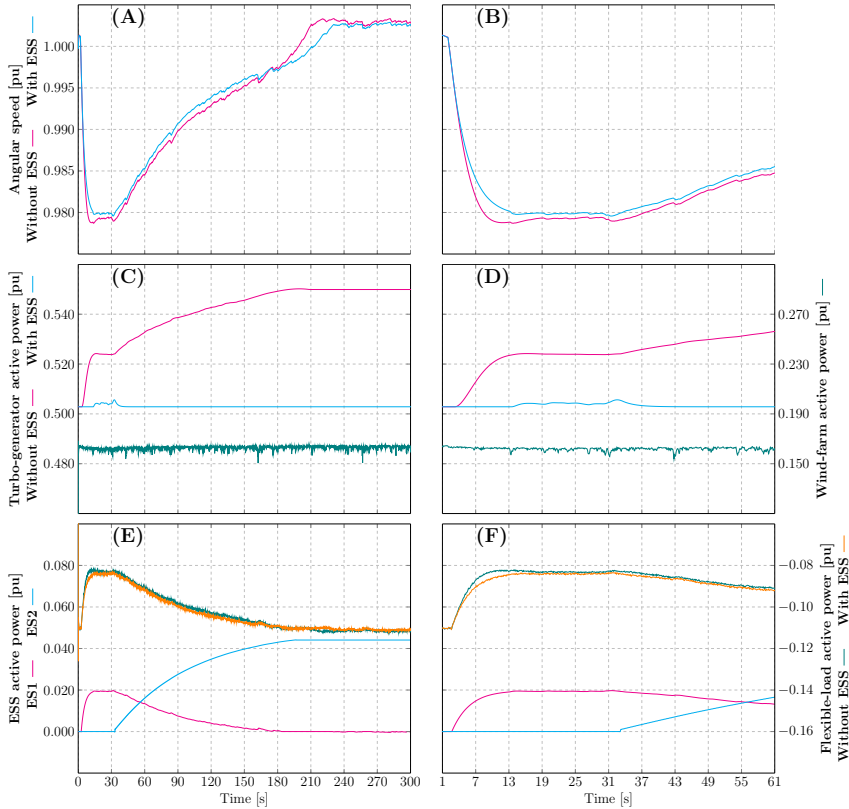


**FIGURE 8.9.** Case-study behavior during a load increase of 3 MW with and without the proposed ESS: Normalized angular speed (A) during the whole transient and (B) detail of the first minute; Turbo-generator and wind-farm active power in pu (C) during the whole transient and (D) detail of the first minute; Active power of the ES devices responsible for primary control (ES1) and secondary control (ES2) (E) during the whole transient and (F) detail of the first minute. © Erick Alves et al, 2021.

ical integration of the curve ES1 in Fig. 8.9-(E) using a step of 100 ms. When compared to the calculated values (1.54 kWh and 30 kWh) from Sec. 8.3.2, the proposed procedure oversized the battery system's active power by 11.5% and its energy by 2.1%. Nonetheless, as opposed to the simulation model used for validation, the proposed procedure 1) requires knowledge of very few ac power systems parameters; 2) relies only on algebraic equations, which are easy to integrate in optimization algorithms typically necessary for techno-economical evaluation of ESSs.

At this point, it is important to recap that the energy of the ES device responsible for primary control is dependent on: 1) the damping  $D_{es}$  provided, 2) the frequency limits  $r_{ss}$  and  $r_{tr}$ , 3) the duration of the arrest ( $t_a - t_0$ ), rebound ( $t_b - t_a$ ) and recovery ( $t_c - t_b$ ) periods, as seen in Eqs. (8.17) to (8.19). Thus,

when defining these variables, it is critical to evaluate if the ESS must provide frequency control uninterruptedly during high-impact, low-probability events. A complete disconnection of the wind farm under full production (12 MW) is an example of such event for the case study presented. Fig. 8.10 presents the results of two simulations of the case study behavior during this condition: Case 3 does not include the ESS in the installation, while Case 4 does. It is important to highlight that, for Case 3, the turbo-generator permanent droop must be increased to guarantee frequency stability and display the same dynamics of Case 4, as seen in table 8.2.

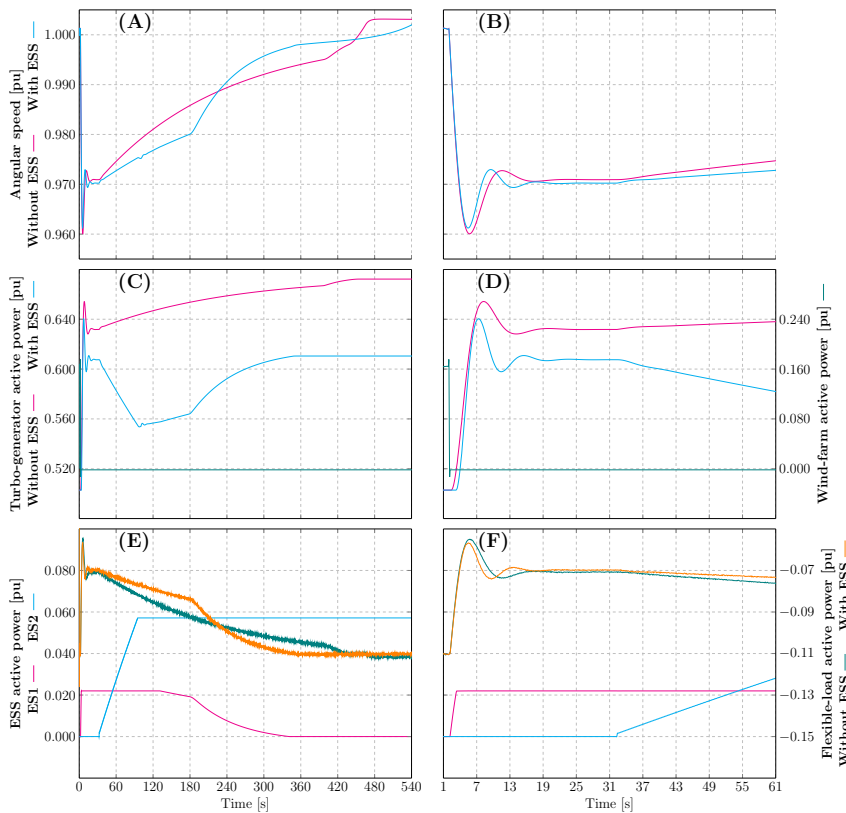


**FIGURE 8.10.** Case-study behavior during the wind farm disconnection under full production (12 MW) with and without the proposed ESS: Normalized angular speed (A) during the whole transient and (B) detail of the first minute; Turbo-generator and wind-farm active power in pu (C) during the whole transient and (D) detail of the first minute; Active power of the ES devices responsible for primary control (ES1) and secondary control (ES2) (E) during the whole transient and (F) detail of the first minute. © Erick Alves et al, 2021.

From a frequency-control point of view, Fig. 8.10-(B) suggests that the angular speed behaves similarly with and without the ESS during the arrest

and rebound period. However, a closer look at Fig. 8.10-(A) reveals that the dynamics of the recovery period in Case 3 and 4 are distinct. This happens because the secondary controller acts differently in these two simulations.

In Case 3, the turbo-generator is the sole contributor to the FRR and, as seen in Fig. 8.10-(C), its active power increases exponentially in the recovery period. As consequence, the angular speed deviation decreases exponentially, until it reaches the deadband of the droop controller.

In Case 4, there are two sources for the FRR: the hydrogen-based ESS (preferential) and the turbo-generator (supplementary). Hence, the secondary controller ramps up the proton exchange membrane fuel cell (ES2) until it reaches its rated power, as seen in Fig. 8.10-(E). At the same time, the angular speed deviation decreases and, as consequence, the droop controller reduces the turbo-generator active power, as shown in Fig. 8.10-(A) and (C). When the ES2 limit is hit, the secondary controller starts increasing the turbo-generator active power. However, the latter is also reduced by its droop controller, because the angular speed is still decreasing. These adversarial contributions continue until the deadband of the turbo-generator droop controller is reached. After that, only the secondary controller is active and the angular speed deviation decreases exponentially, until it reaches the deadband of the ES2 droop controller.

From a sizing frame of reference, the peak active power delivered by the battery system was 1.54 MW and the energy supplied was 95.8 kW h. The peak active power was limited by the nonlinear droop controller and matches the value defined in Sec. 8.3.2. On the other hand, the energy obtained in the simulation is more than 3 times larger the calculated value. Naturally, this happens because the parameters of the 3 MW and 12 MW load-increase events are disparate.

By inspection of Fig. 8.10-(A), one will note that the frequency limit  $r_{tr} = 0.05$  was obeyed, however  $r_{ss} = 0.03$  was not. Moreover, the duration of the arrest, rebound and recovery periods was 3.5 s, 120 s and 230 s. When substituting these new values in Eqs. (8.17) to (8.19), the energy obtained is 113.3 kW h, i.e. the proposed procedure oversized the battery system energy by about 1.5% when compared to the simulation results. This shows that the proposed procedure can produce correct upper-bounds for the ESS power and energy even when large disturbances and nonlinearities are considered.

## 8.4 CONCLUSIONS

This paper reviewed the frequency response theory in ac power systems, highlighting the different time periods (arrest, rebound, recovery) and control actions (inertial, primary, secondary) of the frequency control problem. It also

**TABLE 8.3.** Summary of the ESS parameters obtained using the proposed procedure.

| Param.             | Value        | Param.                | Value            |
|--------------------|--------------|-----------------------|------------------|
| $P_{es1}$          | 1.54 MW      | $E_{es1}$             | 60 kW h          |
| $U_{dc}$           | 1500 V       | $\Delta U_{dc}^{max}$ | 150 V            |
| $T_r$              | 2.1 ms       | $\Delta P_{dc}^{max}$ | 360.5 kW         |
| $p_{es1}^{losses}$ | 25 kW        | $C_{dc}$              | 1.7 mF           |
| $P_{gc}$           | 7.72 MW      | $S_{gc}$              | 9.65 MVA         |
| $U_{2n}$           | 675 V        | $\Delta I_{gca}$      | 0.25 pu          |
| $f_{sw}$           | 5.4 kHz      | $L_{gc}$              | 5.61 $\mu$ H     |
| $L_g$              | 6.92 $\mu$ H | $C_c$                 | 2.5 mF           |
| $f_{res}$          | 1.80 kHz     | $R_c$                 | 0.189 m $\Omega$ |

highlighted the main distinctions among traditional high-inertia systems relying on synchronous machines, and low-inertia systems such as those with high penetration of converter-interfaced generation and microgrids. Grounded on these concepts and some assumptions, it derived analytical equations to rate the energy capacity and active power required by an energy storage system for providing inertial and primary control to an ac power system. The proposed equations rely on parameters typically defined by system operators, industry standards or network codes, namely the steady-state and transient frequency ranges, the maximum rate of change of frequency, the desired equivalent moment of inertia and damping coefficient. Note that these parameters are independent from the technologies or topologies used in the energy storage devices and converters.

Using these results, this work also provided a step-by-step systematic procedure to initially size the remaining components of a converter-interfaced hybrid energy storage system connected to three-phase ac systems, i.e. the shared dc link, the grid converter and its LC filter. Finally, a case study of a wind-powered oil and gas platform in the North Sea was presented. It demonstrated with numerical examples how the proposed equations and the step-by-step procedure can be applied in a practical problem, where simulations in MATLAB Simulink validated the algebraic calculations and showed they slightly oversize energy storage devices. Not least, the case study demonstrated that the proposed method allows the system designer to take advantage of different energy storage technologies and set specific requirements for each storage device and converter in a hybrid system according to the type of frequency control action being provided and requirements set by industry standards and grid codes.

## DATA AVAILABILITY STATEMENT

The models and datasets presented in this study can be found in online repositories. The names of the repository/repositories and accession number(s) can be found at [78].

## FUNDING

This research was funded by the Research Council of Norway under the program PETROMAKS2, grant number 281986, project “Innovative Hybrid Energy System for Stable Power and Heat Supply in Offshore Oil & Gas Installation (HES-OFF)”, and through the PETROSENTER scheme, under the “Research Centre for Low-Emission Technology for Petroleum Activities on the Norwegian Continental Shelf” (LowEmission), grant number 296207.

## 8.5 REFERENCES

- [1] IEEE Std 1547-2018: IEEE Standard for Interconnection and Interoperability of Distributed Energy Resources with Associated Electric Power Systems Interfaces. 1547. IEEE New York, NY (2018). ISBN 978-1-5044-4639-6. URL <https://ieeexplore.ieee.org/servlet/opac?punumber=8332110>. Cited on p. 124, 129, 137, 139, 144.
- [2] IEEE Std 2030.8-2018: IEEE Standard for the Testing of Microgrid Controllers. IEEE New York, NY (2018). ISBN 978-1-5044-5050-8. URL <https://ieeexplore.ieee.org/servlet/opac?punumber=8444945>. Cited on p. 124.
- [3] Qiang Fu, Ahmad Hamidi, Adel Nasiri, Vijay Bhavaraju, Slobodan Bob Krstic, and Peter Theisen. The Role of Energy Storage in a Microgrid Concept: Examining the opportunities and promise of microgrids. *IEEE Electrification Magazine* 1 (2), 21–29 (December 2013). ISSN 2325-5897, 2325-5889. doi: 10.1109/MELE.2013.2294736. Cited on p. 124.
- [4] Goran Strbac, Nikos Hatzigiargyriou, Joao Pecas Lopes, Carlos Moreira, Aris Dimeas, and Dimitrios Papadaskalopoulos. Microgrids: Enhancing the Resilience of the European Megagrid. *IEEE Power and Energy Magazine* 13 (3), 35–43 (May 2015). ISSN 1540-7977. doi: 10.1109/MPE.2015.2397336. Cited on p. 124.
- [5] Sam Koohi-Kamali, V.V. Tyagi, N.A. Rahim, N.L. Panwar, and H. Mokhlis. Emergence of energy storage technologies as the solution for reliable operation of smart power systems: A review. *Renewable and Sustainable Energy Reviews* 25, 135–165 (September 2013). ISSN 13640321. doi: 10.1016/j.rser.2013.03.056. Cited on p. 125.
- [6] A.B. Gallo, J.R. Simões-Moreira, H.K.M. Costa, M.M. Santos, and E. Moutinho dos Santos. Energy storage in the energy transition context: A technology review. *Renewable and Sustainable Energy Reviews* 65, 800–822 (November 2016). ISSN 13640321. doi: 10.1016/j.rser.2016.07.028. Cited on p. 125.
- [7] Mustafa Farhadi and Osama Mohammed. Energy Storage Technologies for High-Power Applications. *IEEE Transactions on Industry Applications* 52 (3), 1953–1961 (May 2016). ISSN 0093-9994, 1939-9367. doi: 10.1109/TIA.2015.2511096. Cited on p. 125.
- [8] Reza Hemmati and Hedayat Saboori. Emergence of hybrid energy storage systems in renewable energy and transport applications – A review. *Renewable and Sustainable Energy*



- Reviews* **65**, 11–23 (November 2016). ISSN 13640321. doi: 10.1016/j.rser.2016.06.029. Cited on p. 125.
- [9] Mohammad Reza Aghamohammadi and Hajar Abdolahinia. A new approach for optimal sizing of battery energy storage system for primary frequency control of islanded Microgrid. *International Journal of Electrical Power & Energy Systems* **54**, 325–333 (January 2014). ISSN 01420615. doi: 10.1016/j.ijepes.2013.07.005. Cited on p. 125.
- [10] Mehrzad M. Bijaieh, Wayne W. Weaver, and Rush D. Robinett. Energy Storage Power and Energy Sizing and Specification Using HSSPFC. *Electronics* **9** (4), 638 (April 2020). ISSN 2079-9292. doi: 10.3390/electronics9040638. Cited on p. 125.
- [11] Mehrzad Mohammadi Bijaieh, Wayne W. Weaver, and Rush D. Robinett. Energy Storage Requirements for Inverter-Based Microgrids Under Droop Control in d-q Coordinates. *IEEE Transactions on Energy Conversion* **35** (2), 611–620 (June 2020). ISSN 0885-8969, 1558-0059. doi: 10.1109/TEC.2019.2959189. Cited on p. 125.
- [12] Vaclav Knap, Sanjay K. Chaudhary, Daniel-Ioan Stroe, Maciej Swierczynski, Bogdan-Ionut Craciun, and Remus Teodorescu. Sizing of an Energy Storage System for Grid Inertial Response and Primary Frequency Reserve. *IEEE Transactions on Power Systems* **31** (5), 3447–3456 (September 2016). ISSN 0885-8950, 1558-0679. doi: 10.1109/TPWRS.2015.2503565. Cited on p. 125.
- [13] Monika Sandelic, Daniel-Ioan Stroe, and Florin Iov. Battery Storage-Based Frequency Containment Reserves in Large Wind Penetrated Scenarios: A Practical Approach to Sizing. *Energies* **11** (11), 3065 (November 2018). ISSN 1996-1073. doi: 10.3390/en11113065. Cited on p. 125.
- [14] Luca Riboldi, Erick F. Alves, Marcin Pilarczyk, Elisabetta Tedeschi, and Lars O. Nord. Optimal Design of a Hybrid Energy System for the Supply of Clean and Stable Energy to Offshore Installations. *Frontiers in Energy Research* **8**, 326 (December 2020). ISSN 2296-598X. doi: 10.3389/fenrg.2020.607284. Cited on p. 125, 146.
- [15] Carlos Gamarra and Josep M. Guerrero. Computational optimization techniques applied to microgrids planning: A review. *Renewable and Sustainable Energy Reviews* **48**, 413–424 (August 2015). ISSN 13640321. doi: 10.1016/j.rser.2015.04.025. Cited on p. 126.
- [16] Mohammad A.A. Al-Jaafreh and Geev Mokryani. Planning and operation of LV distribution networks: A comprehensive review. *IET Energy Systems Integration* **1** (3), 133–146 (September 2019). ISSN 2516-8401. doi: 10.1049/iet-esi.2019.0013. Cited on p. 126.
- [17] Daniel Duckwitz. Power System Inertia: Derivation of Requirements and Comparison of Inertia Emulation Methods for Converter-based Power Plants. *PhD thesis*. University of Kassel Kassel, Germany (March 2019). URL <http://doi.org/doi:10.17170/kobra-20190510451>. Cited on p. 126.
- [18] ENTSO-E. Fast Frequency Reserve – Solution to the Nordic inertia challenge. Technical report ENTSO-E (December 2019). URL <https://www.epressi.com/media/userfiles/107305/1576157646/fast-frequency-reserve-solution-to-the-nordic-inertia-challenge-1.pdf>. Cited on p. 126, 129, 130.
- [19] Gary W. Chang, Ching-Sheng Chuang, Tai-Ken Lu, and Ching-Chung Wu. Frequency-regulating reserve constrained unit commitment for an isolated power system. *IEEE Transactions on Power Systems* **28** (2), 578–586 (May 2013). ISSN 0885-8950, 1558-0679. doi: 10.1109/TPWRS.2012.2208126. Cited on p. 126, 127.
- [20] Yunfeng Wen, Wenyuan Li, Gang Huang, and Xuan Liu. Frequency Dynamics Constrained Unit Commitment With Battery Energy Storage. *IEEE Transactions on Power Systems* **31** (6), 5115–5125 (November 2016). ISSN 0885-8950, 1558-0679. doi: 10.1109/TPWRS.2016.2521882. Cited on p. 126, 127.
- [21] Shrirang Abhyankar, Guangchao Geng, Mihai Anitescu, Xiaoyu Wang, and Venkata Di-

- navahi. Solution techniques for transient stability-constrained optimal power flow – Part I. *IET Generation, Transmission & Distribution* **11** (12), 3177–3185 (August 2017). ISSN 1751-8687, 1751-8695. doi: 10.1049/iet-gtd.2017.0345. Cited on p. 126.
- [22] Guangchao Geng, Shrirang Abhyankar, Xiaoyu Wang, and Venkata Dinavahi. Solution techniques for transient stability-constrained optimal power flow – Part II. *IET Generation, Transmission & Distribution* **11** (12), 3186–3193 (August 2017). ISSN 1751-8687, 1751-8695. doi: 10.1049/iet-gtd.2017.0346. Cited on p. 126.
- [23] Nga Nguyen, Saleh Almasabi, Atri Bera, and Joydeep Mitra. Optimal Power Flow Incorporating Frequency Security Constraint. *IEEE Transactions on Industry Applications* **55** (6), 6508–6516 (November 2019). ISSN 0093-9994, 1939-9367. doi: 10.1109/TIA.2019.2938918. Cited on p. 126.
- [24] Sina Y. Caliskan and Paulo Tabuada. Uses and abuses of the swing equation model. In *2015 54th IEEE Conference on Decision and Control (CDC)* pages 6662–6667 Osaka (December 2015). IEEE. ISBN 978-1-4799-7886-1. doi: 10.1109/CDC.2015.7403268. Cited on p. 126, 127.
- [25] Erick Fernando Alves, Gilbert Bergna-Diaz, Danilo Iglesias Brandao, and Elisabetta Tedeschi. Sufficient Conditions for Robust Frequency Stability of AC Power Systems. *IEEE Transactions on Power Systems* **36**, 2684–2692 (May 2021). ISSN 0885-8950, 1558-0679. doi: 10.1109/TPWRS.2020.3039832. Cited on p. 126, 133, 136.
- [26] R. E. Doherty and C. A. Nickle. Synchronous Machines III - Torque-Angle Characteristics Under Transient Conditions. *Transactions of the American Institute of Electrical Engineers* **XLVI**, 1–18 (January 1927). ISSN 0096-3860. doi: 10.1109/T-AIEE.1927.5061336. Cited on p. 127.
- [27] Charles Concordia. Synchronous machines, theory and performance. Number viii, 224 p. in General Electric Series. Wiley New York (1951). URL [//catalog.hathitrust.org/Record/001617157](http://catalog.hathitrust.org/Record/001617157). Cited on p. 127.
- [28] John J. Grainger and William D. Stevenson. Power system analysis. McGraw-Hill Series in Electrical and Computer Engineering. McGraw-Hill New York (1994). ISBN 978-0-07-061293-8. Cited on p. 127.
- [29] Edward Wilson Kimbark. Power system stability. IEEE Press Power Systems Engineering Series. IEEE Press New York (1995). ISBN 978-0-7803-1135-0. Cited on p. 127.
- [30] P. Kundur, Neal J. Balu, and Mark G. Lauby. Power system stability and control. The EPRI Power System Engineering. McGraw-Hill New York (1994). ISBN 978-0-07-035958-1. Cited on p. 127, 131, 133.
- [31] Jan Machowski, Janusz W. Bialek, and J. R. Bumby. Power system dynamics: Stability and control. Wiley Chichester, U.K 2nd ed edition (2008). ISBN 978-0-470-72558-0. Cited on p. 127, 133.
- [32] Carlos Tavora and Otto M. Smith. Characterization of Equilibrium and Stability in Power Systems. *IEEE Transactions on Power Apparatus and Systems* **PAS-91** (3), 1127–1130 (May 1972). ISSN 0018-9510. doi: 10.1109/TPAS.1972.293468. Cited on p. 127.
- [33] Florian Dörfler and Francesco Bullo. Synchronization and Transient Stability in Power Networks and Nonuniform Kuramoto Oscillators. *SIAM Journal on Control and Optimization* **50** (3), 1616–1642 (January 2012). ISSN 0363-0129, 1095-7138. doi: 10.1137/110851584. Cited on p. 127, 133.
- [34] Gauthier Delille, Bruno Francois, and Gilles Malarange. Dynamic Frequency Control Support by Energy Storage to Reduce the Impact of Wind and Solar Generation on Isolated Power System’s Inertia. *IEEE Transactions on Sustainable Energy* **3** (4), 931–939 (October 2012). ISSN 1949-3029, 1949-3037. doi: 10.1109/TSSTE.2012.2205025. Cited on p. 127.
- [35] I. Egidio, L. Sigrist, E. Lobato, L. Rouco, and A. Barrado. An ultra-capacitor for frequency stability enhancement in small-isolated power systems: Models, simulation and field tests.

- Applied Energy* **137**, 670–676 (January 2015). ISSN 03062619. doi: 10.1016/j.apenergy.2014.08.041. Cited on p. 127.
- [36] Luca Riboldi, Erick F Alves, Marcin Pilarczyk, Elisabetta Tedeschi, and Lars O. Nord. Innovative hybrid energy system for stable power and heat supply in offshore oil & gas installation (HES-OFF): System design and grid stability. In *Proceedings of the 30th European Symposium on Computer Aided Process Engineering (ESCAPE30)* volume A pages 211–216 Milano, Italy (May 2020). Elsevier. doi: 10.1016/B978-0-12-823377-1.50036-7. Cited on p. 127, 141.
- [37] Hamed Ahmadi and Hassan Ghasemi. Security-Constrained Unit Commitment With Linearized System Frequency Limit Constraints. *IEEE Transactions on Power Systems* **29** (4), 1536–1545 (July 2014). ISSN 0885-8950, 1558-0679. doi: 10.1109/TPWRS.2014.2297997. Cited on p. 127.
- [38] Comission Regulation (EU). Network code on requirements for grid connection of generators (April 2016). URL <http://data.europa.eu/eli/reg/2016/631/oj>. Cited on p. 129, 137, 139, 144.
- [39] Joseph H Eto, John Undrill, Ciaran Roberts, Peter Mackin, and Jeffrey Ellis. Frequency Control Requirements for Reliable Interconnection Frequency Response. Technical Report LBNL-2001103 Lawrence Berkeley National Laboratory Berkley, CA (February 2018). Cited on p. 129, 130, 133, 135.
- [40] Comission Regulation (EU). Guideline on electricity transmission system operation (August 2017). URL <http://data.europa.eu/eli/reg/2017/1485/oj>. Cited on p. 129, 135.
- [41] Tine L. Vandoorn, Juan C. Vasquez, Jeroen De Kooning, Josep M. Guerrero, and Lieven Vandevelde. Microgrids: Hierarchical Control and an Overview of the Control and Reserve Management Strategies. *IEEE Industrial Electronics Magazine* **7** (4), 42–55 (December 2013). ISSN 1932-4529. doi: 10.1109/MIE.2013.2279306. Cited on p. 130, 133.
- [42] Salvatore D’Arco and Jon Are Suul. Virtual synchronous machines — Classification of implementations and analysis of equivalence to droop controllers for microgrids. In *PowerTech* Grenoble, France (June 2013). IEEE. ISBN 978-1-4673-5669-5. doi: 10.1109/PTC.2013.6652456. Cited on p. 130.
- [43] Jingyang Fang, Hongchang Li, Yi Tang, and Frede Blaabjerg. On the Inertia of Future More-Electronics Power Systems. *IEEE Journal of Emerging and Selected Topics in Power Electronics* **7** (4), 2130–2146 (December 2019). ISSN 2168-6777, 2168-6785. doi: 10.1109/JESTPE.2018.2877766. Cited on p. 130, 131, 133.
- [44] Jürgen Marchgraber, Christian Alács, Yi Guo, Wolfgang Gawlik, Adolfo Anta, Alexander Stimmer, Martin Lenz, Manuel Froschauer, and Michaela Leonhardt. Comparison of Control Strategies to Realize Synthetic Inertia in Converters. *Energies* **13** (13), 3491 (July 2020). ISSN 1996-1073. doi: 10.3390/en13133491. Cited on p. 130.
- [45] Augusto Matheus dos Santos Alonso, Leonardo Carlos Afonso, Danilo Iglesias Brandao, Elisabetta Tedeschi, and Fernando Pinhabel Marafao. Considerations on Communication Infrastructures for Cooperative Operation of Smart Inverters. In *2019 IEEE 15th Brazilian Power Electronics Conference and 5th IEEE Southern Power Electronics Conference (COBEP/SPEC)* pages 1–6 Santos, Brazil (December 2019). IEEE. ISBN 978-1-72814-180-0. doi: 10.1109/COBEP/SPEC44138.2019.9065382. Cited on p. 130, 133.
- [46] Danilo I. Brandao, Lucas S. Araujo, Augusto M. S. Alonso, Geovane L. dos Reis, Eduardo V. Liberado, and Fernando P. Marafao. Coordinated Control of Distributed Three-and Single-phase Inverters Connected to Three-Phase Three-Wire Microgrids. *IEEE Journal of Emerging and Selected Topics in Power Electronics* pages 1–1 (2019). ISSN 2168-6777, 2168-6785. doi: 10.1109/JESTPE.2019.2931122. Cited on p. 130.
- [47] Federico Milano, Florian Dorfler, Gabriela Hug, David J. Hill, and Gregor Verbic. Foundations and Challenges of Low-Inertia Systems (Invited Paper). In *2018 Power Systems*

- Computation Conference (PSCC)* pages 1–25 Dublin (June 2018). IEEE. ISBN 978-1-910963-10-4. doi: 10.23919/PSCC.2018.8450880. Cited on p. 132, 133.
- [48] Peter W. Sauer, M. A. Pai, and J. H. Chow. *Power system dynamics and stability: With synchrophasor measurement and power system toolbox*. Wiley Hoboken, NJ, USA second edition edition (2017). ISBN 978-1-119-35577-9. Cited on p. 133.
- [49] Danilo I. Brandao, Willian M. Ferreira, Augusto M. S. Alonso, Elisabetta Tedeschi, and Fernando P. Marafao. Optimal Multiobjective Control of Low-Voltage AC Microgrids: Power Flow Regulation and Compensation of Reactive Power and Unbalance. *IEEE Transactions on Smart Grid* **11** (2), 1239–1252 (March 2020). ISSN 1949-3053, 1949-3061. doi: 10.1109/TSG.2019.2933790. Cited on p. 133.
- [50] Comission Regulation (EU). Guideline on capacity allocation and congestion management (July 2015). URL <http://data.europa.eu/eli/reg/2015/1222/oj>. Cited on p. 133.
- [51] Abbas A Akhil, Georgianne Huff, Aileen B Currier, Benjamin C Kaun, Dan M Rastler, Stella Bingqing Chen, Andrew L Cotter, Dale T Bradshaw, and William D Gauntlett. DOE/EPRI Electricity Storage Handbook in Collaboration with NRECA. Technical Report SAND2015-1002 Sandia National Laboratories Albuquerque, NM (January 2015). URL <https://prod.sandia.gov/techlib-noauth/access-control.cgi/2015/151002.pdf>. Cited on p. 134.
- [52] L. Malesani, L. Rossetto, P. Tenti, and P. Tomasin. AC/DC/AC PWM converter with reduced energy storage in the DC link. *IEEE Transactions on Industry Applications* **31** (2), 287–292 (March-April/1995). ISSN 00939994. doi: 10.1109/28.370275. Cited on p. 138.
- [53] W.J. Sarjeant, I.W. Clelland, and R.A. Price. Capacitive components for power electronics. *Proceedings of the IEEE* **89** (6), 846–855 (June 2001). ISSN 00189219. doi: 10.1109/5.931475. Cited on p. 138.
- [54] Infineon Technologies. Power and Sensing Selection Guide 2020 (April 2020). URL [https://www.infineon.com/dgdlac/Infineon-Power\\_and\\_Sensing\\_2020-ProductSelectionGuide-v00\\_01-EN.pdf](https://www.infineon.com/dgdlac/Infineon-Power_and_Sensing_2020-ProductSelectionGuide-v00_01-EN.pdf). Cited on p. 138.
- [55] Paolo Tenti, Alessandro Costabeber, Paolo Mattavelli, Fernando Pinhabel Marafao, and Helmo K. M. Paredes. Load Characterization and Revenue Metering Under Non-Sinusoidal and Asymmetrical Operation. *IEEE Transactions on Instrumentation and Measurement* **63** (2), 422–431 (February 2014). ISSN 0018-9456, 1557-9662. doi: 10.1109/TIM.2013.2280480. Cited on p. 139.
- [56] Remus Narcis Beres, Xiongfei Wang, Marco Liserre, Frede Blaabjerg, and Claus Leth Bak. A Review of Passive Power Filters for Three-Phase Grid-Connected Voltage-Source Converters. *IEEE Journal of Emerging and Selected Topics in Power Electronics* **4** (1), 54–69 (March 2016). ISSN 2168-6777, 2168-6785. doi: 10.1109/JESTPE.2015.2507203. Cited on p. 139.
- [57] Robert W Erickson and Dragan Maksimović. *Fundamentals of Power Electronics*. Springer Boston, MA, USA second edition (2001). ISBN 978-0-306-48048-5. URL <https://doi.org/10.1007/b100747>. Cited on p. 139.
- [58] Marco Liserre, Frede Blaabjerg, and Antonio Dell’Aquila. Step-by-step design procedure for a grid-connected three-phase PWM voltage source converter. *International Journal of Electronics* **91** (8), 445–460 (August 2004). ISSN 0020-7217, 1362-3060. doi: 10.1080/00207210412331306186. Cited on p. 139.
- [59] R. Peña-Alzola, M. Liserre, F. Blaabjerg, R. Sebastián, J. Dannehl, and F. W. Fuchs. Analysis of the Passive Damping Losses in LCL-Filter-Based Grid Converters. *IEEE Transactions on Power Electronics* **28** (6), 2642–2646 (June 2013). ISSN 0885-8993, 1941-0107. doi: 10.1109/TPEL.2012.2222931. Cited on p. 139.
- [60] ABB. Technical data for vacuum cast coil dry-type transformers. Technical Report 1LES100021- ZD ABB Zaragoza, Spain (2016). URL <https://search.abb>.

- [com/library/Download.aspx?DocumentID=1LES100021-ZD&LanguageCode=en&DocumentPartId=&Action=Launch](https://com/library/Download.aspx?DocumentID=1LES100021-ZD&LanguageCode=en&DocumentPartId=&Action=Launch). Cited on p. 140.
- [61] Siemens. The GEAFOL Neo: The optimum foundation for power distribution. Technical Report EMTR-B10021-00-7600 Siemens AG Erlangen, Germany (2017). URL <https://assets.new.siemens.com/siemens/assets/api/uuid:4530574337916a37995ba7471cbab670f92b2948/geafol-neo-en.pdf>. Cited on p. 140.
- [62] K. Jalili and S. Bernet. Design of LCL Filters of Active-Front-End Two-Level Voltage-Source Converters. *IEEE Transactions on Industrial Electronics* **56** (5), 1674–1689 (May 2009). ISSN 0278-0046. doi: 10.1109/TIE.2008.2011251. Cited on p. 140.
- [63] Parikshith Channegowda and Vinod John. Filter Optimization for Grid Interactive Voltage Source Inverters. *IEEE Transactions on Industrial Electronics* **57** (12), 4106–4114 (December 2010). ISSN 0278-0046, 1557-9948. doi: 10.1109/TIE.2010.2042421. Cited on p. 140.
- [64] A. A. Rockhill, Marco Liserre, Remus Teodorescu, and Pedro Rodriguez. Grid-Filter Design for a Multimegawatt Medium-Voltage Voltage-Source Inverter. *IEEE Transactions on Industrial Electronics* **58** (4), 1205–1217 (April 2011). ISSN 0278-0046, 1557-9948. doi: 10.1109/TIE.2010.2087293. Cited on p. 140.
- [65] Jonas Muhlethaler, Mario Schweizer, Robert Blattmann, Johann W. Kolar, and Andreas Ecklebe. Optimal Design of LCL Harmonic Filters for Three-Phase PFC Rectifiers. *IEEE Transactions on Power Electronics* **28** (7), 3114–3125 (July 2013). ISSN 0885-8993, 1941-0107. doi: 10.1109/TPEL.2012.2225641. Cited on p. 140.
- [66] Remus Narcis Beres, Xiongfei Wang, Frede Blaabjerg, Marco Liserre, and Claus Leth Bak. Optimal Design of High-Order Passive-Damped Filters for Grid-Connected Applications. *IEEE Transactions on Power Electronics* **31** (3), 2083–2098 (March 2016). ISSN 0885-8993, 1941-0107. doi: 10.1109/TPEL.2015.2441299. Cited on p. 140.
- [67] Jinming Xu and Shaojun Xie. LCL-resonance damping strategies for grid-connected inverters with LCL filters: A comprehensive review. *Journal of Modern Power Systems and Clean Energy* **6** (2), 292–305 (March 2018). ISSN 2196-5625, 2196-5420. doi: 10.1007/s40565-017-0319-7. Cited on p. 140.
- [68] Joan Rocabert, Ruben Capo-Misut, Raul Santiago Munoz-Aguilar, Jose Ignacio Candela, and Pedro Rodriguez. Control of Energy Storage System Integrating Electrochemical Batteries and Supercapacitors for Grid-Connected Applications. *IEEE Transactions on Industry Applications* **55** (2), 1853–1862 (March 2019). ISSN 0093-9994, 1939-9367. doi: 10.1109/TIA.2018.2873534. Cited on p. 141.
- [69] Lucas S. Xavier, William C. S. Amorim, Allan F. Cupertino, Victor F. Mendes, Wallace C. do Boaventura, and Heverton A. Pereira. Power converters for battery energy storage systems connected to medium voltage systems: A comprehensive review. *BMC Energy* **1** (1), 7 (December 2019). ISSN 2524-4469. doi: 10.1186/s42500-019-0006-5. Cited on p. 141.
- [70] IEC 61892-2:2019 Mobile and fixed offshore units - Electrical installations - Part 2: System design. IEC Geneva, Switzerland (April 2019). ISBN 978-2-8322-6667-0. URL <https://webstore.iec.ch/publication/6083>. Cited on p. 141.
- [71] P Pei, Q Chang, and T Tang. A quick evaluating method for automotive fuel cell lifetime. *International Journal of Hydrogen Energy* **33** (14), 3829–3836 (July 2008). ISSN 03603199. doi: 10.1016/j.ijhydene.2008.04.048. Cited on p. 142.
- [72] Håvard Devold. Oil and gas production handbook: An introduction to oil and gas production, transport, refining and petrochemical industry. ABB Oslo (2013). ISBN 978-82-997886-3-2. URL [https://library.e.abb.com/public/34d5b70e18f7d6c8c1257be500438ac3/Oil%20and%20gas%20production%20handbook%20ed3x0\\_web.pdf](https://library.e.abb.com/public/34d5b70e18f7d6c8c1257be500438ac3/Oil%20and%20gas%20production%20handbook%20ed3x0_web.pdf). Cited on p. 142.
- [73] DNV-GL. Joint Industry Project: Wind-powered water injection. Technical report DNV-GL Høvik, Norway (April 2016). URL <https://www.dnvgl.com/research/>

- [power-and-renewables/pr-win-win.html](#). Cited on p. 142.
- [74] Santiago Sanchez, Elisabetta Tedeschi, Jesus Silva, Muhammad Jafar, and Alexandra Marichalar. Smart load management of water injection systems in offshore oil and gas platforms integrating wind power. *IET Renewable Power Generation* **11** (9), 1153–1162 (July 2017). ISSN 1752-1416, 1752-1424. doi: 10.1049/iet-rpg.2016.0989. Cited on p. 142.
- [75] Erick Alves, Santiago Sanchez, Danilo Brandao, and Elisabetta Tedeschi. Smart Load Management with Energy Storage for Power Quality Enhancement in Wind-Powered Oil and Gas Applications. *Energies* **12** (15), 2985 (August 2019). ISSN 1996-1073. doi: 10.3390/en12152985. Cited on p. 142.
- [76] Saft. Intensium max+ 20p product datasheet (March 2017). URL <https://www.saftbatteries.com/products-solutions/products/intensium%C2%AE-mini-outdoor-energy-storage-system>. Cited on p. 144.
- [77] Siemens. Sinacon pv photovoltaic central inverter: Technical data. Technical Report SIDS-B10020-00-7600 Siemens AG Erlangen, Germany (2020). URL <https://assets.new.siemens.com/siemens/assets/api/uuid:cb65b0d3-6425-48f5-92cb-cc217d2d5285/sinacon-pv-technical-data-en.pdf>. Cited on p. 144.
- [78] Erick F. Alves and Daniel dos Santos Mota. Efantnu/hybrid-ess-design: Review 1 release. Zenodo (March 2021). Cited on p. 144, 147, 152.
- [79] Erick F. Alves. Efantnu/pwrsys-matlab: Initial release. Zenodo (December 2020). Cited on p. 145.



## CHAPTER 9

### *Allocation of spinning reserves for autonomous grids subject to frequency stability constraints and short-term solar power variations*

---

Erick Fernando Alves<sup>1</sup>, Louis Polleux<sup>2,3</sup>, Gilles Guerassimoff<sup>3</sup>, Magnus Korpås<sup>1</sup>, and Elisabetta Tedeschi<sup>1,4</sup>

Journal paper submitted to: *Applied Energy*.  
Pre-print DOI: [10.48550/arXiv.2203.07233](https://doi.org/10.48550/arXiv.2203.07233)



**Open Access** This work is licensed under a Creative Commons Attribution 4.0 International License. It means that unrestricted use, sharing, adaptation, distribution, and reproduction in any medium or format are allowed, as long as the original author(s) and the source are appropriately credited, a link to the Creative Commons license is provided, and any changes made are indicated. To view a copy of this license, please visit <http://creativecommons.org/licenses/by/4.0/>.

© Alves, Polleux, Guerassimoff, Korpås and Tedeschi, 2021.

#### **Author Contributions**

Conceptualization, E.A., L.P., G.G., and E.T.; methodology, E.A., L.P., and M.K.; software, L.P.; validation, E.A. and L.P.; formal analysis, E.A. and L.P.; investigation, E.A. and L.P.; resources, G.G. and E.T.; data curation, E.A. and L.P.; writing - original draft preparation, E.A. and L.P.; writing - review and editing, G.G., M.K. and E.T.; visualization, E.A.; supervision, G.G., M.K. and E.T.; project administration, G.G. and E.T.; funding acquisition, G.G. and E.T.

---

<sup>1</sup>Department of Electric Power Engineering, NTNU, 7034 Trondheim, Norway.

<sup>2</sup>Center for Applied Mathematics, Mines Paristech PSL, 06904 Sophia Antipolis, France.

<sup>3</sup>Research and Development, TotalEnergies, 92400 Courbevoie, France.

<sup>4</sup>Department of Industrial Engineering, University of Trento, 38123 Trento, Italy.



## ABSTRACT

Low-inertia, isolated power systems face the problem of resiliency to power variations. The integration of renewable energy sources, such as wind and solar **photovoltaic**, pushes the boundaries of this issue further. Higher shares of renewables requires better evaluations of electrical system stability, to avoid severe safety and economic consequences. Accounting for frequency stability requirements and allocating proper spinning reserves, therefore becomes a topic of pivotal importance in the long-term planning and operational management of power systems. In this paper, dynamic frequency constraints are proposed to ensure resiliency during short-term power variations due to, for example, wind gusts or cloud passage. The use of the proposed constraints is exemplified in a case study, the constraints being integrated into a mixed-integer linear programming algorithm for sizing the optimal capacities of solar **photovoltaic** and battery energy storage resources in an isolated industrial plant. Outcomes of this case study show that reductions in the levelized cost of energy and carbon emissions can be overestimated by 8.0% and 10.8% respectively, where frequency constraints are neglected. The proposed optimal sizing is validated using time-domain simulations of the case study. The results indicate that this optimal system is frequency stable under the worst-case contingency.

## 9.1 INTRODUCTION

The depletion of mature **O&G** fields reduces the energy return on investment of the field and increases the emission of nitrogen oxides and **GHG** [1]. The use of renewable energy sources in **O&G** operations has therefore become an active research area in recent years. Groups have analyzed this challenge from a broad range of perspectives [2–9]. It is, however, widely accepted that the planning or operation of hybrid energy systems in the **O&G** industry requires the solution of an optimization problem. The objective of such optimization can differ considerably. The power balance of the energy system is, however, a physical constraint that must always be satisfied.

Most **O&G** plants, platforms and vessels are supplied ac power by low-inertia, isolated systems [10]. Large active power variations in and considerable deviations from the system rated frequency can, however, occur where the penetration of renewable energy sources in such systems is high. This is a problem that is also found in other autonomous power system, such as islands [11, 12] and community microgrids [13]. Frequency stability constraints and the proper sizing of spinning reserves, such as **FCR** and **FRR**, are therefore



important dimensioning aspects and should therefore be given special attention in optimization algorithms [14].

Short-term variations caused by cloud passage across solar PV parks or wind gusts at wind farms can furthermore saturate the ramping capabilities of other generators. The relationship between renewable energy sources penetration and variability, size of ESSs, scheduling decisions and frequency stability should therefore be investigated in more detail. Large interconnected and meshed electricity networks also are progressively behaving more as low-inertia systems, as the green shift progresses worldwide and penetration of renewable energy sources continues [15, 16]. Interest in the topic of this paper therefore is wide.

### 9.1.1 Literature review

Reliability-constrained unit commitment is described, for example, in [17–19], and addresses the unit commitment problem during unexpected events such as the severe loss of load, generation or transmission capacity. The strategies applied to mitigate this include  $n+1$  redundancy, and spinning reserve for frequency containment and restoration. [20] for example proposed a two-stage stochastic mixed integer linear programming formulation for the calculation of unit commitment and reserve scheduling, at frequency deviations of 0 and  $\pm 10$  mHz. [21] also discuss formulations for addressing wind power variations and the correct allocation from ESSs of spinning reserves. Generator contingency was, in this, considered to be the largest wind power fluctuation from one optimization time-step to another. Power balances were handled before and after contingencies in these works, and without generator transient period dynamics or ramping capacities being taken into account.

[22] have proposed frequency-constrained unit commitment problem implementation alternatives to circumvent these limitations. [23, 24] thoroughly discuss the challenges of a frequency-constrained model. Options such as the use of maximum ramping capacity or minimum value of inertia were evaluated, but can lead to a nonlinear problem. This can, however, be handled by a Benders decomposition. [25] introduced a nonlinear model that includes frequency security constraints and the dynamics of the transient period. This, however, requires the use of a genetic algorithm to solve the optimization problem. [6] also use a genetic algorithm to optimally size the energy system of an offshore platform interconnected with a wind farm. The maximum ramping capacity of generators and frequency stability limits were furthermore evaluated using time-domain simulations of worst-case scenarios for each candidate solution.

[26] integrated the power drops observed in solar PV, within 15-minute time windows, into the constraints of an optimal planning problem, this accounting for the stochastic variation of solar irradiance. A recent work [27], however, highlights the varying duration and magnitude of the short-term variability of PV plants, and also that maximum perturbation may rise to 60 % of the plant's rated power in less than 30 s. These short-term variations must be taken into account if realistic decisions on storage investment or unit scheduling in optimization algorithms are to be achieved. [14] furthermore provide an updated review of the frequency-constrained unit commitment problem, a classification of the different approaches documented in the literature, and a discussion of their many shortcomings. They also proposed a linear model that includes frequency constraints directly in a mixed integer linear programming algorithm, and that therefore does not require the use of external time-domain simulations in the assessment of solution security. They did not, however, consider the effect of fast short-term variations in renewable energy sources, combined with generator ramping restrictions and use of ESSs on frequency stability.

Challenges therefore still remain in the efficient sizing, planning and operation of autonomous, low-inertia power systems with high renewable energy sources penetration, especially wind and solar PV.

### 9.1.2 Paper contributions

This paper addresses some of the modeling challenges and shortcomings described above, and introduces a set of algebraic frequency stability constraints that can be directly applied to linear optimization formulations of the unit commitment problem in low-inertia autonomous power system with high renewable energy sources penetration. Practical issues such as limited generator ramping capacities and variability of renewable energy sources are taken into consideration. Short-term frequency variations are also used to reduce the conservatism of a unit commitment under uncertainty, which permits complementary FCR and FRR action and a reduction in the power required from ESSs.

These ideas are exemplified in a case study of the integration of a solar PV plant and a battery ESS into an existing isolated industrial installation fed by GTs. A mixed integer linear programming algorithm is used to solve a rolling frequency-constrained unit commitment problem, and to optimally size the installed capacity of solar PV and battery ESS. The renewable energy source short-term variability is evaluated by using a method recently published in [27], that identifies equivalent solar ramping scenarios during cloud passage.

The novel proposal, described in detail in [Sec. 9.2.3](#), are linear constraints for frequency stability that model tolerated frequency dynamics and the complementary [FCR](#) and [FRR](#) action taking place during short-term power variations, such as cloud passage events in solar [PV](#) installations or wind gusts in wind farms. This allows a significant reduction in the amount of [FCR](#) and consequently the rated power of an [ESS](#) designed to support the grid in such events, as demonstrated by the results of the case study in [Sec. 9.3.2](#). The frequency-stability results for the constrained and non-constrained implementation were compared, and major differences were highlighted, being the solution data obtained from this also used in a time-domain simulation to validate the results under the worst-case scenario.

## 9.2 ADDRESSING FREQUENCY STABILITY WITH LINEAR CONSTRAINTS

This section reviews the equations that describe the frequency dynamics of a power system, and the types of spinning reserves required to ensure frequency stability. The rationale for determining spinning reserves by obtaining a set of algebraic expressions from the dynamic equations, and applying these as constraints to the linear optimization problem, is also introduced. The first proposed formulation treats the sudden disconnection of loads or generators. The next formulation addresses the problem of the short-term variation of loads or renewable energy sources, this requiring gradual compensation by dispatchable generators with limited ramping capacity.

### 9.2.1 Frequency stability and spinning reserves

The simplified model of a flywheel spinning at angular speed  $\omega_s$  can be used to express the dynamics of frequency in a power system. The rotating masses of all synchronous generators and motors are represented by an equivalent moment of inertia  $J$ . Generators deliver, at one end of the shaft, energy to the flywheel via torque  $T_G$ . Load removes energy through  $T_L$  at the other shaft end. The natural and controlled damping of the system is represented by coefficient  $B$ . Applying Newton's second law of motion to this simplified model, and multiplying both sides by the angular speed  $\omega$ , therefore gives the following equation [28]:

$$\omega J \dot{\omega} = P_G - P_L - B(\omega - \omega_s) \quad (9.1)$$

where  $P_G$ ,  $P_L$  are respectively the active power delivered by generators and consumed by loads.

Eq. (9.1), which is also known as the Swing Equation, represents the power balance that is required to maintain this system at its rated angular speed  $\omega_s$ . The frequency deviation  $\tilde{f} = \frac{\omega - \omega_s}{\omega_s}$  can, after this equation has been normalized by  $\omega_s$  and by the total apparent power of the generators  $S_n$ , be estimated by [28]:

$$(1 + \tilde{f})M\dot{\tilde{f}} = p_G - p_L - D\tilde{f} \quad (9.2)$$

where  $M, D, p_G, p_L$  are respectively the normalized inertia, damping, and active powers delivered by generators and consumed by loads.

The system is considered to be frequency stable [29] where any power imbalance  $\tilde{f}$  remains within intervals  $\pm r_{tr}$  during transient conditions and  $\pm r_{ss}$  during steady-state conditions. These intervals are often defined in grid codes or industry standards. In Europe,  $r_{ss} = \pm 1\%$  and  $r_{tr} = \pm 3\%$  are specified for generators connected to transmission [30] or distribution systems [31, 32]. Wider limits are normally specified for low-inertia, autonomous systems, for example  $r_{ss}$  between 2 and 5%, and  $r_{tr}$  between 5 and 10% for fixed and mobile offshore units [33].

The minimum controlled damping  $D_{min}$  that generators must provide when assuming a steady-state in Eq. (9.2) ( $\dot{\tilde{f}} = 0$ ), and  $\tilde{f} < 1\%$  and null natural damping from loads, can be approximated by:

$$D_{min}r_{ss} \geq P_b \quad (9.3)$$

where  $P_b = (p_G - p_L)$  represents the maximum continuous imbalance that the power system can withstand and still maintain frequency stability.  $P_b$  also defines the minimum level of spinning reserves that are required for frequency variations to be kept within the permitted range of  $\pm r_{ss}$ . This is therefore referred to as **frequency containment reserve (FCR)** [34]. The assumptions used to derive Eq. (9.3) may underestimate  $D_{min}$  when  $\tilde{f}$  values of more than 1% are possible [35]. A more robust approximation must therefore be given:

$$D_{min}r_{ss}(1 - r_{tr}) \geq P_b \quad (9.4)$$

Note that the **FCR** strategy (proportional control) cannot restore frequency to its rated value. Achieving the zero steady-state error ( $\tilde{f} = 0$ ) therefore requires  $p_G$  and  $p_L$  to be matched by generator re-dispatching, through integral control [28, 36]. This requires additional spinning reserves, which are referred to as **frequency restoration reserve (FRR)** [34]. The action of **FRR**, **FCR** constraining frequency during disturbances to defined bands, therefore can be slow. This is desirable, not just to avoid new disturbances, but also to accommodate the ramping limitations of generators.

A single generator can provide both **FCR** and **FRR**. This may not, however, be the optimal solution from a technical or an economic perspective. **GTs** can, for example, usually provide both types of reserves simultaneously. Excessive activation of **FCR** on **GTs** can, however, increase actuator wear and tear and increase maintenance costs. A more suitable **FCR** could be batteries designed to supply large amounts of power for short periods of time. Their participation in **FRR** will, however, usually require large energy storage capacity, which will increase investment costs and space requirements.

The optimal allocation of spinning reserves can, even for small power systems, therefore quickly become a complex process. An optimization algorithm is therefore often used in sizing and operational decisions. The following sections present the proposed algebraic constraints. These are based on the frequency dynamics of a power system, and can help in the determination of the optimal allocation of **FCR** and **FRR**.

### 9.2.2 Formulation 1: constraints for sudden load or generation loss

The following constraints must be met when considering the assumptions and conditions imposed by Eq. (9.3), for generators participating in **FCR**:

$$\forall m, \forall h, \quad P_{m,h}^{FCR} \leq D_m r_{ss} \quad (9.5)$$

$$\forall m, \forall h, \quad P_m^{min} + P_{m,h}^{FCR} \leq P_{m,h} \leq P_m^{max} - P_{m,h}^{FCR} \quad (9.6)$$

where  $P_{m,h}^{FCR}$ ,  $P_m^{min}$ ,  $P_m^{max}$ ,  $P_{m,h}$  are respectively the assigned **FCR** contribution, the minimum, the maximum and the current commitment of generator  $m$  in time step  $h$ .

The sum of **FCR** provided by all generators is to also, at each time step  $h$ , be greater than the worst-case power disturbance  $P_{b,h}$ :

$$\forall h, \quad \sum_m P_{m,h}^{FCR} \geq P_{b,h} \quad (9.7)$$

$P_{b,h}$  varies with time, because it depends on the worst expected sudden load or generation loss for the current state of the power system. This value is normally, in a security assessment, obtained from the evaluation of possible contingencies. This complex topic is, however, beyond the scope of this work, a simplified approach however being presented in Sec. 9.3.1 and used in this paper. A deeper discussion of this can be found in [37]. Note that Eq. (9.5) can be rewritten based on the assumptions and conditions imposed by Eq. (9.4), where  $\tilde{f}$  values of more than 1% are permitted.

### 9.2.3 Formulation 2: constraints for short-term power variations

In this paper, short-term power variations are considered to be variations that can be compensated for by generators that provide FRR without infringing their permitted ramping rates, and by generators that provide FCR without infringing the permitted frequency variations in steady-state. Examples of these variations in plants fed by renewable energy source include cloud passage across solar PV parks or wind gusts at wind farms.

This formulation requires the following assumptions:

1. A power system in balance and in steady-state before renewable energy source variations at  $t = t_0$ . In other words, in Eq. (9.2)  $\tilde{f}(t_0) = 0$ ,  $\dot{\tilde{f}}(t_0) = 0$  and  $p_G(t_0) = p_L(t_0)$ .
2. Worst-case short-term variations can be approximated by a maximum amplitude  $\Delta p^{RES}$ , a minimum duration  $\Delta T^{RES}$ , and a constant rate of change  $rr^{RES} = \Delta p^{RES} / \Delta T^{RES}$ . This assumption has been corroborated by recently published analysis of short-term wind [38] and solar [27] variability, the determination of these parameters from high-resolution wind speed and solar irradiance measurements also being discussed in detail in these papers.
3.  $\Delta p^{RES}$  is compensated for without infringing the maximum ramping rate  $rr^{FRR}$  of the generators participating in FRR.
4. Short-term renewable energy source power variations are sufficiently smooth. It is therefore reasonable to assume minimal influence of system inertia ( $M\dot{\tilde{f}} \approx 0$ ) during interval  $\Delta T^{RES}$ .

Assumption 1 implies that any power variation in the system can be arbitrarily attributed to either  $p_L$  or  $p_G$  in Eq. (9.2). Eq. (9.8) is obtained based on the assumption that renewable energy source variations affect  $p_L$  and on assumption 2. Eq. (9.9) also accounts for the contributions of all generators that provide FRR in term  $p_G$ , on assumption 3 being here applied.

$$\forall h, \quad p_{L,h} \leq rr_h^{RES} \Delta T_h^{RES} \quad (9.8)$$

$$\forall h, \quad p_{G,h} \leq \sum_m rr_m^{FRR} \Delta T_h^{RES} \quad (9.9)$$

Substituting Eqs. (9.8) and (9.9) into Eq. (9.2) and using assumption 4 gives Eq. (9.10).

$$\forall h, \quad \sum_m rr_m^{FRR} \Delta T_h^{RES} \geq rr_h^{RES} \Delta T_h^{RES} + D\dot{\tilde{f}} \quad (9.10)$$

An algebraic constraint that allocates **FCR** and **FRR** for short-term renewable energy source power variations compensation, is finally obtained based on  $D = \sum_m D_m$  and that the  $\hat{f}$  range in steady state is  $\pm r_{ss}$ :

$$\forall h, \sum_m rr_m^{FRR} \Delta T_h^{RES} - \sum_m D_m r_{ss} \geq rr_h^{RES} \Delta T_h^{RES} \quad (9.11)$$

Note that the constraint in Eq. (9.11) implies that **FCR** and **FRR** are, when  $rr_h^{RES} > \sum_m rr_m^{FRR}$ , activated concurrently. It is therefore implicitly assumed that sudden load variations and simultaneous worst-case renewable energy source power variations were taken into consideration when determining  $P_{b,h}$  in **FCR** sizing. This leads to additional constraints, i.e. that generators  $m$  participating in **FRR** have a total available up and down capacity of  $P_{b,h}$  at each time step time  $h$ :

$$\forall h, \sum_m (P_m^{max} - P_{m,h}) \geq P_{b,h} \quad (9.12)$$

$$\forall h, \sum_m (P_{m,h} - P_m^{min}) \geq P_{b,h} \quad (9.13)$$

$P_{b,h}$  may eventually become asymmetrical, the positive worst-case power variation being different from the negative worst-case power variation. The up and down-ramping capacities of generators can also be distinct, **FCR** and **FRR** being asymmetrical in this situation. Separate parameter sets  $r_{ss}$ ,  $r_{tr}$ ,  $P_{b,h}$ ,  $D_m$ ,  $rr_{h,m}^{FRR}$ ,  $rr_h^{RES}$ ,  $\Delta T_h^{RES}$  should then be considered for up and down reserves. The formulations proposed in this and the previous section can be developed further for this general case but will not, in the interests of brevity, be presented in this paper.

Regarding Assumption 4, note that short-term power variations of renewables typically occur in ramp, as described later in Sec. 9.3.1, and detailed in 9.6 and [27] for solar **PV** and [38] for wind power. A cloud passage would likely take many seconds to complete shade the total area of a MW-scale plant, meaning that the power output would drop approximately in a ramp. Where such ramps are smooth enough, the contribution of the **GTs** inertia for the power balance represented in Eq. (9.2) would indeed be minimal, as turbine governors would have enough time to react to the grid frequency changes and compensate the power imbalance. This is exactly what is being assumed in this formulation.

This concept is better understood in Fig. 9.1, which sketches what happens when a cloud passage occurs in an autonomous power system and where  $P_1, P_2, P_{max}$  represent respectively the power delivered by two **GTs** and their maximum limit,  $P_{PV}$  and  $P_{bat}$  are the power delivered by a solar **PV** farm and a battery **ESS**, and the superscripts **DC** and **PC** indicates respectively the power variations during and post cloud passage.

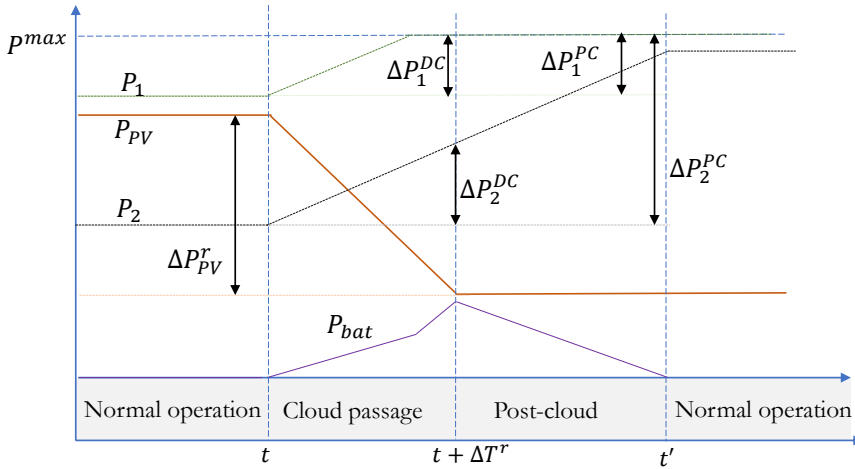


**FIGURE 9.1.** Idealized response of an autonomous power system to a cloud-passage event. © Erick Alves et al, 2022.

The dynamics of short-term power variations are, in summary, different from sudden load or generation loss, the latter being addressed by the constraints proposed in Sec. 9.2.2. The GTs inertia will, in the latter case, be very important to guarantee the power balance represented in Eq. (9.2) and avoid extreme frequency variations, a topic well explored in [39], for instance.

### 9.3 CASE STUDY OF AN INDUSTRIAL INSTALLATION

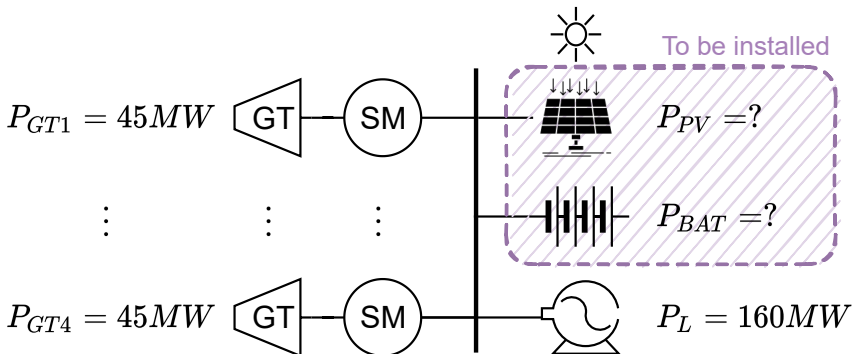


**FIGURE 9.2.** Overview of the case study installation. © Erick Alves et al, 2022.

The case study of an isolated O&G installation with a peak electric power demand of 160 MW is presented in this section, to exemplify the use of the



proposed formulations. This plant is currently equipped with four GTs each of 45 MW. 30 MW of the total load is considered to be non-essential, and can therefore be shed during an extreme contingency. This design therefore allows the critical power demand of 130 MW to be supplied, and a n+1 redundancy for GTs. The operator would like to integrate a solar PV farm and a battery ESS into this plant, to reduce emissions of nitrogen oxides and GHG. FCR and FRR should be supplied by the existing GTs, the battery ESS being sized to provide only FCR. Figure 9.2 presents the proposed architecture and table 9.1 the main technical parameters.

| Parameter       | Unit | Value |
|-----------------|------|-------|
| Rated frequency | Hz   | 50    |
| $r_{ss}$        | Hz   | 0.5   |
| Load            |      |       |
| - Peak          | MW   | 160   |
| - Critical      | MW   | 130   |
| - Non-essential | MW   | 30    |
| GTs             |      |       |
| - Number        |      | 4     |
| - Rated power   | MW   | 45    |
| - Droop         | %    | 10    |
| - Inertia       | s    | 5.51  |

**TABLE 9.1.** Case study parameters

### 9.3.1 MILP algorithm formulation

A mixed integer linear programming algorithm was developed to support the operator's investment decision. The objective of optimization was to find the best performing pair of solar PV (installed capacity  $P_{PV}^{inst}$ ) and battery ESS (installed capacity  $P_{bat}^{inst}$ ) for the plant. Eq. (9.14) shows the objective function,  $c_{PV}$ ,  $c_{bat}$  being the installation costs for solar PV and battery ESS in \$/kW,  $e$  denoting the discount rate of the project and  $c_f$  aggregated fuel costs including  $CO_2$  and  $NO_x$  penalties. Operational costs across the plant's lifetime  $Y_{inst}$  in years take into consideration the fuel consumption  $FC_{m,h}$  of each generator  $m$  at each time step  $h$ , as defined in Eq. (9.15).

$$\min P_{PV}^{inst} c_{PV} + P_{bat}^{inst} c_{bat} + \sum_{y=0}^{Y_{inst}} \sum_{h=1}^{8760} \sum_m \frac{FC_{m,h} c_f}{(1+e)^y} \quad (9.14)$$

$$\forall m, \forall h, FC_{m,h} = a_m P_{m,h} + b_m \quad (9.15)$$

Eqs. 9.16-9.25 express the system operational constraints. Eq. (9.16) ensures that system power is in balance at each time step  $h$ . Note that the ESS does

not take part in permanent load balancing as it is used only for FCR, that is ensuring frequency stability in case of short-term PV drop or large contingency. The energy flows related to charge and discharge therefore are considered negligible compared to the industrial load. The injected solar PV power  $P_{PV,h}^{inj}$  is calculated in Eq. (9.17) using the available PV area  $A_{PV,h}$ , the average irradiance  $I_h$  in time step  $h$ , and derating factor  $d_{PV}$ . Eq. (9.18) integrates  $P_{PV}^{inst}$  into the objective function of Eq. (9.14).

$$\forall h, \quad \sum_m P_{m,h} \geq P_{L,h} - P_{PV,h}^{inj} \quad (9.16)$$

$$\forall h, \quad P_{PV,h}^{inj} \leq d_{pv} I_h A_{PV,h} \quad (9.17)$$

$$\forall h, \quad P_{PV}^{inst} \geq I_h A_{PV,h} \quad (9.18)$$

Eqs. 9.19 to 9.25 express the operational constraints of each generator  $m$  at each time step  $h$ ,  $\rho_{m,h}$  representing the generator on/off status,  $u_{m,h}$  and  $v_{m,h}$  start-up and shut down decisions, and  $T_m^{up}$  and  $T_m^{dn}$  minimum up and down-time.

$$\forall m, \forall h, \quad P_{m,h}^{FCR} \leq \rho_{m,h} D_m r_{ss} \quad (9.19)$$

$$\forall m, \forall h, \quad P_{m,h} \leq \rho_{m,h} P_m^{max} - P_{m,h}^{FCR} \quad (9.20)$$

$$\forall m, \forall h, \quad P_{m,h} \geq \rho_{m,h} P_m^{min} + P_{m,h}^{FCR} \quad (9.21)$$

$$\forall m, \forall h, \quad u_{m,h} - v_{m,h} \geq \rho_{m,h} - \rho_{m,h-1} \quad (9.22)$$

$$\forall m, \forall h, \quad u_{m,h} + v_{m,h} \leq 1 \quad (9.23)$$

$$\forall m, h \geq T_m^{up}, \quad \sum_{k=h-T_m^{up}}^{h-1} \rho_{m,k} \geq T_m^{up} v_{m,h} \quad (9.24)$$

$$\forall m, h \geq T_m^{dn}, \quad \sum_{k=h-T_m^{dn}}^{h-1} \rho_{m,k} \leq T_m^{dn} (1 - u_{m,h}) \quad (9.25)$$

Note that Eqs. 9.20 and 9.21 allocate the FCR for each generator  $m$  defined in Eqs. 9.5 and 9.6 according to a predefined damping  $D_m$ , calculated based on table 9.1 data.  $D_m = P_m^{max} / (\beta_m P_{base})$ .  $\beta_m$  is therefore the GT droop,  $P_{base} = 45$  MW is an arbitrary value adopted for normalization. The total damping of the GTs  $D_{GT} = \sum_m D_m$  may not, however, be sufficient to comply with Eq. (9.7), battery ESS power  $P_{bat}^{inst}$  in this case being sized to provide the remaining FCR. The constraints necessary for this are discussed in the next section, which are based on the formulations proposed in sections 9.2.2 and 9.2.3.

### Battery sizing

The first step in sizing spinning reserves is to apply sudden load or generation loss constraints, a simplified security assessment in this study being used. The loss of a **GT** in operation was therefore considered to be the worst contingency of this type. The system was therefore designed for  $n+1$  redundancy of the **GTs**, the sudden power disturbance term  $P_{b,h}^{sud}$  therefore being defined by Eqs. 9.26 and 9.27.

$$\forall m, \forall h, \quad P_{b,h}^{sud} \leq P_m^{max} \quad (9.26)$$

$$\forall m, \forall h, \quad P_{b,h}^{sud} \geq P_{m,h} \quad (9.27)$$

Cloud passage events at the solar **PV** farm should also be taken into consideration. Integration of these into the mixed integer linear programming formulation is however, in this study, based on the assumption that the optimization algorithm has access to a compact set  $\mathbf{H}^{max}$  of worst-case solar irradiance ramp events. 9.6 summarizes a procedure for building  $\mathbf{H}^{max}$  from high-resolution irradiance time series. Solar irradiance data provided by NREL [40] was used. The wavelet variability model [41] was also employed to take into account the geographical smoothing effect, using Sandia's PV\_LIB Toolbox for Matlab [42]. The datasets used to build  $\mathbf{H}^{max}$  in this study are available in [43], being  $\mathbf{H}^{max}$  for  $h = 11$  presented in table 9.2. The duration and irradiance drop associated with ramp event  $r$  in time step  $h$  are denoted  $\Delta T_{h,r}$  and  $\Delta I_{h,r}^{PV}$ .

| Ramp<br>$r$ | Durat.<br>$\Delta T_{h,r}$<br>[s] | Irr. drop<br>$\Delta I_{h,r}$<br>[kW m <sup>-2</sup> ] |
|-------------|-----------------------------------|--|
| $r_1$       | 2                                 | 0.061  |
| $r_2$       | 19                                | 0.613  |
| $r_3$       | 36                                | 0.778  |
| $r_4$       | 48                                | 0.878  |

**TABLE 9.2.** The first 4 elements of the convex hull  $\mathcal{H}_{11}^{max}$

The worst-case solar **PV** disturbance term  $P_{b,h}^{PV}$  at each time step  $h$  can, where this framework is assumed, be specified using Eqs. 9.28 and 9.29.

$$\forall h, \forall r, \quad P_{b,h}^{PV} \geq d_{PV} \Delta I_{h,r} A_{PV,h} \quad (9.28)$$

$$\forall h, \quad P_{b,h}^{PV} \leq P_{PV,h}^{inj} \quad (9.29)$$

Spinning reserves can be specified where both  $P_{b,h}^{sud}$  and  $P_{b,h}^{PV}$  have been defined and the formulations proposed in sections 9.2.2 and 9.2.3 are applied. **FRR** is sized using Eqs. 9.30 and 9.31, which are obtained when the constraints in Eqs. 9.12 and 9.13 are used.

$$\forall h, \quad \sum_m (\rho_{m,h} P_m^{max} - P_{m,h}) \geq P_{b,h}^{sud} + P_{b,h}^{PV} \quad (9.30)$$

$$\forall h, \quad \sum_m (P_{m,h} - \rho_{m,h} P_m^{min}) \geq P_{b,h}^{sud} + P_{b,h}^{PV} \quad (9.31)$$

FCR is then calculated by combining the minimum damping requirements defined in Eq. (9.7) and the constraint in Eq. (9.11), which assumes that  $\Delta P_{h,r}^{PV}$  is partially compensated for by FRR during a cloud passage. The battery ESS is therefore sized, at each time step  $h$ , to simultaneously compensate for any power deficit between a)  $P_{b,h}^{sud}$ , FCR provided by GTs; and b)  $\Delta P_{h,r}^{PV}$ , FRR provided by GTs for all ramp events in  $\mathbf{H}^{max}$ . Eqs. 9.32 and 9.33 describe these requirements. Finally,  $P_{bat}^{inst}$  is integrated into the objective function of Eq. (9.14) via Eq. (9.34). Note that the proposed sizing is only addressing the maximum power of the ESS, not its energy capacity. To calculate the energy flows demanded by FCR, it is necessary to simulate the grid using more detailed models at sub-second time steps, which cannot be performed using the methodology here proposed. This limitation is later exemplified and further discussed in Sec. 9.4.

$$\forall h, \forall r, \quad P_{bat,h}^{FCR} \geq P_{b,h}^{sud} - P_{m,h}^{FCR} + \Delta P_{h,r}^{PV} - \sum_m (\rho_{m,h} r r_m^{FRR} \Delta T_{h,r}) \quad (9.32)$$

$$\forall h, \quad P_{bat,h}^{FCR} \geq 0 \quad (9.33)$$

$$\forall h, \quad P_{bat}^{inst} \geq P_{bat,h}^{FCR} \quad (9.34)$$

### 9.3.2 Optimal sizing with static and dynamic frequency constraints

| Parameter        | Unit  | Value |
|------------------|---|-------|
| $\gamma^{inst}$  | year  | 20    |
| $rr_m$           | MW s <sup>-1</sup>                              | 0.208 |
| $T_m^{up}$       | h   | 6     |
| $T_m^{dn}$       | h   | 6     |
| $a$              | m <sup>3</sup> h <sup>-1</sup> kW <sup>-1</sup> | 13782 |
| $b$              | m <sup>3</sup> h <sup>-1</sup>                  | 5523  |
| $c_{fuel}$       | \$/m <sup>3</sup>                               | 1.01  |
| $c_{CO_2}$       | \$/t  | 120   |
| $c_{PV}^{inst}$  | \$/kW   | 400   |
| $d_{PV}$         | %   | 80    |
| $c_{bat}^{inst}$ | \$/kW   | 250   |
| $e$              | %   | 3     |

TABLE 9.3. Techno-economic input parameters

The mixed integer linear programming algorithm described in Sec. 9.3.1 was implemented in Gurobi 9.1, using an optimality gap tolerance of 1%. table 9.3 lists the techno-economic parameters used in the optimization. Four scenarios were considered, these being selected to highlight the importance of frequency stability constraints:

1. *Baseline* is the current operation of the case study plant, power generation being based on 4 GTs.
2. *No FC* includes the integration of the solar PV farm, but without any frequency stability conditions. The constraints in Sec. 9.3.1 are therefore omitted.
3. *Static FC* is the full implementation given in Sec. 9.3.1. It adopts  $P_{m,h}^{FCR} = 0$  in Eq. (9.32), which means that the frequency dynamics and the FCR contribution during cloud passage are ignored.
4. *Dynamic FC* includes the FCR contribution in Eq. (9.32).

| Indicator                 | Basel. | No FC  | St. FC | Dyn. FC |
|---------------------------|--------|--------|--------|---------|
| $P_{PV}^{inst}$ [MW]      | 0.0    | 129.76 | 62.00  | 62.00   |
| $P_{bat}^{inst}$ [MW]     | 0.0    | 0.00   | 33.3   | 10.80   |
| CAPEX [M\$]               | 0.0    | 51.9   | 33.1   | 27.5    |
| CO <sub>2</sub> [Mt/year] | 111.3  | 95.4   | 105.7  | 105.7   |
| LCOE [\$/MWh]             | 521.1  | 450.3  | 496.9  | 496.5   |
| Total costs [M\$]         | 9740   | 8870   | 9520   | 9580    |

**TABLE 9.4.** Techno-economic optimization results for each scenario

The results are given in table 9.4. The highest total costs are in the *Baseline* case, minimum costs being in the *No FC* case at a discount of 8.9 % on *Baseline*. This can be explained by the installed capacity of the largest solar PV being 129.76 MW and the decrease of CO<sub>2</sub> emissions being 14.3 % of *Baseline*. These factors also lead to the lowest LCOE and highest CAPEX for all cases. The *No FC* case is, however, unrealistic, as it ignores frequency stability constraints and the need for energy storage. It does, however, provide useful references for maximum theoretical reductions in CO<sub>2</sub> emissions and LCOE.

Adding spinning reserve constraints limits the potential of PV integration, and requires battery ESS capacity, this influencing the CAPEX in opposite directions. The reduction of PV installation costs is, however, bolder for the parameters of this case study. CAPEX is reduced by 36.2 % in the *Static FC* and by 47.0 % in the *Dynamic FC* case, in relation to the *No FC* case. No significant differences are observed in fuel consumption, and therefore CO<sub>2</sub> emissions, between the two frequency constraints cases. Their LCOE and total costs

therefore remain similar. LCOE is reduced by 13.5 % in *No FC*, 4.6 % in *Static FC* and 4.7 % in *Dynamic FC* (on *Baseline*).

It can be argued that the difference between *Static FC* and *Dynamic FC* is marginal for most indicators. Note, however, that the battery ESS capacity in *Dynamic FC* is reduced by 67.6 % in relation to *Static FC*. This shows that ESS capacity can be reduced significantly where the tolerated frequency dynamics and complementary contribution of FCR and FRR modeled in Eq. (9.32) are taken into consideration during a cloud passage event.

Figure 9.3 shows the hourly profiles on Jan 1st of available PV power  $P_{PV,h}^{avail} = I_h A_{PV,h}$ , injected PV power  $P_{PV,h}^{inj}$ , and the calculated battery contribution during a worst-case PV power drop  $P_{bat,h}^{FCR}$ , and exemplifies what takes place at a more granular level. Injected PV power reaches 92.6 MW at 11:00 in the *No FC* case. The injection is, however, curtailed to around 54 MW in the *Static FC* and *Dynamic FC* cases, the difference between these cases being explained by frequency stability constraints being neglected. This allows the mixed integer linear programming algorithm to turn off one GT and creates the opportunity for additional PV capacity.

| Ramp<br>$r$ | St. FC<br>$p_{bat,r}^{FCR}$<br>[MW] | Dyn. FC<br>$p_{bat,r}^{FCR}$<br>[MW] | No FC<br>$p_{bat,r}^{FCR}$<br>[MW] |
|-------------|-------------------------------------|--------------------------------------|------------------------------------|
| $r_1$       | 25.7                                | 3.2                                  | 11.3                               |
| $r_2$       | <b>33.3</b>                         | <b>10.8</b>                          | <b>50.2</b>                        |
| $r_3$       | 23.2                                | 0.7                                  | 50.2                               |
| $r_4$       | 15.3                                | 0                                    | 48.1                               |

**TABLE 9.5.** Required battery ESS capacity for the first 4 elements of the convex hull  $\mathcal{H}_{11}^{max}$

The infeasibility of the *No FC* solution is shown by table 9.5, the table specifying the power deficit between FCR, FRR,  $p_{b,h}^{sud}$  and  $P_{b,h}^{PV}$  given by Eq. (9.32) for the PV ramps stated in table 9.2. Remember that it is assumed that  $P_{m,h}^{FCR} = 0$  in *No FC* and *Static FC*, in Eq. (9.32). This assumption is also used in Eqs. 9.20 and 9.21 in *No FC*. The system may, in *No FC*, face a power deficit of 50.2 MW. Critical PV ramps are  $r_2$  and  $r_3$ , which would undoubtedly lead to a grid blackout.  $P_{bat,r}^{FCR}$  is obtained, in the *Static FC* case, by adding 22.5 MW of one GT loss to 10.8 MW for the imbalance between FRR and PV ramp rate. The generator loss is fully compensated for in the *Dynamic FC* case, by the damping of the remaining GTs. This shows the importance of taking into consideration the damping capabilities of generators participating in FCR and the tolerated frequency deviations.

### 9.3.3 Validation with time-domain simulations

Time-domain simulations implemented in Matlab/Simulink (2021b) were used to validate the battery sizing by the proposed mixed integer linear programming algorithm. Fig. 9.6 presents a schematic diagram of this simulation model. The dynamics of the electricity grid are reduced into active power flows, Eq. (9.2) being used to calculate grid frequency deviation. Battery and solar PV models consist of ideal active power sources, battery ESS adopting a droop control strategy including saturation and only providing FCR. GTs and their governors are represented by a droop model that contain a first-order filter to represent the delay of the actuator, being a time constant of 0.5 s employed. Ramp-rate saturation is added for the FRR component. Other relevant parameter values are given in tables 9.1 to 9.4.

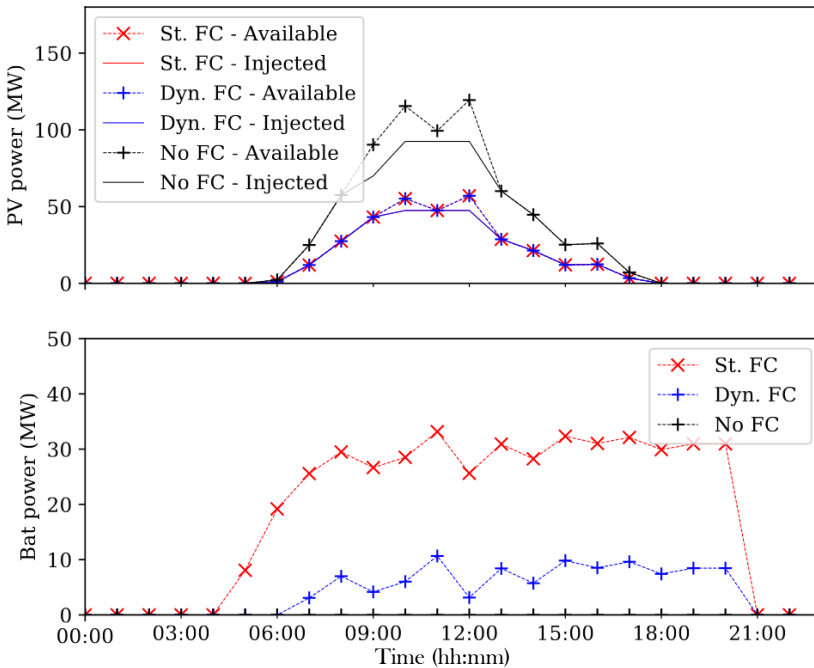


**FIGURE 9.3.** Hourly available and injected PV profile and battery requirements on Jan 1st. © Erick Alves et al, 2022.

The validation consists of simulating the worst-case cloud passage event and the simultaneous loss of one GT, as presented in table 9.2, a check of whether frequency deviation is lower than or equal to  $r_{ss}$  then being carried out. Remark that all other cases will produce smaller frequency drops or lower FRR setpoint rate of change. The power perturbation is generated by applying

a load step that corresponds to  $P_{b,h}^{sud} = 22.5$  MW at  $t = 10$  s, and by simultaneously applying a negative power ramp corresponding to  $r_2$ . The system inertia  $M$  is equivalent to three GTs. Figure 9.4 shows the results of this simulation, including the battery ESS, the GTs power and the grid frequency. Battery support means the frequency drops to 49.5 Hz after the worst-case event, meeting the target of up to 0.5 Hz deviation. The grid frequency has also an oscillatory behavior after the sudden loss of one GT due to the time delay of the turbine governors, which is compensated by the fast action of the battery ESS. A further discussion of this topic is beyond the scope of this paper, but the interested reader can more information in [44].

## 9.4 DISCUSSION

Optimal solar PV and battery ESS capacities were calculated for an industrial plant, by using the formulation of linear frequency constraints and their integration in a mixed integer linear programming sizing problem. Economic and environmental performance is reduced (at +10.8% of  $CO_2$  emissions and +8.0% of total costs) in relation to optimization results without frequency constraints. It was, however, shown that the solution without frequency constraint is not resilient to worst-case events, such as a simultaneous cloud passage and loss of a GT. Taking frequency reserves into consideration in sizing optimization therefore avoids the over-estimation of the benefits of solar power integration, and provides a more robust architecture in terms of power supply security.

The battery ESS capacity requirement was reduced by 67.6% of the static calculation value that neglects the FCR contribution. This was achieved by taking into consideration the frequency deviation tolerance ( $r_{ss} = 0.5$ Hz) in the *Dynamic FC* scenario. Considering simultaneous PV drop and generator loss allows a robust approach, but also leads to conservative and costly ESS sizing. The problem of battery ESS capacity allocation might, in less sensitive applications, take into consideration the highest value of the worst-case PV ramp event and generator contingency, but not both simultaneously. The impact of this on overall costs and  $CO_2$  savings would, however, still be relatively small, primarily due to the marginal effect that the proposed constraints would have on the fuel consumption of GTs, which is the main cost driver in this case study.

The battery energy storage capacity in MW h for FCR is not a dominant cost driver in this problem, and the cost function of Eq. (9.14), as consequence, do not consider it. The actuation time of FRR is usually less than 30 s in a typical EMS for autonomous power system, meaning that, if full FCR capacity (i.e. 10.8 MW) is delivered for 10 events every hour (i.e. 5 minutes in total), the required



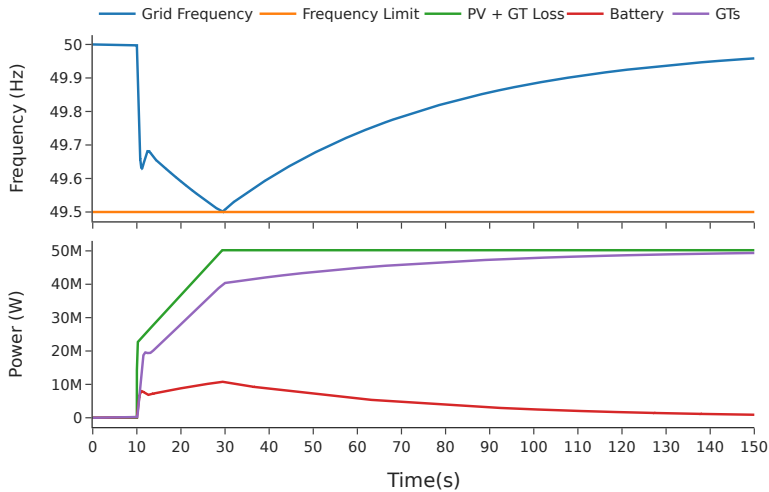


**FIGURE 9.4.** Grid simulation of PV ramp  $r_2$  and one GT loss at  $t = 10$  s. © Erick Alves et al, 2022.

energy will be 0.9 MW h for the selected battery ESS in the case study. Typical losses of ESSs in the MW-range varies between 1 and 2%, the required FCR energy therefore being in the same order of magnitude of the battery ESS losses. Remark that FCR required energy represents only 0.56% of the load demand in the case study (160 MW h) and can be assumed negligible when taking into consideration the accuracy of the model employed in the unit commitment problem and the optimality gap tolerance adopted. Including the battery energy storage capacity in the problem formulation would however be extremely relevant if the ESS was designed to provide FRR, or if the proposed constraints were employed in an operational unit commitment problem designed to provide dispatch setpoints for the GTs and ESS in real-time.

The attentive reader may have noticed that the fuel and  $CO_2$  costs presented in table 9.3 are well above current market prices. The reader may have also noticed that the project discount rate and installation costs for solar PV and battery ESS are lower than the prevailing values in the industry. This was to allow a high penetration of solar PV in the case study installation, to highlight the impact of frequency stability constraints in this scenario. The results of the mixed integer linear programming algorithm are, of course, sensitive to the economic parameters. For example, if the discount rate is doubled, then the installed solar PV capacity will drop to below 9 MW in the *Static FC* and

*Dynamic FC* scenarios. The presentation of a sensitivity analysis in the case study is, however, beyond the scope of this work.

Just considering Eqs. (9.20), (9.21), (9.30) and (9.31) is, in terms of spinning reserves allocation, equivalent to the formulations proposed in [14, 45]. Introducing Eq. (9.34), however, contributes to security sizing problems, as it draws in both formulations. FCR modeling during short-term power variations therefore improves the optimal solution. The validation of the use of a time-domain model that only considers active power flows, shows that this frequency stability proposal can produce valid results. The power management of larger systems is, however, a multi-objective optimization problem with coupled variables, and one in which not only active power flows, but also voltages and reactive power flows, are optimized as discussed in [19]. The inclusion of frequency constraints in such problems, to deal with short-term power variations, is however a topic for future research.

Note as well that a droop with a fixed value of 10% for all GTs was considered in the case study. As briefly discussed in Sec. 9.3.1, the droop value directly affects total system damping. It would therefore also affect the size of the battery ESS. This observation suggests that this value should also be used as a decision variable in the optimization problem. This does, however, lead to a non-linear formulation. Further research on reserve allocation models and mixed integer linear programming formulation should therefore be carried out to circumvent this issue.

It is worth highlighting, at this point, that the constraints proposed in Secs. 9.2.2 and 9.2.3 do not control  $\tilde{f}$ , only assign the correct amount of FCR given bounded values of  $(p_G - p_L)$  and  $M$ . The proposed constraints, in other words, guarantee that the frequency deviation  $\tilde{f}$  remains within intervals  $\pm r_{tr}$  during transient conditions and  $\pm r_{ss}$  during steady-state conditions (i.e. post-disturbance), which is the definition of frequency stability given in [29] and in Sec. 9.2.1.

Note that large values of  $\tilde{f}$  in the negative direction (i.e. lack of power generation) can cause magnetic over-flux in electrical machines and transformers. This situation not only increases losses and heating, but also induced voltage gradient between laminations that can break down the core insulation of these equipment and cause serious damages. This topic is discussed in depth in [39, 46–48] and can be considered a more serious issue than large values of  $\dot{\tilde{f}}$  in low-inertia autonomous power system.

Despite not being explicitly mentioned in Sec. 9.2.1,  $M$  influences the term  $r_{tr}$  in Eq. (9.4), which represents the maximum value of  $\tilde{f}$  during transient conditions, also known as frequency nadir or zenith. This term can therefore be used to include constraints on  $M$ . The model from Eq. (9.2), however, cannot capture the dynamics of the transient period, as it does not include the time

delay of actuators. References [49, 50] have discussed this issue and proposed linearizations and/or analytical solutions that can be employed to include services such as FFR or inertia emulation in the unit commitment problem. The constraints proposed in these references can be included in the formulation proposed in Sec. 9.3.1 where the dynamics of the transient period must be addressed.

In the case study case presented in Sec. 9.3, however, a higher penetration of solar PV is mainly prevented by the  $\tilde{f}$  constraints post-disturbance and the installation costs of the battery ESS, as shown in table 9.4 and discussed in Sec. 9.3.2. The authors therefore consider reasonable to ignore the dynamics of the transient period in this specific case. For a more general problem formulation, the constraints proposed in [49, 50] can be combined with those presented in Sec. 9.2.3. This however will turn the problem into a nonlinear optimization, as the ratio  $\frac{D}{M}$  determines the  $\tilde{f}$  dynamics but each variable will be a decision variables in the optimization. Addressing this issue and developing a convex reformulation of the problem that can be solved by mixed integer linear programming is a relevant topic for future work.

## 9.5 CONCLUSION

The problem of spinning reserves allocation for isolated grids with high penetration of renewable energy sources is addressed in this work. Linear frequency stability constraints were first formulated, to allow integration in a frequency constrained unit commitment (UC) problem, the proposed constraints ensuring the allocation of enough reserves to compensate for short-term renewable variations and generator contingencies. This includes practical issues such as the limited ramping capacities of frequency restoration reserve (FRR). It also takes advantage of short-term frequency variations and the complementary action between frequency containment reserve (FCR) and frequency restoration reserve (FRR).

The reserve allocation strategy is exemplified by a case study in which a mixed integer linear programming (MILP) algorithm is formulated for the optimal sizing of a solar photovoltaic (PV) farm and an energy storage system (ESS). Linear frequency stability constraints are aggregated to ensure the resiliency of the grid, in the event of cloud passage and generator contingency occurring simultaneously. The results show that this method provides an optimal and secure architecture. It also shows that neglecting stability constraints leads to an inoperable solution, and overestimates system profitability and greenhouse gases (GHG) emission savings, by 8.0 and 10.8% respectively.

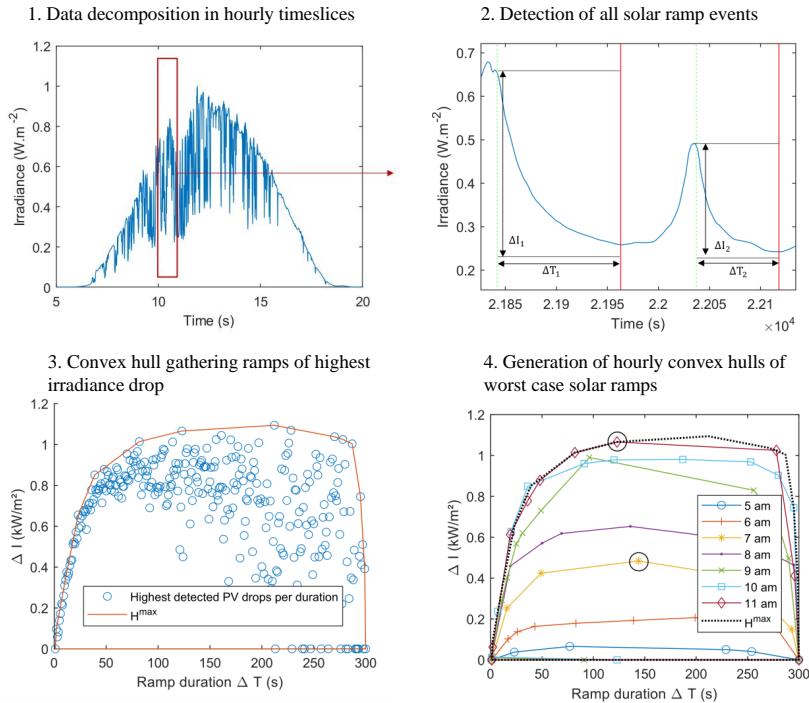


**FIGURE 9.5.** Process of worst-case ramp identification from high-resolution timeseries to convex hulls  $\mathcal{H}_h^{max}$  in the lower-right figure. © Erick Alves et al, 2022.

## DATA AVAILABILITY STATEMENT

The datasets presented in this study can be found in online repositories. The names of the repository/repositories and accession number(s) can be found at [43].

## 9.6 APPENDIX A: GENERATION OF SOLAR PV POWER DROP SCENARIOS

Solar variability is typically measured by irradiance sensors, which generate high-resolution time series. The measurement sampling time must be lower than 5 s if cloud passage events are to be captured. Integrating these time series into a high-level optimization is however impractical, due to time increment discrepancies. Fig. 9.5 summarizes a procedure for extracting ramp scenarios from irradiance sensor time series, as was recently proposed in [27] and applied in Sec. 9.3.

In step 1, high resolution data from sensors is decomposed into hourly

time slices. In step 2, all ramp events within an hour slice are detected. A ramp event  $rr_{PV,h,r}$  is defined by its irradiance drop  $\Delta I_{h,r}$  and ramp duration  $\Delta T_{h,r}$  during cloud passage. In step 3, all events are grouped in a compact set. The hourly convex hull  $\mathcal{H}_h^{max}$  is defined to gather the set of highest irradiance drops for each duration, to allow only the worst-case events to be extracted. This provides a subset of a limited number of ramps. Steps 2 and 3 are then repeated for each hour slice defined in step 1. Finally, in step 4, all  $\mathcal{H}_h^{max}$  are grouped and the global convex compact worst-case ramp set  $\mathcal{H}^{max}$  is obtained.

The solar PV power drop  $\Delta P_{h,r}^{PV}$  is calculated using the irradiance drop according to Eq. (9.35),  $A_{PV,h}$ ,  $I_h$ ,  $d_{PV}$  being the available PV area, the average irradiance, and derating factor, respectively.

$$\Delta P_{h,r}^{PV} = d_{PV} \Delta I_{h,r} A_{PV,h} \quad (9.35)$$

## 9.7 APPENDIX B: POWER SYSTEM MODEL USED FOR VALIDATION

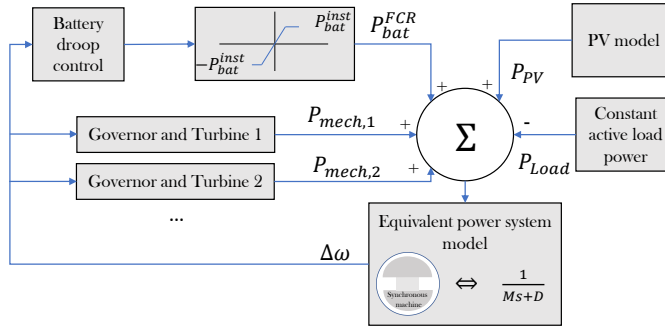


FIGURE 9.6. Power system model implemented in Matlab/Simulink. © Erick Alves et al, 2022.

## 9.8 REFERENCES

- [1] Mohammad S. Masnadi and Adam R. Brandt. Climate impacts of oil extraction increase significantly with oilfield age. *Nature Climate Change* 7 (8), 551–556 (August 2017). ISSN 1758-678X, 1758-6798. doi: 10.1038/nclimate3347. Cited on p. 160.
- [2] Luca Riboldi, Steve Völler, Magnus Korpås, and Lars O. Nord. An Integrated Assessment of the Environmental and Economic Impact of Offshore Oil Platform Electrification. *Energies* 12 (11), 2114 (June 2019). ISSN 1996-1073. doi: 10.3390/en12112114. Cited on p. 160.
- [3] Louis Polleux, John Sandoval-Moreno, Gilles Guerassimoff, and Jean-Paul Marmorat. Impacts of thermal generation flexibility on power quality and LCOE of industrial off-grid power plants. In *Proceedings of 11th International Conference*

- on *Applied Energy* volume 3 page 7 Vasteras, Sweden (2019). Energy Proceedings. ISBN 978-91-985634-2-9. URL <https://www.energy-proceedings.org/impacts-of-thermal-generation-flexibility-on-power-quality-and-lcoe-of-industrial-off-grid-power-plants/>. Cited on p. 160.
- [4] Rodney Itiki, Silvio Giuseppe Di Santo, Cinthia Itiki, Madhav Manjrekar, and Badrul Hasan Chowdhury. A comprehensive review and proposed architecture for offshore power system. *International Journal of Electrical Power & Energy Systems* **111**, 79–92 (October 2019). ISSN 01420615. doi: 10.1016/j.ijepes.2019.04.008. Cited on p. 160.
- [5] Spyridon Chapaloglou, Damiano Varagnolo, and Elisabetta Tedeschi. Techno-Economic Evaluation of the Sizing and Operation of Battery Storage for Isolated Oil and Gas Platforms with High Wind Power Penetration. In *IECON 2019 - 45th Annual Conference of the IEEE Industrial Electronics Society* pages 4587–4592 Lisbon, Portugal (October 2019). IEEE. ISBN 978-1-72814-878-6. doi: 10.1109/IECON.2019.8926739. Cited on p. 160.
- [6] Luca Riboldi, Erick F. Alves, Marcin Pilarczyk, Elisabetta Tedeschi, and Lars O. Nord. Optimal Design of a Hybrid Energy System for the Supply of Clean and Stable Energy to Offshore Installations. *Frontiers in Energy Research* **8**, 326 (December 2020). ISSN 2296-598X. doi: 10.3389/ferg.2020.607284. Cited on p. 160, 161.
- [7] Jing Zhong Tee, Idris Li Hong Lim, Keliang Zhou, and Olimpo Anaya-Lara. Transient Stability Analysis of Offshore Wind With O&G Platforms and an Energy Storage System. In *2020 IEEE Power & Energy Society General Meeting (PESGM)* pages 1–5 Montreal, QC, Canada (August 2020). IEEE. ISBN 978-1-72815-508-1. doi: 10.1109/PESGM41954.2020.9281706. Cited on p. 160.
- [8] Norma Anglani, Salvatore R. Di Salvo, Giovanna Oriti, and Alexander L. Julian. Renewable Energy Sources and Storage Integration in Offshore Microgrids. In *2020 IEEE International Conference on Environment and Electrical Engineering and 2020 IEEE Industrial and Commercial Power Systems Europe (EEEIC / I&CPS Europe)* pages 1–6 Madrid, Spain (June 2020). IEEE. ISBN 978-1-72817-455-6. doi: 10.1109/EEEIC/ICPSEurope49358.2020.9160760. Cited on p. 160.
- [9] Khalid S. Khan, Isabelle V. M. dos Santos, Guilherme B. dos Santos, Maurício B. C. Salles, and Renato M. Monaro. Evaluation of Deep-Water Floating Wind Turbine to Power an Isolated Water Injection System. In *ASME 2021 3rd International Offshore Wind Technical Conference* page V001T01A002 Virtual, Online (February 2021). American Society of Mechanical Engineers. ISBN 978-0-7918-8476-8. doi: 10.1115/IOWTC2021-3522. Cited on p. 160.
- [10] Håvard Devold. Oil and gas production handbook: An introduction to oil and gas production, transport, refining and petrochemical industry. ABB Oslo (2013). ISBN 978-82-997886-3-2. URL [https://library.e.abb.com/public/34d5b70e18f7d6c8c1257be500438ac3/Oil%20and%20gas%20production%20handbook%20ed3x0\\_web.pdf](https://library.e.abb.com/public/34d5b70e18f7d6c8c1257be500438ac3/Oil%20and%20gas%20production%20handbook%20ed3x0_web.pdf). Cited on p. 160.
- [11] Helena Vasconcelos, Carlos Moreira, Andre Madureira, Joao Pecas Lopes, and Vladimiro Miranda. Advanced Control Solutions for Operating Isolated Power Systems: Examining the Portuguese islands. *IEEE Electrification Magazine* **3** (1), 25–35 (March 2015). ISSN 2325-5897, 2325-5889. doi: 10.1109/MELE.2014.2380131. Cited on p. 160.
- [12] Hans-Kristian Ringkjøb, Peter M. Haugan, and Astrid Nybø. Transitioning remote Arctic settlements to renewable energy systems – A modelling study of Longyearbyen, Svalbard. *Applied Energy* **258**, 114079 (January 2020). ISSN 03062619. doi: 10.1016/j.apenergy.2019.114079. Cited on p. 160.
- [13] Nand K. Meena, Jin Yang, and Evan Zacharis. Optimisation framework for the design and operation of open-market urban and remote community microgrids. *Applied Energy* **252**, 113399 (October 2019). ISSN 03062619. doi: 10.1016/j.apenergy.2019.113399.

- Cited on p. 160.
- [14] David Rebollal, Mónica Chinchilla, David Santos-Martín, and Josep M. Guerrero. Endogenous Approach of a Frequency-Constrained Unit Commitment in Islanded Microgrid Systems. *Energies* **14**(19), 6290 (October 2021). ISSN 1996-1073. doi: 10.3390/en14196290. Cited on p. 161, 162, 178.
  - [15] Erik Ørum, Minna Laasonen, Katherine Elkington, Niklas Modig, Mikko Kuivaniemi, Alf Ivar Bruseth, Erik Alexander Jansson, and Anders Danell. Future System Inertia 2. Technical report ENTSO-E Brussels, Belgium (February 2018). URL <https://www.entsoe.eu/Documents/Publications/SOC/Nordic/2018/System-inertia.zip>. Cited on p. 161.
  - [16] Hannele Holttinen, *et al.* System impact studies for near 100% renewable energy systems dominated by inverter based variable generation. *IEEE Transactions on Power Systems* pages 1–1 (2020). ISSN 0885-8950, 1558-0679. doi: 10.1109/TPWRS.2020.3034924. Cited on p. 161.
  - [17] M.A. Fotouhi Ghazvini, Hugo Morais, and Zita Vale. Coordination between mid-term maintenance outage decisions and short-term security-constrained scheduling in smart distribution systems. *Applied Energy* **96**, 281–291 (August 2012). ISSN 03062619. doi: 10.1016/j.apenergy.2011.11.015. Cited on p. 161.
  - [18] S. Goleijani, T. Ghanbarzadeh, F. Sadeghi Nikoo, and M. Parsa Moghaddam. Reliability constrained unit commitment in smart grid environment. *Electric Power Systems Research* **97**, 100–108 (April 2013). ISSN 03787796. doi: 10.1016/j.epr.2012.12.011. Cited on p. 161.
  - [19] Salman Mashayekh and Karen L. Butler-Purry. An Integrated Security-Constrained Model-Based Dynamic Power Management Approach for Isolated Microgrids in All-Electric Ships. *IEEE Transactions on Power Systems* **30**(6), 2934–2945 (November 2015). ISSN 0885-8950, 1558-0679. doi: 10.1109/TPWRS.2014.2377741. Cited on p. 161, 178.
  - [20] Navid Rezaei and Mohsen Kalantar. Economic–environmental hierarchical frequency management of a droop-controlled islanded microgrid. *Energy Conversion and Management* **88**, 498–515 (December 2014). ISSN 01968904. doi: 10.1016/j.enconman.2014.08.054. Cited on p. 161.
  - [21] Yunfeng Wen, Wenyuan Li, Gang Huang, and Xuan Liu. Frequency Dynamics Constrained Unit Commitment With Battery Energy Storage. *IEEE Transactions on Power Systems* **31**(6), 5115–5125 (November 2016). ISSN 0885-8950, 1558-0679. doi: 10.1109/TPWRS.2016.2521882. Cited on p. 161.
  - [22] Carmen Cardozo, Laurent Capely, and Philippe Dessante. Frequency constrained unit commitment. *Energy Systems* **8**(1), 31–56 (February 2017). ISSN 1868-3967, 1868-3975. doi: 10.1007/s12667-015-0166-4. Cited on p. 161.
  - [23] Carmen Cardozo Arteaga. Optimisation of power system security with high share of variable renewables: Consideration of the primary reserve deployment dynamics on a Frequency Constrained Unit Commitment model. *PhD thesis*. Paris Saclay Paris, France (April 2016). URL <https://tel.archives-ouvertes.fr/tel-01304078/>. Cited on p. 161.
  - [24] Yue Yin, Tianqi Liu, Lei Wu, Chuan He, and Yikui Liu. Frequency-constrained multi-source power system scheduling against N-1 contingency and renewable uncertainty. *Energy* **216**, 119296 (February 2021). ISSN 03605442. doi: 10.1016/j.energy.2020.119296. Cited on p. 161.
  - [25] Nga Nguyen, Saleh Almasabi, Atri Bera, and Joydeep Mitra. Optimal Power Flow Incorporating Frequency Security Constraint. *IEEE Transactions on Industry Applications* **55**(6), 6508–6516 (November 2019). ISSN 0093-9994, 1939-9367. doi: 10.1109/TIA.2019.2938918. Cited on p. 161.
  - [26] Tim Schittekatte, Michael Stadler, Goncalo Cardoso, Salman Mashayekh, and Narayanan Sankar. The Impact of Short-Term Stochastic Variability in Solar Irradiance on Optimal Microgrid Design. *IEEE Transactions on Smart Grid* **9**(3), 1647–1656 (May 2018). ISSN

- 1949-3053, 1949-3061. doi: 10.1109/TSG.2016.2596709. Cited on p. 162.
- [27] Louis Polleux, Thierry Schuhler, Gilles Guerassimoff, Jean-Paul Marmorat, John Sandoval-Moreno, and Sami Ghazouani. On the relationship between battery power capacity sizing and solar variability scenarios for industrial off-grid power plants. *Applied Energy* **302**, 117553 (November 2021). ISSN 03062619. doi: 10.1016/j.apenergy.2021.117553. Cited on p. 162, 166, 167, 180.
- [28] Erick Fernando Alves, Daniel dos Santos Mota, and Elisabetta Tedeschi. Sizing of Hybrid Energy Storage Systems for Inertial and Primary Frequency Control. *Frontiers in Energy Research* **9**, 649200 (May 2021). ISSN 2296-598X. doi: 10.3389/fenrg.2021.649200. Cited on p. 163, 164.
- [29] Nikos Hatziaargyriou, *et al.* Stability definitions and characterization of dynamic behavior in systems with high penetration of power electronic interfaced technologies. Technical Report PES-TR77 IEEE Power System Dynamic Performance Committee (May 2020). URL [https://resourcecenter.ieee-pes.org/technical-publications/technical-reports/PES\\_TP\\_TR77\\_PSDP\\_stability\\_051320.html](https://resourcecenter.ieee-pes.org/technical-publications/technical-reports/PES_TP_TR77_PSDP_stability_051320.html). Cited on p. 164, 178.
- [30] Commission Regulation (EU). Network code on requirements for grid connection of generators (April 2016). URL <http://data.europa.eu/eli/reg/2016/631/oj>. Cited on p. 164.
- [31] NEK. NEK EN 50549-1:2019 Requirements for generating plants to be connected in parallel with distribution networks - Part 1: Connection to a LV distribution network. NEK Oslo, Norway (February 2019). Cited on p. 164.
- [32] NEK. NEK EN 50549-2:2019 Requirements for generating plants to be connected in parallel with distribution networks - Part 1: Connection to a MV distribution network. NEK Oslo, Norway (February 2019). Cited on p. 164.
- [33] IEC 61892-2:2019 Mobile and fixed offshore units - Electrical installations - Part 2: System design. IEC Geneva, Switzerland (April 2019). ISBN 978-2-8322-6667-0. URL <https://webstore.iec.ch/publication/6083>. Cited on p. 164.
- [34] Commission Regulation (EU). Guideline on electricity transmission system operation (August 2017). URL <http://data.europa.eu/eli/reg/2017/1485/oj>. Cited on p. 164.
- [35] Erick Fernando Alves, Gilbert Bergna-Diaz, Danilo Iglesias Brandao, and Elisabetta Tedeschi. Sufficient Conditions for Robust Frequency Stability of AC Power Systems. *IEEE Transactions on Power Systems* **36**, 2684–2692 (May 2021). ISSN 0885-8950, 1558-0679. doi: 10.1109/TPWRS.2020.3039832. Cited on p. 164.
- [36] Peter W. Sauer, M. A. Pai, and J. H. Chow. Power system dynamics and stability: With synchrophasor measurement and power system toolbox. Wiley Hoboken, NJ, USA second edition edition (2017). ISBN 978-1-119-35577-9. Cited on p. 164.
- [37] Emanuele Ciapessoni, Diego Cirio, Gerd Kjolle, Stefano Massucco, Andrea Pitto, and Marino Sforina. Probabilistic Risk-Based Security Assessment of Power Systems Considering Incumbent Threats and Uncertainties. *IEEE Transactions on Smart Grid* **7** (6), 2890–2903 (November 2016). ISSN 1949-3053, 1949-3061. doi: 10.1109/TSG.2016.2519239. Cited on p. 165.
- [38] Ásta Hannesdóttir and Mark Kelly. Detection and characterization of extreme wind speed ramps. *Wind Energy Science* **4** (3), 385–396 (July 2019). ISSN 2366-7451. doi: 10.5194/wes-4-385-2019. Cited on p. 166, 167.
- [39] Jan Machowski, Janusz W. Bialek, and J. R. Bumby. Power system dynamics: Stability and control. Wiley Chichester, U.K 2nd ed edition (2008). ISBN 978-0-470-72558-0. Cited on p. 168, 178.
- [40] M. Sengupta and A. Andreas. Oahu Solar Measurement Grid (1-Year Archive): 1-Second Solar Irradiance; Oahu, Hawaii (Data) (2010). Cited on p. 171.
- [41] Matthew Lave, Jan Kleissl, and Joshua S. Stein. A Wavelet-Based Variability Model (WVM) for Solar PV Power Plants. *IEEE Transactions on Sustainable Energy* **4** (2), 501–509 (April



- 2013). ISSN 1949-3029, 1949-3037. doi: 10.1109/TSTE.2012.2205716. Cited on p. 171.
- [42] Sandia National Laboratories. PV Performance Modeling Collaborative | Wavelet Variability Model (2012). URL <https://pvpmc.sandia.gov/applications/wavelet-variability-model/>. Cited on p. 171.
- [43] Erick F. Alves and Louis Polleux. Efantnu/drep-2021-collab-MINESParisTech-NTNU: V0.2 (March 2022). Cited on p. 171, 180.
- [44] Daniel dos Santos Mota, Erick Fernando Alves, Santiago Acevedo-Sanchez, Harald G. Svendsen, and Elisabetta Tedeschi. Offshore Wind Farms And Isolated Oil And Gas Platforms: Perspectives And Possibilities. In *Proceedings of the ASME 2022 41st International Conference on Ocean, Offshore & Arctic Engineering OMAE 2022* Hamburg, Germany (June 2022). ASME. Cited on p. 176.
- [45] Johannes Schiffer, Daniele Zonetti, Romeo Ortega, Aleksandar M. Stanković, Tevfik Sezi, and Jörg Raisch. A survey on modeling of microgrids—From fundamental physics to phasors and voltage sources. *Automatica* 74, 135–150 (December 2016). ISSN 00051098. doi: 10.1016/j.automatica.2016.07.036. Cited on p. 178.
- [46] Erick Fernando Alves and Marco Aurelio de Souza. Analysis of overexcitation relaying set up in synchronous generators for hydro power plants. In *2010 IEEE/PES Transmission and Distribution Conference and Exposition: Latin America (T&D-LA)* pages 298–303 Sao Paulo, Brazil (November 2010). IEEE. ISBN 978-1-4577-0487-1. doi: 10.1109/TDC-LA.2010.5762897. Cited on p. 178.
- [47] Juha Pyrhonen, Tapani Jokinen, and Valeria Hrabovcová. Design of rotating electrical machines. Wiley Chichester, West Sussex, United Kingdom second edition (2013). ISBN 978-1-118-70165-2 978-1-118-70162-1. Cited on p. 178.
- [48] S. V. Kulkarni and S. A. Khaparde. Transformer engineering: Design, technology, and diagnostics. CRC Press Boca Raton 2nd ed edition (2013). ISBN 978-1-4398-5377-1. Cited on p. 178.
- [49] Luis Badesa, Fei Teng, and Goran Strbac. Simultaneous Scheduling of Multiple Frequency Services in Stochastic Unit Commitment. *IEEE Transactions on Power Systems* 34 (5), 3858–3868 (September 2019). ISSN 0885-8950, 1558-0679. doi: 10.1109/TPWRS.2019.2905037. Cited on p. 179.
- [50] Vincenzo Trovato, Agnes Bialecki, and Anes Dallagi. Unit Commitment With Inertia-Dependent and Multispeed Allocation of Frequency Response Services. *IEEE Transactions on Power Systems* 34 (2), 12 (2019). Cited on p. 179.





## CHAPTER 10

### *Optimal Energy Management in Autonomous Power Systems with Probabilistic Security Constraints and Adaptive Frequency Control*

---

Spyridon Chapaloglou<sup>1</sup>, Erick Alves<sup>1</sup>, Vincenzo Trovato<sup>2,3</sup>, and Elisabetta Tedeschi<sup>1,2</sup>

Journal paper submitted to: *IEEE Transactions on Power Systems*.  
Pre-print DOI: [10.48550/arXiv.2208.08953](https://doi.org/10.48550/arXiv.2208.08953)



**Open Access** This work is licensed under a Creative Commons Attribution 4.0 International License. It means that unrestricted use, sharing, adaptation, distribution, and reproduction in any medium or format are allowed, as long as the original author(s) and the source are appropriately credited, a link to the Creative Commons license is provided, and any changes made are indicated. To view a copy of this license, please visit <http://creativecommons.org/licenses/by/4.0/>.

© Chapaloglou, Alves, Trovato and Tedeschi, 2021.

#### **Author Contributions**

Conceptualization, S.C. and E.A.; methodology, S.C. and E.A.; software, S.C.; validation, S.C.; formal analysis, S.C. and E.A.; investigation, S.C. and E.A.; data curation, S.C.; writing - original draft preparation, S.C. and E.A.; writing - review and editing, V.T. and E.T.; visualization, S.C.; supervision, V.T. and E.T.; project administration, E.T.; funding acquisition, S.C. and E.T.

---

<sup>1</sup>Department of Electric Power Engineering, NTNU, 7034 Trondheim, Norway.

<sup>2</sup>Department of Industrial Engineering, University of Trento, 38123 Trento, Italy.

<sup>3</sup>Department of Electrical and Electronic Engineering, Imperial College London, London SW7 2BX, United Kingdom.

## ABSTRACT

The decarbonization of many heavy power-consuming industries is dependent on the integration of renewable energy sources and energy storage systems in isolated autonomous power systems. The optimal energy management in such schemes becomes harder due to the increased complexity and stability requirements, the rapidly varying operating conditions and uncertainty of renewable sources, the conflicting objectives across different timescales, the limited amount of reliable power sources and energy storage. The state of charge management when energy storage is used for multiple services, such as optimal scheduling and frequency support, is one of the most notorious problems in this context. To address this issue, an optimal energy management system is proposed in this paper. It co-optimizes the primary frequency control layer and the dispatch schedule of conventional generators and energy storage by taking advantage of an algorithm that provides adaptive active power demand uncertainty quantification, theoretical guarantees for frequency stability, and bounds for the reserves for frequency support assigned to the energy storage system. A convex reformulation is derived enabling the efficient solution of the involved optimization problem, being a test case of an isolated offshore oil and gas platform presented for validation.

## 10.1 INTRODUCTION

Taking optimal decisions to reduce *i)* fuel consumption, *ii)* GHG emissions, *iii)* equipment degradation and *iv)* system insecurity in power systems with a high share of renewable energy sources is an intricate task. This endeavor requires the solution of problems such as the unit commitment [1], economic dispatch [2], and allocation of reserves for frequency control [3], resulting in complex non-convex optimization formulations. Those have typically conflicting objectives, continuous and binary decision variables, and high uncertainty from particular nodes, such as loads and renewable energy sources. Reliability can, for instance, be increased where more dispatchable units, such as GTs, are kept online for longer periods, as they respond well to fast variations of loads and renewable energy sources. This action may, however, increase fuel consumption, emissions, and equipment degradation, affecting negatively OPEX.

When compared to traditional bulk power systems, this type of optimization can have different characteristics in autonomous power systems, such as isolated industrial plants, O&G platforms, ships, islands, and community micro-

grids. Due to the size and complexity of the problem, several challenges exist in bulk power systems to implement real-time, advanced algorithms for optimal dispatch and real-time allocation of frequency reserves [4]. Such problems can however be addressed in many autonomous power systems due to the limited number of dispatchable power sources, which typically provide simultaneously several ancillary services. The methods for allocation of frequency reserves and tuning of the system damping may also differ considerably between bulk power system and autonomous power system. The system damping is, in the former, adapted using binary decision variables which switch on and off units having a fixed active power-frequency droop, as usually the individual contribution of each unit to the total damping is small. In the latter, the droop of individual units may represent a large portion of the system damping, being therefore necessary to readjust them in real-time using integer variables to obtain optimal results.

Optimization objectives and decisions in autonomous power systems may also be coupled and affected by constraints in different time scales, being *ESSs* remarkable examples of equipment that enhances such dependencies. *ESSs* can, for instance, provide increased flexibility towards the optimal scheduling of fossil-based energy sources and avoid prolonged operation in partial loads, where emissions are much higher. They can also be assigned as spinning reserves for frequency control, which would require less *GTs* on for the same system security requirements and increase environmental gains even further. Where these two grid services are provided simultaneously, the scheduled trajectory of the *ESS*' state of energy may be disturbed, affecting the optimality or even the feasibility of the original schedule. To decide in bulk power systems the effect that the provision of frequency reserves has on the *ESS*' optimal schedule, scenarios such as the worst-case active power disturbance or the N-1 criterion are many times used [3, 5]. These criteria can however be over-conservative in autonomous power systems [6] and the *CAPEX* necessary for a fully-fledged *ESS* may not justify its benefits, being some probability of load shedding and generation curtailment acceptable many times [7]. When it comes to energy management in autonomous power systems with high penetration of renewable energy source, there is therefore a need and potential for better assessment of frequency stability requirements as well as coordination and scheduling of reserves.

### 10.1.1 Literature review

The integration of frequency stability constraints in the scheduling phase of bulk power systems with high penetration of renewable energy source has

been an active area of research in recent years and is well described in the literature [8]. The use of linear constraints had been a typical approach to increase the fidelity of the frequency response in the unit commitment and economic dispatch problems, which are obtained by linearizations and/or analytical solutions of the swing equation model [9–16]. These procedures provide good approximations in bulk power systems, where the largest active power disturbance is a small fraction of the installed capacity and transient and steady-state frequency deviations are usually required to be below 2% of its rated value [5]. Frequency deviations may, on the other hand, be much higher in autonomous power system due to low inertia and limited amount of frequency reserves when compared to the worst-case active power disturbances, causing the effects of non-linear dynamics to be sizeable during large disturbances [17]. Where these non-linear effects are considered, bilinear terms are introduced in the frequency stability constraints, those requiring specialized reformulation-linearization techniques [18–20]. This increase of the optimization model complexity can play an important role in autonomous power system, while it may bring only negligible frequency stability improvements in bulk power system.

The challenge of leveraging optimal system operation and security in autonomous power systems was also addressed recently, being alternatives presented to the deterministic evaluation of the worst-case active power disturbance or the N-1 criterion. References [13, 21–24], for instance, considered the effect of anticipated net load variations and applied dynamic constraints for sizing FCR and required inertia. These works did not evaluate however the impact that re-adjusting the droop of online units, instead of switching on and off units with fixed droops, would have on frequency stability and OPEX. References [9, 15, 20, 25] tried moreover to tackle the problem by applying simplified and static uncertainty models, such as non adaptive and arbitrary uncertainty intervals, distributions, and scenario selection, which have the limitation of not providing probabilistic guarantees.

### 10.1.2 *Paper contributions*

The main contribution of this paper is an algorithm for the EMS of a generalized autonomous power system equipped with an ESS that is capable of simultaneously achieving optimal scheduling and securing system operation under dynamic uncertainty considerations and bounded impact on its optimal scheduling. The proposed algorithm introduces realistic frequency constraints with general applicability, those not being limited to small scale power variations, combined with a probabilistic security analysis based on a novel adaptive

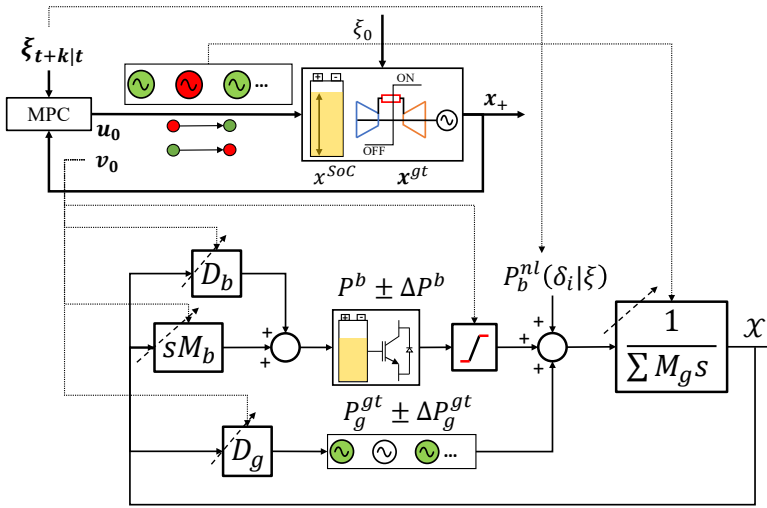


**FIGURE 10.1.** Hierarchical control system schematic where the upper layer optimal discrete time control is integrated with the lower time scale continuous adaptive primary frequency control. © Spyridon Chapaloglou et al, 2022.

power variation uncertainty quantification scheme. This new method allows an EMS to allocate time-varying optimal frequency control reserves with bounded divergence from its optimal state of energy. A simple strong mixed integer linear programming reformulation is derived to efficiently implement the proposed algorithm, whose effectiveness is verified by simulations using the case study of a wind-powered offshore O&G platform.

The rest of the paper is organized as follows. The proposed EMS algorithm and its numerical implementation are presented in Sec. 10.2, while simulations in Matlab/Simulink are used to validate and discuss the various features of the proposed algorithm using the case study of a wind-powered offshore O&G platform in Sec. 10.3. The main conclusions are finally presented in Sec. 10.4.

## 10.2 METHOD

The concept and the methodology proposed in this paper is presented in detail in this section. It assumes the existence of a centralized EMS in an autonomous power system that is capable not only to dispatch a set of  $g$  generators and a single ESS  $b$ , but also to decide, for the primary frequency controllers, the proportional gain (droop)  $D_g$  of each generator, the proportional gain (droop)  $D_b$  and derivative gain (virtual inertia)  $M_b$  of the ESS. Fig. 10.1 shows a conceptual illustration of the proposed scheme for the hierarchical EMS. The set  $v_0$  represents the control inputs to the low-level primary frequency controllers, which

include droop and virtual inertia coefficients, and is embedded into the set of commands  $u_0$  from the EMS. The latter also includes the decisions to startup (green circles) or to shutdown (red circles) the GTs. The techno-economic optimal schedule included in  $u_0$  not only shall be feasible for the actual net load disturbance  $\xi_0$  at  $t = t_0$ , but also will define the inertial support  $\sum_g M_g$  of conventional generators during  $[t_0, t_0 + T]$ , where  $T$  is the time step of the scheduling, further complicating the frequency control problem.

Note that the commands  $u_0$  are given for discrete points of the time interval (i.e.,  $k = 0 \Rightarrow t = t_0$  and  $k = 1 \Rightarrow t = t_0 + T$ ) based on the discrete net load forecasts  $(\xi_{t+0|t}, \xi_{t+1|t})$ . The transition from  $\xi_{t+0|t}$  to  $\xi_{t+1|t}$ , however, can happen at any time in the continuous time interval  $[t_0, t_0 + T]$ . In the proposed EMS algorithm, the power reserves  $\Delta P_g^{gt}$  and  $\Delta P_b$  are decided in an adaptive way respecting the ESS state of energy bounds. The forecast net load values  $\xi_{t+k|t}$  at time  $t$ , along with their corresponding uncertainties, are used to characterize the potential active power disturbances  $P_b^{nl}(\delta_i | \xi)$  that can occur in the interval  $[t_0, t_0 + T]$ . This is illustrated in Fig. 10.2, where the active power disturbance came off at a time  $t_0 \leq t'_0 \leq t_0 + T$ . As the forecasts are uncertain, the active power disturbance amplitude belongs to a value range (orange region), being therefore a function of the underlying probability density (green area) at the next scheduling instance  $k = 1 \Rightarrow t = t_0 + T$ . Where this probabilistic quantification algorithm is applied, the frequency control parameters  $D_g, D_b, M_b$  to be implemented in the current time instance  $t = t_0$  through the command  $v_0$  are decided in an adaptive way. This algorithm is further detailed in Secs. 10.2.3 and 10.2.4.

### 10.2.1 Frequency Control and Reserves Allocation

The non-linear dynamics of the frequency deviation for the center of inertia in an ac power system are given in Eq. (10.1), where  $\mathcal{X} = \frac{\omega}{\omega_s}$ , and  $\omega, \omega_s$  are the center of inertia frequency and its rated value respectively.

$$\dot{\mathcal{X}} = \frac{\mathcal{D}}{\mathcal{M}} (\mathcal{X} - 1) + \frac{P_b^{nl}}{\mathcal{X}\mathcal{M}} \quad (10.1)$$

$$\mathcal{D} \geq \frac{P_b^{nl}}{r_{ss}(1 - r_{tr})} \quad (10.2)$$

$$\mathcal{M} \geq \frac{P_b^{nl}}{\bar{\gamma}} \quad (10.3)$$

It is shown in [17] that if the total system damping  $\mathcal{D}$  is selected as in Eq. (10.2), then  $\mathcal{X}$  will be bounded post-disturbance by  $r_{ss}$  for an instantaneous net active power imbalance  $P_b^{nl}$ , where  $r_{tr}$  is a pre-defined constant bound for



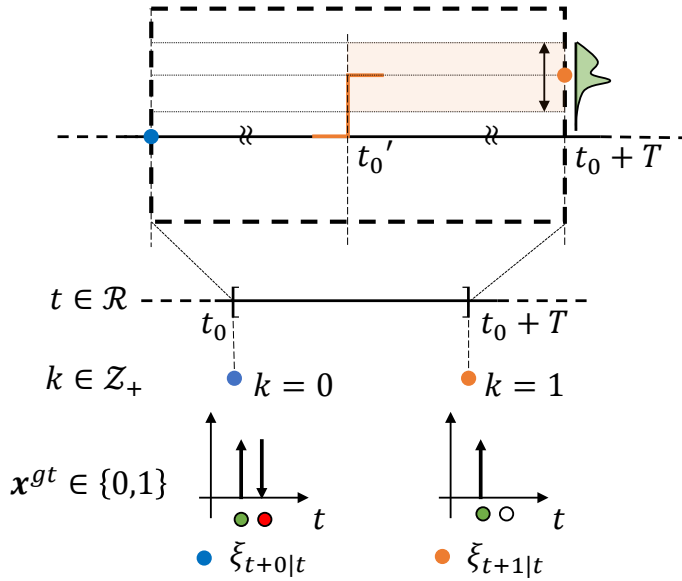


**FIGURE 10.2.** Visualization of the proposed adaptive and probabilistic step-like net active power disturbance quantification at a time instant in the continuous range between the discrete points in time where decisions are taken. © Spyridon Chapaloglou et al, 2022.

the nadir/zenith of  $\mathcal{X}$  during the transient period. Note that the step-response of frequency for active power disturbances is, in most ac power systems, underdamped due to delays of actuators and their non-linearities [26]. Those effects are not modelled in Eq. (10.1) because they influence only the frequency nadir or zenith after the disturbance  $P_b^{nl}$  occurs, being the post-disturbance steady-state value of  $\mathcal{X}$  unaffected [17]. The variables  $r_{ss}$  and  $r_{tr}$  in Eq. (10.2) represent, in other words, the allowed steady-state and transient frequency deviations in per unit of  $\mathcal{X}$ , being usually defined in grid codes or by the system operator.

It is typical to assume  $r_{tr} > r_{ss}$  to provide a safety margin which avoids triggering protection schemes such as under frequency load shedding or over frequency generation curtailment during large disturbances. When  $r_{ss} = r_{tr}$ , there exists no safety margin between steady-state and transient values. It shall also be noted that Eq. (10.2) is valid for any value of  $\mathcal{X}$ , and not only for small deviations around the operating point.

The minimum required inertia  $\mathcal{M}$  is retrieved from Eq. (10.1), assuming that a) the disturbance  $P_b^{nl}$  occurs at  $t = t_0'$ , b) the system was previously in balance ( $\mathcal{X}|_{t=t_0'} = 1$ ), and c) the maximum rate of change of frequency is  $\dot{\mathcal{X}}|_{t=t_0'} = \bar{\gamma}$ , which results in Eq. (10.3).

Ensuring that enough power reserves are available in an autonomous power system is a necessary condition to satisfy the constraints for frequency control imposed by Eqs. (10.2) and (10.3). The values of  $\mathcal{D}$  and  $\mathcal{M}$  depend on the number of online units and their individual parameters, being expressed by Eqs. (10.4) and (10.5), where  $D_g$  and  $M_g$  denote the droop setting and the inertia of each online generator, and  $D_b$  and  $M_b$  are the virtual damping and inertia emulated by the ESS, respectively. The EMS must guarantee that each individual equipment has enough available power capacity to provide the frequency reserves assigned to it, what leads to the constraints in Eqs. (10.6) and (10.7).

$$\mathcal{D} = \sum_g^{N_g} x_g^{gt} D_g + D_b \quad (10.4)$$

$$\mathcal{M} = \sum_g^{N_g} x_g^{gt} M_g + M_b \quad (10.5)$$

$$|\Delta P_b(t)| \leq M_b \bar{y} + D_b r_{tr} \quad (10.6)$$

$$|\Delta P_g(t)| \leq x_g^{gt} D_g r_{tr}, \quad \forall g \in \mathcal{N}_g \quad (10.7)$$

### 10.2.2 Optimal and Bounded Energy Management under Uncertainty

#### Allocation of frequency reserves with bounded energy storage

The EMS must also ensure that enough energy capacity is available in the ESS. This is required not to violate the storage limits when providing frequency control in the current scheduling step  $t_0$  while charge or discharge events had already been scheduled for the next step  $t_0 + T$ , where  $T$  is the time step of the EMS. To deal with this situation, the constraint in Eq. (10.8) is proposed, where  $\Delta E^b(t)$  is a deviation around the optimal scheduled state of energy  $E^b(t)$ , and  $\lambda$  is a user-defined (absolute) percentage value that enables the system operator to define the tolerable departure from the optimal reference state of energy schedule. The proposed constraint allows, in other words, an allocation of frequency reserves to the ESS that is proportional to its current energy level.

$$\Delta E^b(t) \leq \overline{\Delta E^b}(t) = \lambda E^b(t) \quad (10.8)$$

For energy calculations of frequency containment reserves in EMS algorithms, one can assume that  $\mathcal{X} \leq r_{ss}$ ,  $\forall t \in [t_0, t_0 + T]$  when the system is frequency stable [17], this simplification resulting in Eq. (10.9). Remark that, on one hand,  $r_{ss} \leq \mathcal{X} \leq r_{tr}$  during the arrest and rebound periods of frequency containment. On the other hand, those periods combined last only a couple of

seconds, while  $T$  may vary from 5 minutes to 15 minutes in typical EMSs. The integration error would therefore be minimal when adopting this simplification. The latter however allows  $\widehat{\Delta E^b} \leq \overline{\Delta E^b}(t)$  to be enforced in the optimization problem, as described later in Sec. 10.2.3, and to satisfy Eq. (10.8), which avoids excessive deviations of the state of energy from its optimal dispatch.

$$\Delta E^b(t) = \Delta E^b(\mathcal{X}) = \int_{t_0}^{t_0+T} (M_b \dot{\mathcal{X}} + D_b \mathcal{X}) dt =$$

$$M_b \mathcal{X} \Big|_{t_0}^{t_0+T} + D_b \int_{t_0}^{t_0+T} \mathcal{X} dt \leq M_b r_{tr} + D_b r_{ss} T = \widehat{\Delta E^b} \quad (10.9)$$

### Adaptive Uncertainty Quantification

Load uncertainty is, in the proposed method, evaluated not only in rapidly varying loads but also in the intermittency of non-dispatchable power sources, being the net load variation defined as the combination of two random variables  $P^p$ , where  $p = \{\ell, w\}$  corresponds to load and non-dispatchable sources respectively.

To achieve adaptive quantification of the uncertainty for a given prediction horizon  $\mathcal{K}$ , it is sufficient to estimate a time-dependent (conditional) multivariate cumulative distribution function  $\hat{F}_{\mathcal{K}|t}^p$  [27]. Ensembles of random forest models [28] can, therefore, be assembled together to perform multi-step ahead predictions given available datasets  $\mathcal{D}_k^p = \{X_{d,k}^p, P_{d,k}^p\}_{d=1:N_{\mathcal{D}}}, \forall k \in \mathcal{K}$ , where  $X_{d,k}^p$  are the input features and  $P_{d,k}^p$  the available observations for regression representing realizations of each random variable  $P^p$  at the  $k^{th}$  step ahead. For that, individual random forest models are trained for each variable  $P^p$  and lead time  $k \in \mathcal{K}$ . Each random forest is composed of  $|\mathcal{T}|$  auto-regressive trees  $f_{n,k}^p(\cdot)$ ,  $n \in \mathcal{T}$ . The inputs to the trees (regressors)  $\mathbf{x}_r(t)$  are composed only by the current ( $k = 0$ ) and  $L$  lagged values of the corresponding variable, that is  $\mathbf{x}_r(t) = [P_t^p, P_{t-1}^p, \dots, P_{t-L}^p]^T \forall p = \{\ell, w\}$ . Following the procedure described in [27], a point forecast can be calculated for the corresponding prediction horizon  $\mathcal{K}$  using Eq. (10.10), where  $\mathbf{1}\{\cdot\}$  is the indicator function operator,  $N_{\mathcal{D}}$  the number of observations  $P_{d,k}^p$  in the corresponding training datasets, and  $\mathcal{S}_{n,k}(\mathbf{x}_r)$  is the leaf node of the corresponding tree  $n$  and random forest model  $k$  in which the new input  $\mathbf{x}_r(t)$  falls in.

$$\begin{aligned}
\hat{P}_{t+k}^p(\mathbf{x}_r(t)) &= \frac{1}{|\mathcal{T}|} \sum_{n \in \mathcal{T}} f_{n,k}^p(\mathbf{x}_r(t)) \quad \forall k \in \mathcal{K}, p = \{\ell, w\} \\
f_{n,k}^p(\mathbf{x}_r(t)) &= \sum_{d=1}^{N_D} \frac{\mathbb{1}\{X_{d,k}^p \in \mathcal{S}_{n,k}(\mathbf{x}_r(t))\}}{\sum_{m=1}^{N_D} \mathbb{1}\{X_{m,k}^p \in \mathcal{S}_{n,k}(\mathbf{x}_r(t))\}} P_{d,k}^p \Rightarrow \\
f_n^p(\mathbf{x}_r(t)) &= \sum_{d=1}^{N_D} \tau_{d,k}(\mathbf{x}_r(t)) P_{d,k}^p \quad \forall k \in \mathcal{K}, p = \{\ell, w\}
\end{aligned} \tag{10.10}$$

From Eq. (10.10), the conditional expected value  $\hat{\mathbb{E}}[P_{t+k}^p | \mathbf{x}_r(t)]$  of each random variable and lead time can be expressed by the corresponding estimates  $\hat{P}_{t+k}^p$  as a function of time [29]. Time-varying cumulative distribution functions  $\hat{F}_{t+k|t}^p$  can also be inferred [29] for each random variable and lead time as in Eq. (10.11), besides the time-varying estimates of the expectations which can be considered a “mean” multi-step ahead prediction. It is shown in [27] that, using Eq. (10.11), the multi-variate  $\hat{F}_{K|t}^p$  can be approximated by sampling of the marginals  $\hat{F}_{t+k|t}^p$ . By combining the random variables  $P_{t+k}^p$  for  $p = \{\ell, w\}$ , the net load can be also represented as a time-dependent random variable as  $\xi_{t+k}(t) = P_{t+k}^\ell(t) - P_{t+k}^w(t)$  which encapsulates the system disturbance uncertainty for the EMS.

$$\begin{aligned}
\hat{F}_{t+k|t}^p &= \frac{1}{|\mathcal{T}|} \sum_{n \in \mathcal{T}} \sum_{d=1}^{N_D} \tau_{d,k}(\mathbf{x}_r(t)) \mathbb{1}\{P_{d,k}^p \leq P_{t+k}^p\} \Rightarrow \\
P_{t+k}^p &\sim \hat{F}_{t+k|t}^p \left( P_{t+k}^p \mid \mathbf{x}_r(t) \right), \quad \forall k \in \mathcal{K}, p = \{\ell, w\}
\end{aligned} \tag{10.11}$$

Any decision taken by a predictive EMS algorithm relying on that forecast will however be sub-optimal, as the net load  $\xi_0$  that actually hits the system at  $t = t_0$  (see Fig. 10.2) is a realization of the random  $\xi_{t+k}(t)$ . The latter is, in principle, different from the forecasted value due to inevitable forecasting errors, a fact that not only degrades the optimality of the decision in terms of economic value but most importantly is critical to evaluate the active power disturbances which may threaten the system’s frequency stability due to insufficient inertia or damping. It is therefore important to quantify the uncertainty of the random net load  $\xi(t)$  and subsequently of the active power disturbance that can occur in the interval  $[t_0, t_0 + T]$ . For the sake of brevity, this paper will not detail further the uncertainty quantification method, its validation, and how net load scenarios can be generated. The interested reader can however refer to [27]

for a full description. Where the procedure described in [27] is applied, the uncertainty of the net load affecting an isolated autonomous power system can be quantified through the adaptive probabilistic forecasting framework described in this section. This procedure will be exploited in the construction of the security constrained energy management algorithm described in Sec. 10.2.3.

### 10.2.3 Probabilistically Constrained EMS

This section presents how the proposed EMS algorithm integrates into a single optimization problem including the various objectives and multiple time-scale requirements described in Secs. 10.2.1 and 10.2.2. The system dynamics are first expressed in a hybrid state space system to achieve this integration as shown in Eq. (10.12), where  $\mathbf{x}_+$  is the state at the next discrete time,  $\mathbf{u}$  the corresponding control inputs and  $\mathbf{A}, \mathbf{B}$  the corresponding system matrices. Note that  $x^{SoC} = E^b/\bar{E}^b \in [\underline{x}^{SoC}, \bar{x}^{SoC}]$  and  $\mathbf{x}_{1:N_g}^{gt} = \{x_g^{gt}\}_{1:N_g} \in \{0, 1\}$ .

$$\mathbf{x}_+ = \mathbf{A}\mathbf{x} + \mathbf{B}\mathbf{u} \quad (10.12)$$

The optimization problem presented in Eq. (10.13) is then formulated and solved in each discrete time step  $t$ , where  $\delta = \{\delta_k^i\}_{1:K}$  is a random multi-sample,  $\xi = \{\xi_k\}_{0:K-1}$  is the deterministic mean net load forecast including the measured value  $\xi_0$  at  $t = t_0$ , and  $\mathbf{P}_{nl}^b = \{P_{nl}^b(\delta_{k+1}|\xi_k)\}_{0:K-1}$  is the net load perturbation for the whole prediction horizon as a function of the sample and the mean forecast. The control horizon was set to be equal to the prediction horizon  $\mathcal{K}$ , which is a common practice in model predictive control schemes [30].  $|\mathcal{K}| = 6$  is used by the adaptive uncertainty quantification module explained in Sec. 10.2.2, being this value long enough to provide reliable forecasts to some quarters ahead but short enough to limit the additional computational burden and processing time for the EMS.

$$\begin{aligned} \mathcal{P} : & \min_{\mathbf{u}, \mathbf{v}, \mathbf{z}} \{\mathcal{F}(\mathbf{x}_+, \mathbf{z}, \mathbf{u}, \mathbf{v}; \xi)\} \\ \text{where, } \mathcal{F} := & \underbrace{\mathcal{J}(\mathbf{x}_+)}_{\text{states cost}} + \underbrace{\mathcal{J}(\mathbf{z})}_{\text{operation cost}} + \underbrace{\mathcal{J}(\mathbf{u})}_{\text{control cost}} + \underbrace{\mathbf{w}^T \mathbf{v}}_{\text{reserves cost}} \\ \text{s.t. } & \mathbf{C}(\mathbf{x}_+, \mathbf{z}, \mathbf{u}, \mathbf{v}, \xi) \leq \mathbf{0}, \\ & \mathbb{P}(\delta \in \Delta \mid |\xi - \delta| = \mathbf{P}_{nl}^b) \leq \\ & \min\{\mathcal{D}r_{ss}(1 - r_{tr}), \mathcal{M}\bar{y}\} \mathbb{1}_{\{1:K\}} \geq 1 - \epsilon. \end{aligned} \quad (10.13)$$

In the cost function  $\mathcal{F}$ ,  $\mathcal{J}(\mathbf{x}_+)$  represents the cost of having generators online,  $\mathcal{J}(\mathbf{z})$  penalizes the deviation from optimal operating conditions of on-line generators and the ESS,  $\mathcal{J}(\mathbf{u})$  captures the start up cost of generators, and

finally  $\mathbf{w}^T \mathbf{v}$  accounts for costs of activating reserves for frequency control. The decision variables  $\mathbf{v} = [\mathbf{D}_g, D_b, M_b]^T$  used for frequency reserves are weighted by  $\mathbf{w}$  so that different contributions can be assigned to online generators and the ESS to ensure the system frequency stability. In that aspect, the higher the numerical value of the corresponding  $\mathbf{w}$  element, the closer a generator will remain to its optimal operating point, as its contribution to frequency control is penalized. Each term of  $\mathcal{F}$  is described in detail in [27] and expresses the corresponding economical cost defined by coefficients such as GT startup cost, fuel consumption, battery cycling, and so on.

The term  $C(\cdot)$  encapsulates all the constraints related to the operation of the energy system, as described in [27]. The last expression in Eq. (10.13) is a chance constraint that, given the estimated distributions from Eq. (10.11), relates potential instantaneous perturbations for a net load value  $\xi_k$  and the next step sampled net load  $\delta_{k+1}^i$ . Eqs. (10.2) and (10.3) are, in other words, risk-constrained by  $\epsilon$ , which act as a mechanism to leverage cases with rather pessimistic prediction intervals resulting from poor uncertainty range estimation.

The chance constraint complicates, however, the optimization problem. Note that  $\mathcal{P}$  is a stochastic mixed integer nonlinear problem and therefore non-convex, so a standard *scenario approach* cannot be applied. Following [31, 32], a probabilistic set composed of a finite number of samples  $\delta^i \in \Delta^N$  is computed as in Eq. (10.14), being  $\beta$  and  $e$  user defined parameters that tighten the non-violation of the original chance constraint. Note that the number of random variables is  $2|\mathcal{K}|$  because two sources of uncertainty exist (load and renewable power injection) for the whole prediction horizon. The chance constraint can however be replaced by the deterministic set of linear inequalities presented in Eq. (10.15), which transforms the stochastic problem  $\mathcal{P}$  into a robust one, where the set  $\Delta^N$  encapsulates the same risk-volume  $\epsilon$  as the original chance constraint. When solving the corresponding robust program, solutions are not only feasible for the initial  $\mathcal{P}$  but also satisfy the same probabilistic guarantees [33].

$$N \geq \frac{1}{\epsilon} \frac{e}{e-1} \left( \ln \frac{1}{\beta} + 4|\mathcal{K}| - 1 \right) \quad (10.14)$$

$$|\xi - \delta^i| = \mathbf{P}_{nl}^b \leq \min\{\mathcal{D}r_{ss}(1 - r_{tr}), \mathcal{M}\bar{y}\} \mathbb{1}_{\{1:K\}} \quad (10.15)$$

$$\forall \delta^i \in \Delta^N$$

### 10.2.4 Proposed Convex Reformulation

It is not feasible, on one hand, to implement the constraints expressed in Eqs. (10.2), (10.4) and (10.7) directly into a mixed integer linear programming formulation because of the bi-linear terms  $x_g^{gt} D_g$ . It is possible, on the other hand, to take advantage of the following observation: with  $N_g$  generators, there are exactly  $2^{N_g}$  different possible system configurations depending on the values of  $\mathbf{x}_{1:N_g}^{gt} \in \{0, 1\}$ . The status variable  $x_{g,t}^{gt}$  takes a particular value (0 or 1) for each generator and configuration, being therefore feasible to represent it by binary strings of length  $N_g$ . The feasible system configurations are then enumerated by taking all the possible permutations, which can be gathered in a data table  $\mathbf{A}_{cf} [2^{N_g} \times N_g]$ . The variables  $x_{g,k}^{gt}, \forall k \in \mathcal{K}$  can, in this way, be treated as constants given a selected system configuration, being indicator variables  $b_j$  introduced to identify the configuration selected and associate it with the status of the generators by the set of constraints in Eqs. (10.16) and (10.17). Eq. (10.4) can, as consequence, be linearized using  $\mathbf{A}_{cf}$  as in Eq. (10.18).

$$x_{g,k}^{gt} \geq b_j, \{(j, g) \in \mathcal{J} \times \mathcal{N}_g \mid [\mathbf{A}_{cf}]_{j,g} = 1\} \quad (10.16)$$

$$x_{g,k}^{gt} \leq 1 - b_j, \{(j, g) \in \mathcal{J} \times \mathcal{N}_g \mid [\mathbf{A}_{cf}]_{j,g} = 0\} \quad (10.17)$$

$$\mathcal{D} = \mathbf{A}_{cf} \mathbf{D}_g + D_b \mathbb{1}_{\{1:J\}} \quad (10.18)$$

Eqs. (10.2) and (10.3) can also be reformulated using the sampled net active power disturbance terms from Eq. (10.15). This is presented in Eq. (10.19), where  $M_B$  is a big-M value,  $\mathbf{b}_k, \mathcal{D}_k$  correspond to each lead time of the prediction horizon ( $k \in \mathcal{K}$ ) assuming that  $M_g$  are constant values. The different possible configurations are restricted by a type 1 special ordered set constraint as in Eq. (10.20).

$$\begin{aligned} \mathbf{P}_{nl}^b (\delta_{k+1}^i | \xi_k) + M_B \mathbf{b}_k &\leq \mathcal{D}_k r_{ss} (1 - r_{tr}) + M_B \mathbb{1}_{\{1:J\}} \\ \frac{1}{\bar{y}} \mathbf{P}_{nl}^b (\delta_{k+1}^i | \xi_k) &\leq M_g \mathbb{1}_{\{1:N_g\}}^T \mathbf{x}_k^{gt} + M_{b,k} \end{aligned} \quad (10.19)$$

$$\forall \delta_k^i \in \Delta^N, \forall k \in \mathcal{K}$$

$$\mathbb{1}_{\{1:J\}}^T \cdot \mathbf{b}_k = 1, \forall k \in \mathcal{K} \quad (10.20)$$

Eq. (10.7) is similarly linearized using  $\mathbf{A}_{cf}$  and  $M_B$  as in Eqs. (10.21) and (10.22) where  $S_b$  is the system's base power.

$$\begin{aligned}
\mathbf{P}_k^{gt} + M_B \mathbf{b}_k &\leq (\bar{P}^{gt} - D_{g,k} \cdot r_{tr} \cdot S_b) + M_B \mathbb{1}_{\{1:J\}}, \\
(\underline{P}^{gt} + D_{g,k} \cdot r_{tr} \cdot S_b) + M_B \mathbf{b}_k &\leq \mathbf{P}_k^{gt} + M_B \mathbb{1}_{\{1:J\}} \\
\forall k \in \mathcal{K}, \{(j, g) \in \mathcal{J} \times \mathcal{N}_g \mid [A_{cf}]_{j,g} = 1\}
\end{aligned} \tag{10.21}$$

$$\begin{aligned}
\mathbf{P}_k^{gt} + M_B \mathbf{b}_k &\leq M_B \mathbb{1}_{\{1:J\}}, \\
M_B \mathbf{b}_k &\leq \mathbf{P}_k^{gt} + M_B \mathbb{1}_{\{1:J\}}, \\
\forall k \in \mathcal{K}, \{(j, g) \in \mathcal{J} \times \mathcal{N}_g \mid [A_{cf}]_{j,g} = 0\}
\end{aligned} \tag{10.22}$$

The ESS reserves from Eq. (10.6) are reformulated in terms of discharging and charging power as in Eq. (10.23), where  $s_k$  is the discharging binary indicator variable.

$$\begin{aligned}
P_k^{dis} &\leq s_k \bar{P}^b, \\
P_k^{dis} &\leq \bar{P}^b - (D_{b,k} \cdot r_{tr} + M_{k,b} \cdot \bar{\gamma}) \cdot S_b, \\
P_k^{ch} &\leq (1 - s_k) \bar{P}^b, \\
P_k^{ch} &\leq \bar{P}^b - (D_{b,k} \cdot r_{tr} + M_{k,b} \cdot \bar{\gamma}) \cdot S_b, \quad \forall k \in \mathcal{K}
\end{aligned} \tag{10.23}$$

The bound derived in Eq. (10.9) can be easily integrated to  $\mathcal{P}$  through the linear constraints in Eq. (10.24), where  $v = \frac{r_{ss} S_b}{3600 \bar{E}^b}$ .

$$\begin{aligned}
v (M_{b,k} + D_{b,k} T) &\leq \\
\min\{\bar{x}^{SoC} - \underline{x}_{k-1}^{SoC}, \bar{x}_{k-1}^{SoC} - \underline{x}^{SoC}, \lambda x_k^{SoC}\}, \quad \forall k \in \mathcal{K}
\end{aligned} \tag{10.24}$$

Eq. (10.13) may therefore be expressed as a deterministic mixed integer linear programming robust program and solved efficiently by the EMS at each time iteration, as  $\mathcal{F}(\cdot)$  and  $\mathcal{C}(\cdot)$  can be expressed as linear combinations of the optimization variables when including the reformulations proposed in Eqs. (10.15) to (10.24).

### 10.3 SIMULATIONS

The various components of the proposed methodology are demonstrated in this section, namely the adaptive uncertainty quantification and the integration of frequency stability constraints with bounded use of the ESS stored energy in the optimal scheduling. To achieve this goal, the case study of a wind-powered offshore O&G platform is presented, where a reference operation time period is considered (8 hours) involving both regions of smooth, low magnitude and sudden, large net load variations. The reference isolated autonomous power system is composed of 4 identical GTs ( $\mathcal{N}_g = 4$ ) with  $\bar{P}^{gt} = 1.09 \cdot 20.2$  MW,



$\underline{P}^{gt} = 0.2 \cdot 20.2$  MW and a single battery ESS ( $N_b = 1$ ) with  $\bar{E}^b = 20$  MW h,  $\bar{P}^b = 10$  MW,  $\bar{x}^{SoC} = 0.8$ ,  $\underline{x}^{SoC} = 0.2$ . Reference [27] presents the remaining parameter values and model details of this benchmark system. The effectiveness of the proposed methodology is demonstrated using time domain simulations of a 8 h period, corresponding to the complete scheduling time scale, and a simulation step of  $T = 15$  min. The effectiveness of the proposed methodology is then demonstrated with time domain simulations on the scheduling time scale. The optimization problem is solved with *Gurobi 9.1.0* in a 28 physical core multi-node cluster with Intel(R) Xeon(R) CPU E5-2690 v4 @ 2.60 Hz and 25 GB RAM. The solution time of Eq. (10.13) using the proposed formulation is well below 15 minutes, which is assumed here as the minimum threshold for real-time power system scheduling.

### 10.3.1 Capabilities of adaptive uncertainty quantification

A representative example of how the adaptive uncertainty quantification framework works is illustrated in Fig. 10.3, where a case of a sudden active power disturbance was selected since these are the most interesting from a power imbalance perspective. The actual load values  $p^\ell$  are presented with the solid black line and the blue cross ( $p_{t|t}^\ell$ ) indicates the time instant at which a probabilistic forecast is issued. As described in Sec. 10.2.2, the probabilistic forecasts are composed of the expected values  $\hat{\mathbb{E}}[P_{t+k}^\ell | \mathbf{x}_r(t)]$  of the random variable  $P^\ell$ , plotted with solid red line, and the prediction intervals  $\hat{\alpha}(x)$  plotted around them in different shades of green, depending the quantile level  $\tau = \{20\%, 40\%, 60\%, 80\%, 90\%\}$ , for the whole prediction horizon ( $k \in \mathcal{K}$ ). Two extreme quantile values  $Q_\tau^\ell(\mathbf{x}_r(t))$  (for  $\tau = \{5\%, 95\%\}$ ) are plotted with solid green lines, to illustrate that, as expected, most of the randomly generated sample values of load  $\delta^i$  fall inside those. The random load samples  $\delta^i$  are plotted in pink dots and represent one out of two components used for the net load scenarios. These scenarios are fed into the optimization problem  $\mathcal{P}$  through Eq. (10.15), being only 100 of them plotted in Figs. 10.3a to 10.3g for the sake of visualization clarity).

The proposed adaptive uncertainty quantification algorithm generates samples that better describe the size of an active power disturbance as a function of time. Observe that the prediction intervals  $\hat{\alpha}$  and quantiles  $Q_\tau^\ell$  adapt to capture the irregular event of the sudden load increase as the blue cross moves forward in time (i.e., time  $t$  is updated from  $t_0 - 3$  towards  $t_0 + 3$ ), and a new forecast is issued from  $p_{t|t}^\ell$  for the prediction horizon  $t + k|t$ . Note also that, at the initial time  $t = t_0 - 3$  (Fig. 10.3a), the prediction intervals are narrow and all the sampled values  $\delta^i$  (pink dots) fall close and around the actual load values. For

the following intervals (i.e.,  $t = t_0 - 2, \dots, t_0 + 3$ , Figs. 10.3b to 10.3g), however, the uncertainty increases and the prediction intervals  $\hat{\alpha}$  and quantiles  $Q_r^\ell$  expand to capture the possibility of an irregular sudden load increase. Observe that, at the intervals prior to the active power disturbance, random load samples  $\delta^i$  (pink dots) were generated at higher load values in the prediction horizon and close to the actual step (solid black line). The deterministic forecast (solid red line) which expresses the expected predictions ( $\hat{\mathbb{E}}[P_{t+k}^\ell | \mathbf{x}_r]$ ), in contrast, fails to capture the variation adequately, because it is dominated by the inertia of past values (lagged load values in  $\mathbf{x}_r(t)$ ), a common drawback of auto-regressive models.

### 10.3.2 Effect of optimal and bounded frequency support from ESS

To demonstrate the effect of optimally controlling the ESS to provide frequency support for an isolated autonomous power system, a step active power disturbance is considered at time  $t'_0 = 2s$  representing a 0.4 pu load increase from a sudden motor startup, where a single GT is on in the platform of the case study. Simulations were run in Matlab/Simulink 2022a using the model given in Eq. (10.1), which do not include delay of actuators. This simplification facilitates the interpretation of results, not implying however any loss of generality.

Results are illustrated in Fig. 10.4, where the frequency deviation (solid lines) and the rate of change of frequency (dashed lines) for two cases are represented. In the first case (grey lines), the single online GT is the only source of primary frequency control, while, in the second case (black lines), the ESS supports in this task the GT, which has the same droop setting as in the previous case. Observe that the system's response in the first case violates not only the steady-state frequency bound  $r_{ss}$  but also the maximum allowable rate of change of frequency ( $\bar{\gamma}$ ), whereas in the second case both limits are respected. To respect the defined bound in the first case, the GT droop setting must be increased, leading to a larger deviation from the optimal GT operating point, decreased efficiency, increased fuel consumption and emissions. The same droop setting for the GT, on the other hand, can be maintained and the  $r_{ss}$  threshold observed where an optimal participation of the ESS in the primary frequency control has been decided beforehand by the algorithm using an adaptive droop setting. Note also the compliance with the rate of change of frequency limit where the ESS provides virtual inertia. To respect this limit without the ESS support would require an additional GT on, affecting significantly the overall efficiency of the system. The proposed algorithm, in other words, employs an adaptive droop and virtual inertia scheme, enabling not only the optimal scheduling of the power system by avoiding an additional GT on, but also guaranteeing

that the services provided by the ESS to the grid will not cause it to deviate significantly from its optimal schedule, as the use of stored energy is bounded by Eq. (10.24). As a matter of fact, the calculated energy for frequency support provision by the ESS to the described disturbance for  $T$  (15 minutes) is 0.9179  $MWh$  while the bound for  $\lambda = 3\%$  is 0.9369  $MWh$ .

### 10.3.3 Comparative analysis and effect of bounds

To further demonstrate the capabilities of the proposed EMS, a reference operation period is simulated considering: *I*) the default EMS that does not integrate any bounds; *II*) the version that includes frequency variation bounds but not the energy bounds on the ESS; and *III*) the proposed version which includes all of them.

#### System inertia and damping evolution

The results for all EMS versions are aggregated in Fig. 10.5, being the system inertia and damping evolution depicted in Fig. 10.5a and Fig. 10.5b along with the net load signal  $P_b^{nl}(t)$  (solid black line), during a reference period of 8 hours. No frequency and rate of change of frequency containment reserves are considered in case *I*, the droop settings not being optimization variables and the ESS not contributing with virtual inertia. The system inertia  $\mathcal{M}(t)$  (red line in Fig. 10.5a) is therefore just the result of the online GTs based on the optimal techno-economic scheduling, not having any virtual component  $M_b(t)$ . Following the same color notation in both Fig. 10.5a and Fig. 10.5b, the evolution of the system inertia and damping is observed, being the contribution of the ESS in case *II* denoted by the superscript  $f$  (frequency bound) and in case *III* by  $f, e$  (frequency and energy bound).

Two main patterns are evident when observing Fig. 10.5a and Fig. 10.5b. Firstly, more inertia and damping are assigned for both cases *II* and *III* close to the time instants of the sudden net load variations (around 14:00 and 18:00 correspondingly). Secondly, the same inertia and damping are noticed during the relatively constant net load conditions (between 14:00 and 18:00). This effect demonstrates the adaptive capabilities of the proposed EMS algorithm to assign more or less inertia and damping in correspondence with the anticipated net load variations. The larger the variations expected, the more secure the system will be by properly deciding its power and energy reserves. Whether the ESS is not assigned to frequency control, securing the system for possible net load variations would require additional GTs to be on. This is confirmed in Fig. 10.5a during both sudden net load variations, where  $\mathcal{M}(t) \leq \mathcal{M}^f(t)$  (green line) and  $\mathcal{M}(t) \leq \mathcal{M}^{f,e}(t)$  (magenta line). Note also that around those

instants,  $M_b^f(t) \geq 0$  (cyan line) and  $M_b^{f,e}(t) \geq 0$  (blue line), meaning that the additional GT can be avoided by properly assigning virtual inertia to the ESS. Similar observations are drawn from Fig. 10.5b where  $D_b^f(t) \geq 0$  (cyan line) and  $D_b^{f,e}(t) \geq 0$  (blue line) around the sudden variation instants and  $D_b^f(t) = 0$  and  $D_b^{f,e}(t) = 0$  for the rest period.

Remark that the effect of the energy bounds on the ESS are stronger in the damping terms than in the inertia. Fig. 10.5a shows that the signals  $M_b^f(t)$  and  $M_b^{f,e}(t)$  are almost identical for the whole time period, whereas Fig. 10.5b depicts that  $\sup D_b^{f,e}(t) \leq \sup D_b^f(t)$ . This means that the peak contribution of the ESS for case III is smaller than the one for case II. It is indeed possible to observe that  $D_b^{f,e}(t)$  is almost always less than  $D_b^f(t)$ , further demonstrating that version III is more cautious not to overuse the primary frequency control of the ESS.

The comparison of the different methods (I, II, III) is also quantified through the cumulative results of specified key performance indicators in table 10.1. Including bounds on the EMS results in slightly higher fuel consumption and operating costs, which is primarily attributed to higher cumulative operational hours of the GTs. This agrees with the results presented in Fig. 10.5, as securing the system against possible disturbances may be associated with increased inertia requirements. The marginally increased fuel consumption of method III relatively to II (+0.7 %) is justified by the bounded energy contribution of the ESS, which slightly moves the GTs away from their optimal reference set-point. It is also noteworthy in table 10.1 that the incremental cost for including bounds on the use of ESS stored energy (III) compared to case II is negligible, meaning that the optimal GT scheduling is almost not affected by the inclusion of energy bounds in the ESS. The main difference is that the resulting optimal GT trajectory for II is associated with one less GT start up compared to III and slightly lower ESS cycling, reflected on the lower degradation, which is however almost equal in cases I and III.

**TABLE 10.1.** Performance comparison for the whole simulation period.

| Performance indicator          | Method |        |        |
|--------------------------------|--------|--------|--------|
|                                | I      | II     | III    |
| fuel consumption (ON GTs) [kg] | 29,695 | 29,929 | 30,131 |
| fuel costs (ON GTs) [€]        | 8,846  | 8,916  | 8,976  |
| GTs ON time [ $N_g \times T$ ] | 27     | 31     | 31     |
| GTs startup times [-]          | 5      | 4      | 5      |
| ESS degradation [%]            | 0.164  | 0.148  | 0.165  |

### State of charge evolution and energy bounds effect

An additional comparison demonstrating the additional benefits coming from method *III* over method *II* is illustrated in Fig. 10.6. The resulting  $x^{SoC}(t)$  signals from the application of *II* and *III* are depicted in Fig. 10.6a and Fig. 10.6b correspondingly. Notice that both methods respect the upper and lower state of charge limits, as originally designed in the default method *I*. Both trajectories seem to follow similar patterns, i.e. initial discharge until  $k = 9$ , smooth re-bouncing and discharge until  $k = 25$ , and charging until the end. There are however small but important differences, those being clearly depicted in the two zoomed areas ( $k = 11 - 15$  and  $k = 27 - 29$ ), where the maximum allowed energy deviation  $\overline{\Delta E^b}(t)$  from the frequency support offered by the ESS is illustrated with red error bars and the calculated upper bound  $\widehat{\Delta E^b}$  is illustrated with green error bars. It is evident that, for case *II*, there would be requirements for the ESS that could cause it to violate the upper bound  $\widehat{\Delta E^b} > \overline{\Delta E^b}(t)$  at  $k = 11, 14, 27, 29$ , while the method in *III* controlled the ESS in a way that  $\widehat{\Delta E^b} \leq \overline{\Delta E^b}(t)$  is guaranteed for the whole period.

## 10.4 CONCLUSIONS

Achieving optimal energy management in isolated power systems with energy storage and sudden load variations cannot be decoupled from ensuring their secure and robust operation, especially under the presence of intermittent renewable power sources. Even though decisions related to techno-economical operation are conventionally taken in the discrete time, those will inevitably affect the system's stability in its continuous operation and vice versa. To address this problem, this article proposed an energy management algorithm capable of integrating both higher time scale economic objectives and lower time scale stability constraints under adaptive uncertainty considerations. Additional constraints regarding the optimal use of the energy storage for providing flexibility and frequency support with bounded interaction between both services were proposed. A mixed integer linear programming formulation was derived and validated through time-domain simulations for an isolated offshore O&G platform integrating wind power. The results indicated that, under the proposed adaptive uncertainty framework, optimal decisions with dynamic frequency stability guarantees could be achieved and secured the system under an adaptive assessment of possible active power perturbations. This also reduced the conservatism from setting fixed damping and inertia requirements based on the expected worst-case and allowed better scheduling and operation of the GTs for longer periods. At the same time, the optimal sharing of primary frequency control contribution from conventional generators and the energy storage was

found, while ensuring a tolerable impact on the storage optimal state of charge schedule and a negligible impact on the rest energy management objectives.

The presented method targeted a small scale autonomous power systems (an isolated offshore O&G platform), but the formulation is based on general principles and can potentially be applied to bulk power systems, where enough computational resources and proper assumptions (e.g., aggregation of regions/generator groups) are applied to solve the optimization problem within the scheduling period (i.e., 15 min.). Remark that, while possible configurations grow exponentially with the number of generators, a strong mixed integer linear programming structure is preserved in the proposed method, allowing an efficient solution of the resulting optimization problem. A topic for future research therefore may be verifying the applicability of the suggested algorithm to regional dispatch centers that can operate autonomously. From this perspective, a practical implementation in bulk power system also demands a standard framework for real-time command and telemetry of frequency reserves from the dispatch center to local primary controllers, which not only is a topic for future research but also should be addressed by regulatory and standardization bodies.

#### FUNDING

This research was funded by: 1) VISTA - a basic research program in collaboration between The Norwegian Academy of Science and Letters, and Equinor; 2) the Onassis Foundation - Scholarship ID: F ZP 056-1/2019-2020; 3) the Research Council of Norway under the program PETROMAKS2, grant number 281986, project “Innovative Hybrid Energy System for Stable Power and Heat Supply in Offshore Oil and Gas Installation (HES-OFF)”.

#### 10.5 REFERENCES

- [1] Ying-Yi Hong and Gerard Francesco DG Apolinario. Uncertainty in Unit Commitment in Power Systems: A Review of Models, Methods, and Applications. *Energies* **14** (20), 6658 (January 2021). ISSN 1996-1073. doi: 10.3390/en14206658. Cited on p. 188.
- [2] X. Xia and A. M. Elaiw. Optimal dynamic economic dispatch of generation: A review. *Electric Power Systems Research* **80** (8), 975–986 (August 2010). ISSN 0378-7796. doi: 10.1016/j.epsr.2009.12.012. Cited on p. 188.
- [3] Baraa Mohandes, Mohamed Shawky El Moursi, Nikos Hatziargyriou, and Sameh El Khatib. A Review of Power System Flexibility With High Penetration of Renewables. *IEEE Transactions on Power Systems* **34** (4), 3140–3155 (July 2019). ISSN 0885-8950, 1558-0679. doi: 10.1109/TPWRS.2019.2897727. Cited on p. 188, 189.
- [4] Florian Dorfler, Saverio Bolognani, John W. Simpson-Porco, and Sergio Grammatico. Distributed Control and Optimization for Autonomous Power Grids. In *2019 18th European*

- Control Conference (ECC)* pages 2436–2453 Naples, Italy (June 2019). IEEE. ISBN 978-3-907144-00-8. doi: 10.23919/ECC.2019.8795974. Cited on p. 189.
- [5] Commission Regulation (EU). Guideline on electricity transmission system operation (August 2017). URL <http://data.europa.eu/eli/reg/2017/1485/oj>. Cited on p. 189, 190.
- [6] Erick Fernando Alves, Louis Polleux, Gilles Guerassimoff, Magnus Korpås, and Elisabetta Tedeschi. Allocation of spinning reserves for autonomous grids subject to frequency stability constraints and short-term solar power variations. (2022). doi: 10.48550/ARXIV.2203.07233. Cited on p. 189.
- [7] Lukas Sigrist, Luis Rouco, and Francisco Miguel Echavarren. A review of the state of the art of UFLS schemes for isolated power systems. *International Journal of Electrical Power & Energy Systems* **99**, 525–539 (July 2018). ISSN 0142-0615. doi: 10.1016/j.ijepes.2018.01.052. Cited on p. 189.
- [8] Jianqiang Luo, Fei Teng, and Siqi Bu. Stability-Constrained Power System Scheduling: A Review. *IEEE Access* **8**, 219331–219343 (2020). ISSN 2169-3536. doi: 10.1109/ACCESS.2020.3042658. Cited on p. 190.
- [9] Vivek Prakash, Kailash Chand Sharma, Rohit Bhakar, Har Pal Tiwari, and Furong Li. Frequency Response Constrained Modified Interval Scheduling Under Wind Uncertainty. *IEEE Transactions on Sustainable Energy* **9** (1), 302–310 (January 2018). ISSN 1949-3029, 1949-3037. doi: 10.1109/TSTE.2017.2731941. Cited on p. 190.
- [10] Qingxin Shi, Fangxing Li, and Hantao Cui. Analytical Method to Aggregate Multi-Machine SFR Model With Applications in Power System Dynamic Studies. *IEEE Transactions on Power Systems* **33** (6), 6355–6367 (November 2018). ISSN 0885-8950, 1558-0679. doi: 10.1109/TPWRS.2018.2824823. Cited on p. 190.
- [11] Luis Badesa, Fei Teng, and Goran Strbac. Simultaneous Scheduling of Multiple Frequency Services in Stochastic Unit Commitment. *IEEE Transactions on Power Systems* **34** (5), 3858–3868 (September 2019). ISSN 0885-8950, 1558-0679. doi: 10.1109/TPWRS.2019.2905037. Cited on p. 190.
- [12] Vincenzo Trovato, Agnes Bialecki, and Anes Dallagi. Unit Commitment With Inertia-Dependent and Multispeed Allocation of Frequency Response Services. *IEEE Transactions on Power Systems* **34** (2), 12 (2019). Cited on p. 190.
- [13] Ziyang Zhang, Ershun Du, Fei Teng, Ning Zhang, and Chongqing Kang. Modeling Frequency Dynamics in Unit Commitment With a High Share of Renewable Energy. *IEEE Transactions on Power Systems* **35** (6), 4383–4395 (November 2020). ISSN 0885-8950, 1558-0679. doi: 10.1109/TPWRS.2020.2996821. Cited on p. 190.
- [14] Salar Saberi Oskouee, Sadegh Kamali, and Turaj Amraee. Primary Frequency Support in Unit Commitment Using a Multi-Area Frequency Model With Flywheel Energy Storage. *IEEE Transactions on Power Systems* **36** (6), 5105–5119 (November 2021). ISSN 0885-8950, 1558-0679. doi: 10.1109/TPWRS.2021.3074634. Cited on p. 190.
- [15] Tao Ding, Ziyu Zeng, Ming Qu, Joao P. S. Catalao, and Mohammad Shahidehpour. Two-Stage Chance-Constrained Stochastic Thermal Unit Commitment for Optimal Provision of Virtual Inertia in Wind-Storage Systems. *IEEE Transactions on Power Systems* **36** (4), 3520–3530 (July 2021). ISSN 0885-8950, 1558-0679. doi: 10.1109/TPWRS.2021.3051523. Cited on p. 190.
- [16] Vincenzo Trovato. System Scheduling with Optimal Time-varying Delivery Intervals for Frequency Response. *IEEE Transactions on Power Systems* page 16 (February 2022). Cited on p. 190.
- [17] Erick Fernando Alves, Gilbert Bergna-Diaz, Danilo Iglesias Brandao, and Elisabetta Tedeschi. Sufficient Conditions for Robust Frequency Stability of AC Power Systems. *IEEE Transactions on Power Systems* **36**, 2684–2692 (May 2021). ISSN 0885-8950, 1558-0679. doi: 10.1109/TPWRS.2020.3039832. Cited on p. 190, 192, 193, 194.



- [18] Hamed Ahmadi and Hassan Ghasemi. Security-Constrained Unit Commitment With Linearized System Frequency Limit Constraints. *IEEE Transactions on Power Systems* **29** (4), 1536–1545 (July 2014). ISSN 0885-8950, 1558-0679. doi: 10.1109/TPWRS.2014.2297997. Cited on p. 190.
- [19] Yunfeng Wen, Wenyuan Li, Gang Huang, and Xuan Liu. Frequency Dynamics Constrained Unit Commitment With Battery Energy Storage. *IEEE Transactions on Power Systems* **31** (6), 5115–5125 (November 2016). ISSN 0885-8950, 1558-0679. doi: 10.1109/TPWRS.2016.2521882. Cited on p. 190.
- [20] Chengming Zhang, Lu Liu, Haozhong Cheng, Dundun Liu, Jianping Zhang, and Gang Li. Frequency-constrained Co-planning of Generation and Energy Storage with High-penetration Renewable Energy. *Journal of Modern Power Systems and Clean Energy* **9** (4), 760–775 (2021). ISSN 2196-5625. doi: 10.35833/MPCE.2020.000743. Cited on p. 190.
- [21] Carmen Cardozo, Laurent Capely, and Philippe Dessante. Frequency constrained unit commitment. *Energy Systems* **8** (1), 31–56 (February 2017). ISSN 1868-3967, 1868-3975. doi: 10.1007/s12667-015-0166-4. Cited on p. 190.
- [22] Masoud Javadi, Turaj Amraee, and Florin Capitanescu. Look ahead dynamic security-constrained economic dispatch considering frequency stability and smart loads. *International Journal of Electrical Power & Energy Systems* **108**, 240–251 (June 2019). ISSN 01420615. doi: 10.1016/j.ijepes.2019.01.013. Cited on p. 190.
- [23] Yue Yin, Tianqi Liu, Lei Wu, Chuan He, and Yikui Liu. Frequency-constrained multi-source power system scheduling against N-1 contingency and renewable uncertainty. *Energy* **216**, 119296 (February 2021). ISSN 03605442. doi: 10.1016/j.energy.2020.119296. Cited on p. 190.
- [24] Amin Safari, Meisam Farrokhifar, Hossein Shahsavari, and Vahid Hosseinezhad. Stochastic planning of integrated power and natural gas networks with simplified system frequency constraints. *International Journal of Electrical Power & Energy Systems* **132**, 107144 (November 2021). ISSN 01420615. doi: 10.1016/j.ijepes.2021.107144. Cited on p. 190.
- [25] Miguel Carrión, Rafael Zárate-Miñano, and Federico Milano. Impact of off-nominal frequency values on the generation scheduling of small-size power systems. *International Journal of Electrical Power & Energy Systems* **122**, 106174 (November 2020). ISSN 01420615. doi: 10.1016/j.ijepes.2020.106174. Cited on p. 190.
- [26] IEEE Task Force on Turbine-Governor Modeling. Dynamic Models for Turbine-Governors in Power System Studies. Technical Report PES-TR1 IEEE New York, NY (August 2013). URL <https://resourcecenter.ieee-pes.org/publications/technical-reports/PESTR1.html>. Cited on p. 193.
- [27] Spyridon Chapaloglou, Damiano Varagnolo, Francesco Marra, and Elisabetta Tedeschi. Data-driven energy management of isolated power systems under rapidly varying operating conditions. *Applied Energy* **314**, 118906 (May 2022). ISSN 03062619. doi: 10.1016/j.apenergy.2022.118906. Cited on p. 195, 196, 197, 198, 201.
- [28] Leo Breiman. Random Forests. *Machine Learning* **45** (1), 5–32 (October 2001). ISSN 1573-0565. doi: 10.1023/A:1010933404324. Cited on p. 195.
- [29] Nicolai Meinshausen. Quantile Regression Forests. **7** (35), 983–999 (December 2006). ISSN 1532-4435. URL <http://jmlr.org/papers/v7/meinshausen06a.html>. Cited on p. 196.
- [30] E. F. Camacho and C. Bordons. Model Predictive Control. Advanced Textbooks in Control and Signal Processing. Springer London London (2007). ISBN 978-1-85233-694-3 978-0-85729-398-5. doi: 10.1007/978-0-85729-398-5. Cited on p. 197.
- [31] Maria Vrakopoulou, Kostas Margellos, John Lygeros, and Goran Andersson. A Probabilistic Framework for Reserve Scheduling and  $N-1$  Security Assessment of Systems With High Wind Power Penetration. *IEEE Transactions on Power Systems* **28** (4), 3885–3896 (November 2013). ISSN 0885-8950, 1558-0679. doi: 10.1109/TPWRS.2013.2272546.



Cited on p. 198.

- [32] Kári Hreinsson, Maria Vrakopoulou, and Göran Andersson. Stochastic security constrained unit commitment and non-spinning reserve allocation with performance guarantees. *International Journal of Electrical Power & Energy Systems* **72**, 109–115 (November 2015). ISSN 01420615. doi: 10.1016/j.ijepes.2015.02.017. Cited on p. 198.
- [33] Kostas Margellos, Paul Goulart, and John Lygeros. On the Road Between Robust Optimization and the Scenario Approach for Chance Constrained Optimization Problems. *IEEE Transactions on Automatic Control* **59** (8), 2258–2263 (August 2014). ISSN 0018-9286, 1558-2523. doi: 10.1109/TAC.2014.2303232. Cited on p. 198.



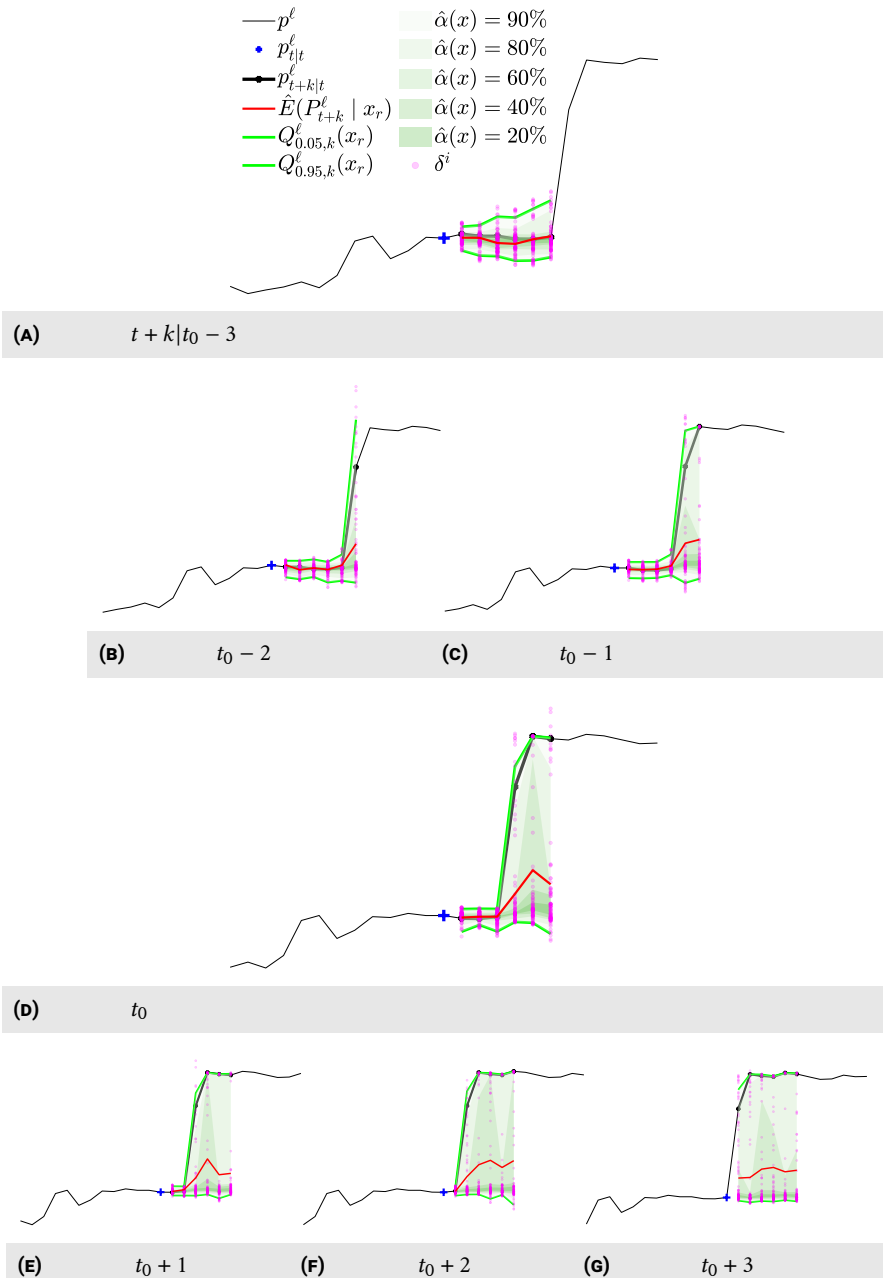


**FIGURE 10.3.** Demonstration of adaptive uncertainty quantification by using auto-regressive probabilistic forecasting for the load time-series. A case for a sudden step-like variation is presented for consecutive lead times (Figs. 10.3a to 10.3g). By updating the estimated prediction intervals it is possible to capture the sudden load variation and draw samples (purple dots) that span an appropriate range of values. © Spyridon Chapaloglou *et al*, 2022.

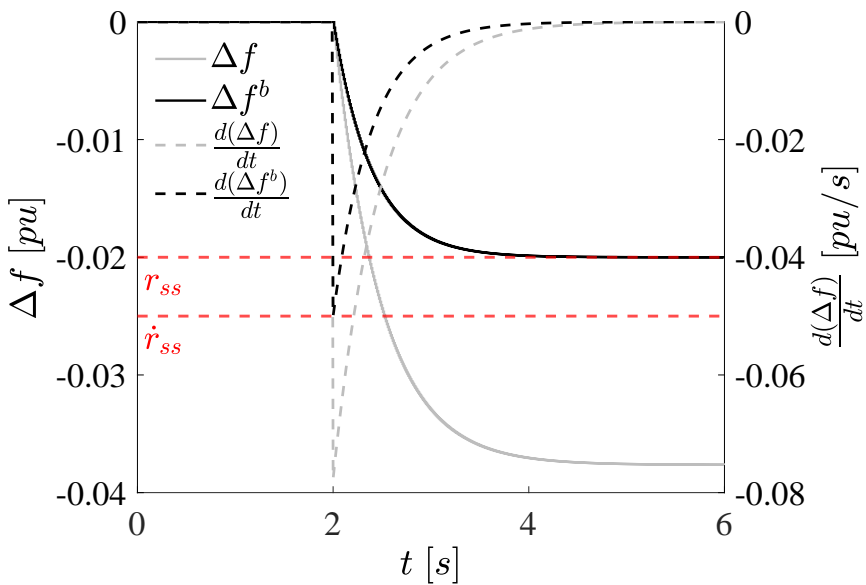
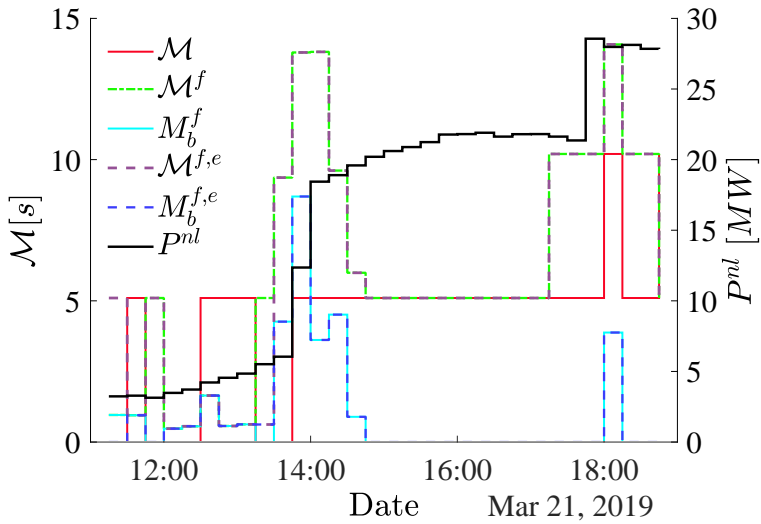
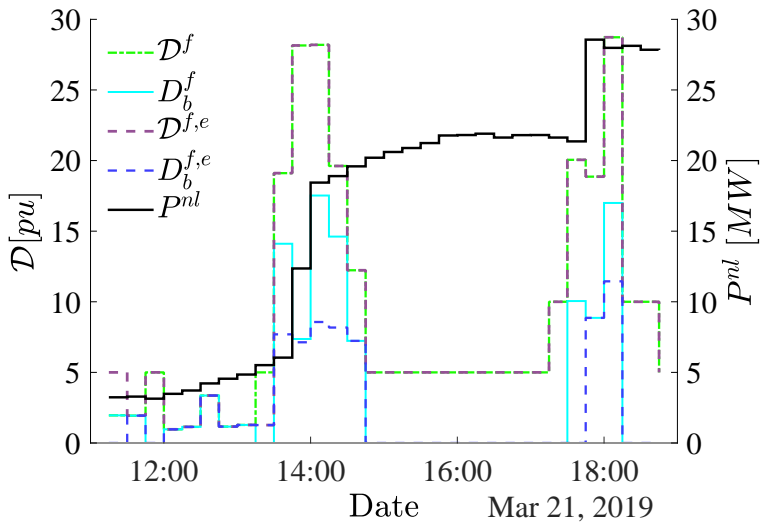


**FIGURE 10.4.** Effect of the optimally calculated participation of the ESS in providing frequency support for a step load change when only 1 GT is on. In contrast with the case of non participation of the ESS to frequency regulation (solid and dashed grey lines), the optimally designed virtual inertia and damping results in a frequency response (solid black) and rate of change of frequency (dashed black) that are bounded by their defined limit values. © Spyridon Chapaloglou et al, 2022.

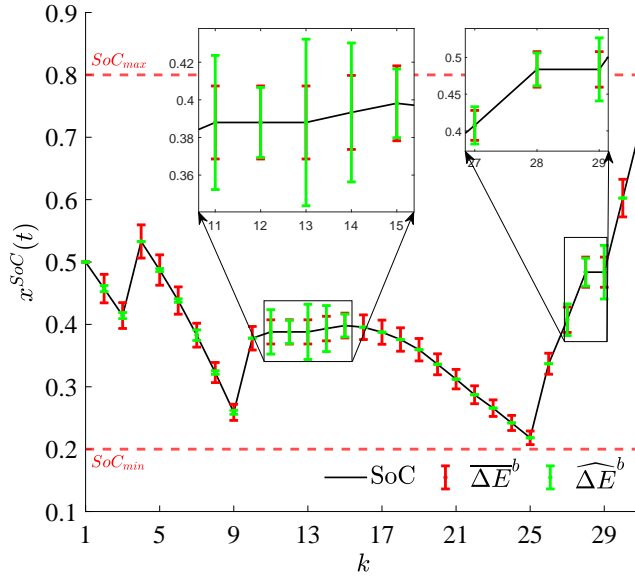


(A) Total system inertia.

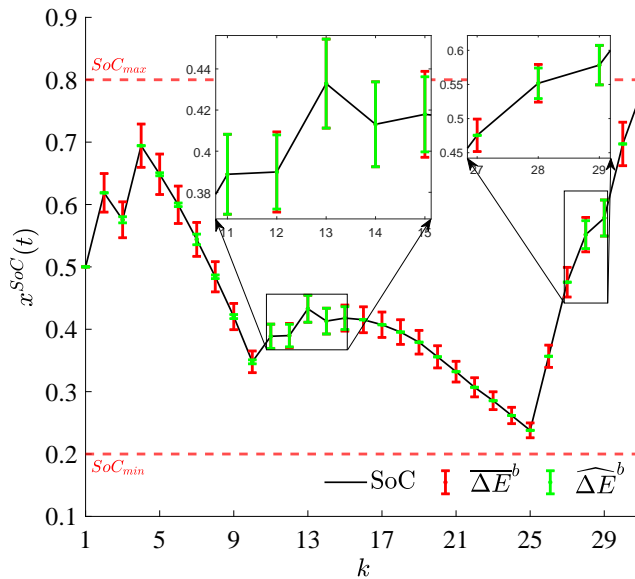


(B) Total system damping.

**FIGURE 10.5.** Trajectories of the optimally designed system inertia (top) and damping (bottom) and optimal split between primary control provision by the GTs and the ESS for different bounds considerations. The simulated results are plotted against the net load signal (solid black) for a case where sudden step-like variations occur. © Spyridon Chapaloglou et al, 2022.



(A) Without bounds on the energy deviation.



(B) With bounds on the energy deviation.

**FIGURE 10.6.** State of charge trajectories from the optimal scheduling and primary control design of the ESS, during the simulation period, for the cases of not including bounds on the resulting energy deviation from the participation in primary frequency control (top) and the one when including the bounds (bottom). © Spyridon Chapaloglou et al, 2022.



Part III

# EPILOGUE





## CHAPTER 11

### *Closing remarks*

---

The overall goal of this doctoral work was to investigate and propose frameworks to optimize **energy storage (ES)** delivering frequency control in autonomous power systems. Most of the results and findings of this thesis were presented in the context of the **Innovative Hybrid Energy System for Stable Power and Heat Supply in Offshore Oil & Gas Installation (HES-OFF)** project using the case study of an offshore **oil and gas (O&G)** platform in the North Sea that shall be interconnected to an offshore wind farm. For this study case, a thorough investigation into equipment sizing methodologies and allocation procedures for frequency reserves was performed, including the use of flexible loads and a centralized **energy storage system (ESS)** composed of electrochemical batteries, electrolyzers, and fuel cells, and the coordination of these reserves in real-time using an energy management algorithm. The insights provided and frameworks proposed, however, were based on general principles that can be expanded and applied to other types of autonomous power systems and microgrids in islanded mode, such as islands, ships, remote communities, and industrial or military installations.

Most of the research efforts were dedicated to the development of power system optimization models and formulations, including the exploration of alternative methods, that could increase the understanding of the core problem at hand: size the reserves to ensure frequency stability. A key task was establishing criteria that could be integrated into power system optimization models for planning and operation to: 1) properly size **variable renewable energy sources (VRESs)** and **energy storage devices (ESDs)**, 2) allocate active power reserves for frequency control, and 3) specify desired properties of **power electronic converters (PECs)**. In this context, models and optimization formulations had to manage two conflicting requirements:

1. *Precision*, which is necessary not only to minimize supply insecurity and expenditures, but also to evaluate non-desired effects, such as reduction of stability margins, increased emissions of **greenhouse gases (GHG)**, or wear and tear of equipment.
2. *Speed*, which is required to solve the unit commitment and dispatch

problem in an acceptable interval of time.

To this end, this Ph.D. thesis had three main objectives, as earlier highlighted in the Preface. The following sections summarize the research work performed, its key ideas, and discusses the main scientific contributions associated with each of the objectives.

### 11.1 OBJECTIVE 1: REVIEW THE ACTIVE POWER BALANCE PROBLEM AND THE PRINCIPLES OF FREQUENCY CONTROL AND STABILITY IN AC POWER SYSTEMS BASED ON FIRST PRINCIPLES

The initial phase of the research work was dedicated to better understanding the HES-OFF concept and identifying the challenges associated with frequency control in autonomous power systems. This preliminary investigation used a bottom-up approach, where detailed models were applied to represent components of the ac power system in autonomous offshore platforms fed by gas turbines (GTs) but where high penetration of wind power is possible. The analyses, using detailed models, focused on frequency and voltage dynamics in a time scale of seconds and evaluated: 1) power quality and stability issues, 2) the effect that load and wind power variations could have on the GTs operation, 3) how ES and faster controls can improve power quality in the HES-OFF concept, and 4) factors that affect ES sizing.

Based on the insights of this investigation, a simplified dynamic model of the HES-OFF concept was developed, resulting in a reduction of simulation time between one and two orders of magnitude. The results of these initial investigations were reported in Chs. 3 and 4, and the obtained simplified model was a stepping stone to the research work reported in Chs. 5 and 6.

This effort was also important in understanding that active power balance and frequency control problems involve optimization of power flows and use of ES in several time scales, where there is coupling between dynamics in these different time scales and a finer granularity (lower than one second) may be required for capturing trade-offs among them. From the faster to the slower frequency dynamics and control, the periods after a large active power disturbance can be divided in arrest, rebound, and recovery periods, while the reserves used to re-establish active power balance in these periods are fast frequency reserve (FFR), frequency containment reserve (FCR) and frequency restoration reserve (FRR), respectively. To capture the dynamics of the arrest and rebound periods, it is necessary to use detailed models for actuators (e.g., valves, PECs) and controllers (e.g., turbine governors, phase-locked loops (PLLs), primary and secondary controllers and their deadbands). The energy requirements for frequency control in the arrest period and FFR, however, are negligible

in capital expenditure (CAPEX) and operational expenditures (OPEX) terms when compared to the demands of FCR and FRR in the rebound and recovery periods. Active power requirements are indeed the main CAPEX driver for ESDs that shall provide FFR, and strategies for effective energy management in these devices are the main OPEX driver. A summary of these insights was reported in Chs. 1 and 8.

## 11.2 OBJECTIVE 2: IDENTIFY GAPS IN CURRENT MODELING PRACTICES THAT CAN AFFECT PLANNING AND OPERATION LOW-INERTIA, AUTONOMOUS POWER SYSTEMS WHERE HIGH PENETRATION OF VRESs EXISTS

The second phase of the Ph.D. research work focused on better understanding how frequency stability constraints are integrated in optimization problems for techno-economic planning and operation of power systems. This process allowed for the identification of some gaps in current modeling practices, which can affect the optimality of solutions in low-inertia, autonomous power systems where high penetration of VRESs exists.

The techno-economical problem involved in planning and operation of power systems requires a granularity in the decision making from five minutes and up to one hour to make the optimization problem tractable from a computational and operational perspective when long time horizons (days, weeks, months, years) are considered. This restriction requires a top-down approach in modeling, where a trade-off between model precision and solution time is necessary. Precision is typically emphasized in elements that have a high participation factor in expenses or critical system constraints, while simplifying assumptions are employed to the rest of the system to speed up calculations. Under this logic, planning optimization problems have traditionally allocated only FRR in their formulation, while operational problems have addressed FCR allocation as well. An overview of these security-constrained active power flow problems was presented in Ch. 2.

Misleading results were, however, obtained where established logic, models, and assumptions used in planning problems of interconnected power systems were applied to low-inertia autonomous power systems in which a penetration of variable VRESs between 25 and 90 % of the installed load was possible. Analyses of results from different cases of the HES-OFF concept suggested that an overestimation of the economic and environmental benefits from VRESs and oversizing of ES capacity may occur where frequency stability constraints and FCR are ignored in planning problems, as described in Chs. 5 and 6. The findings from the HES-OFF project were also corroborated in a different study case depicting a land-based O&G installation where solar photovoltaic (PV) and electrochemical batteries have been employed. This study case is portrayed

in Ch. 9 and suggests that savings in  $CO_2$  and **levelized cost of energy (LCOE)** might be overestimated and **ES** capacity oversized where frequency stability constraints are neglected.

Moreover, it was identified that nonlinear effects can lead to an underestimation of required **FCR** where large frequency deviations occur. Such a condition is more common in low-inertia, autonomous power systems with high penetration of **VRES**, where frequency variations of up to 5% are allowed during transients. To address this issue, Ch. 7 introduced an algebraic equation that provides sufficient conditions for frequency stability where power systems are subject to nonlinear effects and large frequency variations. This equation is based on four parameters that are typically defined according to security assessments, grid codes, or industry standards requirements, and allows frequency stability constraints to be included in power system optimization models without resorting to time-domain simulations or unnecessary linearization of the power balance equations.

Ch. 8 also presents a framework to size hybrid **ESSs** providing **FFR** and **FCR**, where algebraic equations are used to define requirements for the rated energy and power capacity of **ESDs**, and a systematic procedure is presented to specify the main components of **PECs**. The use of algebraic equations allows calculations to be included in optimization problems. Further, the application of this procedure in a case study of the **HES-OFF** project indicates that the system designer can take advantage of storage technologies having distinct characteristics to obtain a certain frequency control performance.

### 11.3 OBJECTIVE 3: EXPLORE HOW FREQUENCY CONTROL AND STABILITY CONSTRAINTS CAN BE INTEGRATED INTO DIFFERENT POWER SYSTEM OPTIMIZATION MODELS

As stated in the previous section, the second phase of the **Ph.D.** research work focused on better understanding how frequency stability constraints are integrated in optimization problems for techno-economic planning and operation of power systems. This process also allowed the formulation of innovative frameworks to include frequency stability constraints in power system optimization models for planning and operation of low-inertia autonomous power systems with high penetration of **VRESs**. Coupling effects in the faster time scales were partially integrated in optimization algorithms when applying proper assumptions, model reduction techniques, and methods from disciplines such as mathematical optimization, data science, and nonlinear control theory.

**Chs. 5** and **6** presented a framework to include frequency stability constraints in the nonlinear optimization problem of a multi-domain energy system

based on time-domain simulations of the surrogate model introduced in Ch. 4. This technique was applied in a planning problem, namely the case study of the HES-OFF project, where a genetic algorithm evaluated simultaneously the system performance in terms of process metrics (energy efficiency and CO<sub>2</sub> emissions) as well as the robustness of the proposed solution to plausible transients (wind power and load variations).

Ch. 9 introduced a framework to include frequency stability constraints in linear optimization problems solved by mixed integer linear programming. The method has been applied to a planning problem using the case study of an industrial plant, where solar PV and battery ESS were sized to reduce the LCOE of the system. The set of constraints proposed in this work modeled faster frequency dynamics and let the battery size be reduced by 67.6% compared to the traditional approaches used in bulk power systems, which typically ignore allowed short-term frequency variations in models and the complementary action between FCR and FRR delivered by batteries and GTs, respectively. Ch. 10 presented an extension of this method to a real-time operational problem, where FFR delivered by the batteries is also allocated. The algorithm for the energy management system (EMS) of a generalized autonomous power system allocates time-varying optimal frequency control reserves (i.e., FFR, FCR and FRR) to achieve optimal scheduling and to secure a frequency stable operation under dynamic uncertainty. The results in both works were validated against time-domain simulations of detailed power system models.

#### 11.4 RECOMMENDATIONS FOR FUTURE RESEARCH

This section presents a summary of the open questions discussed in Chs. 4 to 10 and that continue to be relevant to this date, combined with new insights obtained recently.

This Ph.D. thesis proposed constraints to the unit commitment and dispatch problems aiming to ensure frequency stability and proper allocation of frequency reserves in autonomous power systems. The models developed ignore network topology and voltage dynamics and, therefore, do not consider reactive power flows, rotor angle, and voltage stability. Note that this decision was intentional and part of the trade-off between precision and speed discussed earlier in the introduction of this chapter and throughout this thesis. From a practical perspective, an immediate extension of this work would be to adapt the ideas proposed in Chs. 9 and 10 to optimal power flow problems. From a theoretical outlook, the analysis of voltage and rotor angle dynamics requires detailed models of synchronous machines and converter-interfaced generators. To make the problem more tractable, an approach would be to separate the

analysis into two time scales: slow (frequency) and fast (rotor angle and voltage) dynamics. If such separation holds, the algebraic boundary condition presented in Ch. 7 continues to be valid and a similar analysis can be applied to obtain a new independent set of sufficient conditions for rotor angle and voltage stability. It is fundamental, in this case, to also investigate the conditions under which the time scale separation holds, an effort that may involve an analysis of dc voltage and PLL stability in PEC, as pointed out in Sec. 1.3.

There is also numerous possibilities to be investigated regarding the reliability and maintenance of electrical and electromechanical equipment in industrial installations affected by VRESs and the best control strategies for allocation of frequency reserves to reduce GHG and OPEX simultaneously. As pointed out in Chs. 3 to 6, increased frequency deviations translate into more actuation of turbine governors. This situation increases the wear and tear of electromechanical actuators and torque pulsations at the shaft of electrical machines connected to the grid without a motor drive. It was indicated in Chs. 3, 4 and 9 that large frequency deviations in the negative direction (i.e., lack of power generation) can also cause magnetic over-flux in electrical machines and transformers. This situation may cause serious damages to these pieces of equipment, due to increased losses, heating, and induced voltage gradient between laminations that can break down the core insulation. A more in-depth qualitative and quantitative analysis of how the penetration of VRES influences these reliability and maintenance issues and OPEX is required, as well as an investigation of how controllers and ESDs can be optimized to reduce negative effects.

Where the continuation of the HES-OFF project's research work is considered, the frameworks described in Chs. 8 and 9 can be integrated into the research-based prototype tool in Python available at <https://github.com/RoberAgro/HES-OFF>. An extension of Ch. 8's framework including a simplified model of time delays of controllers and actuators can increase the calculation precision of the active power and energy requirements in the arrest and rebound periods. It is also recommended to evaluate the EMS algorithm proposed in Ch. 10 in the laboratory using hardware-in-the-loop simulation, therefore validating its performance during real-time operation in a production-like environment.

Last, this research has quantified the need for representing the physics of faster dynamics (i.e., in the order of seconds) in optimization models of autonomous power systems. This representation is necessary not only to correctly allocate frequency reserves and size ESSs, but also to rightly assess the economic and environmental benefits of VRESs. Interconnected power systems will behave more and more as a collection of transactive autonomous power systems as the energy transition progresses and the installation of advanced

EMSs, distributed VRES, and ESSs increases. Further research is therefore necessary to expand the ideas introduced in this thesis to the hierarchical investment models applied to interconnected power systems, such as capacity expansion and resource planning models.







## Copyright permissions

---

Below is the complete list of the copyright figures shown in this [Ph.D.](#) thesis.

§ [Fig. 5.1](#)<sup>1</sup> is adapted with permission from:

<sup>1</sup>page 59



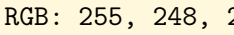
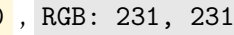


Luca Riboldi, Erick F Alves, Marcin Pilarczyk, Elisabetta Tedeschi, and Lars O. Nord. Innovative hybrid energy system for stable power and heat supply in offshore oil & gas installation (HES-OFF): System design and grid stability. In Proceedings of the 30th European Symposium on Computer Aided Process Engineering (ESCAPE30) volume A pages 211–216 Milano, Italy (May 2020). Elsevier. doi: [10.1016/B978-0-12-823377-1.50036-7](https://doi.org/10.1016/B978-0-12-823377-1.50036-7).  
Copyright © 2020 Elsevier.



## COLOPHON

This thesis was typeset using L<sup>A</sup>T<sub>E</sub>X and the book documentclass. Main text is contained within the dimension of 115 mm (width)/197.2 mm (length), where the horizontal (top:bottom) and vertical (left:right) margin ratios are 1:1. The width of the margin notes is 12 mm. The style of this thesis was adapted from Dr. Andreas Liudi Mulyo's Philosophiæ Doctor thesis *Molecular Beam Epitaxy of GaN/AlGaN Nanocolumns on Graphene: for Potential Application in Ultraviolet Light-Emitting Diodes* [<https://hdl.handle.net/11250/2759464>] and its Overleaf template [<https://www.overleaf.com/latex/templates/phd-v2-alm-template/ghynwwhqbmwr>].

Sebastian Kosch's *Crimson* [<https://github.com/skosch/Crimson>] is set as the running text (11 pt) typeface. Matthew Carter's *Charter* acts as the title (14.4 pt), section (10 pt), subsection (10 pt), and header (8 pt) typefaces. Hermann Zapf's *Palatino* serves as the page (9 pt) typeface. Christian Robertson's *Roboto* [<https://tug.org/FontCatalogue/roboto/>] is utilized for the figure caption (8 pt) typeface. Libertine Open Fonts Project's *Linux Libertine* [<https://tug.org/FontCatalogue/linuxlibertine/>] and Linus Romer's *Miama Nueva* [<https://tug.org/FontCatalogue/miamanueva/>] are used for math/equation (11 pt) and calligraphical (14.4 pt) typefaces. The `textgreek` package [<https://www.ctan.org/pkg/textgreek>] provides Greek letters in normal font (being not *italicized* as in  $\$math\$$  mode).

Six distinct color palettes exploited throughout this thesis are listed as follows:  ,  ,  ,  ,  , and  .

The references were processed by BibTeX/natbib with the backref option enabled and a modified unsrtnat bibliography style. Further details about the packages used in this thesis and its L<sup>A</sup>T<sub>E</sub>X source (template) are available at <https://andreasliudimulyo.github.io/#latex>.

Most of the graphics in this thesis were generated by PGF/TikZ [<https://tikz.dev/>], Draw.io [<https://draw.io/>], and Python [<https://www.python.org/>] using Matplotlib [<https://matplotlib.org/>] and Plotly [<https://plotly.com/python/>] libraries.

*Final Version* as of Tuesday 25<sup>th</sup> April, 2023 at 22:43:11.

ISBN 978-82-326-5254-9 (printed ver.)  
ISBN 978-82-326-5867-1 (electronic ver.)  
ISSN 1503-8181 (printed ver.)  
ISSN 2703-8084 (online ver.)



**NTNU**

Norwegian University of  
Science and Technology